Dissertation zur Erlangung des Doktorgrades

der Fakultät für Chemie und Pharmazie

der Ludwig-Maximilians-Universität München

Chemical modification of cytokine receptors at the surface of living cells

Peter Schultz

aus

Lörrach, Deutschland

2021

Erklärung

Diese Dissertation wurde im Sinne von § 7 der Promotionsordnung vom 28. November 2011 von Frau Prof. Dr. Petra Schwille betreut und von Herrn Prof. Dr. Dirk Trauner von der Fakultät für Chemie und Pharmazie vertreten.

Eidesstaatliche Versicherung

Diese Dissertation wurde eigenständig und ohne unerlaubte Hilfe erarbeitet.

München, 13.01.2021

Peter Schultz

Dissertation eingereicht am 18.01.2021

1. Gutachter: Prof. Dr. Dirk Trauner

2. Gutachterin: Prof. Dr. Petra Schwille

Mündliche Prüfung am 25.02.2021

"The important thing is not to stop questioning."

Albert Einstein

Danksagung

An dieser Stelle möchte ich allen danken, die zum Gelingen dieser Arbeit beigetragen und mich unterstützt haben, nicht nur als Mensch, sondern auch als Wissenschaftler.

Zuerst darf ich mich bei meiner Betreuerin, Frau Prof. Dr. Petra Schwille, für die Möglichkeit meine Promotion in ihrem Forschungslabor zu absolvieren, recht herzlich bedanken. Das Schwille-Labor bietet einen einzigartigen Platz zur freien Entfaltung der eigenen Gedanken und Forschungsinteressen.

Des Weiteren möchte ich Herrn Prof. Dr. Dirk Trauner meinen Dank aussprechen, der nicht nur als offizieller Betreuer meiner Promotion, sondern auch als ständiges Mitglied meines Thesis Advisory Committee viele wichtige Ideen und Entscheidungen anregte.

Sodann möchte ich Herrn Prof. Dr. Reinhard Fässler danken, der mit seiner begeisternden Art während unserer Thesis Advisory Committee Treffen meine Forschungsarbeit förderte.

Ganz besonders aber fühle ich mich Herrn Dr. Thomas Weidemann zum Dank verpflichtet. Als ein wahrer Mentor der alten Schule hat er nicht nur mein wissenschaftliches, sondern auch mein privates Leben nachhaltig geprägt. Darüber hinaus möchte ich ihm danken, dass ich auf dem überaus interessanten Gebiet der Interleukin-4-Rezeptorforschung arbeiten durfte. Frederik Steiert darf ich für seine langjährige Freundschaft und die erfolgreiche Zusammenarbeit herzlich danken. Auch Gosia Poczopko und Dr. Henri Franquelim danke ich, da sie mir viele Tipps im Laboralltag gaben. Die tiefgründigen wissenschaftlichen Diskussionen unseres "Team Signalling" (Thomas, Frederik und Gosia) haben mich stets motiviert und angetrieben und werden mir sehr fehlen.

Ich danke den aktuellen und ehemaligen Gruppenmitgliedern sowie allen Angestellten des Schwille-Labors. Sie haben das Labor zu einem Ort gemacht, an welchen man jeden Morgen gerne zurückkehrte.

Danke auch den fleißigen Korrekturlesern Thomas, Monika und Martin.

Und mein besonderes Dankeschön gilt meiner Familie, meiner Mutter, Daniel, Monika, Martin und Opa für ihre immerwährende Unterstützung und ihren liebevollen Zuspruch. Besonders meiner Mutter, die den Grundstein meiner Karriere durch ihre aufopfernde Art legte, bin ich zutiefst verpflichtet. Zuallerletzt möchte ich mich noch bei meiner Partnerin Sonja bedanken für ihre große Geduld und die bisweilen tröstenden, immer aber motivierenden Worte während des von Corona begleiteten Zieleinlaufs meiner Promotion.

Publications

Peer-reviewed publications:

F. Steiert, E. P. Petrov, **P. Schultz**, P. Schwille, T. Weidemann, *Biophysical journal* **2018**,*114*, 2419-2431.

Z. B. Mehta, N. R. Johnston, M. S. Nguyen-Tu, J. Broichhagen, **P. Schultz**, D. P. Larner, I. Leclerc, D. Trauner, G. A. Rutter, D. J. Hodson, *Sci Rep* **2017**, *7*, 291.

Manuscript in preparation:

P. Schultz*, F. Steiert*, G. Cardone, T. Müller, K. Lang, P. Schwille, and T. Weidemann: Resolving receptor states in living cells by calibrated ratiometric imaging.

* equal contribution to this work

Summary

In this work covalent protein modification was used to analyse the function and conformational states of the Interleukin-4 receptor alpha (IL-4Rα) at the plasma membrane of living cells. The IL-4Rα subunit is a member of the class I cytokine receptor family which is linked to the JAK/STAT pathway and various other important signalling processes related to haematopoiesis and immunity. To explore molecular rearrangements during ligand-induced receptor activation, covalent site-specific fluorescence labelling was established by genetic code expansion (GCE) in combination with biorthogonal click chemistry. The unnatural amino acid N^{ε}-(bicyclo[6.1.0]non-4-yn-9-yl-methoxy)carbonyl-L-lysine (BCNK) was incorporated into the extracellular domain (ECD) of IL-4Rα to function as a site-specific reactive group for covalent coupling of fluorescent tetrazine-dye constructs. Site-specificity, stability, and efficiency of the inverse electron-demand Diels-Alder cycloaddition (IEDDAC) reaction was evaluated by calibrated confocal microscopy, an approach that allows to extract concentrations from confocal cross-sections. Calibration is based on additional fluorescence correlation spectroscopy (FCS) measurements of standard dyes for which a quantitative relation to the conjugated dyes at the cell surface is established.

Varying the parameter space of the click labelling conditions showed that quantitative receptor labelling was not feasible with this molecular system. Side reactions with free thiols, slower coupling kinetics at the cell surface as compared to bulk solution, as well as unknown determinant of the protein surface led to significantly reduced labelling efficiencies. However, the degree of labelling achieved by optimized labelling conditions turned out to represent a robust, reproducible and very sensitive readout. Once these molecular determinants for the reaction would be understood, such a procedure could be used to gain insight into the conformational states at the surface of living cells.

Functional tests addressing ligand binding revealed further complications of the approach. While incorporation of BCNK at the binding epitope abolished ligand binding as expected, incorporation sites distant of the epitope were also affected. Our data suggest that BCNK incorporation, which occurs prior to protein folding, affects the tertiary

structure of the receptor and, thus, labelling-sites must be screened for functionality before experiment. In addition to calibrated imaging, we employed an environment sensitive dye for performing fluorescence lifetime imaging microscopy (FLIM) in the absence and presence of ligand Interleukin-4 (IL-4). The data are in surprising agreement with a previously proposed rearrangement of the two FNIII domains in the receptor ECD. Lifetime changes of labelling-sites located in the linker region between D1- and D2-domains were significant and opposite suggesting a swap movement during activation. Furthermore, the only location of D2 where increased flexibility was gained is a central position of the highly conserved WSXWS motif in the activation loop. Thus, the data highlight the dynamic role of the activation loop for receptor activation in a fashion that cannot be inferred from crystal structures.

Spatiotemporal activation of cell signalling pathways is important for precise signalling. A single click labelling pulse followed by a time-dependent chase of labelled IL-4Rα with calibrated imaging allowed to determine the residence time at the cell surface. The results show that the receptor tail is crucial for internalization. To address the question whether JAK/STAT pathway triggering requires internalized receptors we performed experiments with a covalently biotinylated IL-4 ligand, coupled to a phase separated supported lipid bilayer (SLB). The results show that the type 1 IL-4R complex (IL-4Rα/IL-4/IL-2Rγ) can indeed be assembled at the cell surface. However, a selective activation of the JAK/STAT pathway by the native type 2 IL-4R complex (IL-4Rα/IL-4/IL-13Rα1) could not be concluded, as with this setup trace amounts of ligand stayed in the supernatant. In summary, covalent protein modifications on the IL-4R system displayed various insights into the JAK/STAT pathway activation, such as ECD rearrangements, membrane residence time, as well as subcellular localization and trafficking behaviour.

Table of contents

List of Figures

List of Tables

Abbreviations

AA	Amino acid
AbK	3'-azibutyl-*N*-carbamoyl-L-lysine
APD	Avalanche photo diode
ATP	Adenosine triphosphate
B	Biotin
BCNK	N^{ε}-(bicyclo[6.1.0]non-4-yn-9-yl-methoxy)carbonyl-L-lysine
BP	Band pass
CC	Cross-correlation
CC	Coiled-coil domain
CCE	Change in click efficiency
CE	Cortical endosome
CHR	Cytokine receptor homology domain
CLIC	Clathrin independent carrier
CMV	*Cytomegalovirus*

CP	Cytoplasm
CPP	Counts per particle
CRMI	Calibrated ratiometric imaging
D1/D2	Domain 1/2
DM	Dichroic mirror
DNA	DNA-binding domain
D_t	Diffusion coefficient
EC	Extracellular
ECD	Extracellular domain
EGFP	Enhanced green fluorescent protein
Epo	Erythropoietin
F	Fluorescence signal
FBS	Fetal bovine serum
FCCS	Fluorescence cross-correlation spectroscopy
FCS	Fluorescence correlation spectroscopy
FEP	Free energy perturbation
FERM	Four-point-one, ezrin, radixin, moesin domain
FLIM	Fluorescence lifetime imaging microscopy
FNIII	Fibronectin type III
FOV	Field of view
GCE	Genetic code expansion
GEEC	GPI-AP-enriched early endosomal compartment
GH	Growth hormone
gp130	Glycoprotein 130
GTP	Guanosine triphosphat
H_6-tag	Hexa-histidine-affinity-tag
I4R	IL-4R consensus motif
IEDDAC	Inverse electron-demand Diels-Alder cycloaddition reaction
IFNAR1	Interferon alpha receptor 1
IFNAR2	Interferon alpha receptor 2
IFNα2	Interferon alpha 2

Ig	Immunoglobulin
IL	Interleukin
IL-2Rγ	Interleukin-2 receptor gamma
IL-4Rα	Interleukin-4 receptor alpha
IRS1	Insulin receptor substrate 1
ITIM	Immunoregulatory tyrosine-based inhibitory motif
JAK	Janus kinase
KD	Kinase domain
K_d	Dissociation constant
L2	Loop2
LK	Linker region
LP	Long pass
M	Membrane
MAPK	Mitogen activated protein kinase
MS	Mass spectrometry
N	Number of particles
NA	Numerical aperture
NA	NeutrAvidin
NC	Negative control
nf	Non-fluorescent
NHS	*N*-hydroxysuccinimide ester
NTD	N-terminal domain
o/n	Overnight
P	Excitation power
P	Phosphorylated tyrosine
Pak1	Serine/threonine-protein kinase Pak1
PC	Positive control
PFA	Paraformaldehyde
PI3K	Phosphatidylinositol-3-kinase
PKD	Pseudokinase domain
POI	Protein of interest

PT	Pixel time
Rab	Ras-related in brain
Rac1	Ras-related C3 botulinum toxin substrate 1
Ras	Rat sarcoma
ROI	Region of interest
rt	Room temperature
S	Structure factor
S	State
SH2	Src homology 2
SHIP	SH2-containing phosphatase
SHP-1	SH2-containing phosphatase-1
SLB	Supported lipid bilayer
SOCS	Suppressor of cytokine signalling
STAT	Signal transducer and activator of transcription
T	Triplet
TA	TraptAvidin
TAD	Transactivation domain
TCSPC	Time-correlated single photon counting
TIRF	Total internal reflection fluorescence
TMD	Trans membrane domain
Tpo	Thrombopoietin
trisNTA	Tris nitrilotriacetic acid
tRNA	Transfer ribonucleic acid
TYK2	Tyrosine kinase 2
uAA	Unnatural amino acid
USP18	Ubiquitin specific protease 18
βc	Common beta chain, IL-3Rβ
γc	Common gamma chain, IL-2Rγ

I Introduction

1 Cytokine signalling

Since the development of multicellular organisms, communication between cells has been crucial for survival. Cytokines are important signalling molecules for intercellular communication in the bodies of higher organisms.[1] They regulate vital developmental processes on different time scales, like haematopoiesis, inflammation and immune responses. As disorders of cytokine receptor signalling is associated with a broad spectrum of severe diseases, great medical interest persists. New developments in biochemistry lead to a broad spectrum of powerful tools, which allow manipulation and analysis of cytokine receptors at the single cell level with unprecedented detail and resolution.[2-5]

1.1 Cytokines and the JAK/STAT pathway activation

More than 50 cytokines are known, which are involved in the JAK/STAT pathway.[1] The activated pathway induces proliferation, differentiation, growth or apoptosis.[6] To activate the JAK/STAT pathway, cytokines first bind to their specific receptor on the surface of the target cell (Figure 1.1.1A). Cytokines are rather small single chain polypeptides of about 150 - 200 amino acids (AAs) and various tertiary structures.[6] The concentration levels of cytokines are very low and even in a picomolar range (10^{-10} - 10^{-12} M).[7, 8] The binding of the cytokine ligand leads to an activation cascade by which a member of Janus kinase (JAK) family is first activated. JAKs (JAK1, JAK2, JAK3 and Tyrosine kinase 2 (TYK2)) are about 1000 AA in size and consist of four conserved domains: An N-terminal four-point-one, ezrin, radixin, moesin (FERM) domain, an Src homology 2 (SH2) domain, a pseudokinase domain (PKD, catalytically defective) and the C-terminal kinase domain (KD) (Figure 1.1.1B).[6, 9] All four JAKs recognize two primary sequence motifs that locate

10 - 40 AA C-terminal of the transmembrane domain (TMD) in the receptor's cytoplasmic tail. Proximal to the TMD and therefore close to the inner leaflet of the plasma membrane,

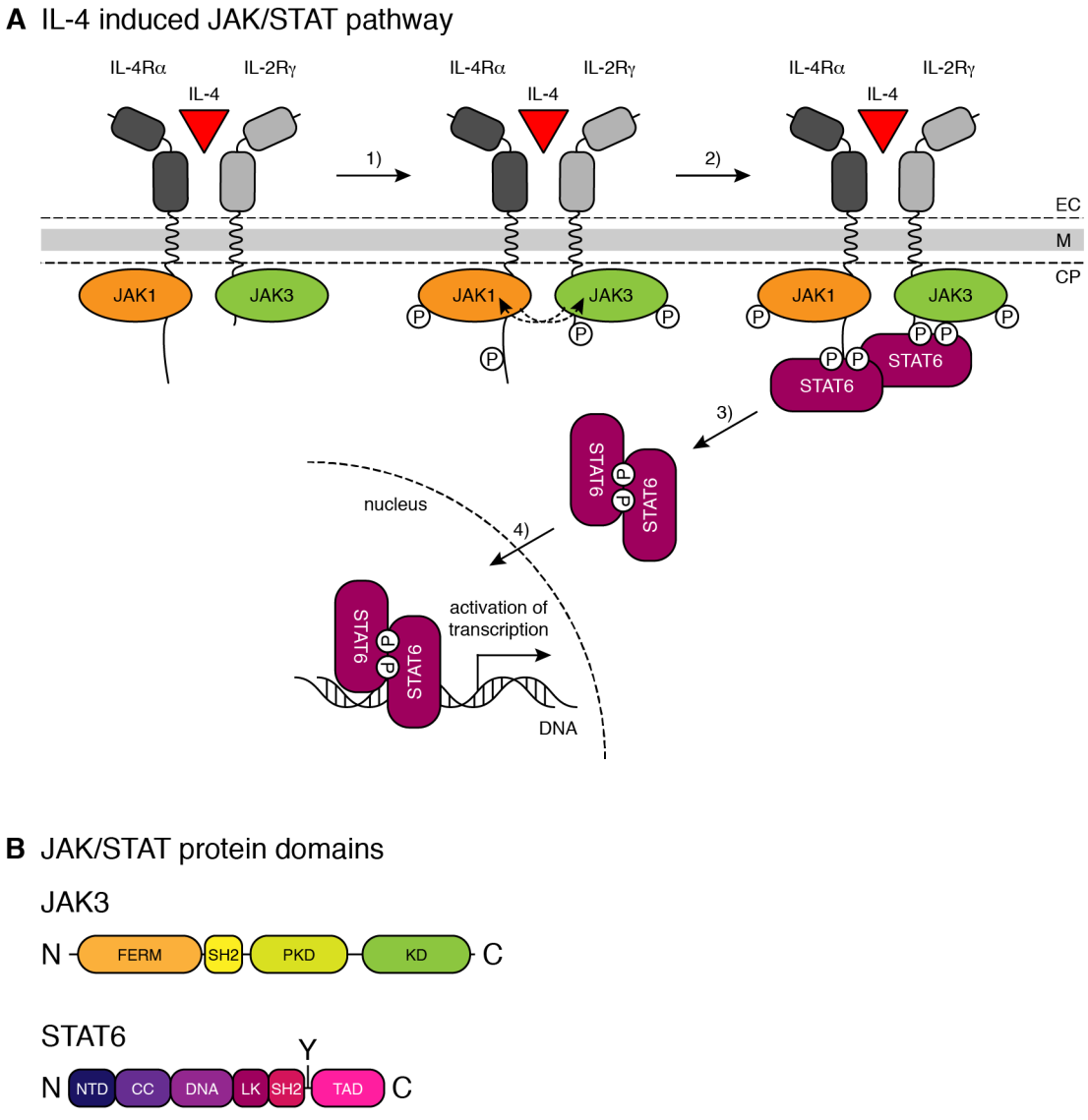

Figure 1.1.1: JAK/STAT pathway activation. A) Mechanism for the JAK/STAT pathway activation by the example of IL-4 type 1 signalling. The IL-4 ligand first binds its high affinity receptor IL-4Rα and then the second receptor IL-2Rγ is recruited. 1) The C-terminal receptor tails are transphosphorylated (dashed arrow) by the activated JAKs. 2) STAT6 is recruited to the phosphorylated receptor tails and is also phosphorylated by the JAKs. 3) Activated STATs dimerize in the cytoplasm, 4) are recruited to the nucleus and activate the DNA transcription. B) The domain structure of JAK3 and STAT6. A conserved single tyrosine (Y) is phosphorylated by JAKs upon activation of the pathway. CP, cytoplasm; EC, extracellular; M, membrane; P, phosphorylated tyrosine.[9-12]

the Box1 motif is bound by the FERM domain and further downstream the Box2 motif is recognized by the SH2 domain of the JAKs. The proline rich Box 1 motif and the hydrophobic Box 2 motif are responsible for determining which JAK binds to which receptor.[13-15] The JAKs are constitutively associated with the intracellular tail of the receptor and remain inactive in the absence of activating ligand. Upon receptor complex formation, JAKs transphosphorylate each other and specific tyrosine residues in the tail of the receptors (Figure 1.1.1A).[9, 16, 17] This is accomplished by the C-terminal KD which is highly regulated by the PKD.[18-21] The phosphorylated tyrosine residues at the receptor tails are docking sites for the transcription factor families of signal transducer and activator of transcription (STAT1-4, STAT5a, STAT5b and STAT6). STATs fulfil a double role by transducing signals from cytokines and simultaneously promoting the transcription of specific genes.[6] STAT proteins contain an N-terminal domain (NTD), a coiled-coil domain (CC) followed by the DNA-binding domain (DNA), a linker region (LK), an SH2 domain and a C-terminal transactivation domain (TAD). The activation of the STAT proteins is induced by JAK phosphorylation of the conserved single tyrosine which is located between the SH2 domain and the C-terminal TAD (Figure 1.1.1B).[10] Most STAT proteins are located as inactive dimers in the cytoplasm of the cell and get rapidly translocated to the nucleus after phosphorylation.[22] All STATs form homo- and heterodimers except for STAT2, which, in addition, can form a complex with other types of transcription factors.[23-25]

1.2 The cytokine class I Interleukin-4 receptor

For many years the cytokines Interleukin-4 (IL-4), Interleukin-13 (IL-13) and their associated Interleukin-4 receptor (IL-4R) have been important pharmacological targets. Both cytokines trigger the development of allergic and asthmatic symptoms. They are also responsible for many other severe diseases and key players in the defence against parasitic infections.[26, 27] Therefore, the IL-4R has been characterized extensively by biochemical as well as biophysical methods since its first isolation. Especially the multitude of microscopy experiments and the associated biophysical data of the receptor

at the cell surface of living cells represent fundamental insights in the field of cytokine receptor research.[28-30] Nevertheless, further research on the receptor is necessary to understand the precise mechanism of activation and the involved pathway partners.

The IL-4R belongs to the class I cytokine receptors.[31] This class is the largest group with 34 receptor chains and also known as the haematopoietic receptor family.[28, 32] The single transmembrane receptors are characterized by their N-terminal extracellular cytokine receptor homology region (CHR), a highly conserved domain, which contains two fibronectin type III (FNIII) domains with an overall length of about 200 AA.[33] Additionally, some receptors contain further domains, as for example immunoglobulin (Ig) domains, extra FNIII domains or a second CHR domain. With this set of various domains many diverse extracellular structures are possible which allow binding of all kinds of ligands such as interleukins, growth factors and haematopoietins.[6, 31] Due to the fact that transphosphorylation is the pivotal step for activation of the pathway, at least two receptor chains are required in a ligand induced receptor complex. Activated receptor complexes occur as homodimers, heterodimers or receptor complexes of higher stoichiometric order.[1, 6, 34] In the non-homodimeric cases, the ligand binds first at the receptor with the highest affinity, which most often is called the alpha chain. The secondarily recruited receptor chains can be either unique for a particular complex or shared between the different ligand-specific alpha chains.[34, 35] The most shared chains are the glycoprotein 130 (gp130), common beta chain (βc, IL-3Rβ) and common gamma chain (γc, IL-2Rγ). These shared chains can form heterodimeric receptor complexes with more than one ligand/receptor pair.[36] Not all alpha chains contain a Box 1/2 motif for JAK binding, but all receptor complexes, the ones with higher stoichiometric order, contain at least two receptor chains for JAK binding. These receptor chains are responsible for initiating the signalling cascade from the plasma membrane of the cell.[6]

The cytokine ligands IL-4 and IL-13 activate the IL-4R, which consists of a heterodimeric pair of single transmembrane receptors. IL-4 and IL-13 belong to the four alpha-helices bundle cytokine family, with antiparallel juxtaposed helices A, C, B, D, two long end-to-end loops and a short beta-sheet (Figure 1.2.1A; PDB: 1IAR).[26, 37] IL-4 binds its receptor alpha chain (IL-4Rα) with the high affinity of 20 - 300 pM.[32]

The IL-4Rα subunit consists of a N-terminal extracellular domain, a single-pass transmembrane alpha-helix and long cytoplasmic tail. The extracellular CHR is formed by two FNIII domains which almost form a right angle in the linker region.[38, 39] The short about 100 AA long FNIII domains form barrel-like structures out of beta-sheets. Ligand binding takes place between the two FNIII domains in the flexible loop region.[26, 33, 37] In the N-terminal FNIII domain, also known as D1-domain, six cysteines form three intra-domain disulfide bonds (two disulfide bonds are conserved in class I cytokine receptors and one is additionally existing in the IL-4Rα).[37] Furthermore, there is a second conserved region in the cytokine receptor class I family, which is located in the membrane proximal FNIII domain (D2-domain), the WSXWS (Trp-Ser-X-Trp-Ser) motif.[32] Both motifs, the disulfide bond as well as the WSXWS motif (WSEWS in IL-4Rα), are important for cytokine receptor binding at the cell surface.[35, 40-43] The alpha-helical transmembrane domain (TMD, 23 AA) connects the N-terminal extracellular domain with the C-terminal cytoplasmic tail. In IL-4Rα, the C-terminal cytoplasmic tail (about 570 AA) is unusually long compared within this family. It contains the Box-motifs specific for JAK1 and five important tyrosine residues for further protein binding and downstream signalling. The first tyrosine (Y497, counting from the N- to the C-terminus) is located within the IL-4R consensus motif (I4R) and is crucial for docking of the insulin receptor substrate 1 (IRS1) and IRS2 proteins. IRS1/2 activates the phosphatidylinositol-3-kinase (PI3K) pathway as well as the Ras GTPase of the mitogen activated protein kinase (MAPK) pathway.[32, 44] The second tyrosine motif is a series of three equally spaced phosphorylation sites (Y575, Y603, Y631). A single STAT6 protein binds the tyrosine motif and is then phosphorylated by the receptor bound JAKs and downstream JAK/STAT signalling takes place.[45] The C-terminal tyrosine (Y713) is located in the immunoregulatory tyrosine-based inhibitory motif (ITIM) and binds the SH2 containing inositol-5-phosphatase (SHIP). The pathway components SHIP as well as the SH2-containing phosphatases (SHP-1 and SHP-2) are counteracting key players, besides other regulative proteins (suppressor of cytokine signalling (SOCS)), in a negative feedback loop for down-regulation of the JAK/STAT pathway.[1, 9, 32, 44]

A IL-4Rα structure components

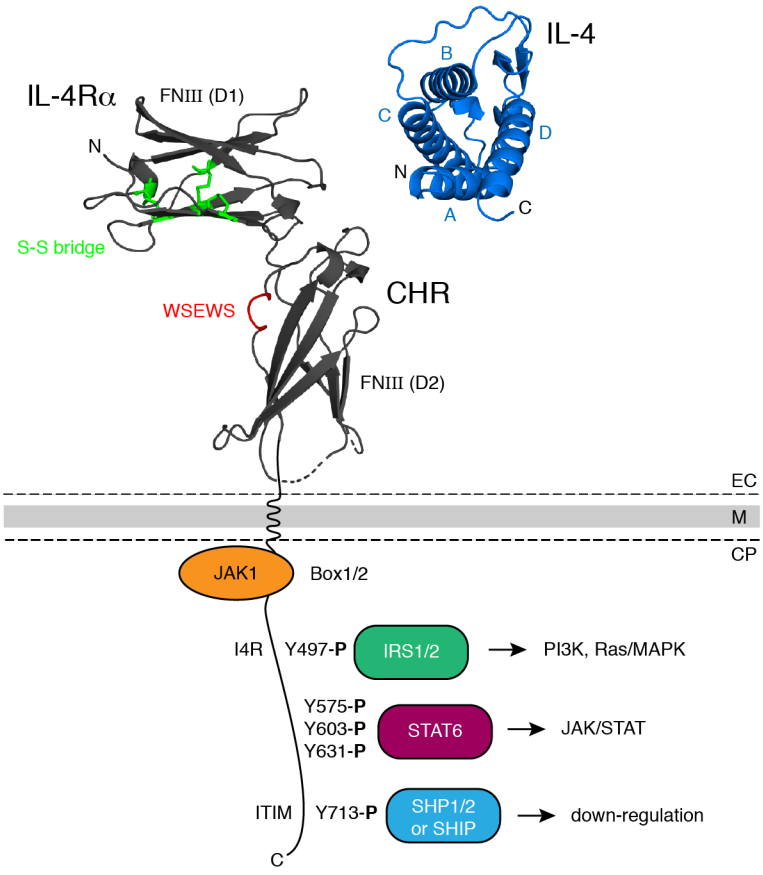

B Heterodimeric IL-4R complexes

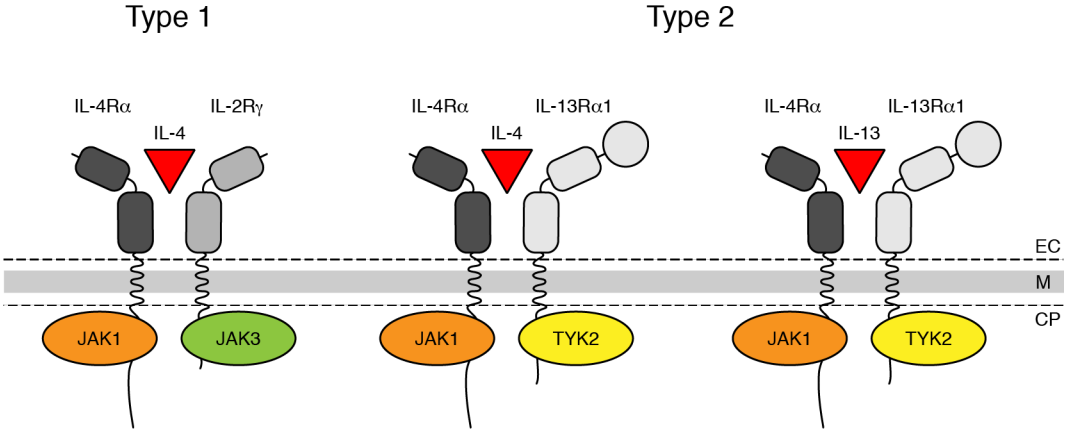

Figure 1.2.1: IL-4Rα type 1 and type 2 complex. A) Topology of the IL 4Rα subunit with the crystalized extracellular domain (PDB: 1IAR) placed on a schematic plasma membrane.[37] The ligand structure shows four alpha-helical domains, in which loop A and C interact with the IL-4Rα whereas the loops A and D interact in the homodimer with the associated low affinity receptor (not shown). The receptor associated kinase JAK1 binds to the receptor at the Box1/2 motif. Many cytoplasmic factors can bind to the phosphorylated IL-4Rα tail and trigger different cell pathways such as PI3K, Ras/MAPK and JAK/STAT, including down-regulation of the JAKs. B) Heterodimerized receptor pairs of the IL-4R complex with their associated kinases JAK1, JAK3 and TYK2. The type 1 complex is formed by IL-4Rα/IL-4/IL-2Rγ whereas the type 2 complex is formed either by IL-4Rα/IL-4/IL-13Rα1 or by IL-4Rα/IL-13/IL-13Rα1. C, C-terminus; CP, cytoplasm; EC, extracellular; M, membrane, N, N-terminus; P, phosphorylated tyrosine.[30, 32, 37]

After IL-4 binds its high affinity receptor IL-4Rα, a second receptor chain is recruited, IL-2Rγ. The ternary complex of IL-4, IL-4Rα and IL-2Rγ is also known as IL-4R type 1 signalling complex (Figure 1.2.1B). The binding of the IL-2Rγ is the last step of the formation of the ternary complex, as it has a neglectable IL-4 binding affinity but a higher affinity for the IL-4/IL-4Rα complex.[26] IL-2Rγ or common gamma chain (γc) is one of the three shared receptor chains in the class I cytokine family and is part of many various receptor complexes with cytokines like IL-2, IL-4, IL-7 IL-9, IL-15 and IL-21. The IL-2Rγ is very small for a shared receptor and consists only of an N-terminal extracellular CHR domain, a single transmembrane region and a short C-terminal cytoplasmic tail, where JAK3 is associated with the Box1/2 motif.[36, 46]

The IL-4R type 1 receptor complex is a very specific signalling complex which is only expressed in haematopoietic cells.[47] IL-4 and IL-4Rα can form an alternative receptor complex with IL-13Rα1, called IL-4R type 2 (Figure 1.2.1B).[48] The IL-13Rα1 extracellular domain contains a CHR domain and, additionally, a third N-terminal immunoglobulin (Ig-) domain. Furthermore, IL-13Rα1 contains a single TMD and slightly longer cytoplasmic tail, compared to IL-2Rγ. The JAK/STAT pathway kinase TYK2 binds to the C-terminal cytoplasmic tail at the Box1 motif.[49] IL-13Rα1, expressed by a wide variety of non-haematopoietic cells like muscle cells, fibroblast, epithelial cells or keratinocytes, is specifically activated by Interleukin-13 (IL-13).[50] . Here, IL-13Rα1 is the high-affinity receptor, whereas IL-4Rα plays the role of a low-affinity co-receptor to form a stable type 2 signalling complex for the JAK/STAT pathway activation.[5, 6, 25, 29, 51]

1.3 Cytokine receptor activation at the cell surface

In recent years, the canonical dimerization model of pathway activation, established in the early nineties of the last century, was intensively revisited.[5, 6, 28, 29, 52] Generally, all the protein-protein-interactions of the signalling cascade follow the law of mass action. It is therefore believed that the affinities and the concentrations of the receptors and ligands are important parameters for the fine tuning of the dynamic equilibrium between the monomeric receptor chains and the full receptor complex.[53] However, quantitative data supporting this model were not available for long. Using FCCS, the surface dimerization of the type 1 IL-4R was even undetectable.[28] In a later study the ligand-induced dimerization was seen under overexpression conditions. However, the estimated affinities for co-receptor recruitment did not support that a large fraction of dimers can be formed in the plasma membrane under physiological conditions.[29] Another research group, using total internal reflection fluorescence (TIRF) microscopy, proposed that kinetic parameters rather than affinities dictate the signalling output of IL-4R.[5] Further evidence for the stepwise recruitment of receptor chains and ligands was provided by antibody-induced pathway activation[54] or the study of monomeric receptor chains at physiological levels.[55-57] In addition, it was shown that ligand mutations in the binding site for the second low affinity receptor inhibits pathway activation.[34, 53] Experiments with modified glass surfaces suggested not only a stepwise, ligand IFNα2-induced dimerization of the interferon receptors IFNAR1 and IFNAR2, it also showed the recruitment of downstream signalling proteins such as TYK2, STAT1, STAT2 and the repressor ubiquitin specific protease 18 (USP18). For this purpose, one of the interferon receptors was covalently attached to the modified and patterned surface by a Halo-tag fusion construct and the recruitment of other pathway components were monitored by TIRF microscopy.[58, 59]

An additional mechanism for receptor activation was proposed in which the receptor domains undergo a conformational change during ligand binding. To probe for conformational changes in the extracellular receptor domains of living cells is extremely challenging. Structural rearrangements were found in homo-dimeric receptors like growth hormone (GH)[60-62], erythropoietin (Epo)[63-66] and thrombopoietin (Tpo)[67, 68]. As

they are already pre-dimerized at the plasma membrane, a trigger for the JAK/STAT pathway activation, such as the receptor rearrangement, is needed. Moreover, receptor chains of heteromeric complexes like IL-2Rβ, IL-2Rγ[69], gp130[70], interferon alpha receptor 1 (IFNAR1) and interferon alpha receptor 2 (IFNAR2)[71] also showed conformational changes. A scissor-like motion was proposed in the EPO receptor that bring cytoplasmic domains and hence the JAKs in close proximity for pathway activation.[63, 64] For the GHR it was proposed that the extracellular domains undergo a rotational as well as a vertical movement.[61, 62] For the tall class II cytokine receptor complexes another motion was proposed. Here, the high affinity receptor IFNAR2 binds its ligand IFNα2 and the second receptor chain IFNAR1 is recruited. The IFNAR1 undergoes an embrace-like rearrangement of the Ig-like domains during the binding process.[53, 72]

A completely different activation mechanism was suggested to take place in the type 1 IL-4R chains. Free energy perturbation (FEP) computing resulted in a linear off-state of the IL-4Rα chain, in which the tryptophan residues of the WSEWS motif (D2-domain) stick to the membrane interface and the receptor rests on the membrane.[35] During the presentation and activation state the receptor moves further away from the membrane surface into the water phase where ligand receptor complex formation takes place. An arginine-tryptophan zipper between the WSEWS (G-strand) motif and two conserved arginine residues (F-strand), stabilized by pi-stacking forces, is closed leading to a rotational movement of the receptor to activate the JAK/STAT pathway.[35] The stem loop (activation loop) between S171 and H197 (F- and G-strand) is not only an important receptor region for conformational changes, it also has direct influence on the ligand binding interface. A very important AA, tyrosine 183 (Y183), which is crucial for proper ligand binding, is located on the apex of this stem loop.[73] The activation loop with its important components is directly up stream of the TMD and is responsible for signal transduction from the ligand through the lipid bilayer to the intracellular tail.[35, 53] However, it remains controversial to which extent the IL-4R is dimerizing in the outer cell membrane or in endosomal structures and whether the receptor is affected by a ligand induced conformational change during activation.

An intricate link between cytokine receptor and JAK/STAT pathway activation and endosomal trafficking was proposed long ago but has been appreciated as an important field just recently as more powerful microscopy technologies were at hand.[74] Endocytosis is a very important process for cells to internalize external protein like cytokines or solutes by carriers and receptors.[75] In addition, to maintain membrane homeostasis, patches with a particular lipid and protein composition are constantly replenished. This involves internalization and secretion of lipid associated material from a diverse pool of small vesicles inside the cell. These endosomal vesicles are highly dynamic and are able to exchange lipids as well as cargo with one another and various kinds of internal membrane systems like lysosomes, endoplasmatic reticulum and Golgi apparatus and alike, a phenomenon that is termed trafficking.[76] Trafficking of receptors through vesicular compartments of different composition plays an important role for the regulation of cell signalling.

The most common uptake mechanism for receptor proteins is the clathrin dependent endocytosis pathway. The phosphorylated target receptors get ubiquitinylated leading to clathrin adaptor protein recruitment and endocytosis through clathrin coated pits.[77-81] Further pathways for receptor internalization are the caveolin-mediated pathway[82, 83], clathrin independent carriers (CLICs)[84], GPI-AP-enriched early endosomal compartments (GEECs)[85, 86] and modification of the actin network through its regulatory proteins.[87-90] One example for an actin polymerization dependent receptor endocytosis mechanism is the internalization of the IL-2R. The interleukin receptor uses a clathrin/caveolin independent and Ras-related C3 botulinum toxin substrate 1 / Serine/threonine-protein kinase Pak1 (Rac1/Pak1) and dynamin-dependent endocytosis mechanism. In addition, the large GTPase dynamin and lipid ordered domains (rafts) are involved.[74, 91-95] As the IL-4R type 1 shares the same IL-2Rγ from IL-2R, a similar mechanism for endocytosis was proposed by Weidemann and colleagues and indeed, overexpression of the receptor components showed the localisation in endosomal structures (Figure 1.3.1). The endosomes share some of the same proteins such as early endosomes (Ras-related in brain (Rab5) and Early endosome antigen 1 (EEA1)) and recycling endosomes (Rab11). Furthermore, the endosomal structures are embedded in the actin cortex near the plasma membrane and

therefore are named cortical endosomes (CEs). As the endocytosis mechanism of the IL-4R is highly Rac1/Pak1 and dynamin-dependent, it could be inhibited with small molecule drugs.[30] Moreover, it was shown that receptor trafficking into CEs is ligand independent resulting in a safety mechanism for JAK/STAT pathway activation by fluctuating ligand concentrations or by microdomain patterning of the heterogeneously distributed plasma membrane.[29, 30, 96] Further experiments with IL-2Rγ and JAK3, members of the IL-4R type 1 complex, revealed that the intracellular tail of the IL-2Rγ as well as an intact JAK3 protein are crucial for proper receptor trafficking, signalling and degradation. IL-2Rγ and JAK3 mutants cause serious diseases of the immune system, as for example the (X-linked) severe combined immunodeficiency ((X)-SCID).[25, 51, 97, 98]

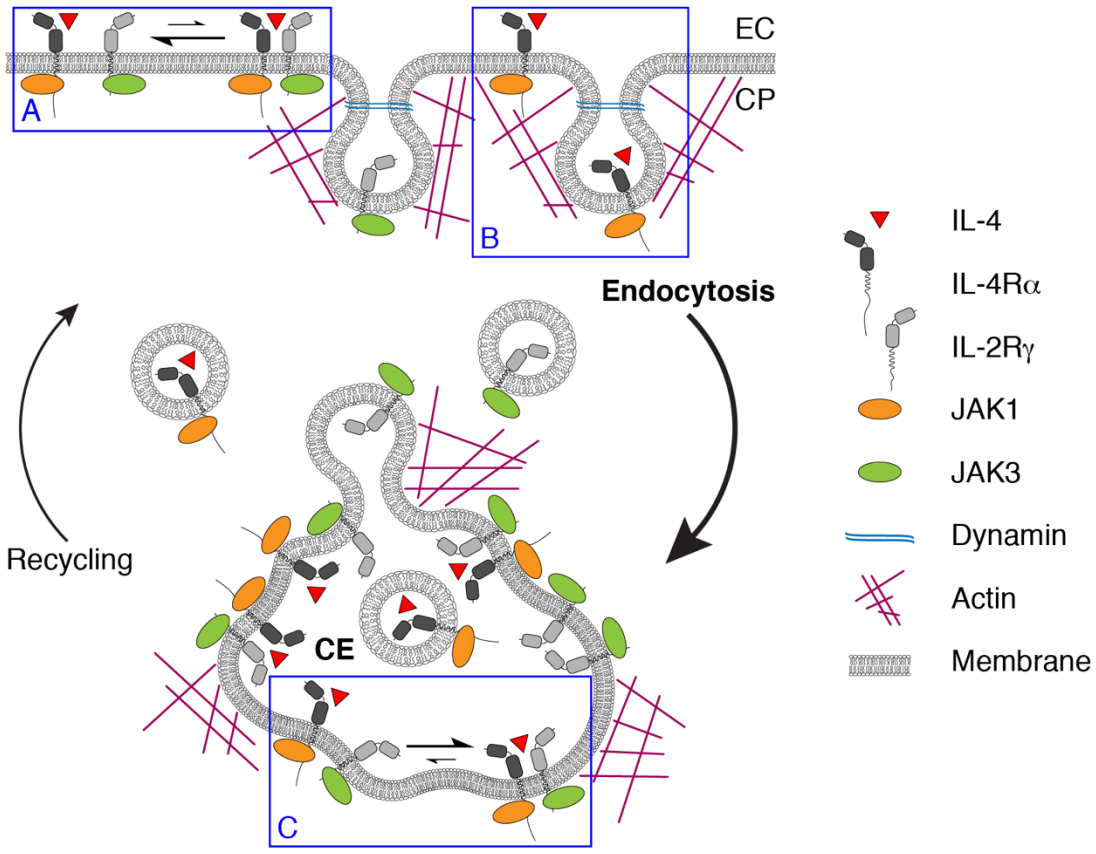

Figure 1.3.1: IL-4R endocytosis pathway. A) Ligand induced homodimerization of the receptors at the plasma membrane of living cells is impeded by their low lateral affinities, which shifts the equilibrium to single receptor chains. B) The continuous internalization of IL-4R subunits is controlled by an actin- and dynamin-dependent endocytosis mechanism. C) The increased receptor density in the small membrane compartment CE is mediated by the relative endocytosis and recycling rates. This high density of receptors

in CEs shifts the equilibrium towards receptor heterodimerization and activation of the JAK/STAT pathway. CE, cortical endosome; EC, extracellular; CP, cytoplasm.[30]

Another reason for receptor endocytosis, besides the spatiotemporal separation from the plasma membrane, is an enrichment of the receptor population. The native expression rate of cytokine receptors at the membrane is very low with about 0.5 - 5 receptors per μm^2.[99] Therefore the formation of the active receptor complex under physiological conditions is very unfavourable thermodynamically and only an increase in the concentration through endocytosis, where a higher receptor to surface area is present, could change that.[29, 30, 96] Nevertheless, the spatiotemporal assembly and composition of the endocytosis machinery has still to be established.[93, 94, 100] To get a better understanding of the IL-4 induced JAK/STAT pathway activation and the proteins involved, covalent modifications of the system are necessary. Fluorescence labelled proteins in combination with different microscopy techniques and mass spectrometry (MS) experiments should shed a new light on the IL-4R induced JAK/STAT pathway activation.

2 *In vivo* protein labelling

The discovery and development of fluorescent proteins improved our understanding of biology drastically.[101-103] Now it is possible to follow molecular processes, as for example cell division[104], protein expression[105] or receptor trafficking[30] in real time with fluorescence microscopy. Yet, fluorescent proteins have some drawbacks, such as a large size, complicated photophysical behaviour and a limited range of colours especially in the far-red region. To overcome these drawbacks, different bioorthogonal labelling methods, like various protein or peptide tags, were developed to modify cellular proteins with organic fluorescent dyes.[106, 107] Compared to fluorescent proteins, these dyes are up to 20 times smaller, have better photophysical properties and are available in all possible colours. Most biorthogonal labelling methods are based on a functional separation of targeting and reporting. First, a bioorthogonal moiety, as for example a

reactive group for a particular chemical conjugation method, is incorporated or attached to the protein of interest, followed by a selective modification step, for instance a fluorescent reporter.[108]

2.1 Genetic code expansion (GCE) and bioorthogonal click reactions

One example of bioorthogonal labelling of proteins is the incorporation of unnatural amino acids (uAAs) via genetic code expansion (GCE) as chemical handle, followed by

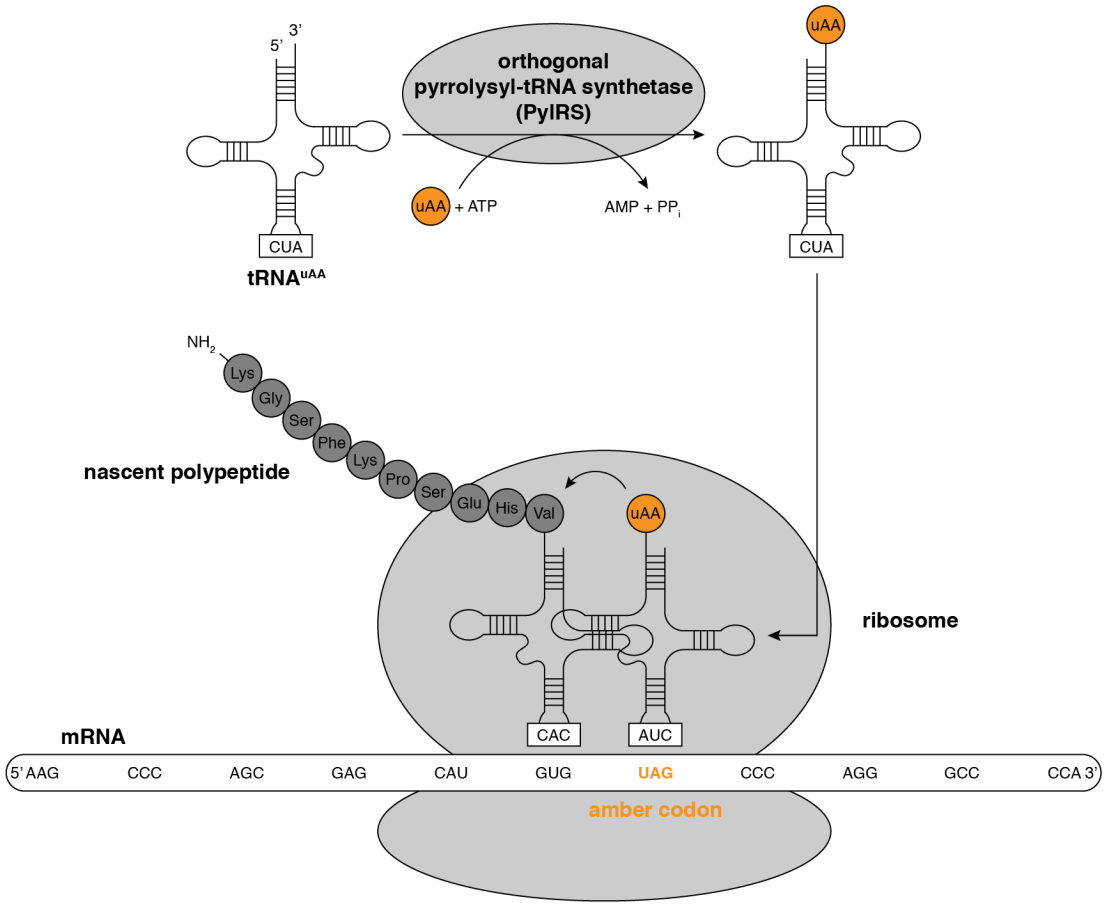

Figure 2.1.1: Genetic code expansion. First the orthogonal Pyrrolysyl-tRNA synthetase (PylRS) loads the unnatural amino acids (uAA) on the transfer ribonucleic acid ($tRNA^{uAA}$) by consumption of energy (ATP hydrolysis). Then the uAA loaded $tRNA^{uAA}$ translocates to the ribosome, binds at the amber codon (UAG) of the messenger RNA (mRNA) and the modified polypeptide chain is formed.[109]

a selective labelling reaction.[110-113] The GCE allows site-specific incorporation of azide or alkene/alkyne functionalized uAAs like L-azidohomoalanine (AHA)[114-116], *N*$^{\varepsilon}$-(1-methylcycloprop-2-enecarboxyamido)-lysine (CpK)[117-119], *N*$^{\varepsilon}$-*p*-azidobenzyloxy-carbonyl lysine (PABK)[120], *N*$^{\varepsilon}$-(cyclooct-2-yn-1-yloxy)carbonyl)-L-lysine (COK)[121-123], *N*$^{\varepsilon}$-(bicyclo[6.1.0]non-4-yn-9-yl-methoxy)carbonyl-L-lysine (BCNK)[112, 113, 119, 124] or *trans*-cyclooct-4-ene-L-lysine (4'-TCOK)[113, 119] into proteins of bacteria, mammalian cells and animals.[112, 119, 125, 126] Thus, the host organism incorporates the uAA with its already existing translational machinery, as for example with the Methionine-tRNA synthetase (MetRS)[114] and the associated tRNA/codon pair. Moreover, highly specific and orthogonal Pyrrolysyl-tRNA synthetase (PylRS)/transfer ribonucleic acid (tRNA^{uAA}) pairs, from *archaea* species, can be used. These systems recognize the amber stop codon (TAG, mRNA level UAG) and incorporate the uAA at its specific position without any interference of the host translational machinery.[127] Figure 2.1.1 illustrates the energy consuming (adenosine triphosphate (ATP) hydrolysis) incorporation process in which the uAA is loaded on the tRNA^{uAA} by its modified uAA-tRNA synthetase. After docking to the artificially introduced UAG-triplet, the ribosome forms the nascent polypeptide and the uAA is incorporated at the UAG position.[112, 113, 128, 129]

The term of bioorthonal reaction was first defined by Carolyn Bertozzi in 2003 as a chemical reaction that can exist inside a living system without perturbing the native biochemical processes.[130] During the last decade, several bioorthogonal labelling strategies with uAA such as Staudinger ligation[114], tetrazole photo-click reaction[117, 118], copper(I)-catalysed azide-alkyne cycloaddition (CuAAC)[131], strain-promoted azide-alkyne cycloaddition (SPAAC)[132] or inverse electron-demand Diels-Alder cycloaddition (IEDDAC)[112] have been developed (Figure 2.1.2). All reaction types can be summarized as so-called click reactions which are defined as very fast and selective conjugations with high yield and insensitivity towards water and oxygen.[108] The IEDDAC is possibly the best bioorthogonal reaction that has been developed to date, with respect to fast reaction rates, selectivity and yield.[127, 133-136]

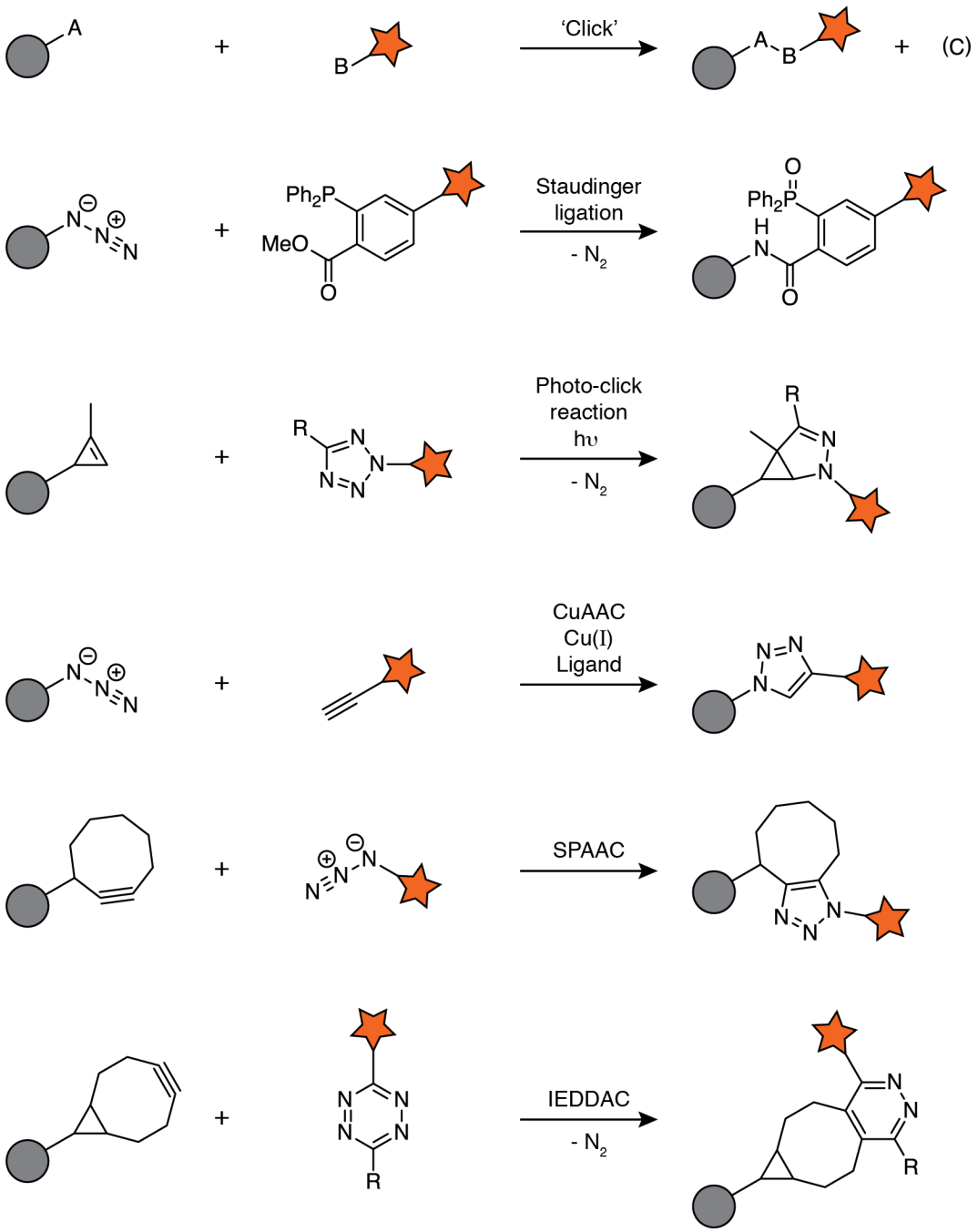

Figure 2.1.2: Important click reaction types. A) The very fast and selective click reaction takes place between a handle at the modified protein of interest and the corresponding reactive group with a fluorescent readout. B) Five examples of important click reactions: Staudinger ligation, reaction between an azide and a triphenylphosphine moiety; Photo-click reaction, a cyclopropene reacts with a tetrazole catalysed by UV-light; CuAAC, Cu (I) catalysed reaction of an azide and an alkyne; SPAAC, reaction between a strained alkyne and an azide; IEDDAC, a strained alkyne forms a covalent bond with a tetrazine moiety with release of nitrogen. Grey circle, protein of interest with incorporated uAA (reactive head group drawn as sticks); orange star, fluorophore attached to coupling-moiety.[128, 137]

2.2 Inverse electron-demand Diels-Alder cycloaddition (IEDDAC)

In this kind of reaction an electron poor diene and an electron rich dienophile undergo a [4 + 2] - cycloaddition reaction. The IEDDAC is typically performed between a 1,2,4,5-tetrazine (diene) and a strained alkene or alkyne (dienophile). The 4π-electrons of the diene and the 2 π-electrons of the dienophile arrange and react in a suprafacial/suprafacial manner leading to the formation of a highly strained bicyclic intermediate. Afterwards, the intermediate undergoes a retro Diels-Alder reaction to form a pyridazine (alkene additional isomerization and oxidation, alkyne direct) and releases nitrogen to reduce the ring tension (Figure 2.2.1).[127, 133-136]

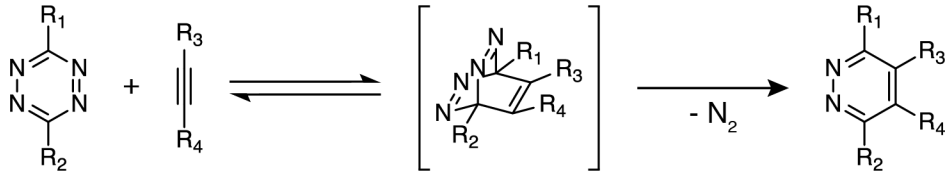

Figure 2.2.1: IEDDAC reaction mechanism. Example mechanism for a reaction between an alkyne and a tetrazine group. First, an bicyclic intermediate is formed by a Diels-Alder reaction and then a retro-Diels-Alder reaction takes place for covalent bond formation with release of nitrogen.[134]

Many compounds have been developed and optimized, leading to the probably fastest reaction kinetics (rate constants up to 10^6 M^{-1} s^{-1}) of a bioorthogonal reaction so far.[138] In addition, IEDDAC not only shows rapid but also fine tuneable reaction kinetics under physiological conditions by means of electron and steric substituents effects. Electron withdrawing groups at the diene and electron donating groups at the dienophile accelerate the reaction kinetics.[127, 135, 139, 140] Steric effects of the reaction partners are another important factor for the reaction kinetics of 1,2,4,5-tetrazines besides the electron withdrawing character of the groups in C3 and C6 position. Even if a strong electron withdrawing group is attached, the mono-substituted tetrazines show a faster reaction kinetics than the di-substituted tetrazines.[141] Not only the diene group has an impact on the reaction kinetics of the IEDDAC; the dienophile and its electron donating groups have an even higher impact.[142, 143] The ring strain in a strained cyclic dienophile

has the highest impact on the reaction kinetics. This effect is independent of the electronic environment of the dienophile and dependent on the ring size and the orientation of the double bond. Both strained cyclic alkenes or alkynes lead to an extraordinary fast reaction kinetics.[144-146] Protic solvents and especially water increase the IEDDAC reaction rate by stabilizing the interaction complex with hydrophobic interactions between the diene and the dienophile and hydrogen bonding with the tetrazine group. The IEDDAC reaction kinetics is almost independent of the solvent pH and possibly increases under acidic conditions.[147-151] Further beneficial characteristics of the IEDDAC are that a low concentration of coupling reagent is necessary, that the reaction is also highly bioorthogonal as well as biocompatible and the IEDDAC is catalyst free and very chemoselective.[127, 137, 152] The labelling reaction between a dienophile and a tetrazine bearing a fluorescent dye molecule shows another advantage, because the tetrazine group quenches the fluorescence of the dye in its unbound state. Only after the IEDDAC took place, the fluorescence increases, leading to a bright signal and, simultaneously, a low background of the unbound fluorophore.[112, 127, 128, 135, 137, 153]

3 Fluorescence microscopy techniques

3.1 Confocal fluorescence microscopy

To visualize biological processes, different techniques were developed, one of the most common being confocal laser scanning microscopy combined with fluorescent probes. We used this technique to get insights in the activation of the JAK/STAT pathway by the IL-4R complex at the surface of living cells. For this reason, receptor modification with GCE, fluorescence labelling with bioorthogonal click chemistry and signal quantification with confocal microscopy were combined to address different biological questions.

Confocal microscopy is based on the physical phenomenon of fluorescence. During excitation of a fluorescent molecule (fluorophore or fluorochrome) with a light source (LED or laser), the molecule absorbs a photon with a specific wavelength. After a short

time period, the fluorochrome then emits a photon with longer wavelength. The absorption occurs in the time scale of femtoseconds. The time interval between absorption and emission is the so-called fluorescence lifetime and is ranged in the time scale of 1 - 10 ns for typical fluorophores. The shift between the excitation wavelength and the emission wavelength is called the Stoke's shift, which is fluorochrome dependent.[154, 155] A graphical illustration of the mentioned processes is described by the Jablonski diagram (Figure 3.1.1). In the diagram, energy (y-axis) is plotted against time

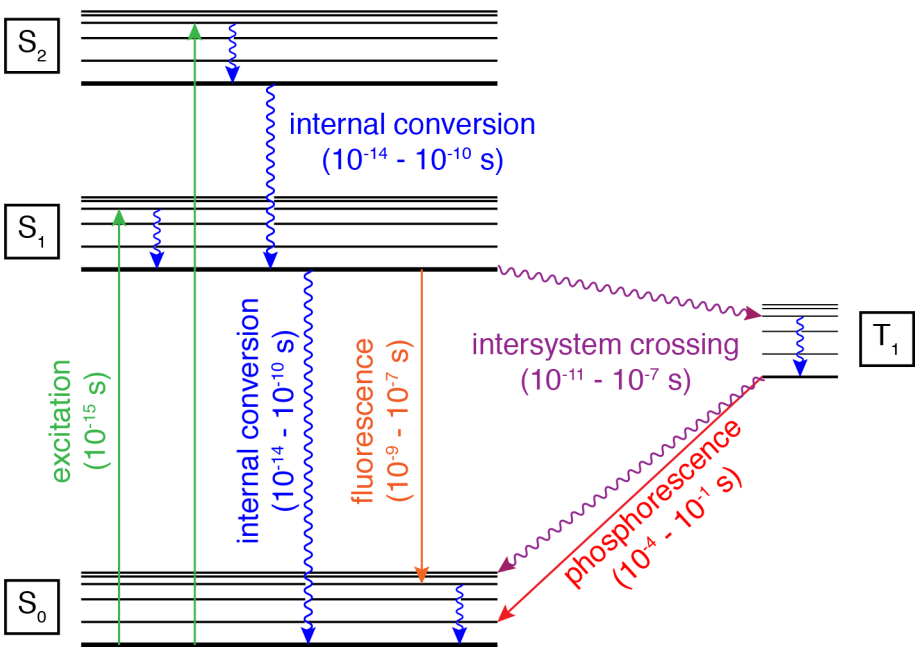

Figure 3.1.1: Jablonski diagram. Electrons of the fluorophore are excited to higher energy states (S_1 - S_n) and then relax back to the ground state (S_0) either by internal conversion or by fluorescence. The fluorophore can also undergo a conversion to a dark state (T1), leading to a blinking behaviour. S: state, T: triplet.[155-157]

(x-axis).[156] Most fluorescent molecules are in their ground state (S_0) at room temperature. The energy gain during absorption of a photon by the fluorochrome leads to higher excited states of the molecule, mostly S_1, but even higher states (S_2, S_n) are possible. Within picoseconds after the excitation event, the energy level of the fluorescent molecule relaxes to the lowest vibrational level of S_1 by a non-radiating transition. Relaxation to the ground state S_0 can then happen most commonly by fluorescence emission of a photon or, rarely, by internal conversion. The excited

fluorochrome can also undergo a non-radiating transition (intersystem crossing) to the dark triple state T_1. The fluorochrome relaxes back from this long-living dark state to the ground state S_0, leading to a blinking effect (dye on/off) with a characteristic lifetime τ_T in the range of microseconds or by phosphorescence.[154-156, 158]

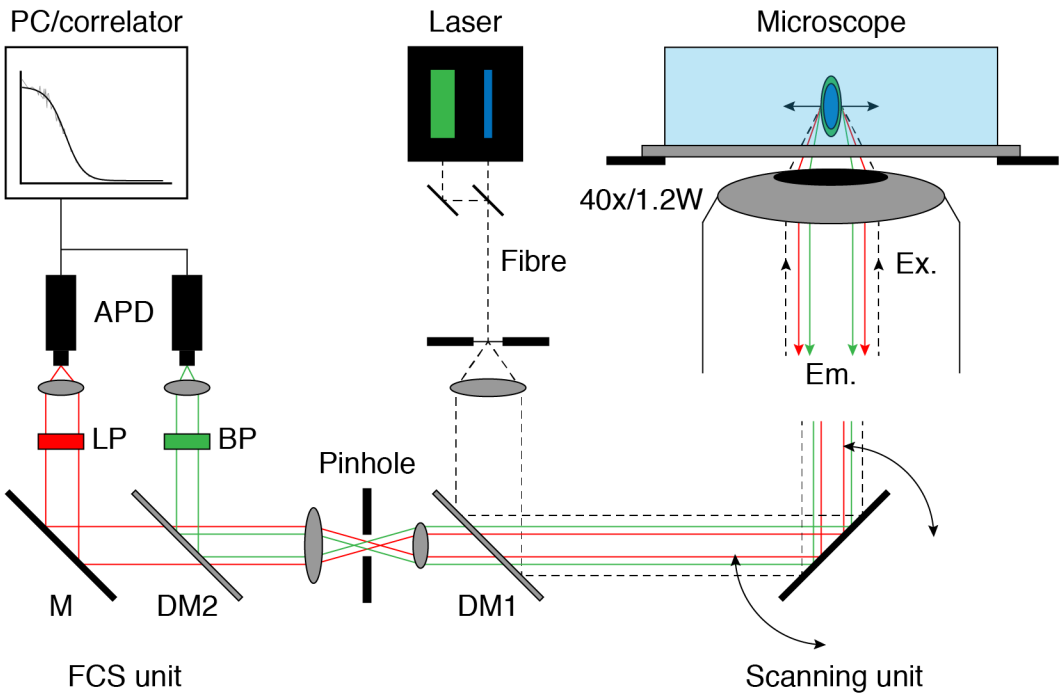

Figure 3.1.2: Confocal laser scanning microscope setup with FCS unit. Schematic representation of a laser scanning confocal microscope equipped with: A laser box, dichroic mirrors (DMs), a scanning unit, a water objective (40x/1.2w), a pinhole, a mirror, avalanche photo diodes (APDs) and a computer for analysis.[159, 160]

The setup of a confocal laser scanning microscope is rather simple (Figure 3.1.2). An argon-ion (488 nm), a DPSS (561 nm) or a HeNe (633 nm) laser is coupled via an optic fibre with the main microscope body. The laser light passes the first dichroic mirror (DM1), then the scanning unit, which scans the sample region, leaves the microscope at the objective lens and excites the sample fluorochrome. The sample emits photons in all directions and some of them travel through the objective lens into the microscope and pass the DM1. Afterwards, the out of focus emission is decreased by the pinhole and one part of the fluorescence light passes the second dichroic mirror (DM2), where the

other emission photons are deflected to the first single-photon counting avalanche photo diode (APD1). The emitted fluorescence light which passes the DM2 is deflected by a mirror to the second APD2. In front of the APDs, emission band pass (BP) and long pass (LP) filters are installed to filter photons in the correct wavelength. The electric signal of the APDs is then fed into a computer for image processing, image analysis or signal correlation.[159] The DMs are designed in a way that excitation light or the light with the shorter wavelength is deflected while the light with the longer wavelength can pass the mirror. Emission BP filters only let pass light of a certain wavelength area, whereas LP filters block all light below a certain wavelength. Common objectives are water-based and have a high numerical aperture (NA) for a small excitation volume (confocal volume).[159-161]

3.2 Fluorescence (cross-)correlation spectroscopy (FCS/FCCS)

Confocal fluorescence microscopy is not only used for image recording, it is also possible to measure physical properties of fluorescent molecules by this tool. Fluorescence correlation spectroscopy (FCS) allows the measurement of diffusion coefficients, concentrations of fluorochromes as well as flow speeds and reaction rates of chemical and biological samples.[161] In a previous investigation, Weidemann and co-workers used FCS in combination with confocal microscopy to count and determine the concentration of nucleosomes in living cells.[162] Similar FCS protocols were established to analyse proteins in different cell compartments.[163] To quantify and improve the covalent labelling of IL-4Rα by click chemistry, a similar quantification approach, with confocal microscopy and FCS, could be established.

In FCS, the measurements of the fluorescent molecule can be taken either in solutions, at membranes or even inside living cells.[154, 160, 164] The dynamic properties of the fluorescent molecule contain information about the size and speed of the moving particle and are well described by the diffusion coefficient D_t. Diffusion of a particle in solution is equivalent to a random walk, where the diffusion coefficient defines the distance which a molecule is travelling in a certain time (unit $\mu m^2 s^{-1}$). FCS is an excellent tool to

measure the diffusion coefficient experimentally, because one can measure the fluctuation of fluorescent particles in and out of the defined confocal volume over a certain period of time (Figure 3.2.1). When fluorochromes are excited at a decent level, the fluorescence intensity *F*(t) is proportional to the particle number *N*(t). The overall fluorescence intensity *F*(t) over time is composed of the average intensity value ⟨*F*⟩ and the small fluctuations $\delta F(t)$ around the average value ⟨*F*⟩ (Equation 3.2.1).[154, 161]

$$F(t) = \langle F \rangle + \delta F(t) \qquad 3.2.1$$

As the small intensity fluctuations $\delta F(t)$ contain information on the system's properties, low particle numbers are necessary, making FCS a single molecule method. To reach the goal of small particle numbers, a confocal volume is necessary, allowing low nanomolar particle concentrations. For example, with a theoretical confocal volume of 1 fL and a desired particle number of 10 particles a reasonable dilution of about 17 nM of fluorescent molecules can be used.[157, 160, 164]

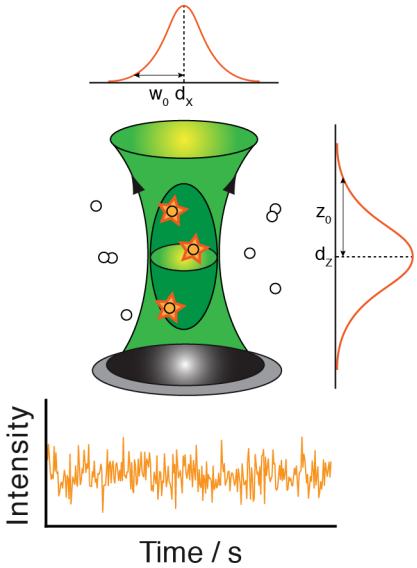

Figure 3.2.1: Confocal volume. Schematic representation of a confocal volume with fluorescent particles, the Gaussian-shaped intensity distribution and a typical FCS intensity fluctuation trace.[159, 165]

In order to get information about the fluorescent particle movement in a sample, the signal of the fast fluctuations in the confocal volume is correlated (auto-correlation analysis). The auto-correlation function $G(\tau)$ compares the self-similarity of fluctuation $F(t)$ to the fluctuation after a defined lag time τ (Equation 3.2.2).[159-161]

$$G(\tau) = \frac{\langle F(t) \times F(t+\tau) \rangle}{\langle F \rangle^2} - 1 = \frac{\langle \delta F(t) \times \delta F(t+\tau) \rangle}{\langle F \rangle^2} \qquad 3.2.2$$

If the lag time τ is short, it is very likely that the fluctuations at timepoint t and $t+\tau$ (self-similarity between $\delta F(t)$ and $\delta F(t+\tau)$) are caused by the same particle, leading to a high auto-correlation $G(\tau)$. In contrast, if the lag time τ is long, it is unlikely that the intensity fluctuations $\delta F(t)$ and $\delta F(t+\tau)$ derive from the same fluorescent particle and it is more likely that they originate from independent molecules. The self-similarity and the auto-correlation $G(\tau)$ are both small.[155, 161] Figure 3.2.2 illustrates the conversion of measured fluctuation data into the measured auto-correlation curve. Two main values

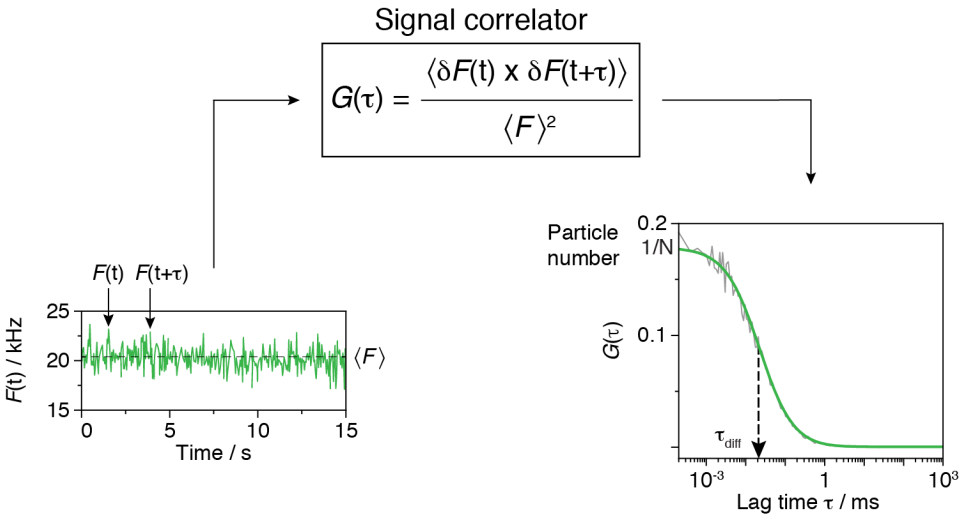

Figure 3.2.2: Fluorescence correlation spectroscopy. Fluctuations of intensity over time are measured and correlated by the function $G(\tau)$ to obtain an auto-correlation curve. The x-axis of the auto-correlation curve represents the diffusion time whereas the y-axis is inversely proportional to the average number of particles.[160]

are extracted from the measured auto-correlation curve after curve fitting with the correct model function. First, the inflection point of the curve shows the average retention time of the particles in the confocal volume (diffusion time, τ_{diff}) on the x-axis. The inverse particle number is represented by the extrapolated curve (zero lag time amplitude) on the y-axis.[154, 160, 162]

To fit the auto-correlation data with a proper model, equation 3.2.2 has to be modified and assumptions have to be made. Equation 3.2.3 shows a proper fit model for the assumption of a single species solution with one diffusion coefficient D_t and an average particle number N in the confocal volume.[166]

$$G(\tau) = \frac{1}{N} \times \left(1 + \frac{4\,D_t\,\tau}{w_0^2}\right)^{-1} \times \left(1 + \frac{4\,D_t\,\tau}{z_0^2}\right)^{-\frac{1}{2}} \qquad 3.2.3$$

As the confocal volume is usually described by an ellipsoid, the 3D structure contains two equal axes in x and y with a radius of w_0 and an elongated z-axis z_0. The axial ratio of the focus in the z-plane and the xy-plane is called the structure factor S (Equation 3.2.4). The diffusion coefficient is defined by the ratio of the xy-plane radius and the diffusion time (Equation 3.2.5). Rewriting of equation 3.2.3 for an average retention time leads to equation 3.2.6.[159, 161, 167]

$$S = \frac{z_0}{w_0} \qquad 3.2.4$$

$$D_t = \frac{w_0^2}{4\,\tau_D} \qquad 3.2.5$$

$$G(\tau) = \frac{1}{N} \times \left(1 + \frac{\tau}{\tau_D}\right)^{-1} \times \left(1 + \frac{\tau}{S^2\,\tau_D}\right)^{-\frac{1}{2}} \qquad 3.2.6$$

The structure factor and the focus volume of a microscope setup can be measured by a calibration measurement of a nanomolar fluorescent dye solution with known diffusion

coefficient D_t. With a defined confocal volume and the structure factor (usually between 4 and 6) at hand, it is possible to calculate the effective volume V_{eff} as well as the concentration c of a solution (Equations 3.2.7 and 3.2.8).[157, 159, 161]

$$V_{\mathrm{eff}} = \pi^{\frac{3}{2}} w_0^2 z_0 = \pi^{\frac{3}{2}} w_0^3 S \qquad 3.2.7$$

$$c = \frac{N}{V_{\mathrm{eff}}} \qquad 3.2.8$$

Fluorescence cross-correlation spectroscopy (FCCS) extends the measurement capacity to another colour channel which allows the analysis of the physical behaviour of double-labelled constructs, as for example co-diffusion or dissociation constants. Like

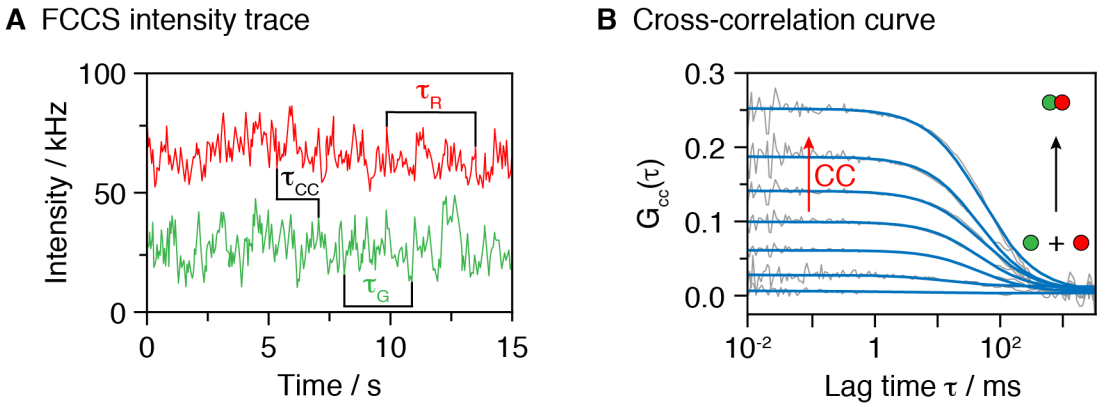

Figure 3.2.3: Fluorescence cross-correlation spectroscopy. A) Intensity traces of a dual-colour FCCS experiment. The intensity signal is not only auto-correlated in its own channel but also cross-correlated (CC) for both channels. B) Dual-colour particles, diffusing through the focal volume together, result in a high cross-correlation amplitude.[159]

in normal FCS, the signal fluctuations of the separate channels are correlated and, additionally, the fluctuations between the dual-colour channels are correlated in FCCS. The amplitude of the cross-correlation curve enhances if the fraction of double-labelled complexes in solution increases (Figure 3.2.3).[159]

Another common feature between FCS and FCCS is the fact that the amplitude of the cross-correlation function is inversely proportional to the number of double-labelled particles. Since the amplitude of the cross-correlation curve is very sensitive to dissociation effects (monomers) or clustering of one species, it is necessary to form a ratio between the cross- and the auto-correlation amplitude to properly monitor binding reactions.[159, 161, 167] For example, biochemical information such as the click labelling or ligand binding efficiency are available by measuring the particle numbers for both colour channels by FCCS.

3.3 Fluorescence lifetime imaging microscopy (FLIM)

Fluorescence lifetime imaging microscopy (FLIM) measures the excited state lifetime of fluorescence molecule after a laser pulse (fs to ps range).[154, 168] The fluorescence lifetime is independent of fluorophore concentration, excitation intensity or photobleaching, but its decay curve is an indicator for the chemical environment of the fluorochrome. Quantitative fluorescence lifetime imaging allows the measurement of pH, ion concentrations, viscosity, polarity or binding to macromolecules.[154, 155, 169]

The fluorescence lifetime, which is in the order of a few nanoseconds (1 - 10 ns), shows a mono- or multi-exponential decay, depending on the fluorochrome. Equation 3.3.1 shows a mono-exponential decay process, with the intensity (I_0) at $t = 0$ and the fluorescence lifetime τ.[154]

$$I(t) = I_0 \, e^{-\frac{t}{\tau}} \qquad 3.3.1$$

FLIM is measured using a conventional confocal laser scanning fluorescence microscope equipped with a synchronized short-pulse laser. Besides other methods, the time domain-based method (time-correlated single photon counting (TCSPC)) to measure the lifetime of a fluorescent molecule is the most common.[154] In TCSPC, the time delay between the laser excitation pulse and the detection of a photon is recorded.

Repeating this process many times results in a histogram of arrival times, which can be modelled by mono- or multi-exponential functions.

4 Protein cross-linking with unnatural amino acids

Besides fluorescent reporters which require microscopic methods, GCE in conjunction with bioorthogonal labelling can be used for proteomics approaches. For example, to identify protein-protein interactions associated with a specific endocytosis route of receptors, covalent cross-linking in combination with mass spectrometry (MS) could be used. GCE allows cross-linking experiments in living organism under native conditions. By site-specific incorporation of a uAA, containing a photo-inducible reactive cross-linking group, protein-protein interactions can be monitored, representing a snapshot of the molecular environment (Figure 4.1A).[170] The reactive group of the uAA has to be chemically stable and bioorthogonal to all functional groups in the cell system before the activation with UV-light.[171] Moreover, the uAA has to be small to prevent inhibitory effects on the interaction. The excitation wavelength should be long in order to reduce photo-damage for biomolecules and cells and the cross-linking efficiency high to capture specific binding events.[170-172] One example of such a photo-inducible reactive cross-linking group is the diazirine group of the uAA 3'-azibutyl-*N*-carbamoyl-lysine (AbK) that has been applied in this work (Figure 4.1B).[173] The diazirine releases nitrogen and forms a reactive carbene intermediate after excitation with UV-light (350 - 365 nm). The reactive carbene has a half-life in the range of nanoseconds and can insert into C-H and heteroatom-H bonds, via a fast non-specific radical reaction, in order to form a covalent cross-link.[171, 172, 174] Drawbacks of this uAA are the reduced cross-linking efficiency by quenching of the carbene intermediate with water and the rearrangement to the more stable diazo isomer, which reacts with nucleophiles and leads to non-specific cross-linking effects. The incorporation of trifluoromethyl and aromatic groups prevents the rearrangement by stabilizing the carbene intermediate and thus reduces non-specific side reactions.[171, 174]

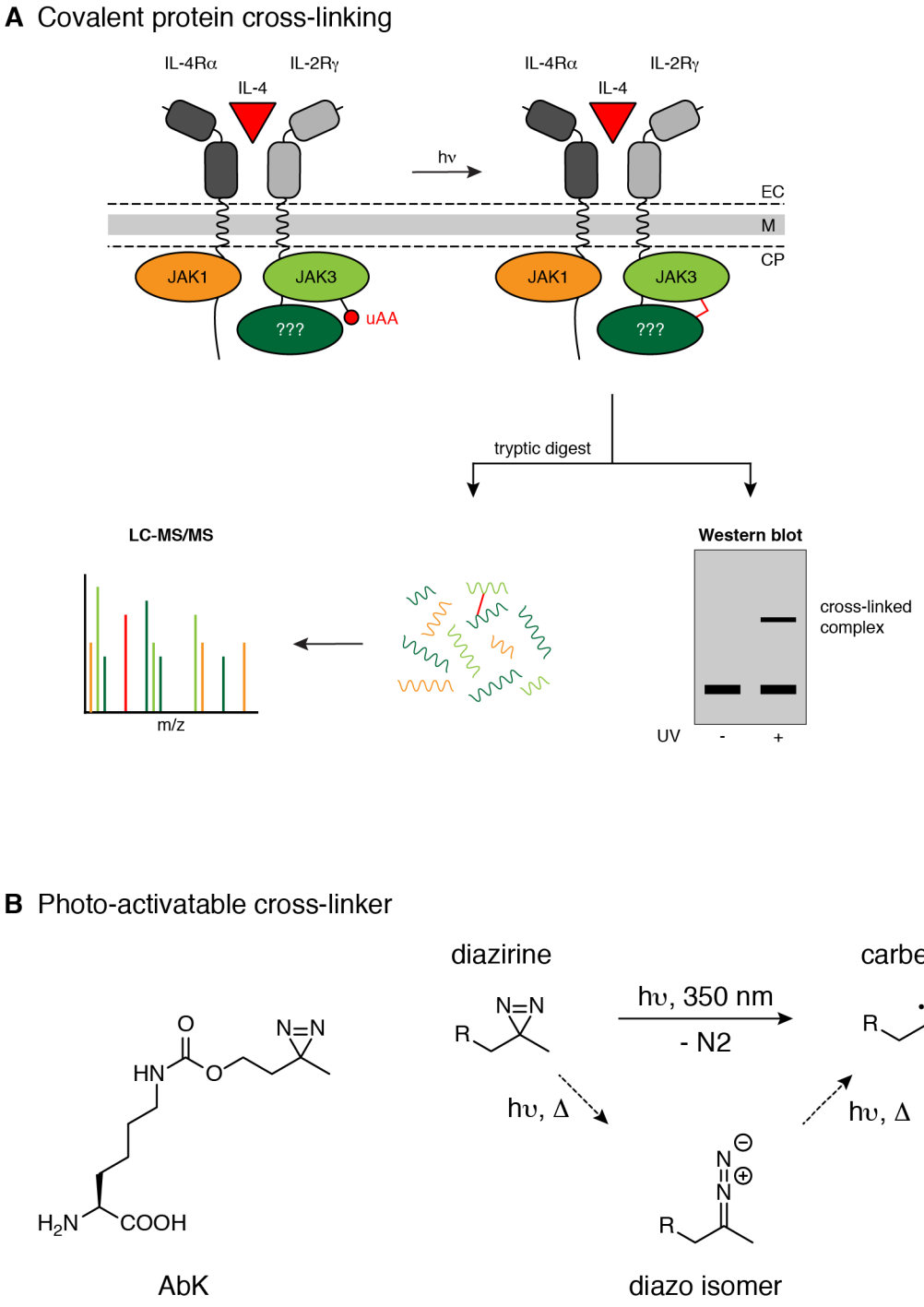

Figure 4.1: Protein cross-linking with uAAs. A) IL-4R type 1 complex with the photo-inducible uAA AbK incorporated in the IL-2Rγ associated kinase JAK3. 1) After the covalent cross-linking by use of UV light, the protein adduct is either analysed as complete protein on a western blot (WB) or it is digested and analysed by mass spectrometry (LC-MS/MS). B) Structure of AbK with its reactive diazirine group. The AbK diazirine group forms a reactive carbene after the irradiation with UV-light and releases nitrogen. AbK can also form a more stable diazo isomer, which leads to non-specific cross-linking effects.[170, 171]

5 Aims of this thesis

Although the IL-4R complex and other structurally strongly related hematopoietic cytokine receptors have been known for decades, many open questions still remain. For example, it is unclear how the silent state of the receptor is stabilized and whether receptor activation involves a conformational change.[35] Furthermore, it is still under debate in which compartment the formation of the receptor complex takes place, on the outer plasma membrane or within endosomal structures such as early endosomes.[30] A key aim of this work is to establish and apply modern techniques of covalent protein modification to address these problems in living cells. In contrast to affinity-tags, a covalent linkage enables longer observation times and therefore a proper quantification of receptor states. Furthermore, we aim to benefit from the nanoscopic spatial resolution provided by the selective chemistry of the uAA introduced by GCE that is subsequently targeted in the extracellular domain at a particular position by bioorthogonal click labelling.

For successful surface expression of modified reactive IL-4R subunits carrying the uAA at specific positions, several parameters associated with the molecular biology of GCE, such as the ratio of receptor, $tRNA^{uAA}$ and uAA-tRNA synthetase, the uAA concentration and the position of the TAG stop codon within the primary sequence have to be addressed. To judge the labelling results quantitatively, we intend to measure particle numbers at the plasma membrane, from where the degree of labelling and receptor occupancy can be derived. An important goal of this work is to comprehensively quantify the parameter space of the IEDDAC click reaction of BCNK and tetrazine-dye constructs under conditions of live cell labelling. Both the results and the calibrated imaging approach will then provide a basis for accelerated optimization of click labelling reactions in other contexts. In addition, we aim to investigate in detail functional consequences of BCNK incorporation on the integrity of the IL 4Rα tertiary structure by ligand binding. Finally, patterned IL-4 deposition on a substrate where cells would grow shall provide a versatile system to study dimerization of IL-4R subunits and, in perspective, cytoplasmic factors of the complex molecular machinery that regulates JAK/STAT pathway by internalization and receptor trafficking. In conclusion, we aim to establish quantitative

methods that combine cell biological, biophysical and biochemical approaches to gather deeper insights into the molecular mechanism of IL-4R mediated signal transduction.

II Materials and Methods

6 Materials

6.1 Plasmids and oligonucleotides

Table 6.1.1: Plasmids used to transiently transfect cells for experiments.

Gene	Plasmid name	Source
EGFP	pc2SV_2xME-EGFP	Schwille group (MPI of Biochemistry)
IL-2Rγ	CMV_H_6-IL2Rγ	Schwille group (MPI of Biochemistry)
IL-2Rγ	CMV_H_6-IL2Rγ-E262TAG-3HA	Cloned in the lab
IL-2Rγ	CMV_H_6-IL2Rγ-E275TAG-3HA	Cloned in the lab
IL-2Rγ	CMV_H_6-IL2Rγ-K272TAG-3HA	Cloned in the lab
IL-2Rγ	CMSV_H_6-IL2Rγ-m5	Schwille group (MPI of Biochemistry)
IL-2Rγ	CMSV_H_6-IL2Rγ-m15	Schwille group (MPI of Biochemistry)
IL-2Rγ	CMSV_H_6-IL2Rγ-m25	Schwille group (MPI of Biochemistry)
IL-2Rγ	CMSV_H_6-IL2Rγ-m35	Schwille group (MPI of Biochemistry)
IL-2Rγ	CMSV_H_6-IL2Rγ-m45	Schwille group (MPI of Biochemistry)
IL-2Rγ	CMSV_H_6-IL2Rγ-m55	Schwille group (MPI of Biochemistry)
IL-2Rγ	CMSV_H_6-IL2Rγ-m65	Schwille group (MPI of Biochemistry)
IL-2Rγ	CMSV_H_6-IL2Rγ-m75	Schwille group (MPI of Biochemistry)
IL-2Rγ	CMV_H_6-IL2Rγ-P266TAG-3HA	Cloned in the lab

IL-2Rγ	CMV_H_6-IL2Rγ-P269TAG-3HA	Cloned in the lab
IL-2Rγ	CMV_H_6-IL2Rγ-S55TAG-3HA	Cloned in the lab
IL-2Rγ	CMV_H_6-IL2Rγ-S81TAG-3HA	Cloned in the lab
IL-2Rγ	CMV_H_6-IL2Rγ-S86TAG-3HA	Cloned in the lab
IL-2Rγ	CMV_IL2Rγ	Schwille group (MPI of Biochemistry)
IL-4Rα	CMV_H_6-IL4Rα-K97TAG	Cloned in the lab
IL-4Rα	CMV_H_6-IL4Rαm266-K22TAG	Cloned in the lab
IL-4Rα	CMV_H_6-IL4Rαm266-K87TAG	Cloned in the lab
IL-4Rα	CMV_H_6-IL4Rα-K97TAG	Cloned in the lab
IL-4Rα	CMV_H_6-IL4Rαm266-D72TAG	Cloned in the lab
IL-4Rα	CMV_H_6-IL4Rαm266-D72TAG-EGFP	Cloned in the lab
IL-4Rα	CMV_H_6-IL4Rαm266-E141TAG	Cloned in the lab
IL-4Rα	CMV_H_6-IL4Rαm266-E141TAG-EGFP	Cloned in the lab
IL-4Rα	CMV_H_6-IL4Rαm266-E189TAG	Cloned in the lab
IL-4Rα	CMV_H_6-IL4Rαm266-E189TAG-EGFP	Cloned in the lab
IL-4Rα	CMV_H_6-IL4Rαm266-E94TAG	Cloned in the lab
IL-4Rα	CMV_H_6-IL4Rαm266-E94TAG-EGFP	Cloned in the lab
IL-4Rα	CMV_H_6-IL4Rαm266-EGFP	Schwille group (MPI of Biochemistry)
IL-4Rα	CMV_H_6-IL4Rαm266-K22TAG-EGFP	Cloned in the lab
IL-4Rα	CMV_H_6-IL4Rαm266-K87TAG-EGFP	Cloned in the lab
IL-4Rα	CMV_H_6-IL4Rαm266-K97TAG	Cloned in the lab
IL-4Rα	CMV_H_6-IL4Rαm266-K97TAG-EGFP	Cloned in the lab
IL-4Rα	CMV_H_6-IL4Rαm266-S30TAG	Cloned in the lab
IL-4Rα	CMV_H_6-IL4Rαm266-S30TAG-EGFP	Cloned in the lab
IL-4Rα	CMV_H_6-IL4Rαm266-S44TAG	Cloned in the lab
IL-4Rα	CMV_H_6-IL4Rαm266-S44TAG-EGFP	Cloned in the lab
IL-4Rα	CMV_H_6-IL4Rαm266-T105TAG	Cloned in the lab
IL-4Rα	CMV_H_6-IL4Rαm266-T105TAG-EGFP	Cloned in the lab
IL-4Rα	CMV_H_6-IL4Rαm266-T113TAG	Cloned in the lab

IL-4Rα	CMV_H_6-IL4Rαm266-T113TAG-EGFP	Cloned in the lab
IL-4Rα	CMV_H_6-IL4Rαm266-T18TAG	Cloned in the lab
IL-4Rα	CMV_H_6-IL4Rαm266-T18TAG-EGFP	Cloned in the lab
IL-4Rα	CMV_H_6-IL4Rαm266-Y13TAG	Cloned in the lab
IL-4Rα	CMV_H_6-IL4Rαm266-Y13TAG-EGFP	Cloned in the lab
IL-4Rα	CMV_H_6-IL4Rαm266-Y183TAG	Cloned in the lab
IL-4Rα	CMV_H_6-IL4Rαm266-Y183TAG-EGFP	Cloned in the lab
IL-4Rα	pc2SV_H_6-IL4Rαm266-EGFP	Schwille group (MPI of Biochemistry)
JAK3	CMV_JAK3-EGFP	Schwille group (MPI of Biochemistry)
JAK3	CMV_JAK3-TagRFP	Schwille group (MPI of Biochemistry)
n/a	SE323_wtPylRS_4×PylT-new-BCNK-mutations	Lang group (Technical University of Munich, Germany)
STAT6	CMV_STAT6	Schwille group (MPI of Biochemistry)
STAT6	CMV_EGFP-STAT6	Schwille group (MPI of Biochemistry)

Table 6.1.2: Oligonucleotides used for cloning.

Oligonucleotide name	Sequence (5' → 3')
IL2Rg_E290_FW	tttctggctgtagcggacgatg
IL2Rg_E290_RV	catcgtccgctacagccagaaa
IL2Rg_E303_FW	tgaagaacctataggatcttgttact
IL2Rg_E303_RV	agtaacaagatcctataggttcttca
IL2Rg_K300_FW	cccaccctgtagaacctagagg
IL2Rg_K300_RV	cctctaggttctacagggtggg
IL2Rg_P294_FW	gacgatgtagcgaattccc
IL2Rg_P294_RV	gggaattcgctacatcgtc
IL2Rg_P297_FW	cgaatttagaccctgaagaa

IL2Rg_P297_RV	ttcttcagggtctaaattcg
IL2Rg_S109stop_FW	gtccagaagtgctagcactatctat
IL2Rg_S109stop_RV	atagatagtgctagcacttctggac
IL2Rg_S114stop_FW	cactatctattctaggaagaaatcacttct
IL2Rg_S114stop_RV	agaagtgatttcttcctagaatagatagtg
IL2Rg_S83stop_FW	ttggaacagctagtctgagcccca
IL2Rg_S83stop_RV	tggggctcagactagctgttccaa
IL4Ra-D72TAG_FW	gtcagtgcgtagaactatacactg
IL4Ra-D72TAG_RV	cagtgtatagttctacgcactgac
IL4Ra-E141TAG_FW	tcaacatttggagttagaacgacccgg
IL4Ra-E141TAG_RV	ccgggtcgttctaactccaaatgttga
IL4Ra-E189TAG_FW	ccacctggagttagtggagcccc
IL4Ra-E189TAG_RV	ggggctccactaactccaggtgg
IL4Ra-E94TAG_FW	cttcaagcccagctagcatgtgaaac
IL4Ra-E94TAG_RV	gtttcacatgctagctgggcttgaag
IL4Ra-K22TAG_FW	ttgcgagtggtagatgaatggtc
IL4Ra-K22TAG_RV	gaccattcatctaccactcgcaa
IL4Ra-K87TAG_FW	gctgctgtggtagggctccttcaag
IL4Ra-K87TAG_RV	cttgaaggagccctaccacagcagc
IL4Ra-K97TAG_FW	agcgagcatgtgtagcccagggc
IL4Ra-K97TAG_RV	gccctgggctacacatgctcgct
IL4Ra-S30TAG_FW	caccaattgctagaccgagctccg
IL4Ra-S30TAG_RV	cggagctcggtctagcaattggtg
IL4Ra-S44TAG_FW	ttttctgctctaggaagcccacac
IL4Ra-S44TAG_RV	gtgtgggcttcctagagcagaaaa
IL4Ra-T105TAG_FW	ccaggaaacctgtaggttcacaccaat
IL4Ra-T105TAG_RV	attggtgtgaacctacaggtttcctgg
IL4Ra-T113TAG_FW	caatgtctccgactagctgctgctg
IL4Ra-T113TAG_RV	cagcagcagctagtcggagacattg
IL4Ra-T18TAG_FW	catgagcatctcttagtgcgagtgga

IL4Ra-T18TAG_RV	tccactcgcactaagagatgctcatg
IL4Ra-Y13TAG_FW	gtctccgactagatgagcatctc
IL4Ra-Y13TAG_RV	gagatgctcatctagtcggagac
IL4Ra-Y183TAG_FW	gctcagtgctagaacaccacct
IL4Ra-Y183TAG_RV	aggtggtgttctagcactgagc
IL4Ram266-TAArev	ttaggaccgcttctcccactg
Lin-hIL2Rg-FW	taaccgcgactctagatc
Lin-hIL2Rg-RV	ggtttcaggctttagggtg
Linker3HA-FW	caccctaaagcctgaaacc
Linker3HA-RV	gatctagagtcgcggtta
pIL13RaDelGFP_F	taaagcggccgcgactct

6.2 Chemicals and reagents

Table 6.2.1: Chemicals and reagents used in this study.

Name	Supplier
4× loading buffer	Bio-Rad Laboratories GmbH (Feldkirchen, Germany)
AbK	Lang group (Technical University of Munich, Germany)
Alexa488-tet2	Click chemistry tools (Scottsdale, AZ, USA)
Alexa568-COOH	Thermo Fisher Scientific (Waltham, MA, USA)
Alexa568-tet1	Lang group (Technical University of Munich, Germany)
Alexa647-tet1	Lang group (Technical University of Munich, Germany)
Anti-HA-tag magnetic micro beads	Thermo Fisher Scientific (Waltham, MA, USA)
ATTO488-COOH	ATTO-TEC GmbH (Siegen, Germany)
ATTO647N-tet1	Lang group (Technical University of Munich, Germany)

ATTO655-COOH	ATTO-TEC GmbH (Siegen, Germany)
BCNK endo	SiChem GmbH (Bremen, Germany)
BCNK exo	SiChem GmbH (Bremen, Germany)
BCNK mix	Lang group (Technical University of Munich, Germany)
BSA	Sigma-Aldrich (St. Louis, MO, USA)
CaCl2	AppliChem (Darmstadt, Germany)
Cholesterol	Avanti Polar Lipids (Alabaster, AL, USA)
Cy3-tet2	Click chemistry tools (Scottsdale, AZ, USA)
Cy5-NHS ester	GE Healthcare (Chalfont St Giles, UK)
Cy5-tet	Lang group (Technical University of Munich, Germany)
Cy5-tet2	Click chemistry tools (Scottsdale, AZ, USA)
Cy5-tet3	Lang group (Technical University of Munich, Germany)
D-(+)-Trehalose	Thermo Fisher Scientific (Waltham, MA, USA)
DMEM	Thermo Fisher Scientific (Waltham, MA, USA)
DOPC (18:1, C9)	Avanti Polar Lipids (Alabaster, AL, USA)
DOPE-ATTO565 (18:1, C9)	ATTO-TEC GmbH (Siegen, Germany)
DOPE-ATTOO655 (18:1, C9)	ATTO-TEC GmbH (Siegen, Germany)
DOTAP (18:1, C9)	Avanti Polar Lipids (Alabaster, AL, USA)
DPBS	Thermo Fisher Scientific (Waltham, MA, USA)
DSPC (18:0)	Avanti Polar Lipids (Alabaster, AL, USA)
DSPE-PEG2000-Biotin (18:0)	Avanti Polar Lipids (Alabaster, AL, USA)
EDTA	Sigma-Aldrich (St. Louis, MO, USA)
Fetal bovine serum	Thermo Fisher Scientific (Waltham, MA, USA)
Fibronectin	Roche (Basel, Schweiz)
Filter paper	Bio-Rad Laboratories GmbH (Feldkirchen, Germany)

Glucose	Sigma-Aldrich (St. Louis, MO, USA)
Glycerol	Sigma-Aldrich (St. Louis, MO, USA)
HA-peptide	Thermo Fisher Scientific (Waltham, MA, USA)
HEPES	Biomol (Hamburg, Germany)
Hoechst 34580	Thermo Fisher Scientific (Waltham, MA, USA)
IL-4	Thermo Fisher Scientific (Waltham, MA, USA)
IL-4-ATTO647N	Müller group (University Würzburg, Germany)
IL-4-Biotin	Müller group (University Würzburg, Germany)
ImmobilonP membrane 0.45 µm	Merck (Darmstadt, Germany)
jetPRIME®	Polyplus transfection (Illkirch, Frace)
KCl	Roth (Karlsruhe, Germany)
KH_2PO	Roth (Karlsruhe, Germany)
Blotting paper	Bio-Rad Laboratories GmbH (Feldkirchen, Germany)
MeOH	Thermo Fisher Scientific (Waltham, MA, USA)
$MgCl_2$	Merck (Darmstadt, Germany)
$MgSO_4$	Merck (Darmstadt, Germany)
Na_2HPO_4	AppliChem (Darmstadt, Germany)
NeutrAvidin	Thermo Fisher Scientific (Waltham, MA, USA)
Neutravidin-Oregon Green 488	Thermo Fisher Scientific (Waltham, MA, USA)
NP40	Sigma-Aldrich (St. Louis, MO, USA)
Paraformaldehyde	AppliChem (Darmstadt, Germany)
Poly-L-lysin	Sigma-Aldrich (St. Louis, MO, USA)
Protein standard	Bio-Rad Laboratories GmbH (Feldkirchen, Germany)
SiR-tet2	Lang group (Technical University of Munich, Germany)

Sphingomyelin (18:0)	Avanti Polar Lipids (Alabaster, AL, USA)
Superblock	Thermo Fisher Scientific (Waltham, MA, USA)
TrapAvidin	Kerafast Inc. (Boston, MA, USA)
triNTA-Alexa674N	Schwille group (MPI of Biochemistry, Germany)
Tris base	Sigma-Aldrich (St. Louis, MO, USA)
Trypsin	Thermo Fisher Scientific (Waltham, MA, USA)
Tween 20	G-Biosciences (St. Louis, MO, USA)
Versene	Thermo Fisher Scientific (Waltham, MA, USA)
Protein standard	Bio-Rad Laboratories GmbH (Feldkirchen, Germany)

6.3 Growth media and buffers

Table 6.3.1: Growth media and buffers used in this study.

Name	Composition
4% PFA	4% paraformaldehyde in DPBS
Air buffer	150 mM NaCl, 20 mM HEPES pH 7.4, 20 mM D-(+)-trehalose, 15 mM glucose, 5.4 mM KCl, 0.85 mM $MgSO_4$, 0.6 mM $CaCl_2$, 0.15 mg mL^{-1} BSA
Fibronectin	10 µg mL^{-1} in DPBS
IL-4	10 µg mL^{-1} in PBS with 0.1% BSA
IP lysis buffer	10 mM Tris HCl pH 7.5, 150 mM NaCl, 0.5 mM EDTA, 0.5% NP-40
IP wash buffer	10 mM Tris HCl pH 7.5, 150 mM NaCl, 0.5 mM EDTA
Lysis buffer	25 mM Tris-HCl pH 7.2, 150 mM NaCl, 5 mM $MgCl_2$, 1% NP-40, 5% Glycerol, protease inhibitor and phosphatase inhibitor
PBS	137 mM NaCl, 2.7 mM KCl, 1.8 mM KH_2PO_4, 10 mM Na_2HPO_4, pH = 7.4
SLB buffer	150 mM NaCl, 10 mM HEPES, pH 7.4

TBST	137 mM NaCl, 2,7 mM KCl, 19 mM Tris base, 1 mL Tween 20 per litre, pH 7.4

6.4 Antibodies

Table 6.4.1: Antibodies used in this study.

Name	Supplier
IL-2Rγ (E-7)	Santa Cruz Biotechnology Inc. (Heidelberg, Germany)
IL-4-Alexa488 (8D4-8)	Thermo Fisher Scientific (Waltham, MA, USA)
JAK3 (#3775)	Cell Signalling Technology (Frankfurt am Main, Germany)
pY-STAT6 (SAB4504546)	Sigma-Aldrich (St. Louis, MO, USA)
STAT6 (D3H4)	Cell Signalling Technology (Frankfurt am Main, Germany)

6.5 Technical equipment

Table 6.5.1: Technical equipment used in this study.

Instrument	Specification and manufacturer
Cell incubator	HERAcell 150i Thermo Fisher Scientific (Waltham, MA, USA)
Centrifuge 1	5424R Eppendorf AG (Hamburg, Germany)
Centrifuge 2	5804R Eppendorf AG (Hamburg, Germany)
Confocal microscope 1	Zeiss LSM780, C-Apochromat 40x/1.2 water immersion objective Carl Zeiss (Oberkochen, Germany)
Confocal microscope 2	SP8 Falcon, HCX PL APO 63x/1.2 motCORR CS water immersion objective Leica Microsystems (Wetzlar, Germany)

Gel-electrophorese	PowerPac Basic with champer Bio-Rad Laboratories GmbH (Feldkirchen, Germany)
Horizontal shaker	IKA HS 501 digital IKA-Werke GmbH & Co. KG (Staufen, Germany)
Imager	Amersham Imager 600 GE Healthcare (Chalfont St Giles, UK)
Laser 1	Argon-Ion laser Lasos (Jena, Germany)
Laser 2	White-light laser, NKT superK EXTREME NKT Photonics (Birkerod, Denmark)
Microscope cell culture	Zeiss AX10 Carl Zeiss (Oberkochen, Germany)
Microscope-slide power meter	S170C Thorlabs (Munich, Germany)
Multi-well imaging slides 1	Nunc™ Lab-Tek® II 8-well chamber slides Thermo Fisher Scientific (Waltham, MA, USA)
Multi-well imaging slides 2	µ-Slide 8-well ibidi GmbH (Gräfelfingen, Germany)
Roller shaker	IKA Roller 6 digital IKA-Werke GmbH & Co. KG (Staufen, Germany)
Scale	XA 205 Dual Range Mettler Toledo (Giessen, Germany)
Spectrophotometer	NanoDrop™ 2000 Thermo Fisher Scientific (Waltham, MA, USA)
Sterile bench	SAFE2020 Thermo Fisher Scientific (Waltham, MA, USA)
Ultrapure water	Milli Q Advantage A 10 Merck KGaA (Darmstadt, Germany)
Water bath	WNB 10 Memmert GmbH & Co. KG (Schwabach, Germany)
WB semi-dry blotter	PierceG2 FastBlotter Thermo Fisher Scientific (Waltham, MA, USA)

7 Methods

7.1 Cloning

Receptor constructs were cloned as described before.[28, 29, 175] The plasmids, CMV_H_6-IL4Rαm266-TAG-EGFP with various TAG stop codon positions, were created from CMV_H_6-IL4Rαm266-EGFP by site-directed mutagenesis (GeneArt Site-Directed Mutagenesis System; Invitrogen; Carlsbad, Ca, USA) with forward and reverse primer pairs (Table 6.1.2, all oligos in 5' → 3' direction). The BCNK-tRNA synthetase/4×-tRNA^{BCNK} construct was used as previously reported.[124] The vector contains the BCNK-tRNA synthetase with upstream an EF-1α promoter and a cassette of four tRNAs^{BCNK} with separate U6 promoters. The negative control 2xLyn-EGFP, cloned by Thomas Weidemann (Schwille group, MPI of Biochemistry), contains an early SV40 promotor, followed by two N-terminal lyn kinase sequence repeats (MGCIKSKRKDNLNDDE, single repeat, one letter code) and an enhanced green fluorescent protein (EGFP). The IL-4Rα full-length construct CMV_H_6-IL4Rα-K97B was also created by side-directed mutagenesis (GeneArt Site-Directed Mutagenesis System; Invitrogen; Carlsbad, Ca, USA) of CMV_H_6-IL4Rα-EGFP as described above. H_6-IL4Rαm266 TAG stop codon mutants without the C-terminal EGFP-tag (CMV_H_6-IL4Rαm266-TAG) were cloned by deletion of the EGFP sequence by PCR (Table 6.1.2) followed by a blunt ligation of the vector. The cross-linking constructs CMV_H_6-IL2Rγ-TAG-3HA were cloned by, first, incorporation of the 3HA-affinity-tag (YPYDVPDYA, single repeat, one letter code) via a synthetic DNA fragment (NEBuilder HiFi DNA Assembly Kit; New England Biolabs; Ipswich, MA, USA) followed by the TAG stop codons via site-directed mutagenesis (GeneArt Site-Directed Mutagenesis System; Invitrogen; Carlsbad, Ca, USA) (Table 6.1.2) into the vector CMV_H_6-IL2Rγ. The CMSV_H_6-IL-2Rγ truncation mutants were cloned by Gosia Poczopko (Schwille group, MPI of Biochemistry). All other plasmids used in this study were already available in the Schwille group (MPI of Biochemistry; Table 6.1.1). The AA and DNA sequence of the protein constructs is attached in the Appendix (Chapter 16).

7.2 Cell culture

Adherent HEK293T cells were cultured in antibiotics and Phenol-Red-free DMEM (Thermo Fisher Scientific; Waltham, MA, USA), supplemented with 10% fetal bovine serum (Thermo Fisher Scientific; Waltham, MA, USA) at 37°C and 8.5% CO_2. Cells were regularly passaged (sub-confluency) by trypsinisation. Therefore, cells were carefully washed with 1× phosphate buffered saline (PBS) and incubated with 0.05% trypsin-EDTA (Thermo Fisher Scientific; Waltham, MA, USA) for 2 min at 37°C. Trypsin was inactivated by growth medium and cells were collected through centrifugation for 2 min at 1000 rpm. The obtained pellet was resuspended in fresh growth medium and cells were seeded at a density range of 1 – 3×10^5 cells per T75 flask (15 mL, 75 cm^2, Thermo Fisher Scientific; Waltham, MA, USA).

7.3 Cell transfection

HEK293T cells were seeded 24 h before transfection in a Nunclon™ 12-well multiwell plate (Thermo Fisher Scientific; Waltham, MA, USA). At 40 – 60% confluence, cells were transfected with jetPRIME® (Polyplus transfection; Illkirch, France) at a DNA : jetPRIME® ratio of 100 ng : 0.3 µL (0.5 - 2 µg DNA per well). After 4 h, the growth medium was replaced and the cells were incubated at 37°C and 8.5% CO_2. For GCE expression, BCNK (100 mM, dissolved in 100 mM NaOH) was added to the growth medium (neutralized with 100 mM HCl) to reach a final concentration of 0.5 mM.

7.4 GCE expression assay

18 h after transfection, HEK293T cells were carefully washed with PBS, were harvested with 1× Versene (Thermo Fisher Scientific; Waltham, MA, USA) and DPBS (Thermo Fisher Scientific; Waltham, MA, USA). The cells were washed twice with DPBS and

stored on ice for 20 min. Then, Cy5-NHS ester (GE Healthcare UK limited, UK) in DPBS (1 µg mL^{-1}) was added and cells were incubated for 5 min at 4°C. The labelled cells were washed three times with air buffer on ice and were seeded on fibronectin (10 µg mL^{-1} in DPBS) pre-coated Nunc™ Lab-Tek® II 8-well chamber slides (Thermo Fisher Scientific; Waltham, MA, USA). Confocal images were taken with a LSM780 ConfoCor3 (Carl Zeiss; Oberkochen, Germany), with avalanche photo-diode detectors and a C-Apochromat 40x/1.2 water immersion objective. The membrane was segmented by our self-developed ImageJ script and the intensities, measured under the same imaging conditions, were compared.

7.5 Covalent click labelling

The transfected and GCE expressing HEK293T cells were carefully washed with PBS 18 – 24 h after transfection. Then, the cells were harvested with 1× Versene (Thermo Fisher Scientific; Waltham, MA, USA), washed twice with air buffer and stored on ice for 20 min before tetrazine-dye in air buffer (0.2 – 1.6 µM) was added and cells were incubated for 2 – 120 min at 4°C. The labelled cells were washed five times with air buffer on ice and were seeded on fibronectin (10 µg mL^{-1} in DPBS) pre-coated Nunc™ Lab-Tek® II 8-well chamber slides (Thermo Fisher Scientific; Waltham, MA, USA). Finally, the cells were imaged with a LSM780 ConfoCor3 (Carl Zeiss; Oberkochen, Germany).

7.6 Receptor ligand binding assay

18 – 24 h after transfection HEK293T cells were carefully washed with PBS and were harvested with 1× Versene (Thermo Fisher Scientific; Waltham, MA, USA) and air buffer. The cells were washed three times with air buffer and were seeded on fibronectin (10 µg mL^{-1} in DPBS) and poly-L-lysin (Sigma-Aldrich, St. Louis, MO, USA) pre-coated Nunc™ Lab-Tek® II 8-well chamber slides (Thermo Fisher Scientific; Waltham, MA, USA). 1 h later, IL-4-A647N (50 nM) was added to the cells and incubated for 30 min at rt. The cells

were washed twice with air buffer and were imaged with a LSM780 ConfoCor3 (Carl Zeiss; Oberkochen, Germany).

7.7 Receptor surface lifetime assay

HEK293T cells were click-labelled as described in chapter 7.5. After the fifth washing step, cells were resuspended in fresh growth medium (± IL-4) and were incubated at 37°C and 8.5% CO_2. After certain periods of time, cells were cooled down to 4°C, were washed twice with ice-cold DPBS (Thermo Fisher Scientific Waltham, MA, USA) and the extracellular proteome was labelled with Cy5-NHS (GE Healthcare UK limited, UK) in DPBS (1 µg mL^{-1}). Then the cells were washed twice with DPBS and were fixed with 4% PFA in DPBS for 10 min at 4°C. In the next step, the cells were washed with air buffer on ice and were seeded on fibronectin (10 µg mL^{-1} in DPBS) and poly-L-lysin (Sigma-Aldrich, St. Louis, MO, USA) pre-coated Nunc™ Lab-Tek® II 8-well chamber slides (Thermo Fisher Scientific; Waltham, MA, USA). Confocal images were taken with a LSM780 ConfoCor3 (Carl Zeiss; Oberkochen, Germany).

7.8 Calibrated ratiometric imaging (CRMI)

Before the actual imaging, the microscope performance and the confocal detection volume were monitored by FCS measurements of ATTO488, Alexa568 and ATTO655 (25 nM) in water. Because of varying cover slide thicknesses, the correction collar of the C-Apochromat 40x/1.2 water immersion objective was manually adjusted to a maximum photon count. The detection volume is defined as $V_{\mathrm{eff}} = \pi^{3/2} w_0^2 z_0$. The beam waist w_0 of the confocal detection volume for each of the three laser lines (488, 561, and 633 nm) was determined by the diffusion time τ_{D} and the translational diffusion coefficient D_t of the corresponding fluorophore via the relation $w_0 = \sqrt{4 D_{\mathrm{t}} \tau_{\mathrm{D}}}$. Diffusion coefficients of 414 µm² s^{-1} (ATTO488), 370 µm² s^{-1} (Alexa568) and 426 µm² s^{-1} (ATTO655) at 25°C were adjusted to a temperature of 28°C in the measurement chamber.[163, 176, 177] As the

diffusion coefficient of Alexa568 was not described before, the diffusion times of Alexa568 and RhodaminB (diffusion coefficient of 450 µm² s⁻¹ at 25°C) were compared.[178] The elongation of the Gaussian-shaped detection volume z_0 was received from the fit.

Fluorophores used for imaging (EGFP, Alexa568-tet1, Cy5-tet1, Cy5-tet2, Cy5-tet3 and IL-4-ATTO647N) were diluted to 100 nM in air buffer or in case of purified EGFP in PBS pH 7.4. The tetrazine-dye constructs were mixed with a 500-fold excess of BCNK (stock 100 mM in NaOH), HCl (neutralization of NaOH) was added and the solution was incubated for 30 min at rt. FCS measurements were performed for a range of laser powers. The same beam path, filter and pinhole settings were applied as for confocal imaging. Various acquisition times ranging from 3 to 15 min, depending on laser power, were used. Auto-correlation functions were fitted with a 3D diffusion model,

$$G(\tau) = \frac{1}{N} G_{3D}(\tau) \qquad 7.8.1$$

$$G_{3D}(t) = \left(1 + \frac{\tau}{\tau_{3D}}\right)^{-1} \left(1 + \frac{\tau}{S^2\,\tau_{3D}}\right)^{-\frac{1}{2}} \qquad 7.8.2$$

where N denotes the number of particles in the detection volume, τ_{3D} the diffusion time of freely diffusing particles and S the structural parameter defined as z_0/w_0 (Equations 7.8.1 and 7.8.2). The ratio of the fluorescence intensity F to the particle number N ($CPP = F/N$) leads to the molecular brightness (quantum yield, counts per particle (CPP)).

The total laser power P_0 was measured using a microscope-slide power meter (S170C; Thorlabs; Munich, Germany) behind the objective lens. The excitation power density in the focal spot is defined as $2P_0/(\pi w_0^2)$, with the beam waist w_0 obtained by the detection volume calibration with diffusian standards.

Confocal images were taken by a laser scanning microscope LSM780 (Carl Zeiss; Oberkochen, Germany), equipped with a ConfoCor3 unit, avalanche photo-diode

detectors (APDs) and a C-Apochromat 40x/1.2 water immersion objective (Carl Zeiss; Oberkochen, Germany). Images were recorded as 16-bit arrays in photon counting mode with filter settings for EGFP (495 - 530 nm, bandpass), Alexa568-tet1 (580 nm, longpass) and IL-4-ATTO647N/Cy5-tet1-3 (655 nm, longpass). The confocal pinhole was set to 37 µm (EGFP and A568-tet1 imaging) or 40 µm (EGFP and IL-4-ATTO647N/Cy5-tet imaging) and the pixel dwell time to values between 12 - 50 µs. Laser power was adjusted in such a way that the fluorescence intensity of bright pixels is below 1 MHz.

The membrane of single cell images was located with a custom ImageJ segmentation script (developed by Giovanni Cardone; Imaging Facility, MPI of Biochemistry) which uses the Otsu's method to find the largest linked membrane area. Photon counts of the segmented area were divided by the pixel dwell time to yield in fluorescence intensities. Then, the number of emitting molecules was obtained by dividing the fluorescence intensities by the FCS-based molecular brightness. A correction for the non-fluorescent molecules p_{nf} ($p_{nf} = 0.25$ for EGFP and $p_{nf} = 0.32$ for IL-4-A647N) was applied by increasing the number of molecules by a factor of $1/(1-p_{nf})$. To obtain the click labelling efficiency or the IL-4-ATTO647N occupancy, the rations between A568-tet1/Cy5-tet1-3 and EGFP particles or IL-4-ATTO647N and EGFP particles were formed. To analyse receptor densities at the plasma membrane, EGFP particle numbers were rescaled to an elliptical cross-section and determined by our detection volume calibration ($A_{eff} = \pi w_0 z_0$).

7.9 Fluorescence cross-correlation spectroscopy (FCCS)

Pre-transfected HEK293T cells were prepared as described in chapter 7.6. After 1 h, IL-4-A647N (20 nM) was added and the cells were incubated for 30 min at rt. Measurements were performed with IL-4-A647N in the supernatant. In addition, cells expressing different IL-4Rα* constructs were click labelled with Cy5-tet2 (1.6 µM in air buffer, 30 min at 4°C) as previously described in chapter 7.5 and were seeded on fibronectin (10 µg mL^{-1} in DPBS) and poly-L-lysin (Sigma-Aldrich, St. Louis, MO, USA),

pre-coated Nunc™ Lab-Tek® II 8-well chamber slides (Thermo Fisher Scientific; Waltham, MA, USA). A LSM780 ConfoCor3 (Carl Zeiss; Oberkochen, Germany), with avalanche photo-diode detectors and a C-Apochromat 40x/1.2 water immersion objective, was used for FCCS measurements. During the experiment, cells with similar fluorescence intensity levels in the green and red channel were selected. The confocal detection volume was positioned on a homogeneous area of the bottom membrane on the cell. Fluorescence fluctuation data, 6 runs with a length of 20 s, were measured and data with slow intensity drifts or intensity spikes were discarded. To fit the auto-correlation functions of both channels, a model containing diffusion in 3D and 2D as well as a triplet component were applied (Equations 7.9.1, 7.9.2, 7.9.3 and 7.9.4).

$$G(\tau) = \frac{1}{N}\, G_{\mathrm{T}}(\tau)\, G_{3\mathrm{D}}(\tau)\, G_{2\mathrm{D}}(\tau) \qquad 7.9.1$$

$$G_{\mathrm{T}}(\tau) = 1 + \frac{f_{\mathrm{T}}\, e^{-\tau/\tau_{\mathrm{T}}}}{1 - f_{\mathrm{T}}} \qquad 7.9.2$$

$$G_{3\mathrm{D}}(t) = f_{3\mathrm{D}} \left(1 + \frac{\tau}{\tau_{3\mathrm{D}}}\right)^{-1} \left(1 + \frac{\tau}{S^2\, \tau_{3\mathrm{D}}}\right)^{-\frac{1}{2}} \qquad 7.9.3$$

$$G_{2\mathrm{D}}(t) = \frac{1 - f_{3\mathrm{D}}}{1 + \tau/\tau_{2\mathrm{D}}} \qquad 7.9.4$$

N represents the total particle number, f_{T} the fraction of particles in triplet state, τ_{T} the characteristic triplet residence time, $\tau_{3\mathrm{D}}$ the diffusion time of freely diffusing particles, S the structural parameter, $\tau_{2\mathrm{D}}$ the diffusion time of membrane bound particles, and $f_{3\mathrm{D}}$ the fraction of molecules of the freely diffusing species ($n_{3\mathrm{D}} = f_{3\mathrm{D}}\, N$). The structural parameter S was fixed to 6 during fitting, the triplet time was constrained to values between 1 and 100 µs, the 3D diffusion time to values between 100 µs and 3 ms, and the 2D diffusion time to values between 3 and 300 ms. After fitting and evaluation of the auto-correlation date, only cells with at least two proper runs in both the green and red channel were considered for cross-correlation analysis. A 2D diffusion model was used to fit the

cross-correlation function. Auto- and cross-correlation amplitudes were corrected for noncorrelated background, and spectral cross-talk from the green to the red channel (1%).[159] To estimate the diffusion coefficient of various receptor constructs, the size of the confocal volume was determined by measuring the diffusion of ATTO488 or ATTO655 in ddH_2O at 28°C. The previously reported diffusion coefficients of 414 $\mu m^2 s^{-1}$ for ATTO488 or 426 $\mu m^2 s^{-1}$ for ATTO655 measured at 25°C were adjusted to 28°C.[176, 177]

7.10 Fluorescence lifetime imaging microscopy (FLIM)

Transfected HEK203T cells were labelled, as described in chapter 7.5, with Cy3-tet2 (1.6 µm in air buffer, 30min at 4°C). Then the cells were seeded on fibronectin (10 µg mL^{-1} in DPBS) pre-coated Nunc™ Lab-Tek® II 8-well chamber slides (Thermo Fisher Scientific; Waltham, MA, USA). Time-domain FLIM recordings were performed on a SP8 FALCON confocal laser scanning microscope (LEICA; Wetzlar, Germany), equipped with a LEICA HCX PL APO 63x/1.2 motCORR CS water immersion objective (LEICA; Wetzlar, Germany). Excitation laser light at 561 nm was provided by a pulsed white-light laser (NKT superK EXTREME; NKT Photonics; Birkerod, Denmark) with 40 MHz repetition rate. Measurements were carried out at 23°C in an incubation chamber. The membrane area was determined, in the time channel with maximum photon counts, by using the ImageJ membrane segmentation script. To improve the statistics (>10 000 peak photon counts per cell), the photon counts of all segmented pixels were summed up to a single fluorescence decay curve. The fluorescence decays were fitted with a two-component exponential reconvolution routine using maximum likelihood estimation. A saturated solution of erythrosine B quenched with potassium iodide was used to measure the instrument response function.[179] The reported lifetimes (Equation 7.10.1) are the intensity-weighted average lifetime of two components with lifetimes τ_1 and τ_2 and amplitudes A_1 and A_2:

$$\tau_{av} = \frac{A_1 \tau_1^2 + A_2 \tau_2^2}{A_1 \tau_1 + A_2 \tau_2} \qquad 7.10.1$$

7.11 Phase separated supported lipid bilayer (SLB) preparation

First, small unilamellar vesicles (SUVs) were formed. Therefore, lipids (1 - 25 mg mL^{-1}), dissolved in chloroform, were mixed in a glass vial and then gently dried with a stream of N_2 followed by incubation with high vacuum for 1 h. The residue was resuspended in SLB buffer to a final concentration of 10 mM and was sonicated for 10 min. The formed multilamellar vesicles (MLVs) were aliquoted (20 µL) and stored at -20°C. During experiments, an aliquot was diluted with SLB buffer in a glass vial to a final concentration of 1 mM and was sonicated until the emulsion got clear, resulting in SUVs. Then the incubation chambers were prepared by gluing (Norland glue 68; Norland Products; Cranbury, NJ, USA) freshly cleaved mica (d = 8 - 12 mm) on top of a Nunc™ Lab-Tek® II 8-well chamber slide (thickness #1; Thermo Fisher Scientific; Waltham, MA, USA). The slide was incubated for 15 min under UV-light (365 nm). Afterwards, the SUVs (50 µL) were placed on top of the mica and CaCl2 (1 µL, 100 mM) was added. The SUVs were incubated for 1 min at rt, then the chamber was filled with prewarmed SLB buffer (200 µL) and the chambered slide was incubated for 20 min at 65°C on a heat block. After incubation, the formed SLB was washed 10 times with prewarmed SLB buffer (200 µL) and was cooled down slowly over a time period of 1 h. Then the buffer was exchanged to air buffer for cell experiments by gently washing (10× 200 µL) the SLB, previously transfected cells were seeded on the artificial membrane and confocal imaging was performed.

7.12 Immunoprecipitation (IP) and western blot (WB)

HEK293T cells (2 - 3×10^5) were seeded on a Nunclon™ 6-well multiwell plate (Thermo Fisher Scientific; Waltham, MA, USA) and were transfected with plasmid DNA (2 - 4 µg) as described above. 24 hours after transfection, the cells were washed with PBS and were incubated with lysis buffer (1 mL). Cells were transferred to a tube, incubated on ice for 30 min and were centrifuged at 1×10^4 g at 4°C. Then the supernatant was transferred into a fresh tube and was either processed in an immunoprecipitation assay or analyzed by western blot (WB).

For the HA-affinity-tag immunoprecipitation (IP) assay, 50 µL of anti-HA-tag magnetic micro beads were equilibrated with washing buffer and the supernatant of the cell lysis was added. The beads were incubated for 1 h on ice with shaking and were placed in a strong magnetic field. Then the beads were rinsed with wash buffers (3× 300 µL) and ddH_2O (300 µL) and samples were eluted with 100 µL HA-peptide (2 mg mL^{-1}). The fractions were analyzed by WB.

The lysates or IP fractions were incubated with 4× loading buffer (Bio-Rad Laboratories GmbH; Feldkirchen, Germany) for 10 min at rt and were loaded (15 µL) on the SDS-PAGE gel (10 - 12%, Bio-Rad Laboratories GmbH; Feldkirchen, Germany). In addition, a protein standard (Biorad Precision Plus Protein Dual Xtra Strandard; Bio-Rad Laboratories GmbH; Feldkirchen, Germany) was loaded. The gels were performed in 1× SDS running buffer with 200 V (constant) for 35 min. Then the denatured proteins were transferred to the WB membrane (ImmobilonP membrane 0.45 µm; Merck; Darmstadt, Germany). Therefore, the membrane was first incubated with MeOH for 2 min and washed with transfer buffer, blotting paper (Bio-Rad Laboratories GmbH; Feldkirchen, Germany) was simultaneously soaked with transfer buffer for 5 min. The components were stacked on the blotting cassette of the semi dry blotter (PierceG2 FastBlotter; Thermo Fisher Scientific; Waltham, MA, USA) and the proteins were transferred at 25 V and 1.3 A for 7 min. After the protein transfer, the membrane was blocked in 20 mL superblock solution (Thermo Fisher Scientific; Waltham, MA, USA) for 1 h at rt. The primary antibody was diluted in superblock solution (10 mL) in a 50 mL tube, the membrane was added and the tube was rotated at 4°C overnight (o/n). Then the membrane was washed with T-BST (4× 10 min) and was incubated for 1 h at rt in the HRP containing secondary antibody, diluted in superblock solution (10 mL). In the

following step, the membrane was washed again in T-BST (4× 10 min), placed in super signal solution (Thermo Fisher Scientific; Waltham, MA, USA) for 5 min and the bioluminescence signal was detected (Amersham Imager 600; GE Healthcare; Chalfont St Giles, UK).

7.13 Receptor truncation and cross-linking experiments

HEK293T cells (3.2×10^4) were seeded on an ibidi slide (ibidi GmbH; Gräfelfingen, Germany) coated with fibronectin (10 µg mL^{-1} in DPBS). After 24 h, the cells were transfected either with the IL-2Rγ truncation mutants or the IL-2Rγ TAG mutants and JAK3-EGFP and GCE constructs were incubated in growth medium supplemented with AbK (0.5 mM) for 18 h. Then the cells were washed three times with air buffer and incubated with trisNTA-Alexa647 (40 nM) for 30 min before they were washed again with air buffer and were imaged at a LSM780 ConfoCor3 (Carl Zeiss; Oberkochen, Germany).

III Results

8 Bioorthogonal covalent receptor labelling in living cells

8.1 Labelling strategies for plasma membrane receptors

There are many ways of labelling the extracellular domain of cell surface membrane receptors. Most of the methods involve non-covalent binding of bioorthogonal tags, whose labelling efficiency depends on the binding kinetics of the interaction partners (Figure 8.1.1A). Previously, Weidemann and colleagues showed by non-covalent labelling with a nitrilotriacetic acid (trisNTA) dye construct and a hexa-histidine-tag (H_6-tag) that labelling of IL-4R components is completed within minutes and that the method can be used for FCCS to study receptor dimerization *in vivo*.[29] Another approach is the covalent fluorescent labelling of a receptor ligand with chemical tools as, for example, *N*-hydroxysuccinimide ester (NHS ester) or maleimide coupling.[28, 30] These chemically modified ligands are excellent labels because of their high natural affinities and can be used for ligand receptor colocalization or receptor dimerization studies. However, one major drawback of this labelling method is the limit of ligand independent experiments as the binding pocket of the receptor is already occupied. Further disadvantages of non-covalent labelling are the limited spatiotemporal localization of the interaction partners due to dissociation within several minutes as well as interfering environmental influences.[180, 181] To overcome these drawbacks, many bioorthogonal methods were developed for covalent fluorescence labelling of cell membrane receptors, as for example click reactions (Chapter 2.1). The most prominent reactions take place between a functional group of an incorporated uAA and its corresponding reactive group. For instance, in the very fast IEDDAC click reaction, the strained alkene or alkyne moiety of the uAA and a tetrazine-dye conjugate form a stable covalent bond (Figure 2.2.1).

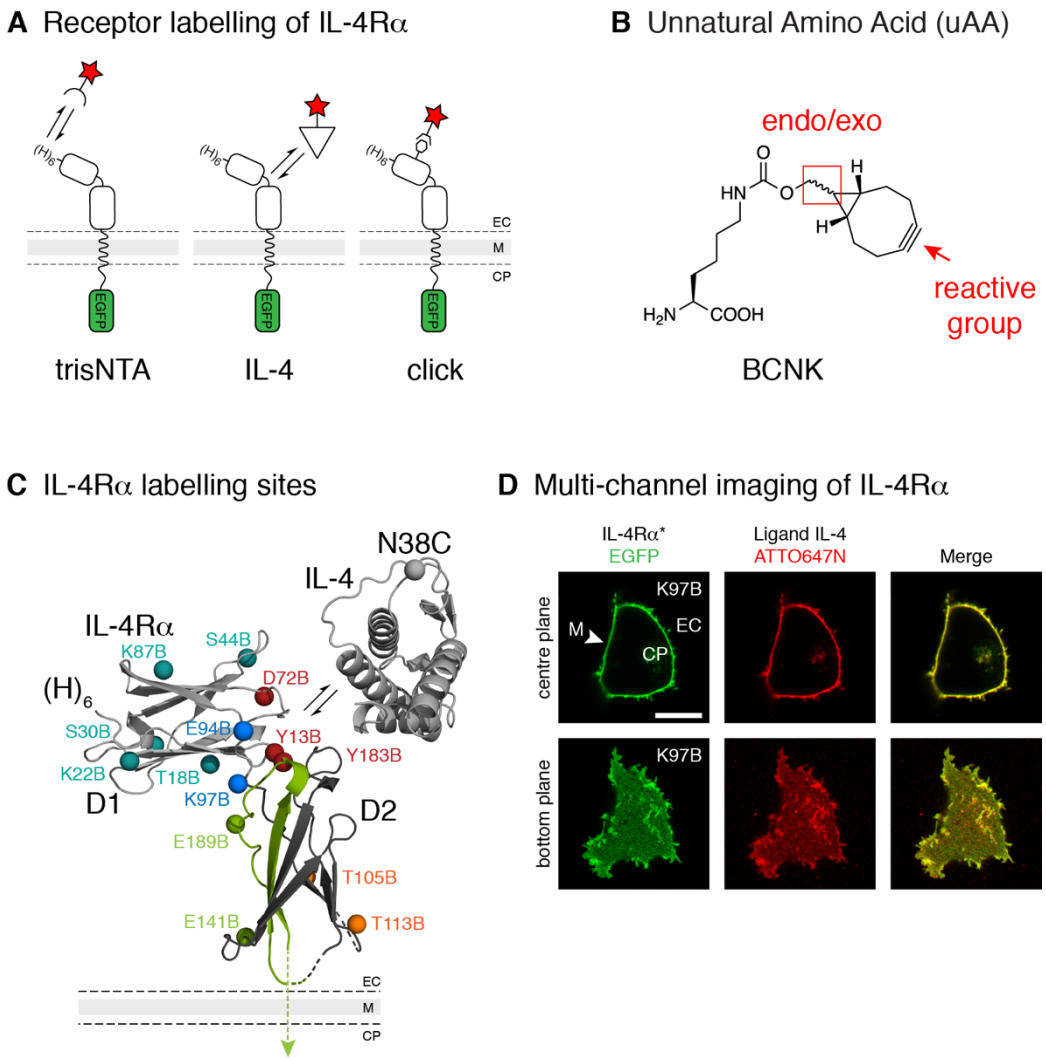

Figure 8.1.1: Labelling strategies for plasma membrane receptors. A) Schematic representation of three different labelling methods for transmembrane receptors. The trisNTA and IL-4 ligand labelling are non-covalent methods, whereas click labelling is covalent. B) BCNK as uAA incorporated in the IL-4Rα* by GCE with its highlighted reactive headgroup, the strained cycloalkyne moiety, and its endo- and exo-conformations. C) Crystal structure of the cytokine receptor IL-4Rα (PDB: 1IAR) containing different BCNK mutations (magenta spheres) in the primary sequence and occupied with the ligand IL-4.[37] D) HEK293T example cell expressing IL-4Rα* (green) was incubated with IL-4-A647N ligand (red). CP, cytoplasm; EC, extracellular; M, membrane. Scale bar: 9 μm.

In this study, we characterized the site-specific click labelling at the surface of living cells by modifying the class I cytokine receptor IL-4Rα amino acid structure with the uAA BCNK. The BCNK modified receptor contains a strained cycloalkyne motif as a reactive group for the IEDDAC reaction with a tetrazine-fluorophore construct (Figure 8.1.1B). Moreover, the BCNK molecule, with its bicyclic ring systems, allows an endo- and

exo-conformation. The IL-4Rα is a single transmembrane receptor with two extracellular barrel-shaped fibronectin domains, D1 distal and D2 in proximity of the plasma membrane, an alpha-helical transmembrane domain and an intrinsically disordered intracellular tail (Figure 1.2.1A). To study the labelling efficiency of the extracellular domain, a truncated non-signalling IL-4Rα construct (IL-4Rα*; H_6-IL-4Rαm266-EGFP; amino acids 1 - 266; mature numbering) with an N-terminal H_6-tag and a C-terminal enhanced green fluorescent protein (EGFP) was used (Figure 8.1.1A). We observed that the EGFP is only expressed when the amber stop codon is suppressed (GCE) by addition of BCNK in the cell growth medium. The signal of EGFP positive receptors showed negligible presence in internal membranes and a sufficiently slow turnover at the plasma membrane. Additionally, the EGFP-tag allowed an easy and precise segmentation for the plasma membrane of living cells. All these properties make this receptor an excellent target for the quantification of plasma membrane associated signals.

As a starting point, different mutants were cloned via site-directed mutagenesis to introduce the amber stop codon (TAG). For this purpose, the crystal structure of IL-4Rα (PDB: 1IAR) was used to identify possible mutation candidates in which the side chain of the amino acid points at the hydrophilic water surface of the receptor (Figure 8.1.1C).[37] Each important region of the receptor was covered with single stop codons: In the D1-domain T18, K22, S30, S44 and K87 (teal) were mutated as membrane distal mutations, whereas in the D2-domain T105, T113 and E141 (orange, green) as membrane proximal mutations were cloned. The mutations Y13, D72 and Y183 (red) are located in the binding pocket of the ligand IL-4 and are crucial to the activation of the receptor.[73] Moreover, E94 and K97 (blue), mutations in or near the linker region of the receptor between the D1- and D2-domain, were mutated. E189 (green) is a special mutation, because the stop codon is located in the important WSXWS (X = E189) motif. In previous studies, this motif was shown to be involved in many important processes, such as expression, folding, ligand binding and pathway activation.[32, 35, 40, 41, 182-184]

Proper ligand binding of IL-4 labelled with ATTO647N (IL-4-A647N) is a good readout for receptor expression, folding and functionality of the modified IL-4Rα (Figure 8.1.1D). IL-4 is a four alpha-helical protein which binds to the IL-4Rα binding pocket very

selectively and with a low dissociation constant (K_d) of 20 - 300 pM.[32] Two point mutations were incorporated into the ligand IL-4 at position N38C and F82D. Mutation F82D led to a longer interaction time ($k_{off} = 0.46 \times 10^{-3}$ s^{-1}; $t_{1/2} = 25$ min) of the receptor with its ligand whereas mutation N38C was used for covalent fluorescence labelling through maleimide coupling with ATTO647N (courtesy of Prof. Dr. Thomas Müller; Julius-Maximilians-University Würzburg).[180, 185]

8.2 Cell surface expression of BCNK modified IL-4Rα*

In the first experimental attempts with GCE, cell surface expression levels of BCNK modified receptors were screened under different experimental conditions. For this purpose, the eukaryotic cell line HEK293T was used as a model system for quantification. These cells are easy to maintain, transfect and they are well suited for microscopy. Furthermore, they show high incorporation rates of uAA, which is important for proper GCE.[186] To quantify the IL-4Rα* expression, first the proteome of the cell surface was covalently labelled with Cy5-NHS in the 633 nm channel (Figure 8.2.1A). The Cy5 signal was used for segmenting the plasma membrane with the self-developed ImageJ plug-in (Chapter 8.3). The mask created by the software in the 633 nm channel was then transferred to the 488 nm channel and the fluorescence signal from EGFP expression was measured (Figure 8.2.1B). The EGFP signal of the BCNK modified receptors were compared to the EGFP signal of wt receptor expression. To better control the expression components needed in the GCE, a two-plasmid approach was used. The first plasmid contained the IL-4Rα* with one stop codon (TAG) at different locations in the coding sequence and the second plasmid coded for four copies of the TAG-specific $tRNA^{BCNK}$ and the cognate BCNK-tRNA synthetase. Upstream to the receptor coding sequence, a strong *Cytomegalovirus* (CMV) promoter was located. The HEK293T cells were transiently transfected with the plasmids and were kept under standard media supplemented with BCNK for at least 18 h.

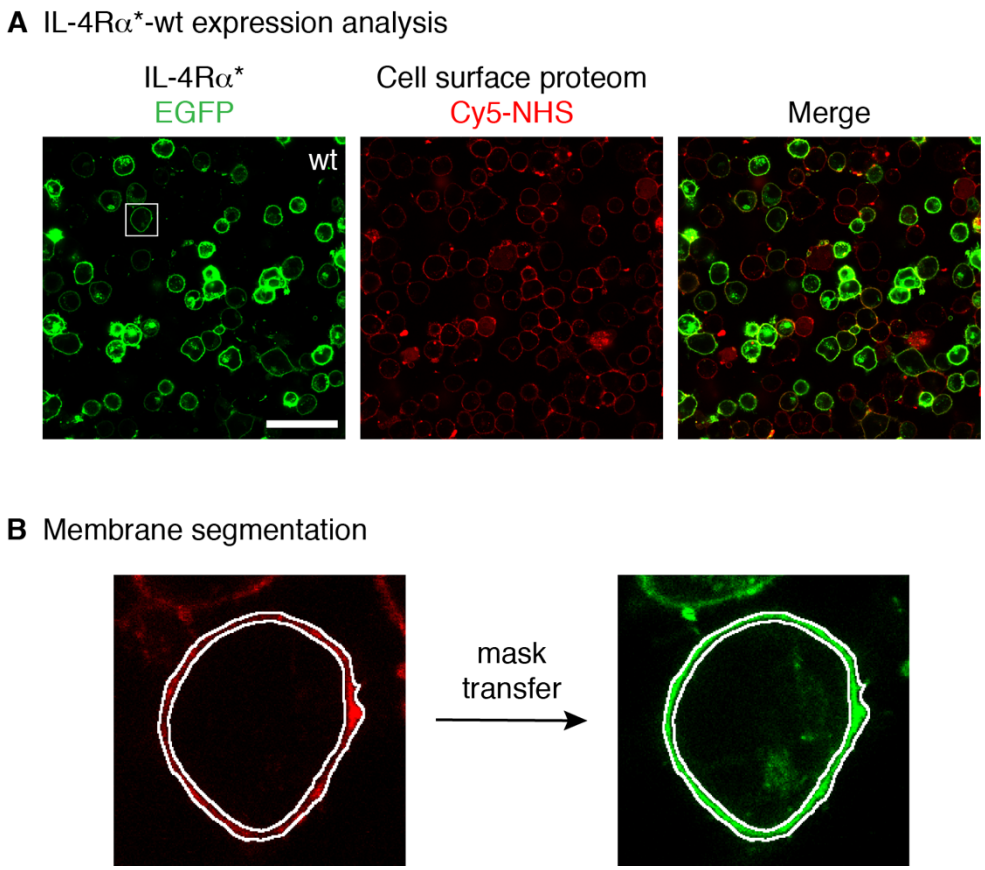

Figure 8.2.1: Cell surface proteome labelling. A) HEK293T cells were transiently transfected with the wt IL-4Rα* plasmid (green), the extracellular cell surface proteome was labelled with Cy5-NHS ester (red) and the cells were imaged by confocal microscopy. B) A mask (white) was created in the red channel by the ImageJ plug-in, which was then transferred to the green channel, and the intensity of the green signal was analysed. Scale bar: 50 µm.

Since the DNA for the IL-4Rα* and the GCE machinery were located on different plasmids, the expression levels with several DNA combinations had to be tested (Figure 8.2.2). All expression levels with BCNK modified receptors were strikingly decreased compared to IL-4Rα* wt expression. The ratios with almost equal amounts of DNA only showed a slight variation, whereas the ratios with a high amount of either of the two plasmids displayed a reduced receptor expression. Another important characteristic of the IL-4Rα* was the selective localization at the cell surface. As automated image analysis is very sensitive to false signals, as for instance from receptors stuck in the protein synthesis machinery, cell pictures were compared. They showed a clear variation of the different false positive signals from the cytoplasm of the cell (Figure 8.2.2, red

arrows). The combination of the ratio one to four of IL-Rα*-K97B (B, BCNK modified) and BCNK-tRNA synthetase/tRNA^{BCNK} DNA represented the lowest intracellular background signal and a high cell surface expression and was therefore used in further experiments (Figure 8.2.2, white arrows).

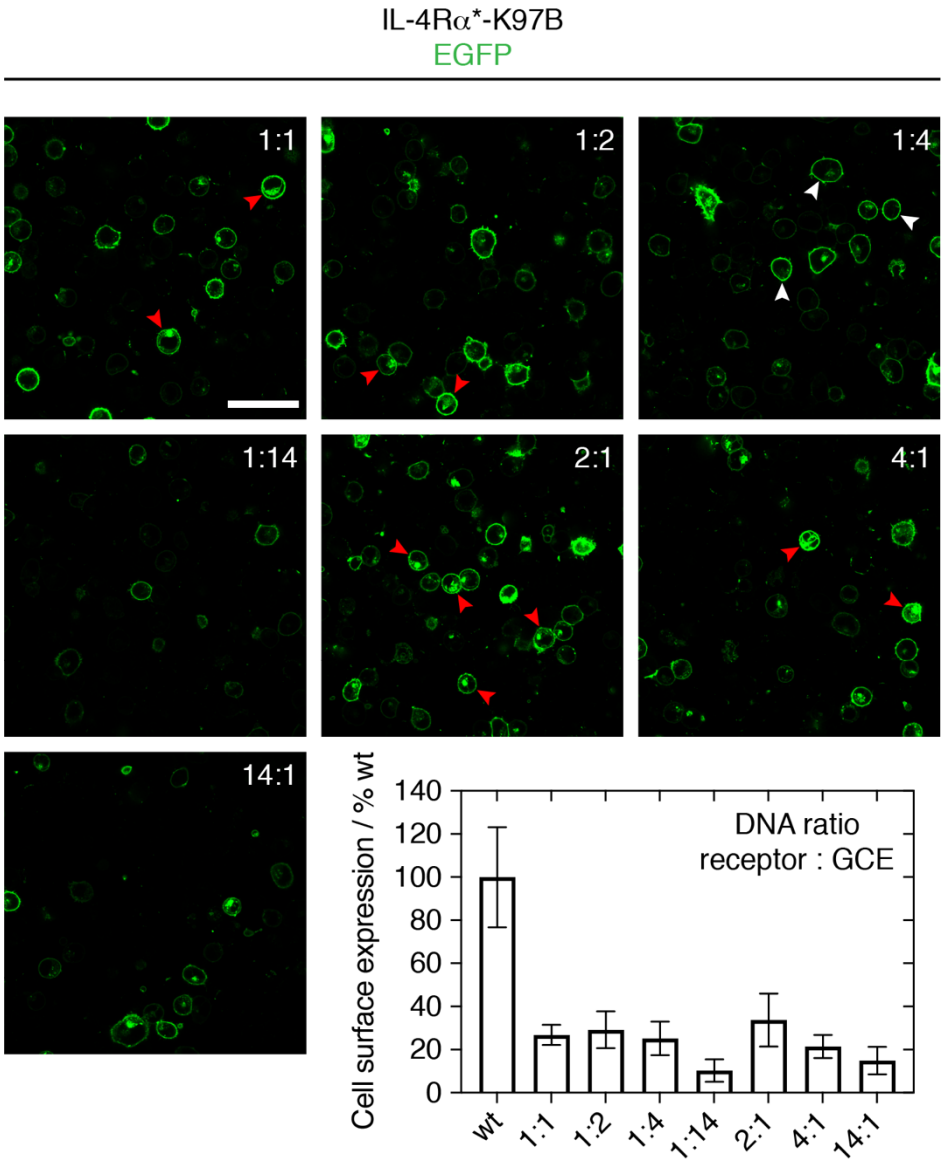

Figure 8.2.2: IL-4Rα* expression with different DNA ratios. Cells were transfected with different ratios of the two plasmids, IL-4Rα* (green) plasmid with a stop codon at position K97B *vs.* BCNK-tRNA synthetase/tRNA^{BCNK} plasmid. After 18 h, the cell membrane was labelled with Cy5-NHS and the expression levels on the surface of living cells were measured and compared to the expression level of the wt construct.

Red arrows, cells with intracellular background signal; white arrows, cells with membrane specific localization of signal. Scale bar: 50 µm.

Another important factor for the protein expression with GCE is the concentration of uAA in the growth medium. As the survival rate of HEK293T cells depends on the concentration, due to toxic effects of BCNK at higher concentrations, it should be kept as low as possible. In previous studies BCNK concentrations between 0.05 and 1 mM

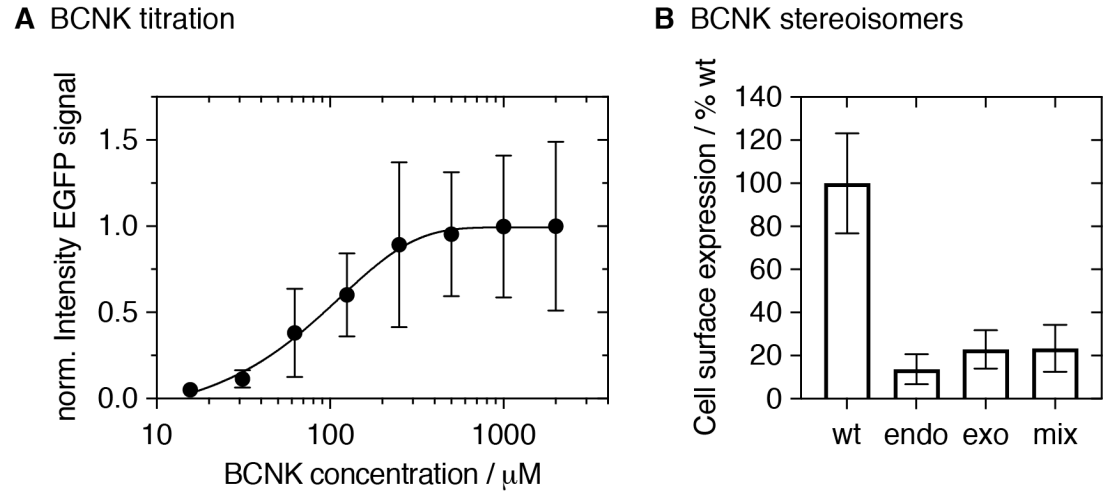

Figure 8.2.3: BCNK concentrations and synthetase selectivity. A) HEK293T cells, transfected with the IL-4Rα*-K97B plasmid, were incubated with different concentrations of endo/exo BCNK or alternatively B) with different stereoisomers of BCNK. The cell surface was labelled with Cy5-NHS, imaged by confocal microscopy and the expression levels were either normalized to the highest intensity level or were compared to the expression level of the wt IL-4Rα*.

were reported.[112, 113, 119, 187] Our titration of BCNK in growth media showed a range between 0.25 and 2 mM in which full expression takes place (Figure 8.2.3A). However, concentrations above 2 mM BCNK in growth media led to apoptosis of HEK293T cells. To accomplish full expression of IL-4Rα* and cause as little stress as possible to the cells, a concentration of 0.5 mM was used in this study.

Comparing the stereo-selectivity of the BCNK-synthetase for endo and exo BCNK showed a clear prevalence for the exo-form (Figure 8.2.3B). This is in line with previous

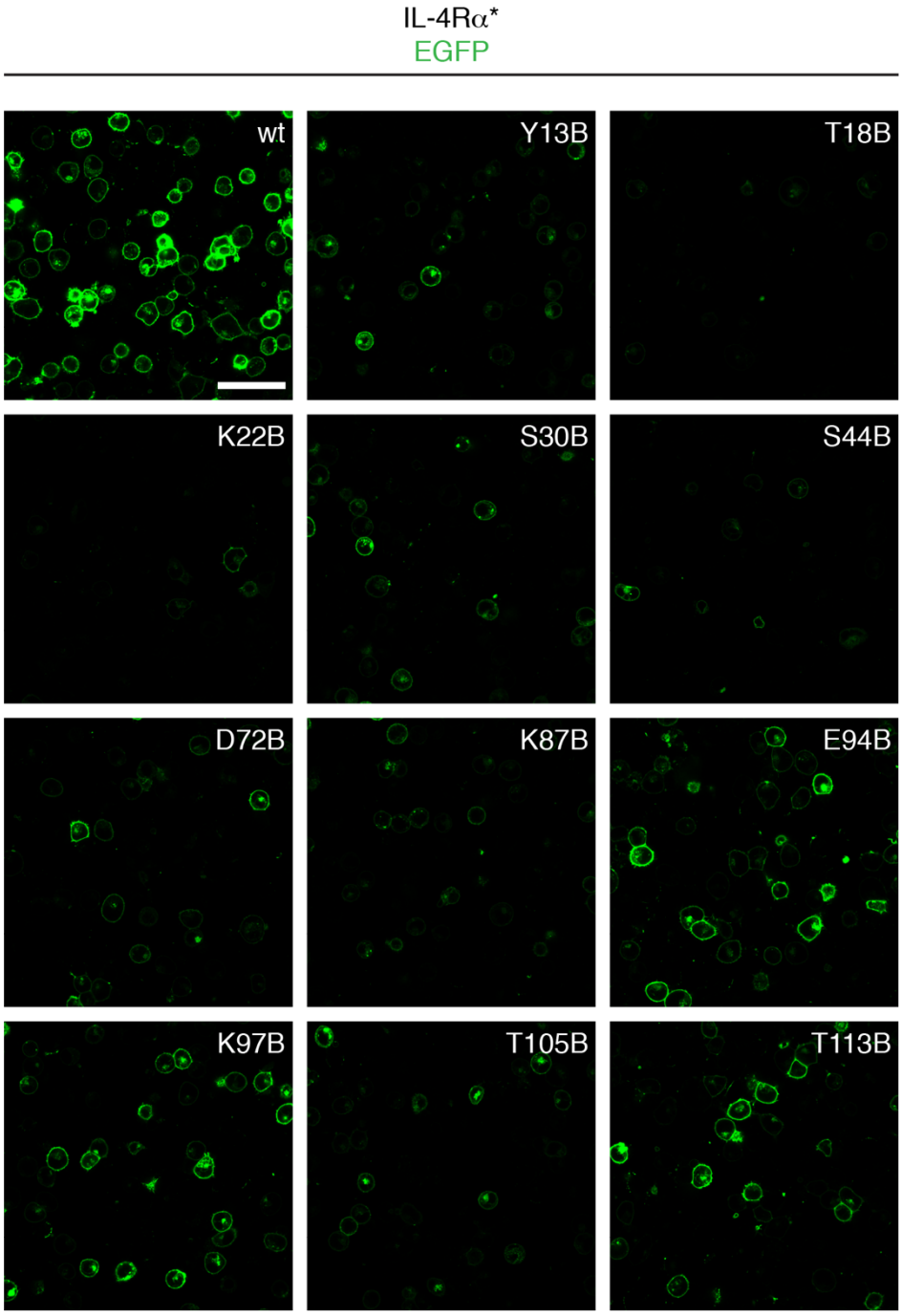
IL-4Rα*
EGFP
wt
Y13B
T18B
K22B
S30B
S44B
D72B
K87B
E94B
K97B
T105B
T113B

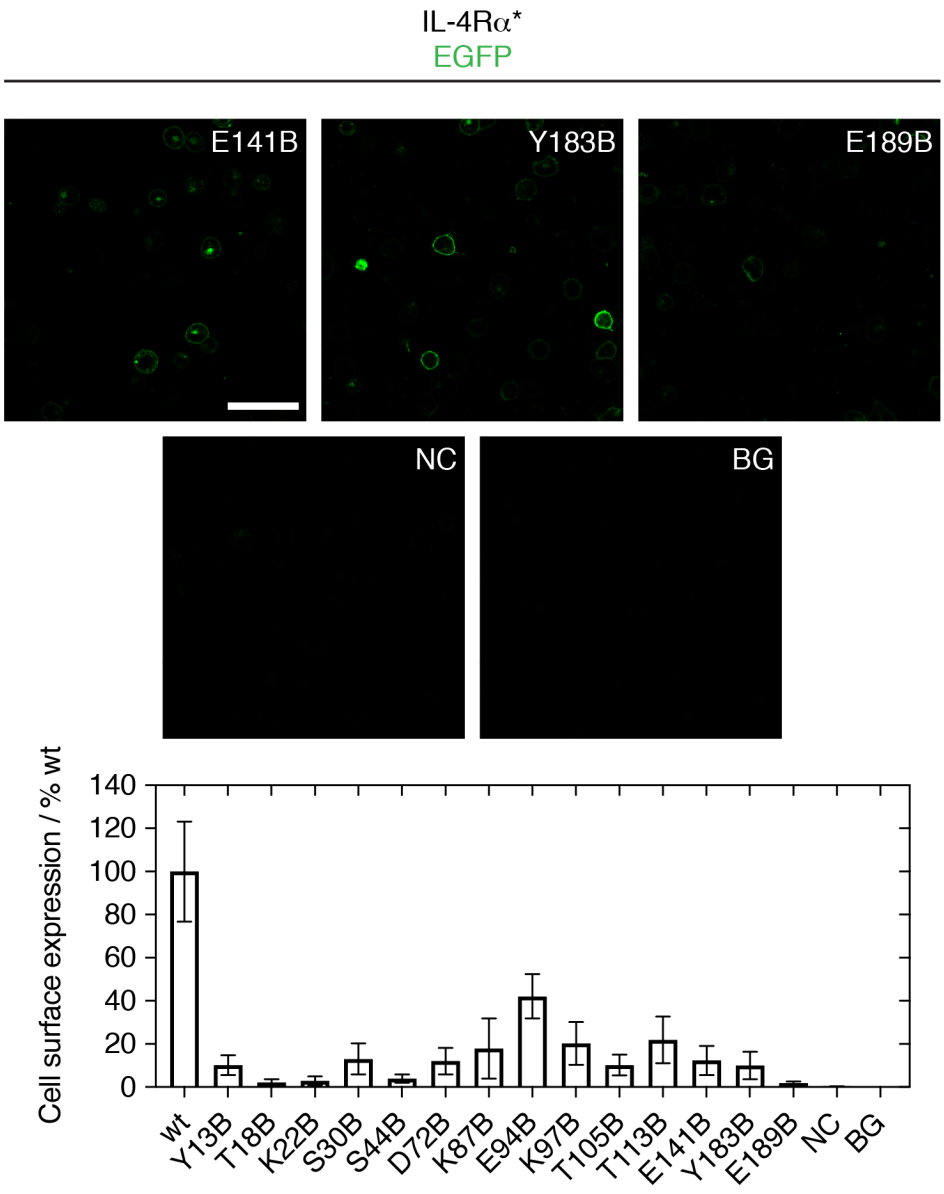

Figure 8.2.4: Expression levels of different IL-4Rα* mutations. Cells expressing the various BCNK mutations in the extracellular domain of the IL-4Rα* (green) were labelled with Cy5-NHS, imaged and analysed by our self-developed ImageJ script. Receptor expression levels were compared to wt receptor cells and showed an overall reduced receptor density for the BCNK modified receptors at the surface of living cells. Scale bar: 50 µm.

literature, which reports the same result of a higher expression level with exo BCNK.[112, 119] In these studies, western blot data of the protein expression in whole cell lysates were compared. With our single cell microscopy approach, however, both the expression levels and the proper localization of the receptor, at the surface of living cells, can be

analysed. Since the BCNK, provided by our collaborator Prof. Dr. Kathrin Lang (Technical University of Munich), is a mixture of endo/exo BCNK with a ratio of about 1 : 4, proper expression levels of the IL-4Rα* are expected to mainly reflect exo BCNK.

Expression levels of the mutant library were screened and compared to the wt IL-4Rα* abundance (Figure 8.2.4). The data showed a reduced expression level in all locations where the particular amino acid was replaced by BCNK. These results are comparable to previously published data of GCE in IL-12Rα with BCNK.[124] Furthermore, the expression system is tight as cells lacking BCNK (NC) showed negligible fluorescence, which was in the range of the auto-fluorescence of untransfected cells (BG). Interestingly, a modification at the X-position in the important WSXWS motif (E189B) led to the lowest expression rate observed. The WSXWS motif is crucial for receptor expression, folding and stability at the plasma membrane of cells.[35, 40, 41, 183, 184] Mutant K97B, positioned in the linker region between the D1- and D2-domains, was chosen as our standard labelling-site, because it showed a high cell surface expression, was separated from the direct impact of the cell membrane, did not interfere with ligand binding and showed one the highest labelling efficiencies (see next chapters).

After we had managed to express the BCNK modified IL-4Rα* mutants, different tetrazine-dye constructs were tested for a successful IEDDAC reaction. HEK293T cells expressing various IL-4Rα* mutants were therefore labelled with Alexa647-tet1 (A647-tet1), SiR-tet2, ATTO647N-tet1 (A647N-tet1) and Cy5-tet1 (Figure 8.2.5). Cells incubated with A647-tet1 and SiR-tet2 (old sample) showed no visible fluorescence associated with the plasma membrane. With A647N-tet1 a high intracellular background signal was detected indicating uptake of non-conjugated dye. The high internalization rate was caused by the positive charge of the A647N-tet1, as cells prefer positively charged materials for unspecific uptake. For this reason, highly negative charged fluorophores such as Cy5-tet1 were preferentially used for further experiments.

In summary, GCE leads to overall reduced expression level with a drastic effect of the uAA concentration. As the variation of expression levels is unpredictable with our current understanding of protein folding and transport along the secretory pathway, a library with different mutants at surface accessible positions over the protein of interest (POI) is

necessary. Furthermore, the charge of the used fluorophores is crucial to minimize intracellular background signal. In our experiments, a proper extracellular labelling was

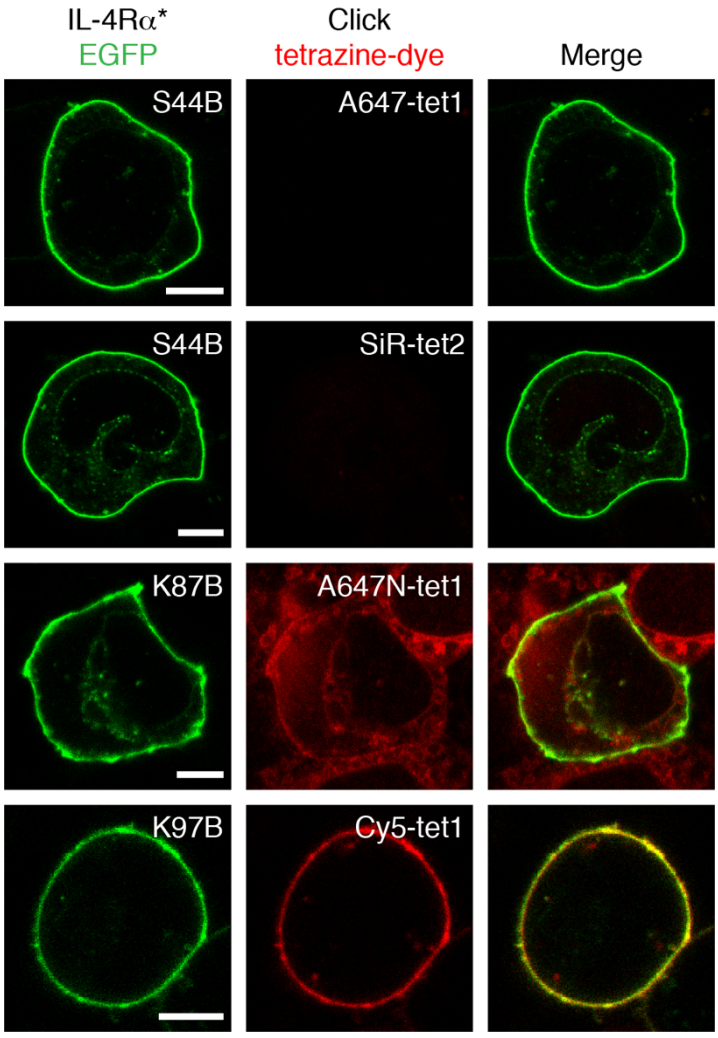

Figure 8.2.5: Covalent click labelling with different tetrazine-dye constructs. HEK293T cells expressing different IL-4Rα* mutants (green) were labelled with various tetrazine dye constructs (red). Cells incubated with A647-tet1 (upper row) and SiR-tet2 (upper middle row) did not show significant product formation for unknown reasons, whereas those incubated with positively charged A647N-tet1 displayed a high disturbing background signal inside the cells (lower middle row). Only cells labelled with Cy5-tet1 (and other negatively charged dyes) displayed a clean fluorescence signal from the plasma membrane (lower row). Scale bar: 6 and 9 µm.

achieved only by negatively charged tetrazine-dye constructs. Since simple imaging of the membrane of living cells only allows a relative comparison of these signals, a quantification approach was developed.

8.3 Calibrated ratiometric imaging (CRMI)

To investigate the activation mechanism of the IL-4R and the JAK/STAT pathway, an exact quantification of the click labelled system is desirable. Therefore, we developed (in collaboration with Frederik Steiert and Thomas Weidemann, Schwille group, MPI of Biochemistry) an advanced medium throughput approach to quantify fluorescence signals at the plasma membrane of living cells. Calibrated ratiometric imaging (CRMI) converts a fluorescence signal into particle numbers and concentrations, by combining laser scanning confocal microscopy and in solution fluorescence correlation spectroscopy (FCS) (Figure 8.3.1A). To combine both microscopy techniques, it is important that the same settings are used for confocal imaging and FCS. This results in the same-sized confocal detection volume (voxel, observation volume, confocal spot) and the same molecular brightness (quantum yield, counts per particle (*CPP*)) of the fluorophore for both measurement conditions. As experiments with living cells are time consuming, different experimental days can be combined by calibration with FCS. Furthermore, FCS can monitor the performance of the microscope and give information on the day-to-day variance of aging laser intensity, varying batches of microscope slides and temperature drifts. Therefore, FCS calibration measurements with fluorescent standard dyes were performed providing the molecular brightness and the diffusion time of the fluorophore. Both are easily accessible and excellent key parameters for the microscope performance.

The first step of our CRMI approach requires the segmentation of the region of interest (ROI) in the confocal images (Figure 8.3.1B). Then, the pixel counts are divided by the residence time of the laser at each position (pixel time (PT)) resulting in the intensity per pixel. A further conversion to the particle number per pixel is provided by dividing the intensity per pixel by the *CPP* of the particular dye. By determining the size of the

detection volume (w_0, z_0, V_{eff}), a rescaling of the particle number into the concentration is possible. Experiments with two colour channels, such as receptor and ligand, directly represent biochemical information, for example the ligand labelling efficiency. For a particular chemical system with covalent receptor labelling, the click labelling efficiency can be measured.

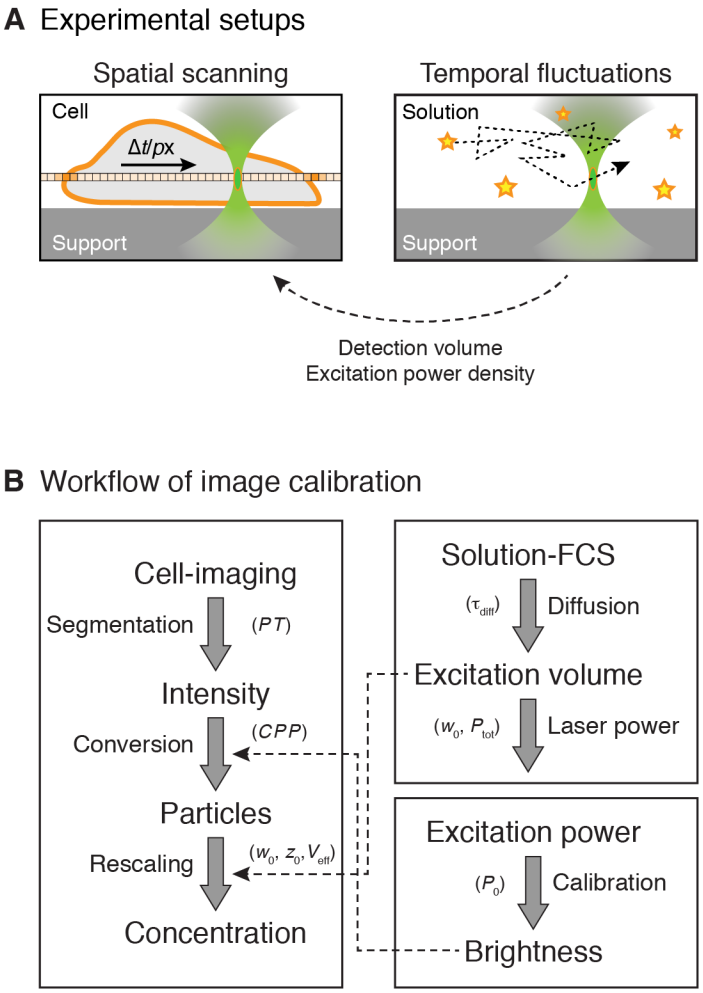

Figure 8.3.1: Calibrated ratiometric imaging. A) Simplified representation of the two measurement situations, laser scanning confocal microscopy (left) and in solution fluorescence correlation spectroscopy (FCS, right), used for CRMI. B) Workflow of the image calibration with FCS: imaging, segmentation, conversion to particle number and concentration (right); FCS calibration steps with diffusion standard, power density and in solution calibration measurements (left).

The workflow of CRMI involves two sets of reference measurements: First, the daily determination of the diffusion reference in parallel with the cell experiments and, second brightness reference plots, which were measured once during the project. The diffusion standards (ATTO488, Alexa568 and ATTO655) for each laser channel were measured with the same imaging settings and hardware on neighbouring wells at the same chambered microscopy slide, before and after the experiment (Figure 8.3.2). Besides the quality control of the microscope, the diffusion reference measurements provide information about the dwell time of a particle in the observation volume (diffusion time, τ_{diff}) and the detection volume dimensions (w_0, z_0 and V_{eff}). A precise detection volume for all laser lines was determined by weighted channel fitting of the diffusion standard measurements with an axis ratio z_0/w_0 as an independent fit parameter and a fixed correction factor (± 10%) for small differences between imaging and FCS acquisition. The *CPP* was obtained by dividing the mean fluorescence intensity *F* (kHz), derived from the intensity trace, by the number of particles *N* from the fit of the corresponding correlation function.

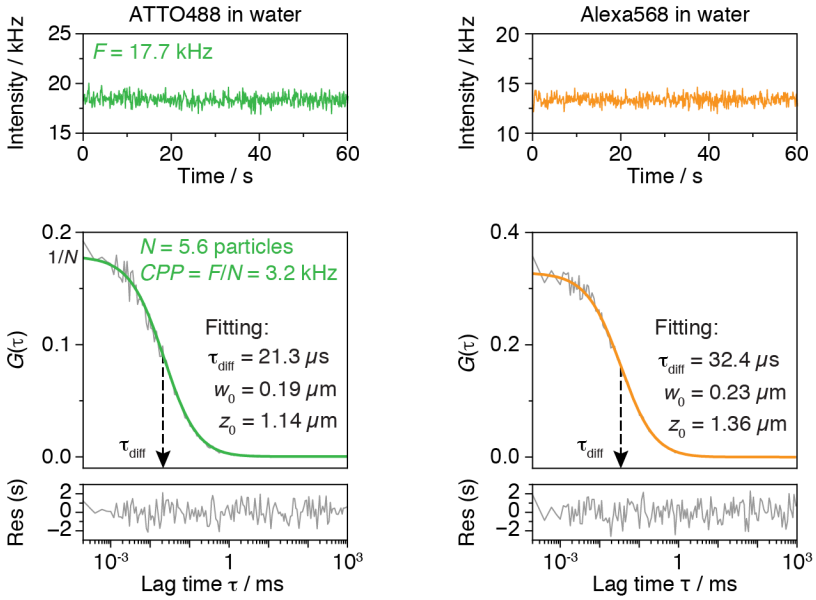

Figure 8.3.2: FCS diffusion standards. Example in solution FCS curves of the ATTO488 and Alexa568 diffusion standards as they were measured in a pseudo-cross-correlation setup in the neighbouring wells on the same chambered microscopy slide as the sample cells on each experimental day. Fitting returned the diffusion times that were used to calibrate the excitation volume for each colour channel.

The excitation power density (P_0) was calculated by dividing the total laser output (P_{tot}), measured with an external power meter, by the beam waist of the particular laser channel. Next, we measured the molecular brightness of the imaging dyes at varying low laser intensities. Therefore, EGFP or tetrazine-dye constructs (e.g. Alexa568-tet1) were diluted in PBS pH 7.4 or air buffer (100 nM), were incubated with BCNK (0.5 µM) for solution conjugation and finally measured by FCS. The BCNK-tetrazine conjugation is necessary in order to increase the fluorescence intensity after the click reaction, because the tetrazine-group quenches the intensity of the fluorophore molecule.[188] The resulting linear brightness reference plots were consistent with FCS data from the bottom membrane of living cells (Figure 8.3.3A, courtesy of Frederik Steiert). As *in vitro* FCS measurements are easier to handle, less noisy and more accurate, this simplification is a huge advantage in the experimental setup. Slow internal cell processes like cytoskeleton rearrangements, actin dependent membrane trafficking or transient aggregation prior to internalization affect the total fluorescence and the correlation function. The errors (2 - 4%) of the solution measurements were even too small to be displayed in the graph representing the high accuracy of the molecular brightness measurements (Figure 8.3.3B).

Cells with transiently transfected receptor construct showed a broad range of intensities and therefore the imaging settings had to be adjusted to the dynamic range of the avalanche photodiode (APD) detectors. The brightness reference plots, covering the excitation power range of our experiments, showed a linear behaviour of the *CPP* for all dyes used. These calibration plots in combination with the daily diffusion reference measurements allowed the determination of precise *CCP* values for each imaging session. Furthermore, the slope of the linear fit curves of the brightness reference plots exhibited the superior performance of synthetic dyes (Alexa568, ATTO647N and Cy5) with respect to fluorescent proteins (EGFP). To reduce the background signal in single cells measurements, cells were imaged at the centre plane resulting in a continuous thin line for the plasma membrane. They were either imaged one by one in small frames or, if the expression level was high enough, as cell ensembles in a larger field of view. In these larger images, single cells were then cut out by hand leading also to a data collection of single cell images. Next, the plasma membrane was segmented by an

ImageJ-script (developed by Giovanni Cardone, Imaging Facility, MPI of Biochemistry) which uses the Otsu-algorithm to find the largest continuous membrane area. The pixel

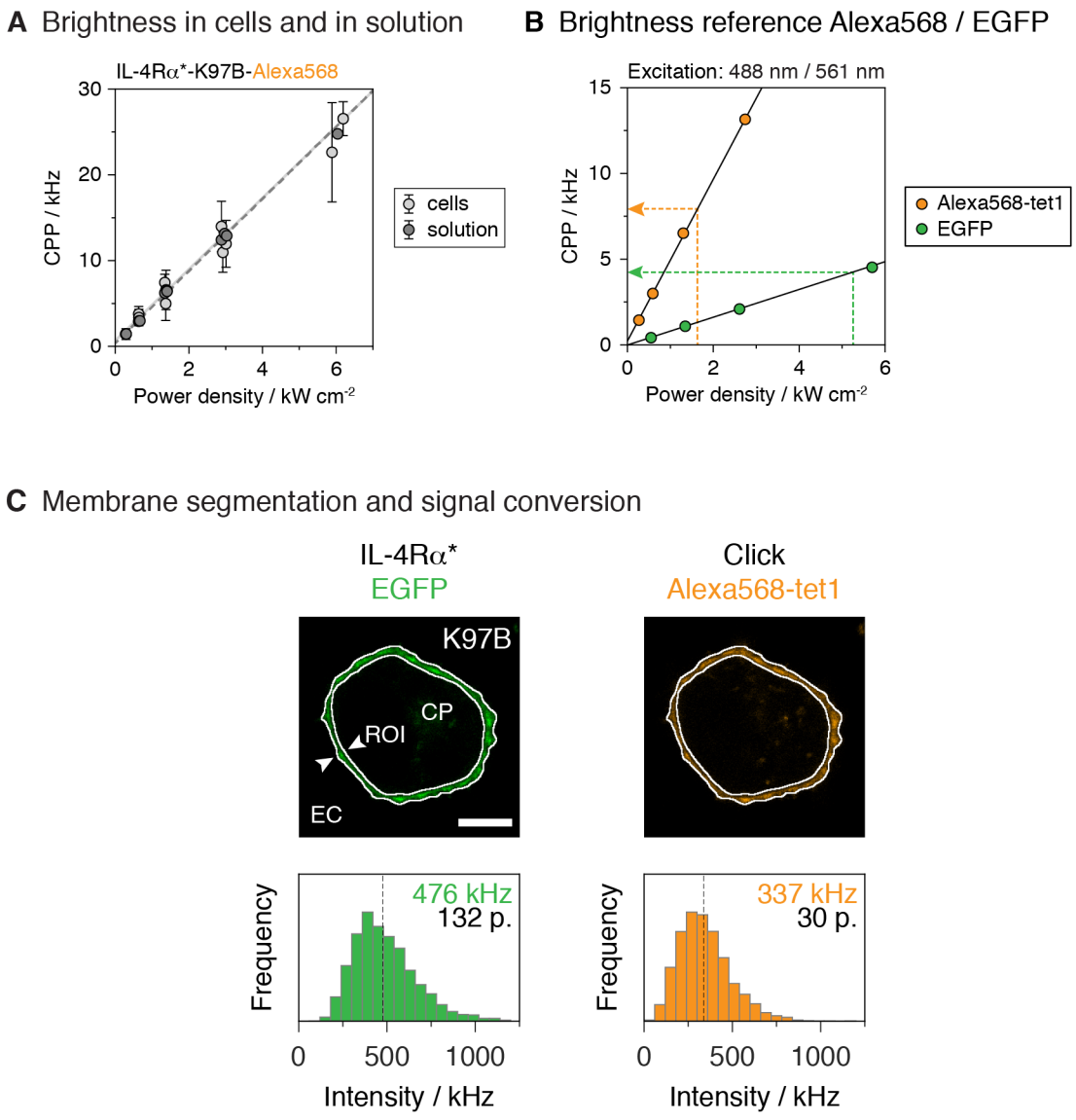

Figure 8.3.3: Brightness reference plots measured by FCS. A) FCS based brightness reference plot of A568-tet1 measured in solution or at the membrane of living cells. B) Brightness reference plot with the *CPP* of the EGFP and A568-tet1 fluorophores measured by in solution FCS experiments and plotted against the power density. The organic A568-tet1 showed a superior performance compared to the protein EGFP, which is shown by its steeper slope (kindly provided by Frederik Steiert). C) An example cell treated with the CRMI procedure showed a particle number of 132 EGFP-tagged and 30 simultaneously A568-tet1-tagged receptors leading to a labelling efficiency of about 23%. CP, cytoplasm; EC, extracellular; ROI, region of interest. Scale bar: 6 µm.

counts of the ROI as well as other important parameters were exported in data tables for both colour channels. The combination of FCS calibration and confocal imaging led to an average 132 receptors per pixel and 30 Alexa568-tet1 molecules per pixel, representing a labelling efficiency of about 23% in the IL-4Rα* mutant K97B example cell (Figure 8.3.3C).

8.4 Efficiency of the covalent IL-4Rα click labelling reaction

After we had established the suitable expression system of BCNK modified IL-4Rα* by GCE, the amount of click labelled receptors at the membrane of living cells was analysed by CRMI. The reaction kinetic of the bioorthogonal IEDDAC reaction depends not only on the functional group (strained alkene or alkyne) of the uAA but also on the steric and electronic properties of the tetrazine group. Therefore, BCNK and three common tetrazine-groups conjugated with different negatively charged dyes for extracellular labelling were tested (Figure 8.4.1A). 3,6-Di(pyridin-2-yl)-1,2,4,5-tetrazine (tet1) was previously described as an excellent tetrazine-group for extracellular labelling, due to its reduced internalisation rate. The uptake kinetics was disturbed by the bulky ring system forming a steric hindrance. The smaller 3-phenyl-1,2,4,5-tetrazine (tet2) was depicted as functional group for intracellular labelling and with its sterically favoured ring system showed improved reactivity.[112, 135] 3-methyl-6-phenyl-1,2,4,5-tetrazine (tet3) was chosen for this study as a functional group which is often used for tetrazine-dye conjugates by commercial sources. HEK293T cells were transfected with the standard mutant K97B, labelled at the maximum tetrazine concentration (1.6 µM) and incubation time (30 min) on ice. These conditions represent the limit reached with our experimental setup for *in vivo* labelling (Chapter 8.5).

The combination of labelling on ice and negatively charged tetrazine-dye constructs reduced the membrane uptake drastically and led to a negligible amount of internalized dye for all tetrazine groups (Figure 8.4.1B, white arrows). Brightness reference curves for the receptor bound EGFP and the different tetrazine-Cy5 fluorophores (100 nM), incubated with BCNK (0.5 µM) in PBS pH 7.4 or air buffer, were generated by in solution

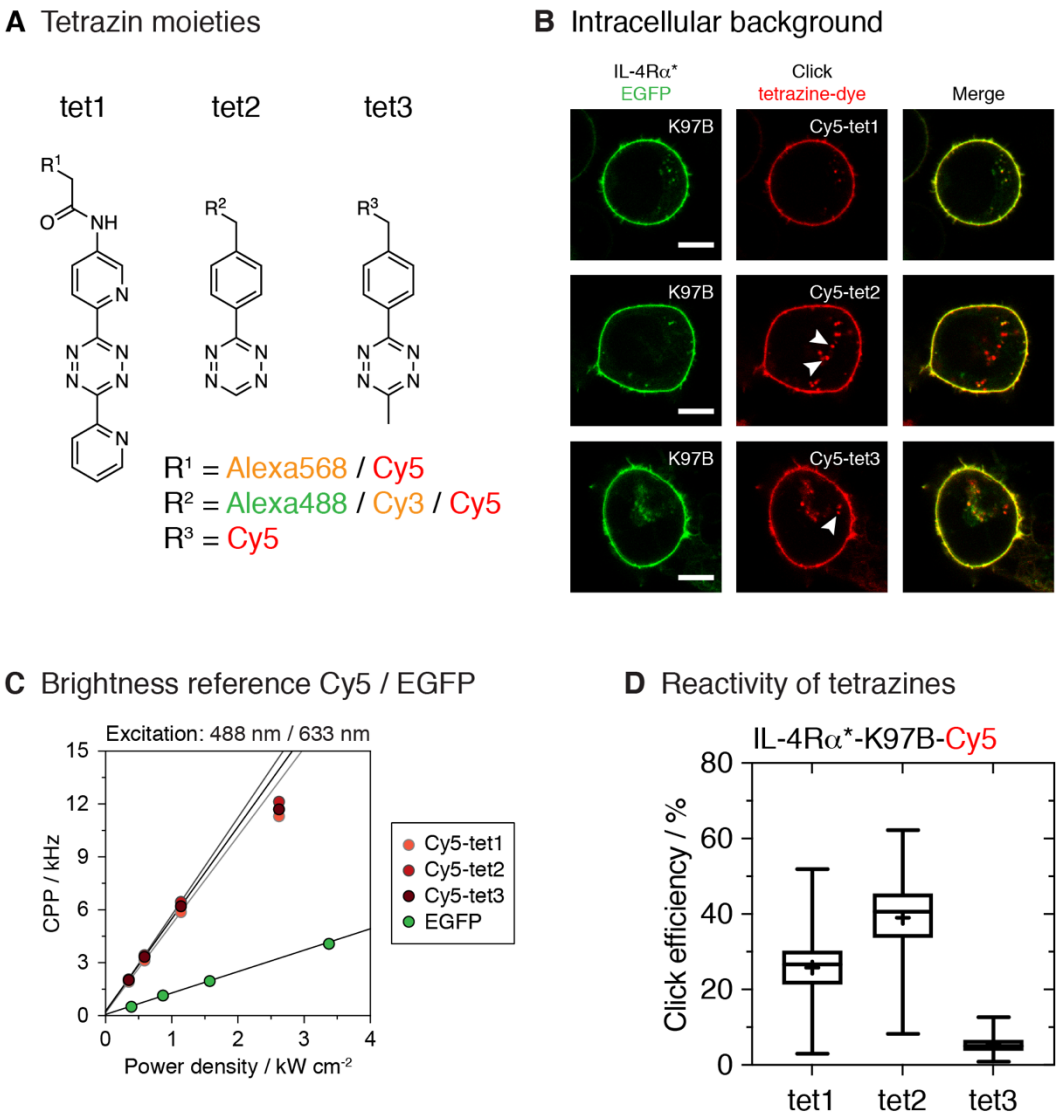

Figure 8.4.1: Click labelling efficiency of different tetrazine-groups. A) Schematic representation of the different tetrazine-dye constructs used in this study. B) HEK293T cells expressing the standard receptor IL-4Rα*-K97B (green) were incubated with different tetrazine-Cy5 constructs (1.6 µM, red) for 30 min on ice and imaged by confocal microscopy. Only a small intracellular background signal of unbound dye was detected for all tetrazine-dye constructs (white arrows). C) Brightness reference plot of the fluorophores EGFP and the different tetrazine-Cy5 constructs (courtesy of Frederik Steiert). D) Labelling efficiency of the reaction between the different tetrazine-groups and the BCNK modified receptor K97B in HEK293T cells. Cy5-tet2 showed the highest efficiency, followed by Cy5-tet1 and Cy5-tet3. Scale bar: 6 µm.

FCS measurements. The data fit in the EGFP channel showed a linear progression for the whole laser range. The tetrazine-Cy5 constructs showed a linear dependence as well. However, due to saturation of the excited state, the curve displayed a depression

at higher laser powers (Figure 8.4.1C). Image analysis by CRMI (R/G = Cy5/EGFP) revealed that the click labelling efficiency for cell membrane receptors is far from saturation (Figure 8.4.1D). The different tetrazines showed the following labelling efficiencies: Cy5-tet2 worked best with about 39 ± 10%, followed by Cy5-tet1 with about 26 ± 7% and only about 5 ± 2% for the Cy5-tet3 construct.

To verify the results of the CRMI analysis, we measured the ligand binding efficiency of the BCNK modified receptors and the click efficiency with Cy5-tet2 by single cell FCCS (Figure 8.4.2A). HEK293T cells expressing the different receptor constructs were labelled under equilibrium conditions with 20 nM IL-4-A647N in the supernatant. The focal volume of the FCCS measurement was positioned in the bottom membrane of the adherent cells leading to more stable intensity traces(Figure 8.4.2A, white cross).[29] In order to compare the cross-correlation amplitude of the BCNK modified receptors with defined biological systems, native IL-4Rα* (PC; wt IL-4Rα*) and 2xLyn-EGFP with IL-4Rα* without EGFP (NC) were expressed and labelled with IL-4-A647N. To measure reasonable fluorescence intensities with FCCS, the expression levels were kept low with the *Simian Virus 40* (SV40) promoter. Only when the two fluorophores, EGFP of the receptor and A647N of the ligand, moved together through the confocal volume, an increase in the cross-correlation amplitude was detectable (Figure 8.4.2B, blue arrow).

The PC showed a cross-correlation of nearly 50%, marking the highest possible cross-correlation in our setup, whereas co-diffusion of the NC was not detectable (Figure 8.4.2C). The IL-4-A647N occupied mutant K97B showed a comparable cross-correlation amplitude similar to the PC, while the cross-correlation of the mutant Y13B, located in the ligand receptor interface, was in the range of the NC and represented the inhibitory effect of the bulky BCNK. Next, the click efficiency of the mutant K97B was analysed by FCCS. For this reason, HEK293T cells were transiently transfected either with IL-4Rα*-K97B or with K97B lacking EGFP and 2xLyn-EGFP (NC-Cy5) and were labelled with Cy5-tet2 (1.6 µM) for 30 min on ice. The cross-correlation amplitude of the clicked cells were compared to the mean value of the ligand experiment, although subtle spectral differences between the ATTO647N and Cy5 fluorophores were present. The click labelling efficiency of about 38% relative to the positive control was perfectly in line with the results of the CRMI (39 ± 10%) analysis. In addition, dual-colour FCCS confirmed

A IL-4Rα* labelled with ligand or click

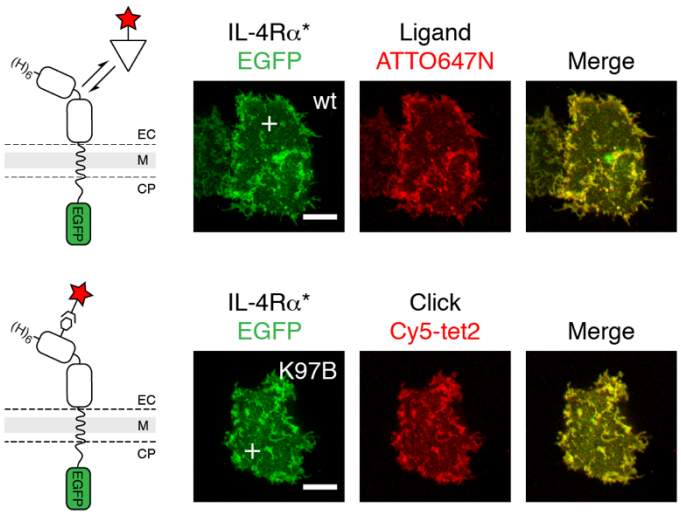

B FCCS auto- and cross-correlation curves

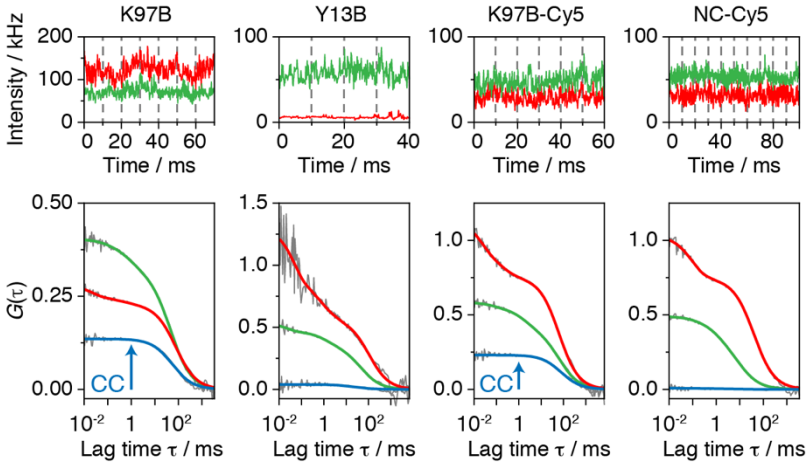

C Receptor co-diffusion with fluorescent-tag

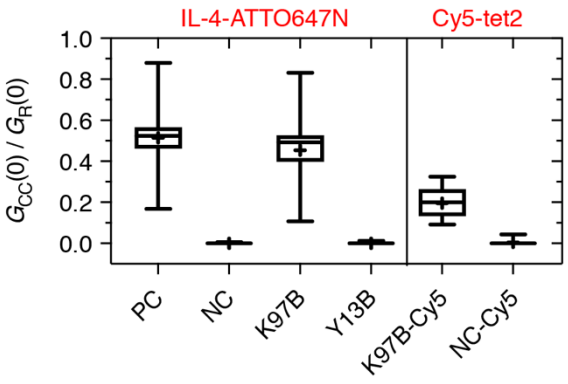

Figure 8.4.2: FCCS of BCNK modified receptors labelled with different dye-tags. A) Example HEK293T cells, expressing the BCNK modified IL-4Rα* (green), were labelled either with IL-4-A647N (red, upper row) or Cy5-tet2 (red, lower row), and single point FCCS (white cross) was measured at the bottom membrane. B) Auto- and cross-correlation curves of K97B and Y13B cells labelled with IL-4-A647N. Diffusion of fluorophores through the confocal volume led to increased cross-correlation curve (blue arrow). C) Cross-correlation ratio reflecting the number of dual-coloured particles with respect to EGFP. PC, wt IL-4Rα*; NC, plasma membrane localized 2xLyn-tagged EGFP co-expressed with IL-4Rα* lacking EGFP; Y13B, IL-4Rα* mutant with BCNK at the neutralizing position #13; K97B-Cy5, IL-4Rα* mutant clicked at the non-neutralizing position #97; NC-Cy5, IL-4Rα*-K97B lacking EGFP incubated with Cy5-tet2 and 2xLyn-EGFP. Analysed by Frederik Steiert. Scale bar: 6 µm.

that the receptor and the fluorophore are covalently bound to each other and move jointly through the plasma membrane driven by lateral diffusion (Figure 8.4.2B, blue arrow). The NC-Cy5 cells, with the two control constructs, showed no cross-correlation (Figure 8.4.2C). These results confirm that the CRMI method is a highly effective and accurate method to analyse different biological problems quantitatively.

To gain more flexibility in our experimental setup, we shifted the click reaction channel to the 561 nm laser line and used the 633 nm laser line for IL-4-A647N binding. Negatively charged Alexa568 in combination with the bulky tet1-group (A568-tet1) were chosen as a tetrazine-dye construct for extracellular receptor labelling with reduced dye internalization. First, linear brightness reference plots with EGFP and A568-tet1 were generated by FCS measurements of EGFP or A568-tet1 (100 nM) with excess amounts of BCNK (0.5 µM) in solution (Figure 8.4.3A, courtesy of Frederik Steiert). Then, the detection of membrane associated fluorescence by covalent IL-4Rα* labelling and the associated background for the shorter wavelength tetrazine-dye construct was addressed (Figure 8.4.3B). Potentially, there are two major contributors for high background signals: First, autofluorescence of cellular components, which increases with shorter excitation wavelength, and, second, membrane bound BCNK that is not conjugated to IL-4Rα*. HEK293T cells were transfected either with K97B or with the wt IL-4Rα* in combination with the GCE machinery and BCNK (NC), addressing the natural occurring TAG stop codons of other cell proteins. To improve the labelling conditions for living cells, the incubation time on ice was reduced to 5 min leading to a slightly lower click efficiency of about 19.4 ± 3.4% compared to Cy5-tet1. In addition, to get a better understanding of the actual particle numbers at the cell membrane, the labelling efficiencies (ratio of particle number per pixel) were rescaled to a two-dimensional

receptor density (particles per µm²), which increased the spread of the signal due to the broadly distributed expression levels. The possibility of rescaling implies two assumptions, a perpendicular scan path through the plasma membrane and an elliptical cross-section ($A_{eff} = \pi w_0 z_0$).

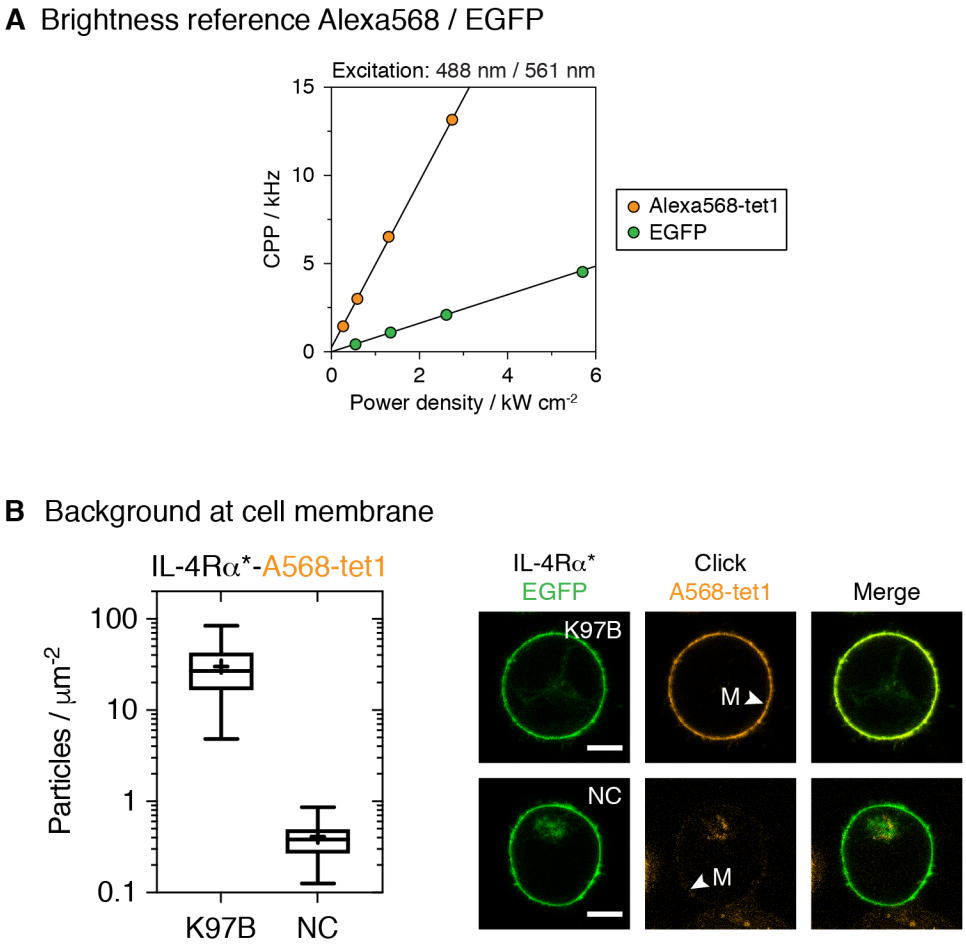

Figure 8.4.3: Background signal of A568-tet1 at the plasma membrane. A) Linear brightness reference plot of EGFP and A568-tet1 measured by in solution FCS (courtesy of Frederik Steiert). B) HEK293T cells expressing either IL-4Rα*-K97B or the wt receptor combined with the GCE machinery were labelled with A568-tet1 (1.6 µM) for 5 min on ice and were imaged by confocal microscopy. Cells without BCNK incorporated showed a 20 - 30-fold reduction in membrane labelling, by comparing the number of A568-tet1 labelled receptors per µm². M, membrane. Scale bar: 6 µm.

Both the size (z_0) of the focal spot and the radius (w_0) were determined by single colour FCS calibration measurements of defined fluorescent molecules (ATTO488 and

Alexa568). The cells showed an average signal of about 30 ± 17 particles μm^{-2} for the A568-tet1 labelled cell membrane whereas the NC showed less than one particle μm^{-2}, confirming the result that background signals are indeed very small. Moreover, the possibility to precisely analyse such small concentrations represents a huge advantage of the CRMI method and, in addition, makes it possible to compare small data variations.

Furthermore, we compared the click labelling efficiency of A568-tet1 or the ligand binding efficiency of IL-4-A647N, with wt, BCNK modified or clicked IL-4Rα*, to the receptor population at the membrane of living cells. For this purpose, a linear brightness reference plot with EGFP and IL-4-A647N was generated by in solution FCS (Figure 8.4.4A). Then transfected HEK293T cells with the wt IL-4Rα* or the standard mutant K97B were labelled with A568-tet1, IL-4-A647N or were first clicked and then incubated with IL-4-A647N, whereas wt IL-4Rα* was only labelled with IL-4-A647N. The receptor expression levels with the wt construct or GCE showed two populations: One small population was centred at about 15 receptors μm^{-2} for the wt IL-4Rα* and about 30 receptors μm^{-2} for K97B. Another more broadly and evenly spread population was located between roughly 30 - 300 receptors μm^{-2} for the wt receptor and 50 - 500 receptors μm^{-2} for the mutant K97B (Figure 8.4.4B/C/D). As the same gap was observed for the expression of the wt receptor with the SV40 and K97B with the CMV promoter, this seems to be a common feature of the HEK293T cell line and the transient transfection with viral promotors (Figure 8.4.4E).

Theoretically, a microscopy setup with at least three APDs and appropriate filter sets is required to test for the click labelling efficiency and the ligand occupancy of IL-4Rα*-K97B at the same time in a three-colour experiment. A crosstalk of about 8.3% into the 561 nm channel with A568-tet1 had to be accounted for, when applying IL-4-A647N in the same well. The click labelling efficiency, representing the reaction between the IL-4Rα*-K97B and A568-tet1, showed a homogenous distribution (x-axis) over the entire range of expression levels (Figure 8.4.4B). The spread on the y-axis (click-labelling efficiency) was additionally governed by image related uncertainties. These data showed that the labelling efficiency of the established method for cell surface

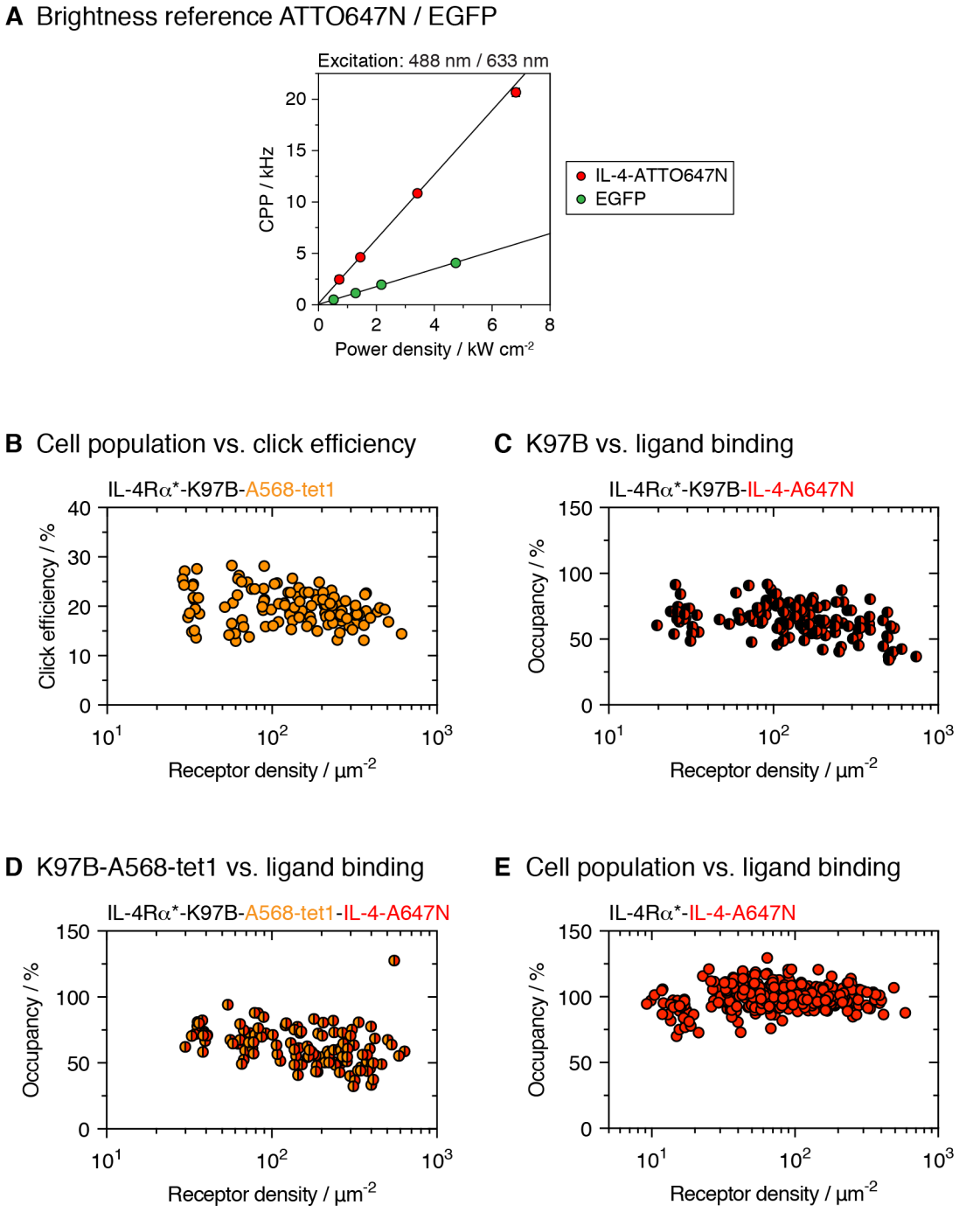

Figure 8.4.4: Click labelling and ligand binding efficiency of the IL-4Rα* population. A) FCS based linear brightness reference plot of EGFP and IL-4-A647N measured in solution (courtesy of Frederik Steiert). B) CRMI analysis of HEK293T cells expressing IL-4Rα*-K97B labelled with Alexa568-tet1, C) IL-4-A647N and D) both. E) As a reference, cells were transfected with the wt IL-4Rα* which was incubated with IL-4-ATTO647N. A gap separating two ranges of expression levels was detected for both viral promoter systems. The efficiency of the click and ligand labelling was consistent over the whole cell populations.

click labelling was independent of the receptor density. Furthermore, the receptor occupancy for ligand binding stayed the same before or after the click reaction (Figure 8.4.4C/D). Nevertheless, the receptor binding efficiency of IL-4-A647N displayed an overall reduction in the K97B mutant compared to the wt IL-4Rα* (Figure 8.4.4E).

These results lead to the conclusion that ligand binding is independent of the type of exposed functional group, BCNK or BCNK-Alexa568, since it shows identical cellular distributions. Unexpectedly, the click labelling efficiencies of all three tested tetrazine-dye constructs stayed far below 100%. This is not related to low signal quality since we determined a neglectable background signal at the cell membrane of less than a single receptor per μm^2. The degree of labelling measured by CRMI were in quantitative agreement with our FCCS analysis in live cells. In addition to imaging, FCCS showed co-diffusion of the IL-4Rα*-K97B with the ligand IL-4-A647N or the click label A568-tet1 on a molecular level.

8.5 Parameters for the click labelling of IL-4Rα

The previous experiments with BCNK modified IL-4Rα* and different tetrazine-groups showed that the click reaction is far from saturation. To obtain saturation, the parameter space for click labelling was investigated in detail for appropriate standard reaction conditions. For this purpose, three important parameters for the reaction kinetics, the concentration of the tetrazine-dye construct, the labelling time and the temperature were varied.

Cells expressing the mutant K97B were labelled with various concentrations of A568-tet1 for 5 min on ice. The optimal concentration of 1.6 µM was consistent with what has been reported in literature.[189, 190] The click labelling efficiency showed a concentration dependent but non-linear slope similar to a Michaelis-Menten saturation curve (Figure 8.5.1A). As the incubation time was kept constant, the click efficiency was proportional to the reaction rate. In addition, the negligible background of CRMI led to a suitable fit function that intersected the origin. For the experimental setup, with a low number of

receptors (picomolar range) at the surface of the cells and a large access of tetrazine-dye in homogenous solution, a pseudo-first order reaction mechanism with a linear slope was expected. However, the non-linear data had to be fitted with a saturation function ($(A_{max} \times c)/(1 + c/c_{sat})$; plateau 25.4%, c_{sat} = 1.3 µM) which is often used to describe a two-state transition, such as in fluorescence. One possible explanation for this discrepancy may be a spatial competition at the cell surface by the conjugated dye, which inhibits the diffusive approach of free tetrazine-dye construct to neighbouring BCNK receptors. This could either be caused by exclude volume effects or electrostatic repulsion of the double negatively charged A568-tet1. Furthermore, as for the IEDDAC reaction a suprafacial/suprafacial positioning is necessary, the reaction of a protein surface bound BCNK at the membrane surface of cells represents a highly anisotropic environment. In this area the molecular collisions seemed to be governed by a superposition of three- and two-dimensional search modes. However, in our experiments, A568-tet1 concentrations beyond 1.6 µM led to an increase in background signal from internalized fluorescent dye, rendering this concentration regime impractical.

In the following step, a kinetic study of the click labelling reaction, with the highest and lowest A568-tet1 concentration, with K97B and different incubation times, was made (Figure 8.5.1B). Both curves showed two components in the fit, a steep slope at the beginning and a rather flat progression later on. The lower concentration (0.2 µM) decreased the reaction rate drastically, which demonstrated the diffusion-controlled behaviour of the IEDDAC reaction at the surface of living cells. The data were fitted with a combination of two first-order exponential curves. Both concentrations showed an identical first time constant of about 1.2×10^{-2} s^{-1} representing a possible reaction of BCNK and A568-tet1 in a thin shell around the cell surface. The second-rate constants, about 1.7×10^{-4} s^{-1} for 0.2 µM and 9.0×10^{-4} s^{-1} for 1.6 µM, may be governed by the effects of the concentration dependent slow exchange between the shell and bulk solution as well as self-inhibition by stepwise accumulation of tetrazine-dye conjugate on the cell surface. None of the curves reached a plateau. This result confirmed again that the labelling efficiency is far from saturation.

Since it is common to use relatively high concentrations of tetrazine-dye constructs, problems with fluid phase uptake were assumed and standard labelling was therefore

performed with pre-chilled cells on ice. The effects on the labelling efficiency and the receptor trafficking at the membrane of living cells at different temperatures, during labelling, were addressed systematically. HEK293T cells were transfected with the IL-4Rα*-K97B mutant and were labelled with A568-tet1 (1.6 µM) for five respectively 30 min on ice, 21°C or 37°C. Only a small increase in the labelling efficiency was detected for the different temperatures as well as for the prolonged incubation times (Figure 8.5.2C). These findings were in good agreement with the previously shown kinetic data, in which 60 - 70% of the receptor population was already labelled within the first two minutes and saturation was almost reached after five minutes. Moreover, receptor populations, as for example nascent receptors or receptors in endosomal structures, were still able to capture a tetrazine-dye during the incubation time. According to the van't Hoff approximation, a temperature increase of 33°C results in an approximately eight- to ten-fold acceleration of the initial reaction rate. But this increased reaction rate was not translated into click labelling efficiency. As the second flat slope of the reaction kinetic represented a highly diffusion-controlled labelling, the temperature-dependence of the reaction was very weak. In conclusion, higher temperatures or longer incubation times do not further increase the yield of the labelling reaction. Assuming that there is a turnover of the plasma membrane, the results suggest that internalization rates for labelled and unlabelled receptors are the same.

The efficiency of the click labelling reaction at the membrane of living cells as well as the analysis with CRMI were highly reproducible. Labelling reactions under standard reaction conditions with the IL-4Rα* mutant K97B, 1.6 µM A568-tet1 and an incubation time of 5 min on ice, over the time period of more than one year, showed a minimal variation (Figure 8.5.1D). The horizontal dashed line represents the mean labelling efficiency of 18.9 ± 3.6% over all experiments, whereas the grey bar represents the distribution of one standard deviation of the mean value. To measure the labelling efficiency, either 20 - 40 handpicked single cells with a field of view (FOV) of 52 µm^2 (Figure 8.5.1D, left side) or a diverse cell ensemble within a FOV of 212 µm^2 (Figure 8.5.1D, right side) were measured. Both imaging strategies led to the same mean values, as, with CRMI, large expression level variations were cancelled out and user bias was

negligible. The larger spread of the mean values for the bigger FOV method was caused by the lower magnification which limited the pixel statistics.

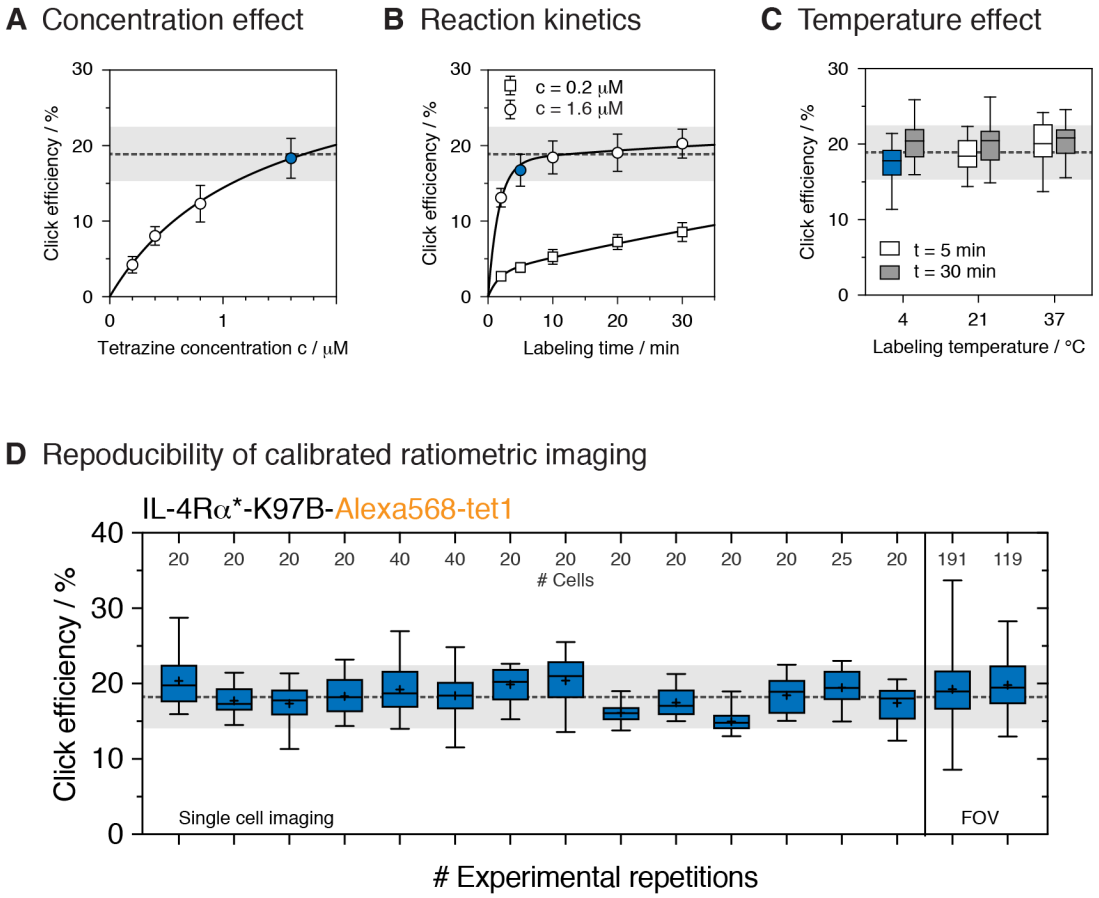

Figure 8.5.1: Reaction conditions and reproducibility of IL-4Rα* click labelling. A) Concentration dependent non-linear increase in click labelling efficiency of K97B and Alexa568-tet1. The data were fitted with a saturation curve of type $(A_{max} \times c)/(1 + c/c_{sat})$ resulting in a plateau of 25.4% and saturation concentration of 1.3 µM. B) Influence of the concentration of Alexa568-tet1 (0.2 µM vs. 1.6 µM) on the reaction rate of the IEDDAC on the surface of living HEK293T cells. Both concentrations represent a biphasic behaviour with a fast time constant of about 1.2×10^{-2} s^{-1} for both at the beginning and a time constant of about 1.7×10^{-4} s^{-1} for 0.2 µM and about 9.0×10^{-4} s^{-1} for 1.6 µM for the second slope. C) Temperature and incubation time effects on the labelling efficiency of BCNK modified IL-4Rα* with Alexa568-tet1 were measured. Only a small increase in labelling efficiency was detected for the 5 min incubation times, representing the diffusion-controlled mechanism of the click reaction at the surface of living cells. D) IL-4Rα* mutant K97B click labelling in HEK293T cells withA568-tet1 under standard reaction conditions, over the time period of more than one year, showed an extraordinary precision in the labelling efficiency analysed by CRMI. Standard click labelling conditions highlighted in blue.

Another factor which can influence the labelling efficiency drastically is the chemical stability of the reaction components involved. First, the long-term stability of the tetrazine-dye construct in air buffer, the standard buffer for labelling, was confirmed. Aliquots of 1.6 µM A568-tet1 were stored at 4°C for up to 24 h and cells expressing K97B were labelled for 5 min on ice. The data obtained did not only show that the tetrazine-group is stable in air buffer, they also confirmed the high reproducibility of the click reaction as described before (Figure 8.5.2A).

Next, the effects of buffer composition on the labelling efficiency were analysed. IL-4Rα* K97B expressing HEK293T cells were labelled under standard reaction conditions with A568-tet1 dissolved in three different buffers. PBS, a buffer which contains only salts, was compared to air buffer, which contains salts, sugars and the protein bovine serum albumin (BSA). Air buffer was developed for live cell imaging and ensures that cells stay in good condition for several hours, whereas PBS leads to apoptosis within several minutes to an hour. To include a protein free labelling environment, air buffer was also tested without BSA. Moreover, the labelling reaction was performed in growth media containing natural AA and the undefined protein mix fetal bovine serum (FBS). All four buffers showed the same labelling efficiency and are suitable for the reaction between BCNK and A568-tet1 (Figure 8.5.2B). Since growth media led to background fluorescence by its ingredients, air buffer containing BSA turned out to be the best buffer for HEK293T cells and was used for further experiments.

Not only the stability of the tetrazine-group is crucial for the reaction efficiency but also the stability of the BCNK group is important. It is well known that the strained triple bond of the BCNK can undergo an addition reaction with various thiol groups (in different oxidative states).[191-195] BCNK may lose its activity after incorporation and transport along the secretory pathway or by thiol containing proteins and cysteine, which are present in the growth medium of HEK293T cells. All these impacts on the labelling efficiency were measured. For this reason, HEK293T cells transfected with the K97B plasmid were incubated twice for 1 h at 37°C with either DMEM or DMEM supplemented with 10% FBS. The labelling was carried out at two different concentrations, the standard concentration of 1.6 µM (Figure 8.5.2C, left) and a low concentration of 0.2 µM (Figure 8.5.2C, right). With both concentrations a reduced labelling efficiency could be detected

for the two different growth media. In DMEM, only cysteine contained a free thiol group, whereas in DMEM supplemented with FBS an unknown protein assemble with free thiol groups was present. FBS also contains BSA which possibly can react with its free thiol

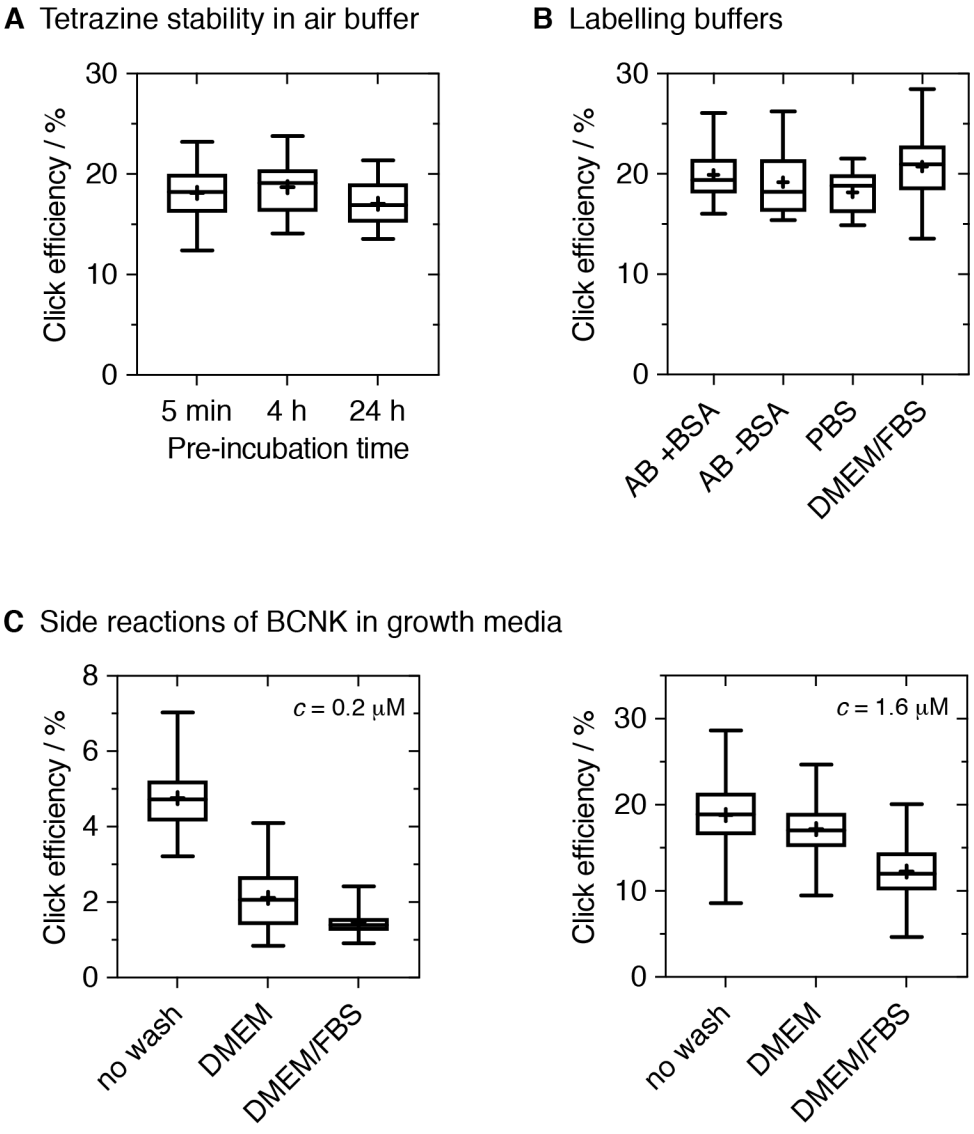

Figure 8.5.2: Side reactions of BCNK and Aleaxa568-tet1 labelling. A) The stability test of Alexa568-tet1 in air buffer at 4°C, over a time period of 24 h, showed a high persistence of the tet1-group in aqueous solution. B) Standard labelling reactions with Alexa568-tet1 for 5 min on ice in different solvents had no influence on the reaction efficiency in K97B expressing HEK293T cells. C) The negative effect of free thiol groups on the BCNK reactive group was analysed by expression of IL-4Rα*-K97B at the membrane of HEK293T cells, combined with two additional washing steps with growth media ± FBS and standard labelling with A568-tet1 at two different concentrations (0.2 μM, left side and 1.6 μM, right side). Both experiments showed a clear reduction of the click labelling efficiency at cells with medium exchange.

group and BCNK. The previous buffer data (Figure 8.5.2B) showed that the labelling efficiency was not affected by the amount of BSA in air buffer, but the labelling reaction was carried out on ice for only 5 min. This amount of time and temperature seemed too little to show a clear effect on the labelling reaction. When cells were incubated over a longer period of time at 37°C, certain side reactions took place. The effects on the labelling reaction were different for both concentrations. In the case of higher tetrazine-dye concentration, the effect of a side reaction with an unknown substance and BCNK reduced the reactivity of surface expressed receptors. However, in the case with lower concentration, two effects were involved for the reduced labelling efficiency. First, the side reaction of BCNK with an unknown substance and, second, the slow diffusion of free BCNK out of the cytoplasm reservoir of the cell. This leads to the assumption that free BCNK diffuses in the same regions as the receptor and catches tetrazine-dye constructs before the receptor can be labelled, which was confirmed by an additional reduction of the labelling efficiency of the IL-4Rα extracellular domain.

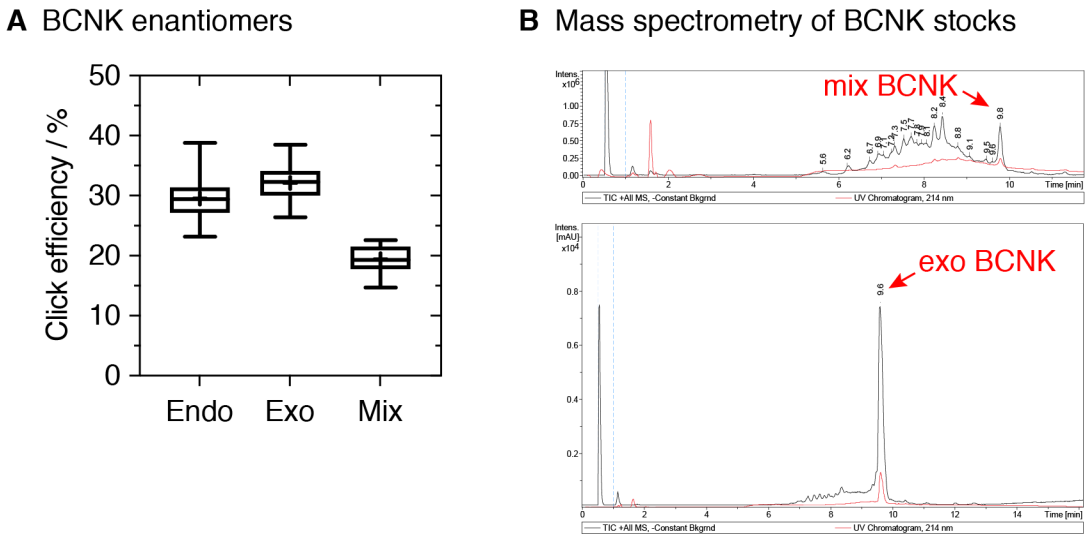

Figure 8.5.3: Click labelling efficiency of endo, exo and mix BCNK. A) HEK293T cells expressing the IL-4Rα*-K97B mutant incubated with different types of BCNK (endo, exo or a mix of both) and labelled with Alexa568-tet1 under standard reaction conditions. The enantiomer pure BCNK cells showed a slightly higher click efficiency than the mixed BCNK sample. B) Mass spectrometry data of endo/exo BCNK (mix) and exo BCNK revealed the purity of the used samples.

In a next step, a comparison for the labelling efficiency was made between commercially available BCNK enantiomers and the BCNK mixture provided by our collaboration partner Prof. Dr. Kathrin Lang (Technical University of Munich). HEK293T cells transfected with the K97B plasmid were incubated for 18 h in growth medium supplemented with endo, exo or mix BCNK to a final concentration of 0.5 mM. Then the cells were labelled under standard reaction conditions with A568-tet1. The mixture of endo/exo BCNK showed the same labelling efficiency as described above, whereas the enantiomers endo or exo BCNK showed an increased labelling efficiency (Figure 8.5.3A). The enantiomers endo and exo BCNK also displayed various labelling efficiencies. IL-4Rα* expressed with exo BCNK exhibited not only a higher cell surface expression but also a higher labelling efficiency. One factor for the increased labelling efficiency of the BCNK enantiomers could be their degree of purity. Mass spectrometry (MS) data of mix BCNK revealed higher amounts of impurities in the sample compared to endo/exo BCNK which led to the decreased click labelling efficiency (Figure 8.5.3B). The purer BCNK samples did not show a 100% click efficiency and confirm the proposed mechanism of a side reaction after the BCNK is incorporated into the receptor IL-4Rα*.

In addition to the influence of the reactive groups involved in the click reaction, both the effect of the labelling-site positions in the receptor and the effect of the ligand binding on the labelling reaction of different receptor mutants were addressed (Figure 8.5.4A; red, high click efficiency; blue, low click efficiency). For this purpose, transfected cells were harvested, incubated with IL-4 and labelled with A568-tet1 under standard reaction conditions (Figure 8.5.4B). The CRMI results of the IL-4 bound receptors were compared to the non-occupied ones. The 14 positions of the IL-4Rα* ECD showed a click labelling efficiency ranging between about 5% (blue) and 20% (red) for the non-occupied receptors. The D1-domain revealed a higher average value for the click labelling efficiency, with the only exception of Y13B in the ligand binding pocket, than the membrane proximal D2-domain. The close proximity to the cell membrane may lead to a general reduction of the site accessibility of BCNK. Similar results for the two domains and the linker region were measured with the occupied IL-4Rα*, which displayed a small structural rearrangement in the quaternary structure (Chapter 9.2). Moreover, the

A Site-specific click labelling

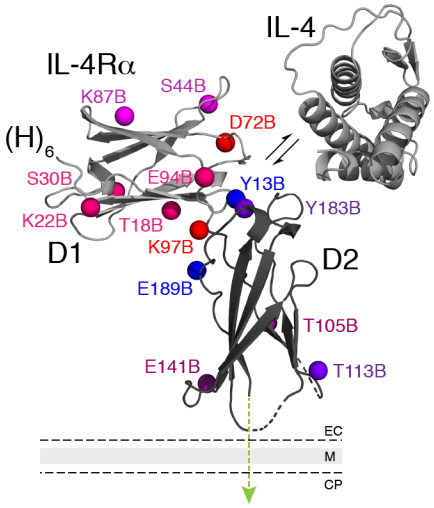

B Ligand induced click efficiency shift

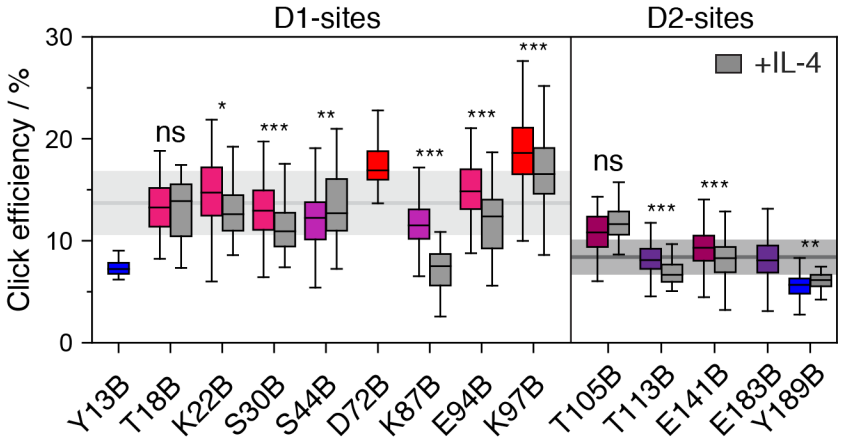

C Receptor expression vs. click efficiency

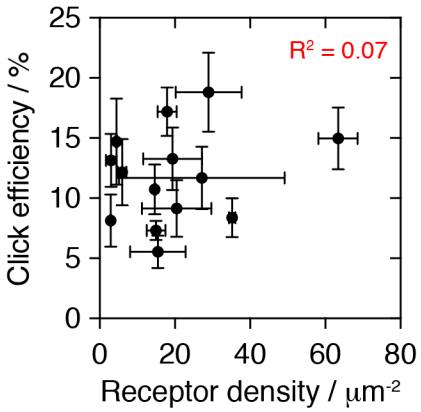

Figure 8.5.4: Site-specific IL-4Rα* click labelling. A) Crystal structure of the IL-4 occupied IL-4Rα* (PDB: 1IAR) representing the click labelling efficiency (red, high efficiency; blue, low efficiency) of the different mutants.[37] B) HEK293T cells expressing the different IL-4Rα* mutants were labelled with A568-tet1 under standard reaction conditions either with or without the simultaneous incubation with ligand IL-4. The membrane distal D1-domain, except Y13B, showed an increased click efficiency of the non-occupied receptor compared to the membrane proximal D2-domain (grey line/area, average click efficiency ± one average standard deviation). The occupation of the receptor led to slight variances in the labelling efficiency for most of the mutants. ***$P < 0.001$ (Welch's t-test).C) Absent correlation between the mean click labelling efficiency and the average receptor expression.

average click labelling efficiency of the different mutants did not correlate with the mean expression levels of the receptor (Figure 8.5.4C).

In summary, with CRMI we established an excellent tool to analyse confocal cell images for biological relevant processes such as the receptor accessibility at the membrane, the ligand binding efficiency or even the quantification of the click labelling reaction at the cell membrane. The calibration with FCS was also used to quantify receptor expression levels and allowed the optimization of the GCE method for our system. All employed tetrazine-groups for the click labelling of BCNK modified receptors showed a rather low reaction efficiency. Although a quantitative covalent labelling of mutant K97B under standard reaction conditions has never been achieved, the conditions could be optimized to turn the labelling efficiency into a very reproducible readout. A higher tetrazine-dye concentration or labelling time slightly increased the labelling efficiency, confirming a diffusion controlled labelling process at the surface of living cells. The thiol side reactions of BCNK, which decreased the click labelling efficiency, took place either in the growth media or alongside the secretory pathway in cells. Nevertheless, it was possible to compare the different mutations of the IL-4Rα* for their site-specific labelling efficiency and the influence of the ligand on the reaction.

9 Ligand induced IL-4Rα activation mechanism

9.1 BCNK modified IL-4Rα functionality studies

As proper IL-4 binding to the receptor is crucial for JAK/STAT pathway activation, the IL-4Rα* modification with BCNK should not interfere with the binding. Previous results showed that the modification with BCNK or clicked with the tetrazine-dye construct leads to a reduction in ligand binding (Figure 8.4.4A). In order to gain detailed insights into GCE modified receptors, different mutants and the labelled ligand IL-4-A647 in combination with CRMI were further investigated (Figure 9.1.1A).

First, the influence of the supplemented uAA BCNK in the cellular medium on ligand binding efficiency was tested with the wt IL-4Rα* construct. After transfection, the cells

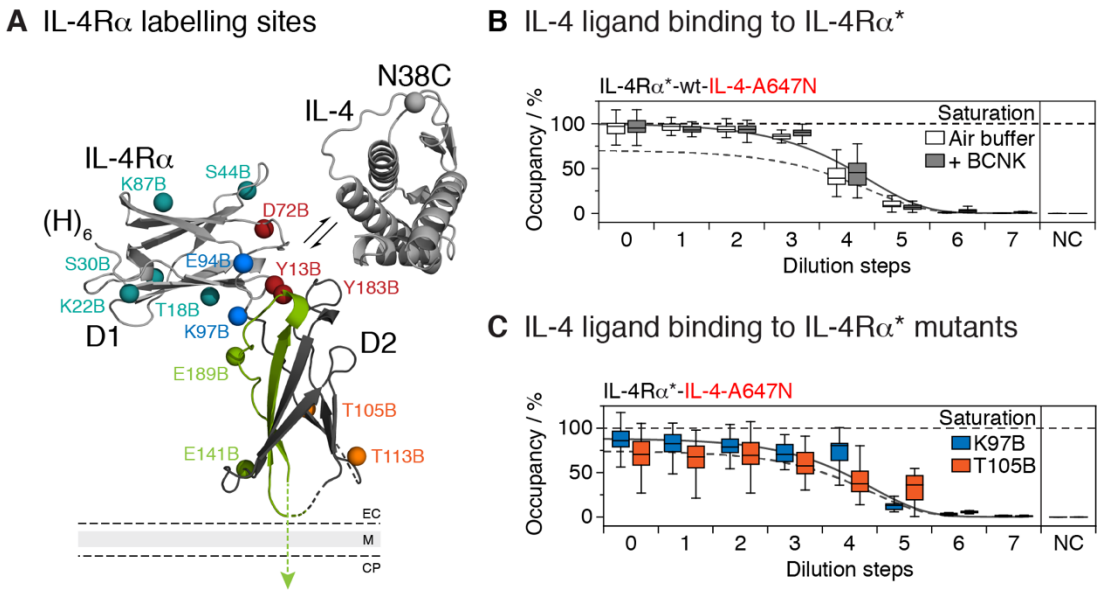

Figure 9.1.1: Titration of IL-4-A647N ligand to analyse BCNK modified IL-4Rα*. A) Crystal structure of the class I cytokine receptor IL-4Rα (PDB: 1IAR) bound to its ligand IL-4. Different BCNK mutation sites in the primary sequence are indicated by coloured spheres as well as the labelling position of the ligand.[37] B) HEK293T cells transfected with the wt IL-4Rα* were incubated with growth media ± BCNK and the labelled ligand IL-4-A647N was titrated. An inhibitory effect on ligand binding was not detected. C) Cells expressing the mutants K97B and T105B showed a clear reduction of the binding efficiency for the same ligand titration experiments.

were incubated with growth media ± BCNK, then with various concentrations of IL-4-A647 and imaged by confocal microscopy. Calibrated imaging, in which the intensity signal is calibrated by FCS and converted to particle numbers, combined with the ratio of ligand ATTO647N signal divided by receptor EGFP signal (R/G) provides directly the occupancy of the receptors at the cell surface. At saturation, both samples, either with or without BCNK, showed an identical saturation level of the titration curve (Figure 9.1.1B). These results confirmed that BCNK did not unspecifically bind at the membrane of living cells. Furthermore, a free cysteine at position C182, near the binding pocket, did not interact with BCNK and reduce ligand binding capacity of the GCE-expressed receptors. The quantitative labelling of the wt IL-4Rα* also confirmed that the CRMI approach was capable of analysing confocal images for the receptor ligand binding efficiency at the membrane of living cells. We also measured the same ligand dilutions with two IL-4Rα* mutants, the standard mutant K97B and the D2-domain mutant T105 (Figure 9.1.1C). Both showed the same slope of the ligand binding efficiency as the wt IL-4Rα*, but they never reached a saturation plateau of 100%. Mutant K97B ended up at 85% and T105B at 71%, which represented the inhibitory effect of the incorporated BCNK on the ligand binding of IL-4Rα*.

In the next step, the ligand binding efficiency of all IL-4Rα* mutants was measured, in order to investigate the effect of the site-specifically incorporated BCNK on the ligand binding. HEK293T cells expressing the different mutants were labelled with the saturating concentration of 10 nM and were imaged with ligand excess in the supernatant. The labelling efficiencies of the different BCNK modified receptors were compared to the positive control (PC; wt IL-4Rα*) and the negative control (NC; 2xLyn-EGFP). The CRMI results could be divided in five groups: The first group, located in the D1-domain (T18B, K22B, S30B, S44B and K87B; teal), showed a site-specific reduction in labelling which led to ligand binding efficiency of about 61 - 95% (Figure 9.1.2A). The second group consisted of mutants located in the D2-domain (T105B and T113B; orange) which showed a very precise binding efficiency of about 77 - 78%. Two mutations placed in the linker region, between the D1- and D2-domain, were labelled with an efficiency of 91% for E94B and 84% for K97B (blue). Mutations at the centre of cluster I and II of the binding epitope (Y13B, D72B and Y189B; red) showed a strong

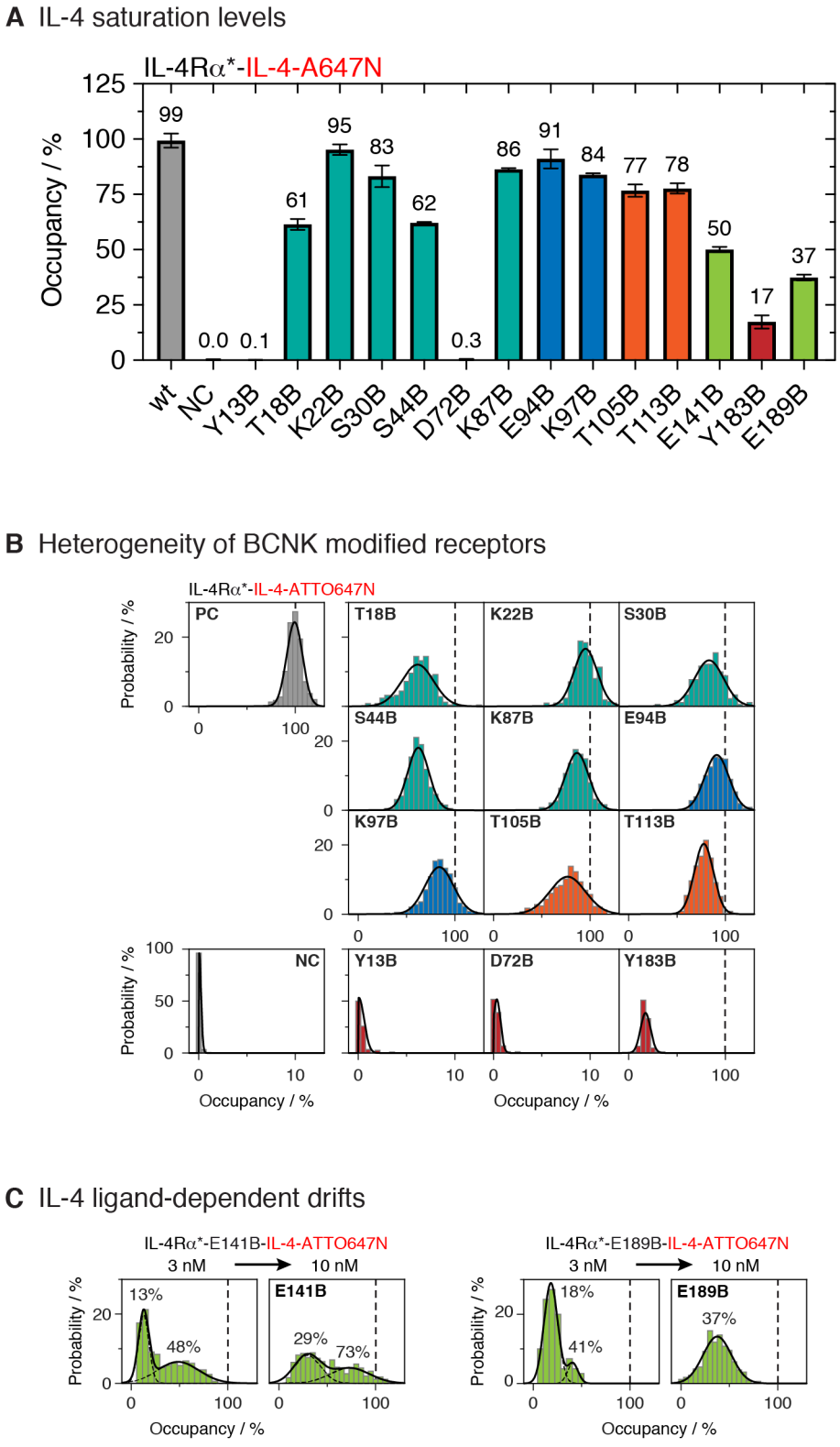

Figure 9.1.2: IL-4-A647N ligand binding histograms of IL-4Rα* mutants. A) Cells expressing the different IL-4Rα* mutants were incubated with IL-4-A647N (10 nM) and were analysed by CRMI. Mutants in the

D1-domain (teal) and D2-domain (orange) as well as in the linker region (blue) showed a slight reduction of the labelling efficiency. On the other hand, the mutants in the binding pocket (red) and in or near the activation loop (green) showed drastic inhibition on the ligand binding efficiency. B) The GCE-expression of all mutants exhibited a Gaussian-shaped normal distribution, C) except for the mutants E141B and E189B with a bimodal-shaped distribution, representing two distinct receptor populations. The bimodal distribution shape of E141B and E189B could be changed by the IL-4-A647N concentration.

inhibition.[37, 73, 180] These mutants were previously analysed via alanine screening in combination with surface plasmon resonance spectroscopy and showed a strongly reduced binding affinity for the ligand IL-4 by the following order Y13A > D72A > Y183A > E94A.[73] The mean values of the residual IL-4 binding efficiency were in exactly the same order and were slightly higher than the negative control (NC). The mutations E141B and E189B (WSEWS motif; green) of the fifth group were at or in close proximity to the activation loop and exhibited a strong effect of the BCNK modification on the ligand binding. The ligand binding efficiency of E141B with 50% and E189B with 37% was clearly reduced.

Furthermore, we were interested in the heterogeneity of the GCE-expressed receptor population at the plasma membrane of living cells. The quantification of proper ligand binding was an excellent tool to analyse the receptor populations in detail. For this purpose, the data of the previous experiment with the different mutants and the ligand IL-4-A647N were plotted as histograms (Figure 9.1.2B). All mutants showed a homogenous Gaussian-shaped normal distribution with small variations in their width, except the mutants E141B and E189B, which exhibited a bimodal-shaped distribution indicating two conformationally distinct populations of the BCNK modified IL-4Rα* (Figure 9.1.2C). The allosteric effects of both mutations led to an overall reduced ligand binding efficiency. These effects on the binding efficiency and the form of the distribution were controlled by the concentration of ligand. With a low non-saturating ligand concentration, a pronounced bimodal-shaped distribution was formed for both mutants.

The correlation of the ligand binding efficiency with the click labelling efficiency in the IL-4Rα* mutant K97B, measured simultaneously in a three-colour experiment, displayed a homogenous Gaussian-shaped normal distribution for the ligand binding as well as for the click reaction (Figure 9.1.3A). On the other hand, the mutant E141B showed a bimodal-shaped distribution for both efficiencies which led to the conclusion that the

labelling efficiency was affected by the confirmation and population of the receptor. A possible interaction partner for the BCNK modified IL-4Rα* mutant E141B is the lysin at position 195 (K195) on the activation loop, which is located directly in front of the TMD. Figure 9.1.3B shows the crystal structure (PDB:1IAR) of the D2-domain with a possible oriented BCNK structure incorporated at position E141B.[37] The carbonyl oxygen of the BCNK forms an hydrogen bond to the nitrogen atom of the lysine amine-group. This interaction may cause the effects of the bimodal distributions for ligand binding and the click labelling of the mutant E141B. The similarly behaving mutant E189B, located in the important activation loop within the WSXWS motif, also shows a hydrogen interaction to the lysine at position 97 (K97), confirming a possible interaction dependent ligand inhibition.

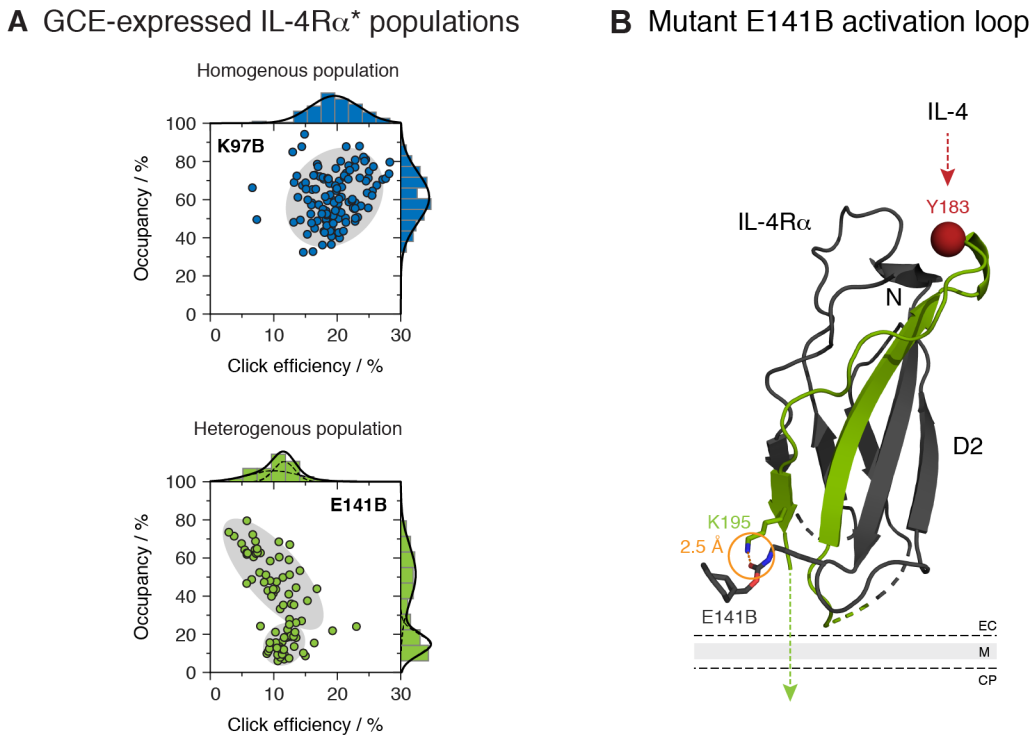

Figure 9.1.3: Click labelling efficiency *vs.* ligand binding efficiency. A) The click labelling efficiency and the ligand binding efficiency for the IL-4Rα* mutant K97B follows Gaussian-shaped normal distributions (grey area). However, for mutant E141B a bimodal distribution was not only measured for the ligand labelling but also for the click reaction (two grey areas). B) A modification of the IL-4Rα D2-domain (PDB: 1IAR) with a BCNK structure displays the possible H-bond interaction between the carbonyl oxygen of the BCNK and the amino-group of K195 located on the activation loop.[37]

Taken together, BCNK modified receptors show a slightly reduced ligand binding capacity whereas mutations in the binding pocket and allosteric positions, in or near the activation loop, have a pronounced inhibitory effect. Furthermore, the ligand binding efficiency data of the IL-4Rα* mutants K97B and Y13B are in good agreement with the FCCS data displayed above (Figure 8.4.2C). The ligand occupancy data as well as the click labelling efficiency also show that different populations of receptors, with various conformations, are located at the plasma membrane. These conformations display two distinct receptor distributions. A possible hydrogen bond interaction of the BCNK and K195 could explain the bimodal distribution of mutant E141B.

9.2 Ligand induced reorientation of the IL-4Rα domains

The remarkable reproducibility of the degree of labelling and the high sensitivity of the CRMI method raised the idea to use the covalent labelling as a readout in order to infer details about site accessibility and thus receptor conformations in their native environment, the plasma membrane of living cells. For this purpose, the data exhibited in Figure 8.5.4A were re-evaluated for their change in click efficiency (CCE). The CCE represents the difference of the click efficiencies measured for the IL-4 occupied and non-occupied receptor (Figure 9.2.1A). Almost all mutants showed a reduced click labelling efficiency in their occupied structure, except for the mutants T18B and T105B, which did not change significantly. This reduction in efficiency is probably caused by a higher stiffness of the receptor in the ligand-bound conformation, which impairs with the click reaction. Only the mutants S44B and E189B displayed a positive effect of the ligand binding for the click labelling efficiency. Both IL-4Rα* labelling-sites were located at special positions, S44B in the D1-domain loop 2 near the binding pocket and E189B in the WSXWS motif on the activation loop (Figure 9.2.1B).[37] Loop 2 (L2) is a very hydrophobic loop and shows a high flexibility in different IL-4Rα crystal structures (PDB: 1IAR, 3BPL and 3BPO).[37, 48] As the BCNK molecule contains a hydrophobic head group, an interaction with the flexible hydrophobic loop is conceivable (Figure 9.2.1C). This molecular interaction may lead to a kind of activation mechanism of the mutant S44B

when IL-4 gets bound, which is presented by the increased click labelling efficiency. Similar structural rearrangements were proposed for the activation loop in the D2-domain with the WSXWS mutant E189B. Ligand binding seems to lead to a rearrangement of the activation loop triggering the intracellular signalling cascade.[35, 182] Such small rearrangements are hard to detect, but CRMI in combination with site-specific click labelling points in the direction of the proposed activation mechanism.

To investigate further in a possible receptor rearrangement during ligand binding, an assay was designed on the basis of viscosity changes in the close surroundings of the IL-4Rα*. Cy3 and its specific change in fluorescence lifetime due to viscosity changes was previously described.[196] A rearrangement of the receptor domains into the direction of the cell membrane or to each other would reduce the degrees of freedom, which is equivalent to an increased viscosity and leads to a longer fluorescence lifetime of Cy3. All IL-4Rα* mutants, except the inhibitory labelling-sites in the ligand binding pocket, were expressed in HEK293T cells and labelled with Cy3-tet2. The cells were imaged by FLIM and the fluorescence lifetime signal at the membrane was analysed. Our data showed that the D1-domain only moved slightly after ligand binding, more specifically, the viscosity was decreased which led to a shorter fluorescence lifetime of the mutations K22B and K87B (Figure 9.2.1D). Mutations in or near the linker region, such as T18B and K97B, exhibited a more pronounced effect in the fluorescence lifetime after ligand binding. Especially the fluorescence lifetime of the mutant K97B was drastically increased, whereas another mutant's lifetime in the linker region, mutant E94B, was decreased. These results display a major reorientation of the two domains around the linker region governed by ligand binding. The D2-domain mutations T105B, T113B and E141B did not show any change in fluorescence lifetime, which supports the theory that the receptor stands perpendicularly at the membrane in the activated and deactivated state. However, the fluorescence lifetime of the D2-domain mutant E189B, located in the WSXWS motif, was drastically decreased after ligand binding. These results indicate that a rearrangement of the activation loop as well as in the D1- and D2-domain takes place during ligand binding (Figure 9.2.1E).

A Click efficiency shift

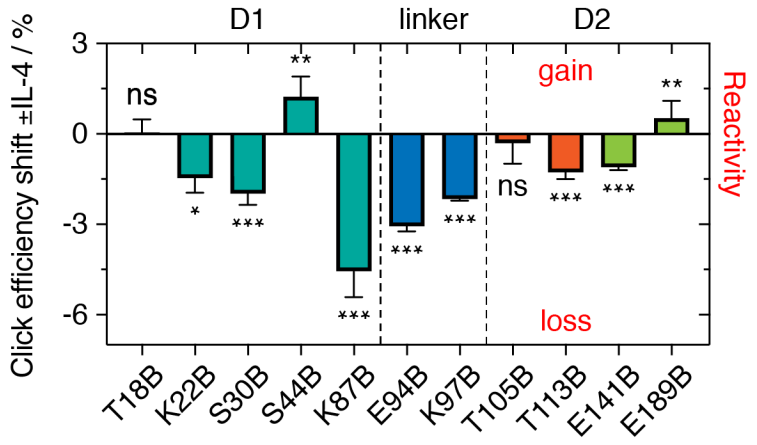

B Structural flexibility of IL-4Rα

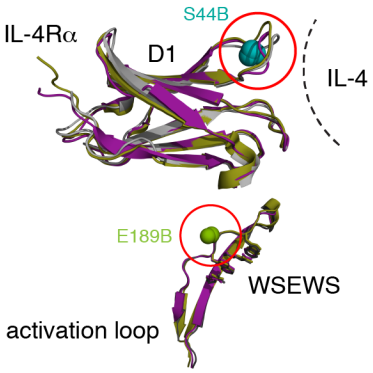

C Hydrophobic loop

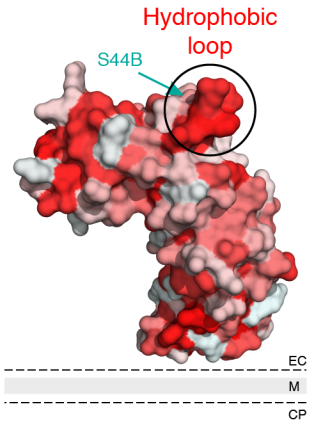

D Microviscosity analysis

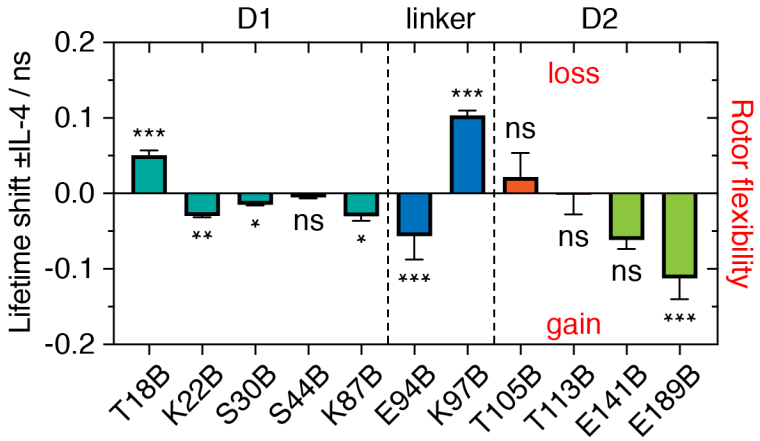

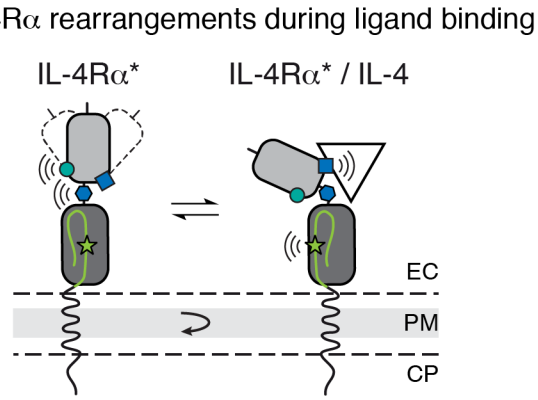

Figure 9.2.1: Ligand induced receptor movement. A) The change in click efficiency (CCE), represented by the difference in labelling efficiency between occupied and non-occupied receptors, was re-evaluated. All IL-4Rα* mutants, except for mutant S44B and E189B, showed a slight reduction or no reduction at all in the CCE. ***$P < 0.001$ (Welch's t-test). B) Crystal structure of the D1-domain and the activation loop (PDB: 1IAR, 3BPL and 3BPO) with the two mutations S44B and E189B (red circle).[37, 48] C) Hydrophobicity representation of the protein surface; red, hydrophobic residues; white, hydrophilic residues. D) Micro-viscosity measurements of Cy3-tet2 at the indicated locations in dependence of IL-4 (lifetime shift). Mutants in the linker region (T18B, E94B and K97B) and in the activation loop (E189B) showed particularly large changes suggesting a rearrangement of the D1- and D2-domains as well as the activation loops. ***$P < 0.001$ (Welch's t-test). E) Schematic model of the involved rearrangements during IL-4 ligand binding.

In conclusion, the site-specific labelling of IL-4Rα* revealed a reorientation of the receptor during ligand binding, which may lead to a tighter structure with an overall reduced click labelling efficiency. Only the mutants S44B and E189B showed a higher click efficiency, representing the flexibility of the domains (loop 2 and activation loop) involved. Furthermore, the fluorescence lifetime shifts displayed a rearrangement of the two FNIII domains (D1 and D2) around the linker region and a movement in the activation loop, which possibly triggers the JAK/STAT pathway activation.

9.3 IL-4Rα membrane lifetime revealed by covalent click labelling

An important question which could be addressed by a covalently labelled IL-4Rα is the lifetime of the receptor at the membrane of living cells. The surface lifetime is important for ligand binding, receptor dimerization and the subsequent activation of the JAK/STAT pathway. To determine this property, three different receptor constructs were compared, the truncated receptor IL-4Rα*, the truncated receptor without the C-terminal EGFP and

the full-length receptor IL-4Rα. HEK293T cells expressing the K97B mutant of each receptor version were labelled with Cy3-tet2 and incubated for different time periods in growth media (± IL 4) at 37°C. To stain the plasma membrane for segmentation, the cell surface proteome was labelled with Cy5-NHS, the cells were fixed with paraformaldehyde (PFA) and were imaged by confocal microscopy. The truncated IL-4Rα* used in this study showed almost negligible internalization during the entire 8 h that have been measured (Figure 9.3.1A). A faster internalization was measured for the IL-4Rα* lacking the intracellular C-terminal EGFP-tag. Both constructs were incubated with saturating concentrations of IL-4, which slightly reduced the internalization rates. However, the full-length receptor displayed an exponential-like decay for the membrane lifetime, with a rather similar half-life of about 41 min for the non-occupied receptor and about 38 min for the occupied receptor. Not only the decay of the lifetime was different for the three receptor constructs, but also the standard deviations of the values were higher for the truncated receptor constructs. These data suggest a natural mechanism for the full-length IL-4Rα degradation, whereas the degradation mechanism for the truncated receptor (± EGFP) was disturbed. In addition, the slow internalization rate of the truncated receptor IL-4Rα* led to a stable receptor population at the cell membrane, which made this construct particularly suitable for the quantification of the click experiments.

One possible explanation for the different internalization rates is the diffusion behaviour of the various receptor constructs at the cell membrane. Single transmembrane receptors such as IL-4Rα diffuse freely in the membrane of living cells. The intracellular tail of the receptor constructs consisted of either the disordered full-length tail with 569 AA or a truncated tail with only 35 AA and, in addition, for one construct an EGFP-tag. These diverse tails may drastically influence the diffusion of the receptors. An FCCS experiment was designed in order to analyse the diffusion coefficient of the receptor constructs. HEK293T cells were transfected with various receptor constructs and were labelled by click labelling (Alexa488-tet2 (A488-tet2) or Cy5-tet2), by ligand binding (IL-4-A647N) or both and were analysed by FCCS. The wt IL-4Rα* showed the similar diffusion coefficients of 0.16 ± 0.05 μm^2 s^{-1} and 0.14 ± 0.06 μm^2 s^{-1} for the occupied and non-occupied receptor and were consistent with previously reported

A IL-4Rα internalization

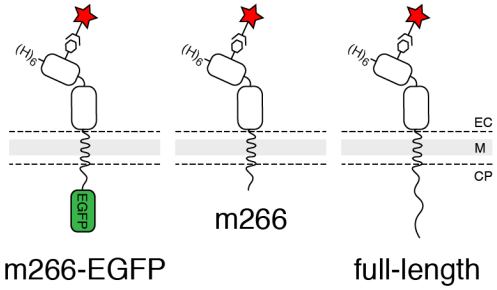

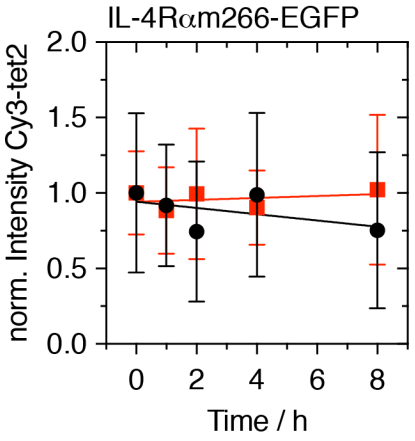

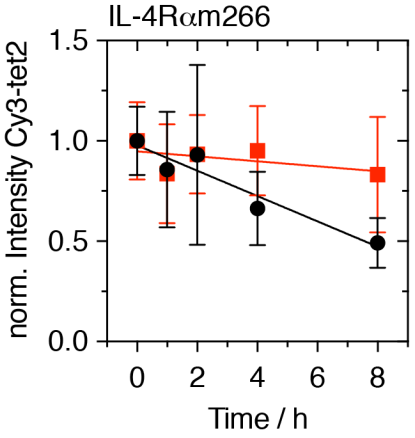

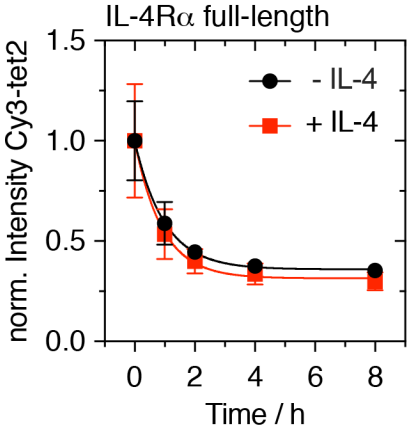

B IL-4Rα diffusion coefficient

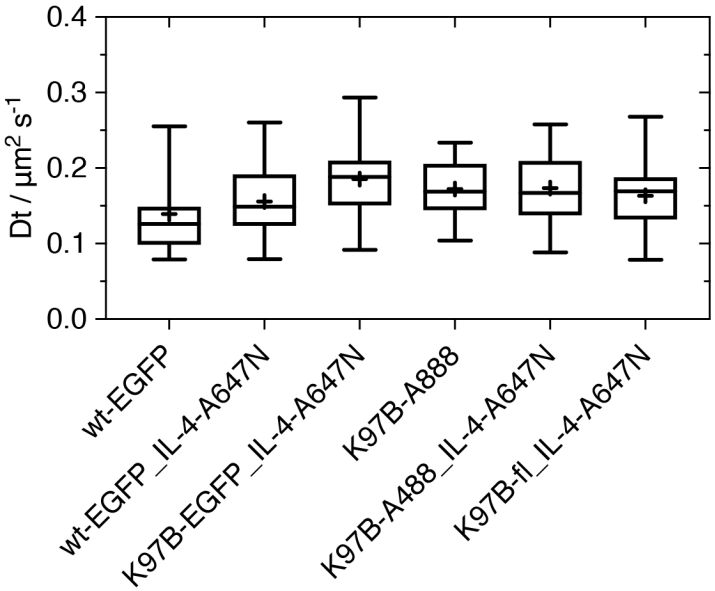

Figure 9.3.1: Cell membrane lifetime of IL-4Rα constructs. HEK293T cells expressing the IL-4Rα* constructs K97B ± EGFP and full-length IL-4Rα were labelled with Cy3-tet2 and were incubated for various times in growth media (± IL-4). Then the cells were fixed with paraformaldehyde (PFA), labelled with Cy5-NHS for membrane segmentation, and were imaged by confocal microscopy. Only the full-length receptor showed an exponential-like decay of the membrane lifetime. The two other constructs showed a very slow linear internalization rate, which led to a stable receptor population at the cell membrane and revealed that the receptor tail is important for the internalization and degradation behaviour. B) Cells expressing different receptor constructs were either labelled with Alexa488-tet2 (A488-tet2) or directly incubated with IL-4-A647N and FCCS was measured at the bottom membrane. All constructs, occupied or non-occupied, showed a similar diffusion behaviour with a diffusion coefficient of about 0.16 ± 0.05 $\mu m^2 s^{-1}$ and 0.14 ± 0.06 $\mu m^2 s^{-1}$.

values (Figure 9.3.1B).[29, 197] The incorporation of the single uAA BCNK into the ECD did not influence the diffusion behaviour of the receptor. The A488-tet2 labelled mutant K97B with the deletion of the C-terminal EGFP showed, in its occupied or non-occupied state, the same diffusion coefficient as the EGFP-tagged wt IL-4Rα*. Further FCCS measurements with the full-length IL-4Rα*, equipped with a long unordered tail, resulted in the similar diffusion coefficient as for the truncated receptor version. These results lead to the conclusion that the intracellular region of the receptor does not particularly regulate the diffusion behaviour at the cell membrane. However, it seems that the TMD is important for the diffusion, as all receptor constructs contain the same TMD sequence, which leads to the same diffusion coefficient results. Although the different C-terminal IL-4Rα* tails do not change the diffusion behaviour of the receptors, they are important for the internalization and degradation of the receptor (Chapter 11).

In summary, experiments with the labelled ligand IL-4-A647N confirmed that the BCNK modification of the IL-4Rα* interferes with the ligand binding in all mutants, resulting in a lower efficiency. In addition, labelling-sites in the ligand binding pocket or at allosteric positions (activation loop) were even more reduced in ligand binding. The comparison between the ligand binding efficiency and the click labelling efficiency exhibited that various populations of receptors are located at the plasma membrane for the mutants near or in the activation loop. Almost all mutants, except for S44B and E189B, showed a reduced IL-4Rα* site-specific labelling. This result suggests a more compact quaternary structure of the receptor after ligand binding. Furthermore, a certain flexibility in the L2-loop and in the activation loop can be assumed. A fluorescence lifetime shift of the viscosity sensor Cy3-tet2 confirmed the rearrangement of the activation loop during

ligand binding and, in addition, displayed a further reorientation of the two receptor domains D1 and D2 around the linker region. The formation of the new receptor orientation during ligand binding, especially in the activation loop, may lead to the activation of the JAK/STAT pathway. Further experiments with click labelled receptor constructs showed a very fast internalization half-life, with about 40 min, for the full-length receptor, whereas the truncated constructs stayed at the membrane for hours. This makes the truncated receptor construct IL-4Rα* a perfect example system for the quantification of the click labelling reaction at the membrane of living cells. As the internalization of the receptor is a rather fast process, the question arose which part of the membrane the activation of the JAK/STAT pathway takes place in.

10 IL-4R activation from the plasma membrane

The location and the precise mechanism of the IL-4R dependent JAK/STAT activation is still unclear. Most hematopoietic cytokine receptors express only a few receptor copies (< 1 μm^{-2}) at the cell surface. Thus, low lateral affinity has been suggested to represent a safety mechanism that prevents ligand-independent dimerization and false signalling. In 2014, Weidemann and Bökel proposed endocytosis as a mechanism to increase the concentration of receptors in small membrane compartments tethered in the actin cortex, called cortical endosomes (CE).[30] Obeying the law of mass action, a higher number of IL-4R subunits per membrane area shifts the equilibrium towards receptor heterodimerization, making endocytosis an important step for the JAK/STAT pathway activation. Nevertheless, it might also be possible that the receptor complex is activated at the outer plasma membrane as well as within CEs leading to a spatiotemporal diversification of branching signalling pathways.

One convenient way of investigating the formation of the type 1 IL-4R complex at the membrane of living cells is to immobilize ligand IL-4 in resolvable patterns on a solid support that leads to recruitment of the receptor subunits in the plasma membrane. This was achieved by coupling a biotinylated ligand to phase separating supported lipid bilayers (SLBs) on top of which transfected cells with labelled receptors were growing. Supported lipid bilayers lack the dynamic membrane turnover and thus represent a controlled testbed to quantify interactions that lead to ternary complex formation within the lipid bilayer.

IL-4 (N38C, F82D) was attached to biotin via maleimide coupling similar to IL-4-A647N mentioned before (courtesy of Prof. Dr. Thomas Müller; Julius-Maximilians-University Würzburg). The ligand IL-4-Biotin (IL-4-B) was presented by phase separated SLBs in a molecular sandwich composed of NeutrAvidin (NA) and the biotinylated lipid DSPE-PEG2000-Biotin (Figure 10.1A). Figure 10.1B shows the lipid composition (lipid mix 1 and 2) of the SLBs, which consists of unsaturated lipids forming the lipid disordered (Ld) domain, and saturated lipids which were located in the lipid ordered (Lo) domain. Cholesterol in this mixture is important for the size and the proper formation of phase

A Domain-specific receptor recruitment

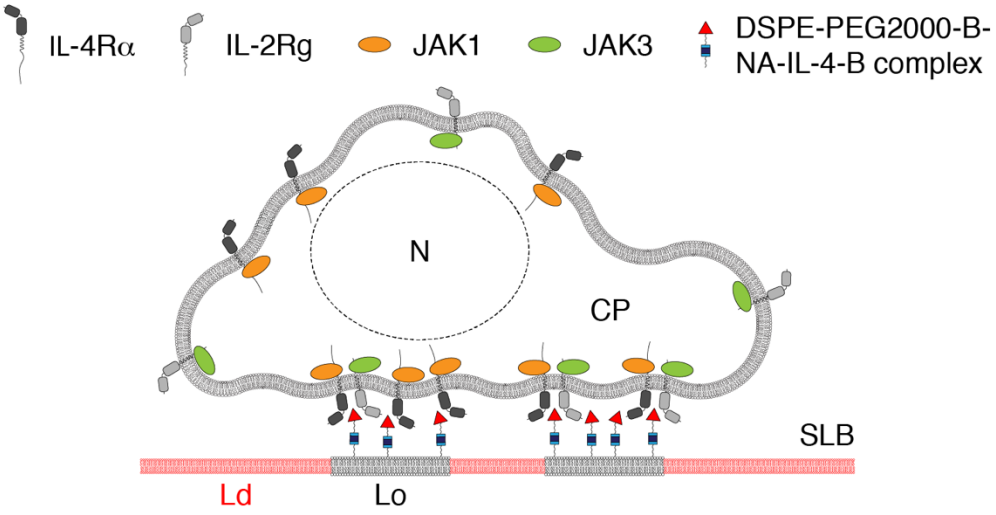

B SLB lipid composition

lipid mix1 / lipid mix2:

Ld	DOPC (18:1, C9)	34.95	lipid matrix of Ld-domain
Ld	DOTAP (18:1, C9)	5.0	positive charge for cell attachment
Ld	DOPE-ATTO655 (18:1, C9)	0.05	fluorescent label
Lo	DSPC (18:0) / SM (18:0)	39.9	lipid matrix of Lo-domain
Lo	DSPE-PEG2000-Biotin (18:0)	0.1	protein binding site
Ld/Lo	Cholesterol	20.0	phase separation

C Phase separated SLB

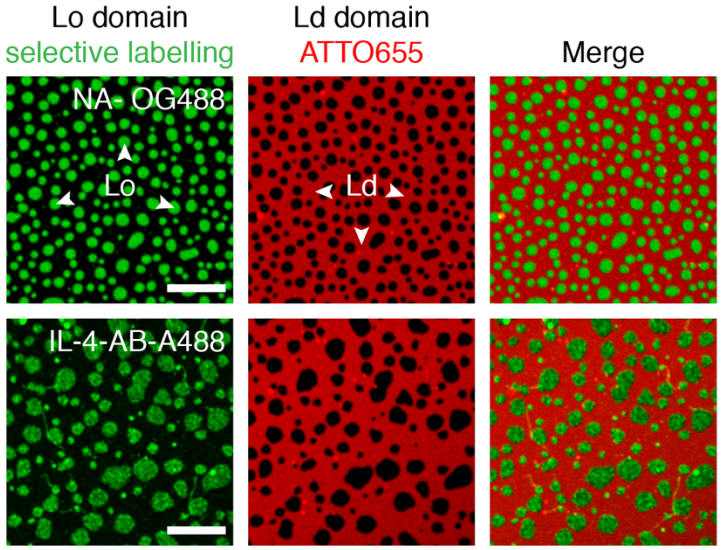

Figure 10.1: Phase separated supported lipid bilayers. A) Schematic figure of an adherent cell located on a phase separated supported lipid bilayer (SLB). The SLB contains fluorescently labelled lipid disordered domains (Ld, red) and unlabelled lipid ordered domains (Lo, black). The Lo domains contain a biotinylated fatty acid (DSPE-PEG2000-Biotin), which NeutrAvidin (NA) and the biotinylated IL-4 (IL-4-B) complex binds to. The SLB bound IL-4-B recruits the type 1 IL-4R complex at the membrane of transfected HEK293T cell. B) Composition of the lipid mixtures used to form the SLBs. Difference between lipid mix1 and mix2 is the lipid matrix of the Lo domain (DSPC vs. SM). C) A SLB (lipid mix 1 lacking DOTAP, upper row) was incubated with NeutrAvidin-Oregon Green 488 (NA-OG488, green) and imaged by confocal microscopy. The excess of ligand at the SLB surface was confirmed by immunostaining with an IL-4 specific antibody labelled with the fluorophore Alexa488 (IL-4-AB-A488) (green, lipid mix 2, lower row). Scale bar: 11 µm.

separated membranes. Control experiments with labelled NeutrAvidin-Oregon Green 488 (NA-OG488) and an Alexa488 labelled IL-4 specific antibody (IL-4-AB-A488) showed in a phase separated lipid membrane that NA and IL-4-B indeed co-localized perfectly in the Lo domains of the SLB (Figure 10.1C), where the lipid anchor DSPE is supposed to be highly enriched. Thus, spatial phase separation of SLBs can be used to trigger receptor subunit recruitment within the plasma membrane.

Having established a protocol for SLBs presenting the ligand IL-4 exclusively in Lo domains, cells were seeded on top. HEK293T cells were harvested 24 h after transfection with IL-4Rα* and carefully seeded on the SLB (Figure 10.2, upper row). As HEK293T cells did not attach to surfaces coated with a SLB by themselves, DOTAP had to be added to the lipid mix that constitutes the membrane. DOTAP is an unsaturated, positively charged fatty acid, which preferentially locates in the Ld domain. The positive charged fatty acid interacts with the negatively charged cell surface and therefore promotes cells to attach to the SLB surface (Figure 10.2, middle row). We observed that too high concentrations of DOTAP led to deformation of the SLB and recruitment of DOPE-ATTO655 near the cell membrane (Figure 10.2, lower row). However, for both membranes with DOTAP, a localization of the EGFP-tagged IL-4Rα* signal, in the ligand containing Lo domains, was clearly visible.

Experiments with labelled NeutrAvidin-tetramethylrhodamine (NA-TMR) confirmed the recruitment of IL-4Rα* into the Lo domain, whereas membranes without IL-4-B did not show any recruitment of the receptor (Figure 10.3A). This observation suggests that the recruitment of the receptor IL-4Rα* into Lo domains is faithfully triggered by immobilized ligand.

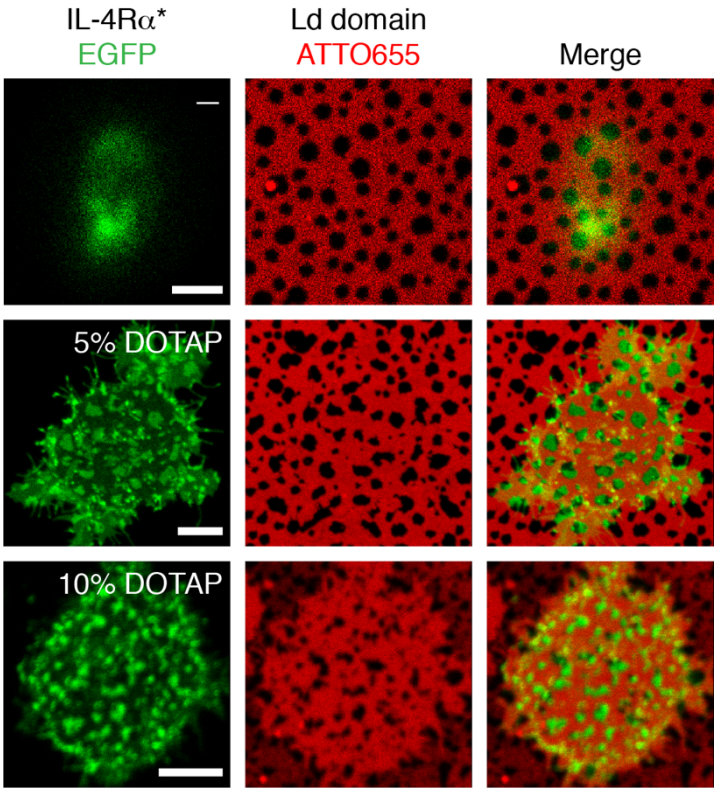

Figure 10.2: IL-4Rα* recruitment to positively charged phase separated SLBs. HEK293T cells expressing IL-4Rα* (green) did not attach to a SLB (red) coated surfaces (lipid mix 1 lacking DOTAP, upper row). After the incorporation of DOTAP, a positively charged fatty acid, an attachment of the cells on the SLB surface and a localization of the IL-4Rα* in the ligand coated Lo domains were confirmed (lipid mix 1, middle row). A low DOTAP ratio in the SLB was important to avoid membrane distortion and accumulation of Ld domain lipids like DOPE-ATTO655 at the cell surface level (lipid mix 1 with 10% DOTAP, lower row). Scale bar: 6 µm.

To extend these investigations to the formation of signalling competent receptor complexes at the membrane of living cells, HEK293T cells were transfected with the entire type 1 receptor set consisting of IL-4Rα*, IL-2Rγ and JAK3-tRFP. Since JAK1 is endogenously expressed in HEK293T, this protein has not been included for overexpression; Tag-RFP fused to JAK3 has been used as proxy for IL-2Rγ localization. 24 h after the transfection, cells were harvested and were added to the SLB coated with the NA/IL-4-B sandwich. Strikingly, both receptors of the type 1 complex, IL-4Rα* and IL-2Rγ were indeed recruited into the Lo domains in a IL-4 dependent manner,

suggesting dimerizing in the plasma membrane can take place under these conditions of overexpression (Figure 10.3B).

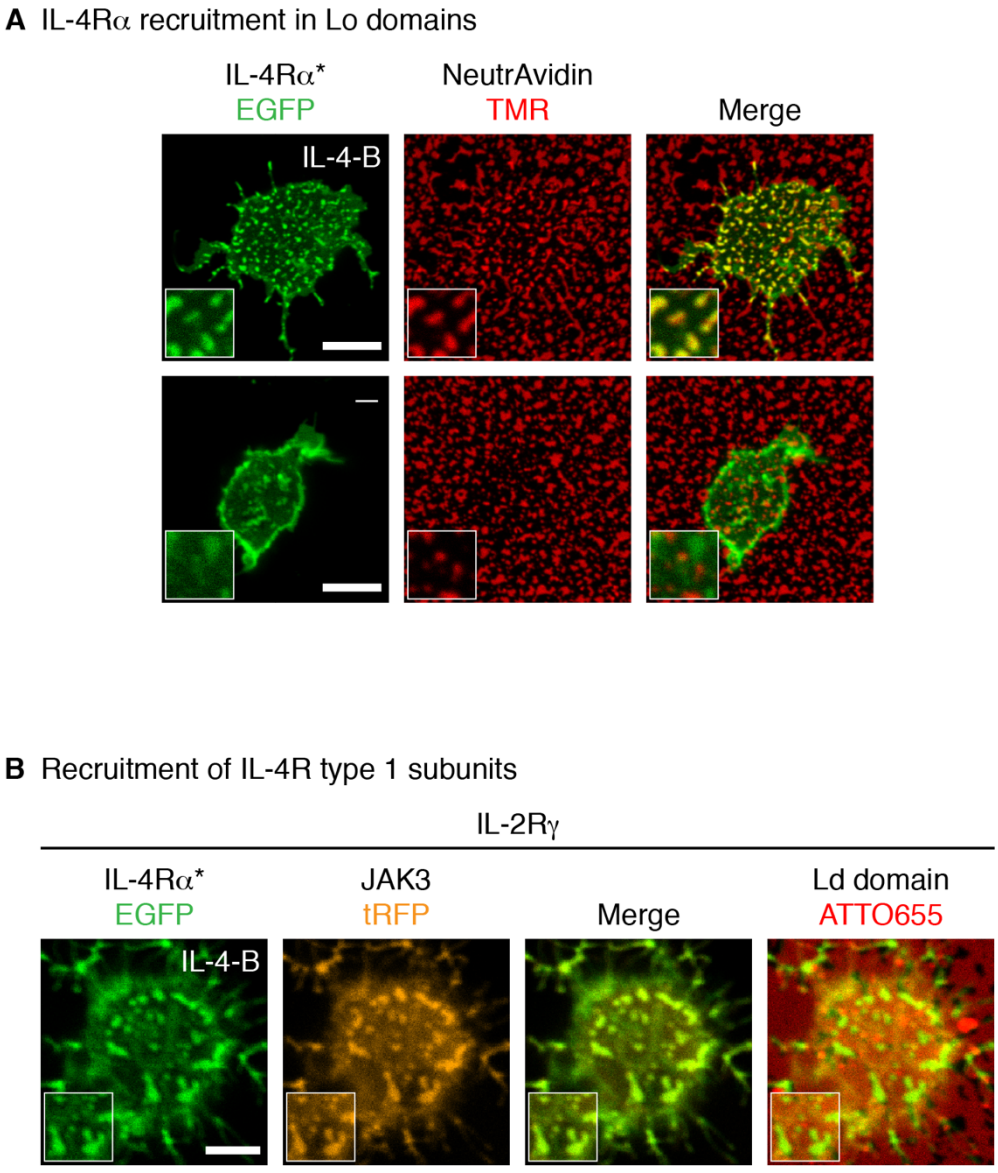

Figure 10.3: Heterodimerization of IL-4R subunits. A) The recruitment of IL-4Rα* into the IL-4-B coated Lo domains was confirmed by confocal imaging of the receptor signal (green) and the NeutrAvidin-tetramethylrhodamine (NA-TMR) signal (red) (lipid mix 1, upper row). Cells loaded on a IL-4-B free SLB did not show any patterned IL-4Rα* surface signal (lipid mix 1, lower row). B) HEK293T cells expressing the type 1 IL-4R complex (L-4Rα*, green) were loaded on a IL-4-B coated surface (red) and showed a heterodimerization of the receptor subunits as well as an additional colocalization of the associated kinase JAK3-tRFP (orange) into the Lo domains. Scale bars: 11 and 6 µm.

We further optimized the experimental setup to form SLBs with larger Lo domains. For this reason, the saturated fatty acid DSPC was replaced by sphingomyelin (SM), which is known to form larger Lo domains (personal communication Dr. Henri Franquelim). With these larger Lo domains cells bound to the SLB with higher efficiency and, thus, better imaging was possible (Figure 10.4, upper row). Images of the negative control confirmed again that cells can influence the membrane behaviour of the SLB. The cells pushed the Lo domains outwards to the side of their support area to create a larger access to the DOTAP containing Ld domain (Figure 10.4, lower row).

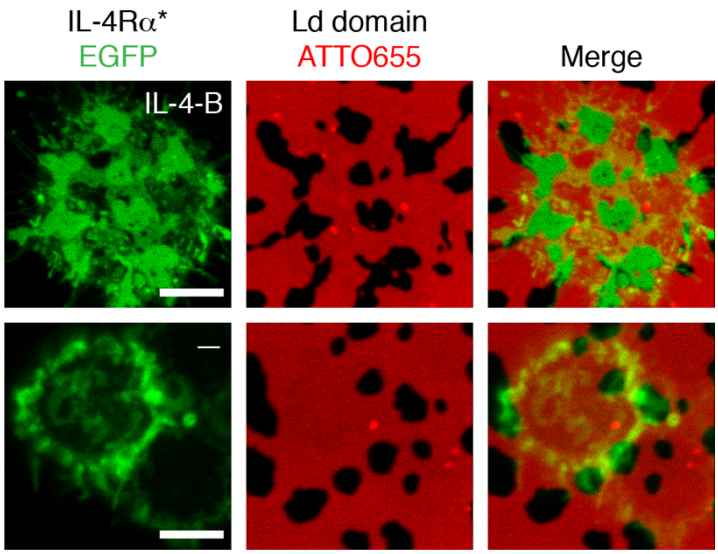

Figure 10.4: Optimization of the Lo domain size. To increase the Lo domain size, DSPC was replaced by the saturated fatty acid sphingomyelin (SM) (lipid mix 2, red). The ligand dependent recruitment of IL-4Rα* (green) into the Lo domains was confirmed by confocal microscopy (upper row). On membranes lacking the ligand IL-4-B an absent recruitment of IL-4Rα* as well as an exclusion of Lo domains, controlled by the HEK293T cells, were observed (lower row). Scale bar: 6 µm.

Next, we tested the activation of the JAK/STAT pathway by the type 2 IL-4R endogenously expressed in HeLa cells. The cells were transfected with fluorescent EGFP-STAT6 and after 18 h the medium was replaced with DMEM lacking FBS. After 6 h of starvation, the HeLa cells were seeded on the SLB. After 1 h of incubation, a significant recruitment of EGFP-STAT6 into the nucleus and a rise of the fluorescence intensity inside the nucleus was observed (Figure 10.5A, upper row). The control

experiment with a SLB without IL-4-B showed no such STAT6 translocation (Figure 10.5A, middle row). Cells in the same chamber as the SLB with ligand but located next to the phase separated membrane also showed STAT6 translocation suggesting that some portion of IL-4-B dissociates from the SLB. Such a false positive STAT6-translocation could either be explained by residual IL-4-B attached to the Ld domain of SLBs or by trace amounts of IL-4-B from the supernatant (Figure 10.5A, lower row). In conclusion, cells can be activated on top of SLBs by immobilized ligand, suggesting the canonical model of ligand induced ternary complex formation and the subsequent STAT activations via the JAKs may indeed be triggered from the cell surface once the receptor densities are sufficiently high. However, the sandwich system presenting IL-4-B at the SLB may not be stable enough to rule out a partial activation from bulk solution.

To address this issue, SLBs were prepared and after 1 h the supernatant was removed and added to HEK293T cells in another well. The HEK293T cells were transfected with EGFP-STAT6. The induced cells were lysed and the phosphorylation of EGFP-STAT6 was analysed by western blotting (WB). Figure 10.5B shows the following outcome: In agreement to literature, HEK293T cells do not express STAT6 endogenously at a detectable level (lane 1), overexpressed EGFP-STAT6 is not induced by growth media or by HEK293T itself (lane 2), and stimulation of the cells with IL-4 or IL-4-B leads to pathway activation and phosphorylation of EGFP-STAT6 (lanes 3 and 4). However, phospho-STAT6-bands (pY-STAT6) were, unexpectedly, much more pronounced for cells stimulated with the supernatant than cells stimulated by the intact SLB (lanes 5 and 6). We assume, the smaller band for the SLB probe is mainly related to the very small numbers of cells loaded on the SLB. In our system the half-life of the sandwich composed of the Lo-preferring lipid, NA and IL-4-B was not sufficiently long to prevent the release of free IL-4-B in the supernatant.

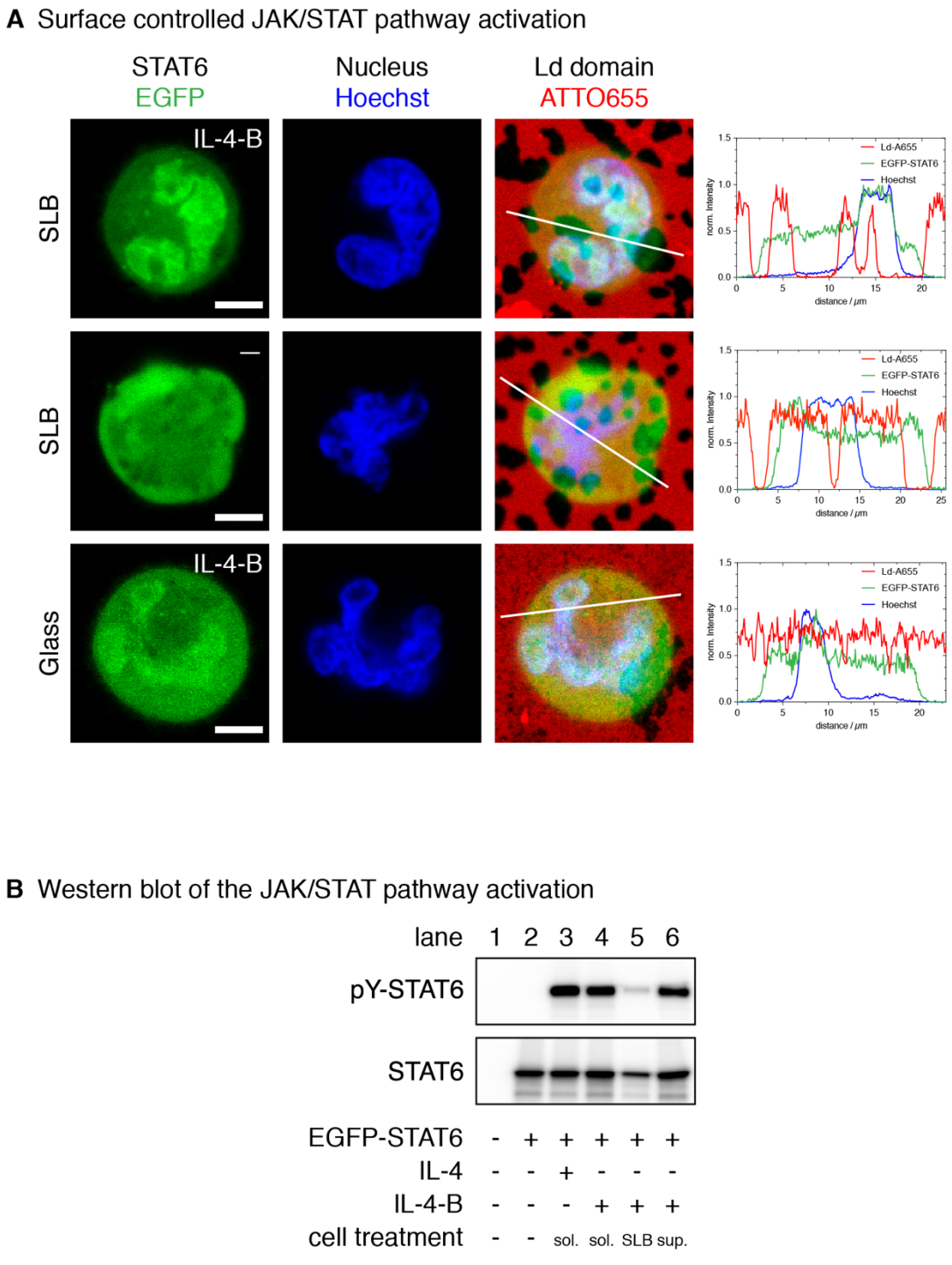

Figure 10.5: Surface controlled JAK/STAT pathway activation. A) Starved HeLa cells (IL-4R type 2 complex) showed a recruitment of transfected EGFP-STAT6 (green) to the pre-stained nucleus (blue) after the activation by the SLB (red) bound IL-4-B (lipid mix 2, upper row). EGFP-STAT6 of cells on SLBs lacking the ligand were not recruited to the nucleus (lipid mix 2, middle row). Cells expressing EGFP-STAT6, which were located in the same well as the IL-4-B coated phase separated SLB but not on top, also showed a pathway activation either by a non-phase separated SLB or by free IL-4-B in the supernatant (lipid mix 2, lower row). Line profiles are normalized to the highest value of fluorescence intensity. B) The JAK/STAT

pathway activation in HEK293T cells, transfected with EGFP-STAT6, was monitored by the phosphorylation signal of EGFP-STAT6 (pY-STAT6) on a WB. The STAT6 signal on the WB represents the number of cells and the transfection efficiency. Native cells (lane 1) did not express STAT6 in a detectable amount and overexpression of EGFP-STAT6 did not interfere with pathway activation (lane 2). Only if IL-4 was added, a pathway activation took place (lanes 3 and 4). HEK293T cells incubated on the IL-4-B coated SLB also showed an induction of the pathway although the number of cells was low (lane 5). Furthermore, the WB showed that the IL-4-B membrane complex was not stable enough during a longer period of time and therefore the supernatant of the SLB contained significant amounts of free IL-4-B which interfered with the experiment (lane 6). Scale bar: 6 µm.

To improve the experimental setup, we followed two strategies: First, we tightened the interaction between IL-4-biotin and the SLB in order to reduce the amount of dissociated ligand. NA was replaced by TraptAvidin (TA), which is a modified version of streptavidin with two point mutations for extended complex lifetimes.[198, 199] Second, we aimed to show recruitment for the full-length receptor subunits to investigate potential differences mediated by downstream factors bound to the cytoplasmic tails. Full-length receptor subunit expressed with a C-terminal GFP, in particular the IL-4Rα chain, express poorly and, what is worse, change the morphology of the cell. Therefore, to label the different full-length receptors, the extracellular H_6-tag specific dye trisNTA-A647 was used. The trisNTA-affinity-tag, loaded with three complexed Ni^{2+} ions, is capable of coordinating up to six imidazole rings from adjacent histidine side chains. H_6-tag and trisNTA binding takes place in an 1:1 ratio with a K_d of about 6 - 20 nM.[29, 181] As the binding process of trisNTA-A647 to the receptor is not covalent, it is necessary to measure the cells under equilibrium conditions to avoid dissociation during washing steps ($k_{off} = 0.34 \times 10^{-3}\ s^{-1}$; $t_{1/2} = 34$ min).[181] Unfortunately, the fluorescent construct trisNTA-A647 showed some false positive signals in the Lo domains of HEK293T cells expressing IL-4Rα* (Figure 10.6A, upper row, white arrows). This occurred because commercially available TA contains a C-terminal H_6-tag. The trisNTA-A647 signal was also seen on SLBs without ligand (Figure 10.6A, lower row, white arrows) but no background signal was detected on the untreated SLB without any loaded TA, confirming that the false positive signal was caused by the TA H_6-tag (Figure 10.6B). Expression and purification of a H_6-tag free TA were not possible.

In summary, the results showed that the IL-4-B can be bound to a SLB surface by NA, but the complex was not stable enough for a longer period of time to selectively induce

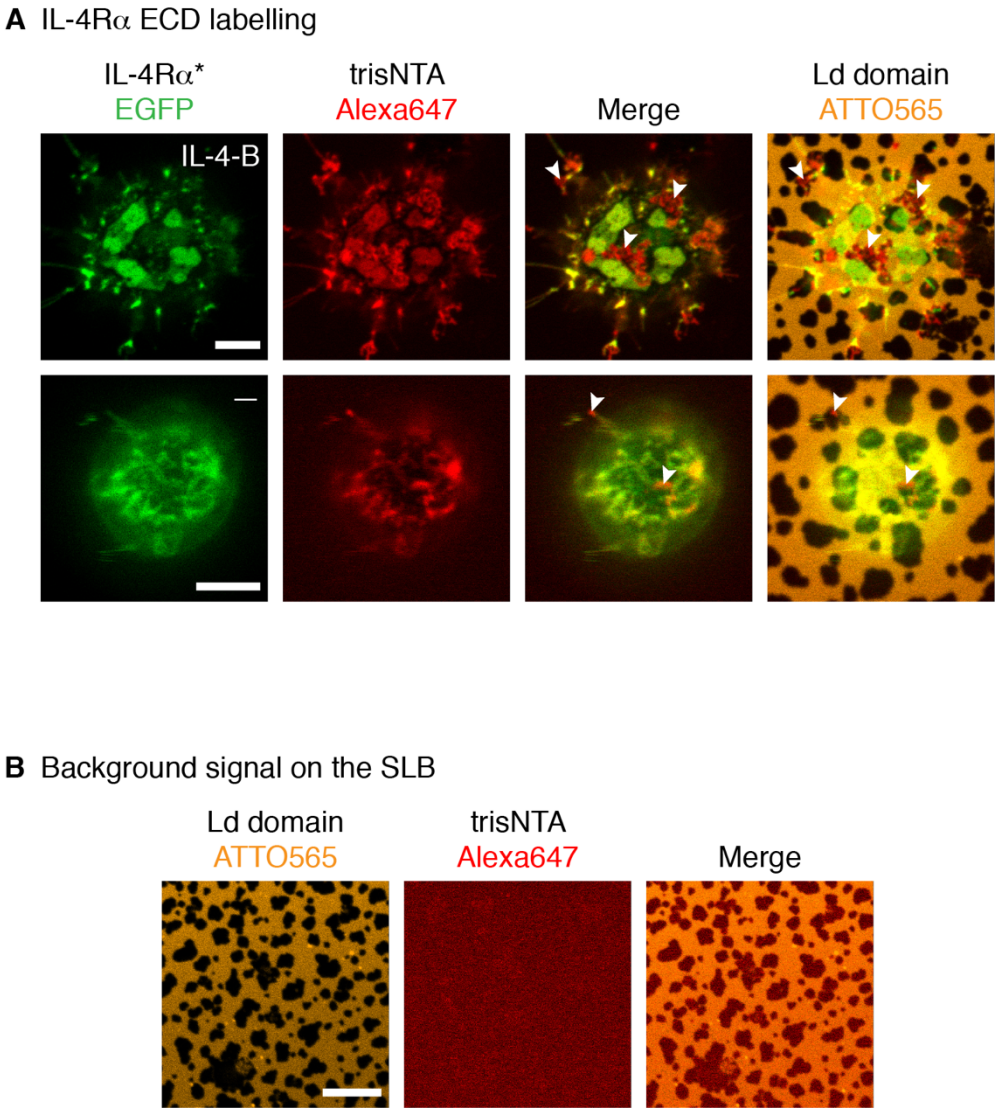

Figure 10.6: IL-4Rα* recruitment to the SLB by TraptAvidin. A) HEK293T cells expressing IL-4Rα* (green) were seeded on a SLB (orange) and the receptor was labelled with the H_6-tag specific trisNTA-A647 (red) dye. The ligand dependent recruitment of L-4Rα* into Lo domains was confirmed by confocal imaging (upper row with ligand, lower row ligand absent). Ligand binding to the Lo domains was realised by TraptAvidin (TA), a biotin specific coupling protein with extended complex lifetime. The commercially available TA contains a H_6-tag which interfered with the receptor specific labelling leading to the formation of false positive signals (white arrows). B) The control experiments with an untreated SLB confirmed that the trisNTA-A647 binds to TA and not to the positively charged membrane. Scale bars: 6 and 11 µm.

the JAK/STAT pathway from the cell membrane of living HeLa cells. The imaging of IL-4Rα* or full-length IL-4Rα with the more stable TA complex could not be achieved, since TA contains a H_6-tag the fluorophore trisNTA-A647 binds at and the purification of tag-free TA was not possible. Nevertheless, it was possible to localize the IL-4Rα* into

the IL-4-B coated Lo domains of the SLB and, in addition, the second receptor of the type 1 complex IL-2Rγ and its associated kinase JAK3-tRFP formed a receptor heterodimer at the surface of living HEK293T cells.

11 Trafficking into cortical endosomes (CEs)

11.1 Intracellular receptor tail truncation mutants of IL-2Rγ

The Rac1/Pak1 and dynamine-dependent endocytosis of the IL-4R complex is essential for the JAK/STAT pathway activation.[29, 30] In collaboration with Gosia Poczopko (Schwille group, MPI of Biochemistry), we aimed to identify unknown proteins by means of residue specific cross-linking in combination with mass spectrometry (MS). AbK, an uAA for photo-induced cross-linking, reacts covalently with AA in its near surroundings. The cross-linking product can then be analysed by MS to find new interaction partners of the type 1 IL-4R complex.

As the reactive AbK is rather small, only interaction partners in the immediate vicinity of the reactive group could be cross-linked and potentially identified. It has been shown that co-expression of IL-2Rγ and JAK3 leads to cortical endosomes. Thus successful endocytosis can be visually tested by confocal microscopy.[29, 30] We used this assay to first narrow essential regions at the cytoplasmic tail in H6-IL-2Rγ that serve as a binding platform for unknown protein factors which are important for receptor endocytosis. A truncation series of the intracellular H_6-IL-2Rγ tail was cloned, expressed together with JAK3-EGFP in HEK293T cells and imaged by confocal microscopy. The tail of the H_6-IL-2Rγ was truncated after every tenth AA beginning from the fifth AA (m5) after the transmembrane region. The H_6-IL-2Rγ was visualized by H_6-tag specific trisNTA-A647 fluorophore. H_6-IL-2Rγ and JAK3-EGFP expressed in HEK293T cells formed CEs near the plasma membrane (Figure 11.1.1, white arrows). The EGFP signal of JAK3 colocalized with the trisNTA-A647 when the H_6-tag was present. A low background at the cell membrane and the glass surface was visible for trisNTA-A647. Mutant m75 - m55 showed CEs comparable with the parental receptor. Receptor mutants m45 and m35 localized at the cell membrane, but trafficking to CEs was not detected. The truncated receptors m25 - m5 did not show recruitment of JAK3 to the cell membrane where the H_6-IL-2Rγ mutants were located. Mutant m5 is a truncated version with an impaired Box1 motif and is therefore signalling incompetent. The tail region until m25

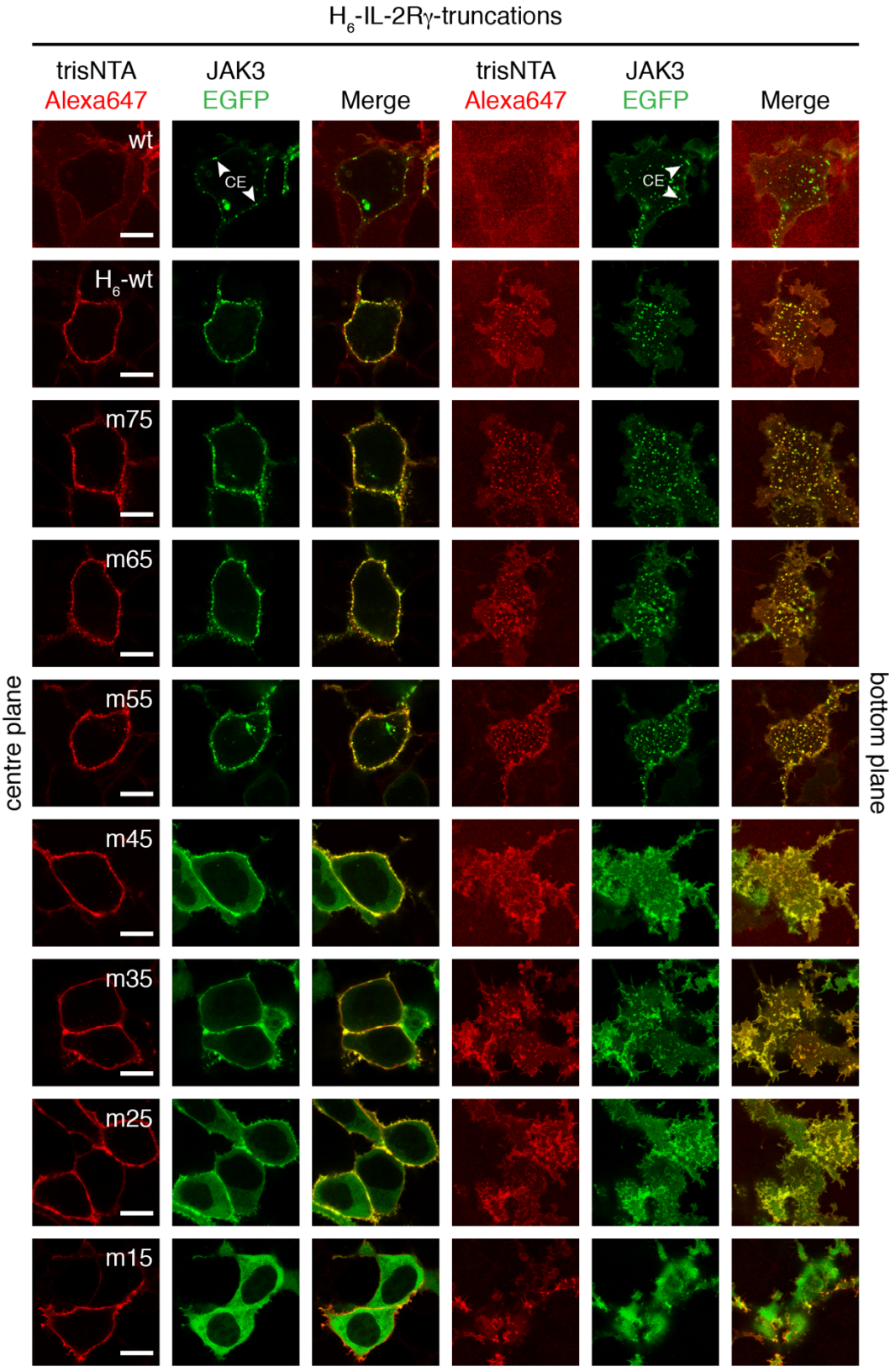
H6-IL-2Rγ-truncations
trisNTA Alexa647
JAK3 EGFP
Merge
trisNTA Alexa647
JAK3 EGFP
Merge
wt
H6-wt
m75
m65
m55
m45
m35
m25
m15
CE
CE
centre plane
bottom plane

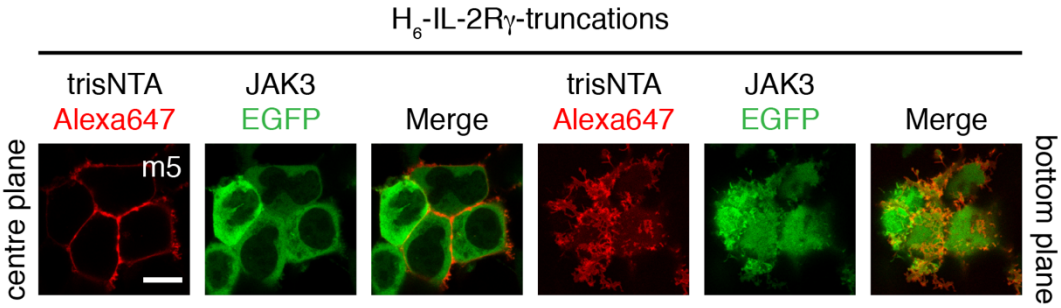

Figure 11.1.1: IL-2Rγ tail truncation mutants. HEK293T cells expressing the C-terminal H_6-IL-2Rγ truncation mutants and JAK3-EGFP (green) were labelled with the H_6-tag specific fluorophore trisNTA-A647 (red) and imaged by confocal microscopy. Cells expressing the receptor lacking the H_6-tag showed a small amount of background signal at the cell surface. The wt receptor and the mutants m75 - m55 were trafficking into CEs whereas the mutants m45 and m35 showed membrane localization of JAK3-EGFP, but trafficking into CEs was not detected. In the m25 - m5 mutant cells only homogenously distributed JAK3-EGFP and no formation of CEs was seen. In collaboration with Gosia Poczopko (Schwille group, MPI of Biochemistry). Scale bar: 11 µm.

was important for JAK3 binding whereas the region until m45 was important for trafficking into CEs (Figure 11.1.1).

In the next step, we analysed the trafficking behaviour of the truncated H_6-IL-2Rγ into preformed CEs. For this purpose, HEK293T cells were triple transfected with full-length IL-2Rγ and JAK3-EGFP for CE-formation supplemented with the H_6-tagged truncation mutants H_6-IL-2Rγ-5m-m75. CEs were visible for all DNA combinations. All H_6-tagged receptors, wt or truncated versions, ended up in the preformed CEs (Figure 11.1.2). Only mutant m5 showed a slightly reduced trafficking ability, maybe due to the incomplete Box1 motif. Thus, the mutants m45 - m5 can traffic into CEs but cannot form them. In this case, trafficking of the truncated receptor was not receptor tail specific and rather an unspecific diffusion process, in which the truncated receptor gets internalized when endosomal structures are formed.

All in all, the truncation experiments at the H_6-IL-2Rγ tail with mutant m45 and m35 presented a region which was clearly important for JAK3 recruitment to the cell membrane, CE formation and receptor trafficking into them. Moreover, the truncation mutants m25 - m5 also showed a lack of CE formation and, in addition, the membrane recruitment was disturbed. These results encourage the idea of cross-linking experiments in the specific tail-region of the m45 and m35 mutants.

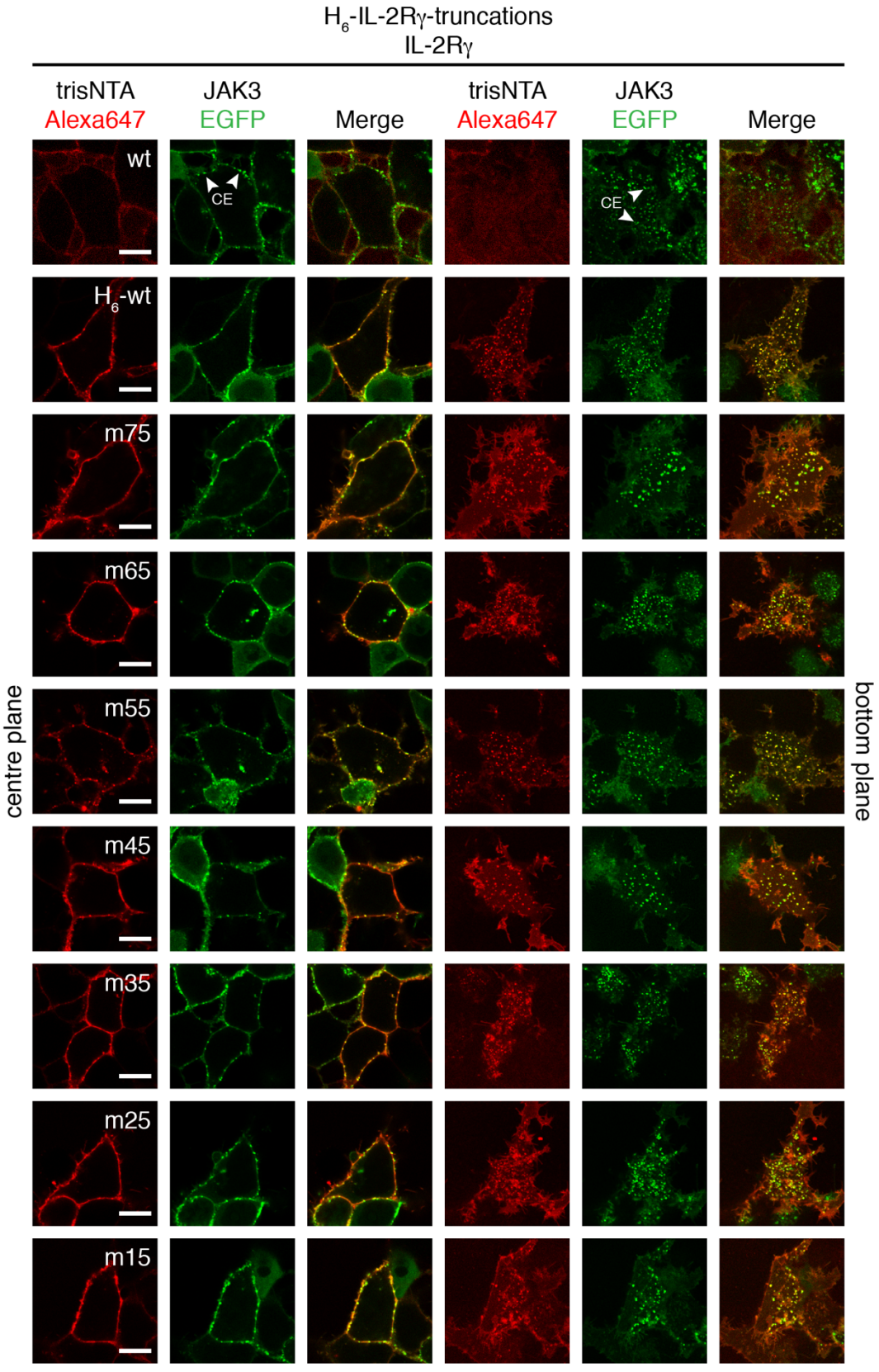
H6-IL-2Rγ-truncations
IL-2Rγ
trisNTA Alexa647
JAK3 EGFP
Merge
trisNTA Alexa647
JAK3 EGFP
Merge
wt
H6-wt
m75
m65
m55
m45
m35
m25
m15
CE
CE
centre plane
bottom plane

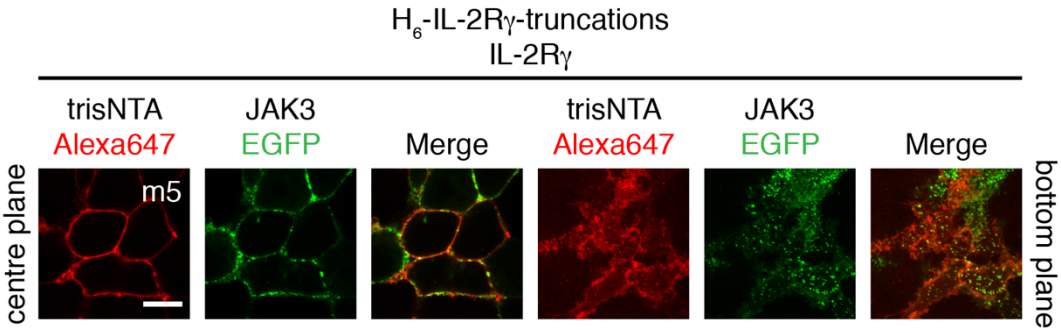

Figure 11.1.2: IL-2Rγ tail truncation mutant trafficking into preformed CEs. In HEK293T cells, CEs were formed by expression of full-length IL-2Rγ and JAK3-EGFP (green). Cells expressing the wt or mutant H_6-IL-2Rγ truncation mutants (red) showed trafficking of the expressed receptors in the preformed CEs by colocalization of the JAK-EGFP signal and the H6-tag specific trisNTA-A647 signal. Moreover, mutant m5, with its incomplete Box1 motif, showed a reduced trafficking rate in preformed CEs. In collaboration with Gosia Poczopko (Schwille group, MPI of Biochemistry). Scale bar: 11 µm.

11.2 Covalent cross-liking of endocytosis factors

After the localization of an important region (A287 - R306, mature numbering) in the IL-2Rγ tail for CE formation and trafficking, the suggested cross-linking approach should be established. The interaction of IL-2Rγ and JAK3 is a well-known, strong protein interaction and an excellent pair to test and improve the cross-linking procedure.[46] JAK3 binds the IL-2Rγ intracellular tail at the Box1 motif, a nine AA long proline rich sequence. We cloned five Box1 mutants and three control mutants in the extracellular domain (ECD) for incorporation of AbK via GCE. Furthermore, the IL-2Rγ was equipped with a C-terminal triple haemagglutinin-tag (3HA-tag) for an immunoprecipitation (IP) assay to concentrate the low abundance receptor. Only if the AbK is properly incorporated, full-length receptors are expressed, which can then be purified and concentrated by means of the 3HA-affinity-tag. For a cleaner and more specific sample an N-terminal H_6-tag was also present to perform tandem IP as well as fluorescence imaging control experiments. First of all, the expression and proper localization of the receptor mutants at the membrane of living cells were tested with confocal microscopy (Figure 11.2.1). For this purpose, HEK293T cells were transiently transfected with uAA modified IL-2Rγ (H_6-IL-2Rγ-TAG-3HA; mature numbering) and JAK3-EGFP. Then the cells were labelled with trisNTA-A647 for receptor detection and imaged. The wt control cells showed both

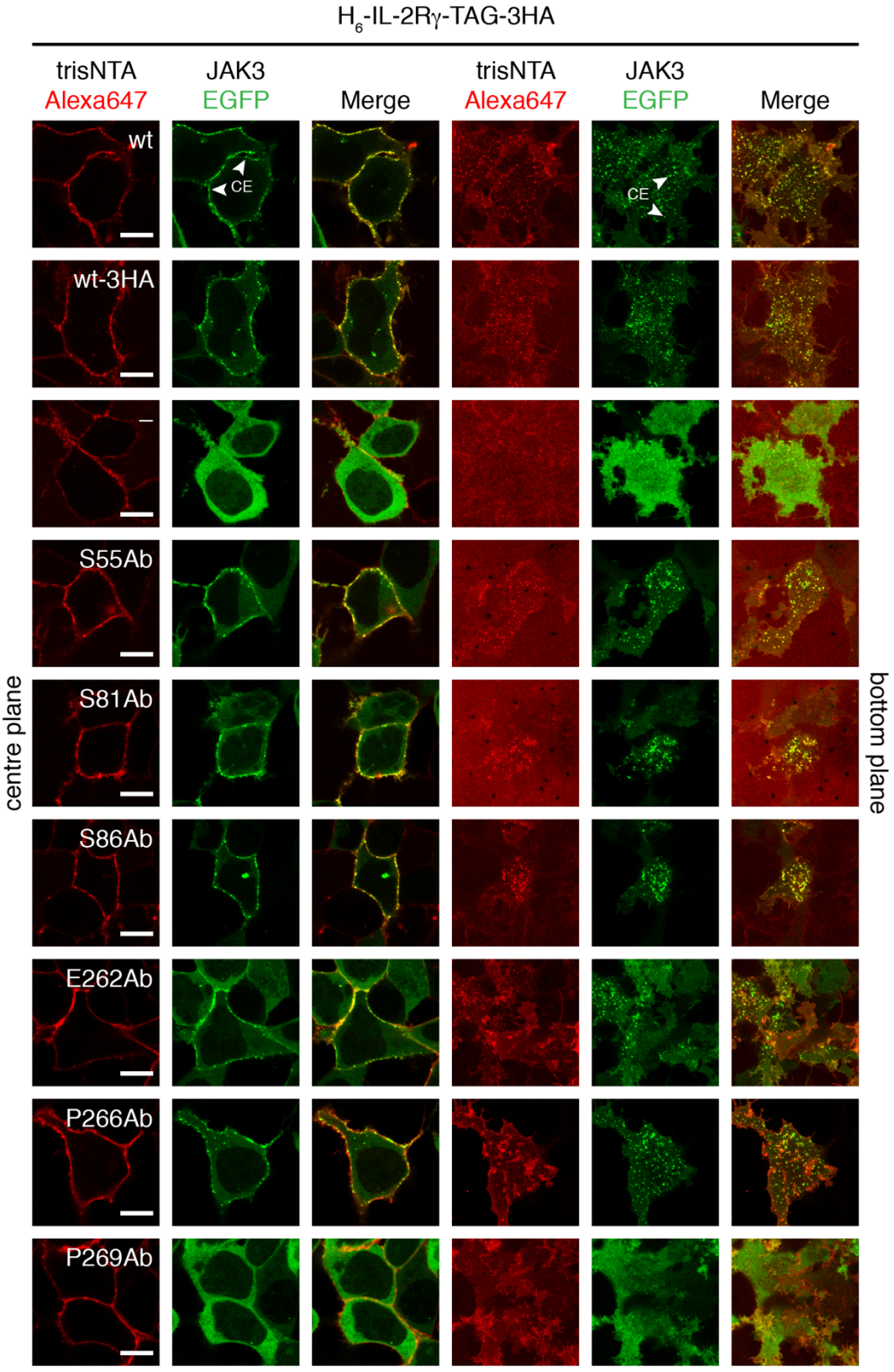
H6-IL-2Rγ-TAG-3HA
trisNTA Alexa647
JAK3 EGFP
Merge
trisNTA Alexa647
JAK3 EGFP
Merge
wt
wt-3HA
–
S55Ab
S81Ab
S86Ab
E262Ab
P266Ab
P269Ab
CE
CE
centre plane
bottom plane

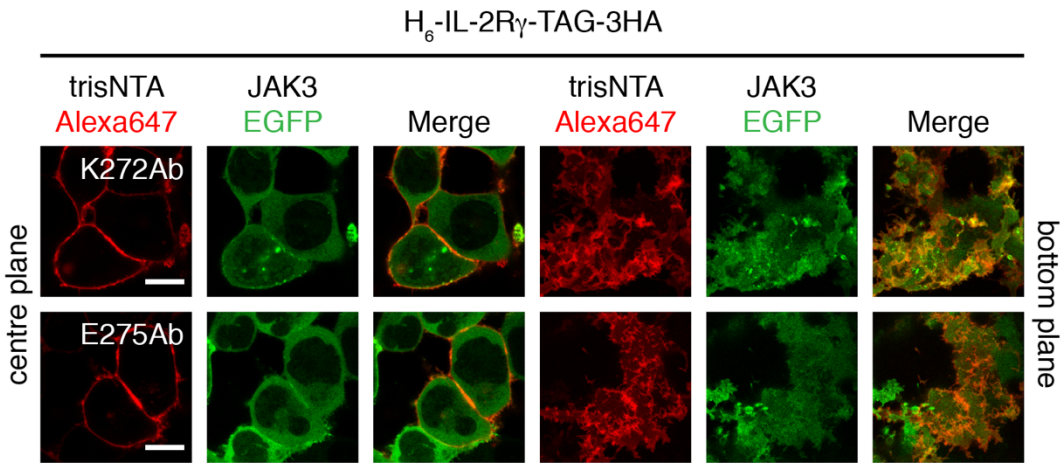

Figure 11.2.1: Membrane localization of H_6-IL-2Rγ-TAG-3HA mutants. HEK293T cells expressing the AbK modified H_6-IL-2Rγ-TAG-3HA mutants and JAK3-EGFP (green) were labelled with trisNTA-647A (red) at the N-terminal H_6-tag. The wt constructs, the ECD mutants (S55Ab, S81Ab and S86Ab) and the Box1 motif mutants (E262Ab and P266Ab) showed CE formation and localization. The C-terminal Box1 motif mutants P269Ab, K272Ab and E275Ab did not form CEs and JAK3-EGFP was homogenously distributed in the cytoplasm of the cells. Scale bar: 11 µm.

proper localization on the cell surface and in CEs, allowing the conclusion that the C-terminal 3HA-tag does not interfere with expression, localization and trafficking into CEs of the wt IL-2Rγ. Furthermore, the negative control without the receptor displayed a low background signal on the cell surface with trisNTA-A647 labelling and a homogenous cytoplasmic distribution of JAK3. All ECD mutants (S55Ab, S81Ab, S86Ab; Ab, AbK modified) as well as the Box1 mutants E262Ab and P266Ab were properly expressed at the cell surface and showed trafficking into CEs. On the other hand, the Box1 mutants P269Ab, K272Ab and E275Ab localized on the membrane, but the formation of CEs was suppressed. These findings confirm that the intact Box1 motif, especially the C-terminal part, is important for CE formation.

A missing incorporation of AbK into the intracellular domain, by the termination of translation, can lead to truncated receptor fragments with an intact ECD and a shortened tail. This was not possible for mutations in the ECD, because the short protein fragments are supposed to be degraded soon after their formation. As the truncated receptors may interfere with experimental settings and results, such as the replacement of full-length with truncated receptors in ligand induced receptor dimers, further analysis of the

truncated receptor population is necessary. To address the question whether two different receptor populations were expressed, one population ending at the amber stop

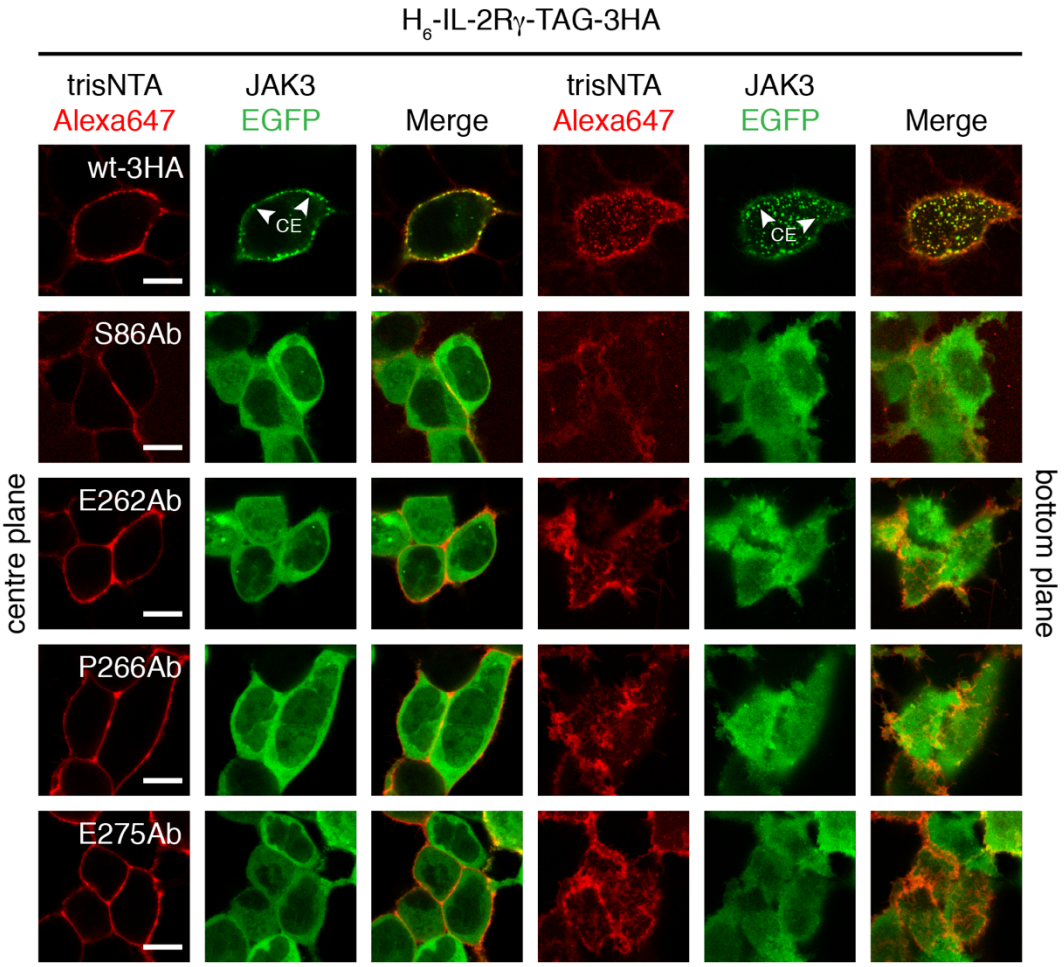

Figure 11.2.2: Expression without AbK of H_6-IL-2Rγ-TAG-3HA mutants. To distinguish between the two different populations of full-length and truncated receptors, HEK293T cells were transfected with H_6-IL-2Rγ-TAG-3HA mutants and JAK3-EGFP (green) and incubated with cell growth media lacking AbK. The receptors were labelled N-terminally with trisNTA-A647 (red). Cells transfected with the wt receptor showed CEs, whereas in cells with the ECD mutants membrane localized receptors and CEs were absent. The Box1 motif mutants showed a membrane localization of a truncated receptor population which JAK3-EGFP was not able to bind at. Scale bar: 11 µm.

codon where AbK is incorporated and another population ending at the designated stop codon of the open reading frame, experiments without the addition of AbK into the cell growth media were performed. The cells were transfected with receptor DNA and

JAK3-EGFP and were cultivated for 24 h in growth media in the absence of AbK. All three ECD mutants showed JAK3-EGFP signal in the cytoplasm but receptor signal on the membrane of cells was not detected, only the usual background of trisNAT-A647 showed up (Figure 11.2.2). All Box1 motif mutants of truncated H_6-tagged IL-2Rγ were localized in the cell membrane, representing one of the two receptor populations expressed in the previous experiment with AbK supplemented in the growth media. This result also showed that the CEs in the mutant E262Ab and P266Ab are only formed by one receptor population, the full-length receptor with incorporated AbK. JAK3-EGFP was not able to bind to the truncated receptor population. Moreover, the lack of AbK and the two receptor populations confirm the results of the experiments with the truncated receptor tail, in which the m25 - m5 mutants were located at the plasma membrane but were not able to form CEs or recruit JAK3 to the membrane.

To distinguish between the two receptor populations, an IP approach to select the full-length receptor with the C-terminal 3HA-tag was set up. Before an MS experiment was performed with purified protein samples, a WB analysis was made. This fast analysis method was used to optimize the IP assay ensuring a high protein concentration, which is necessary for MS analysis. First, we tested different H_6-IL-2Rγ-3HA and JAK3-EGFP DNA ratios as well as the IP assay to increase the protein concentration. For this purpose, HEK293T cells were transiently transfected, lysed after 24 h, concentrated with IP for 3HA-affinity-tag and analysed by western blot (IL-2Rg ECD antibody and EGFP antibody) (Figure 11.2.3). The WB analysis of the cell lysate showed a single band in all transfected cells for each H_6-IL-2Rγ-3HA and JAK3-EGFP (lanes 1 - 9). The wt receptors lacking the 3HA-tag were located slightly beneath the other bands because of their reduced molecular size (lanes 10 and 11). All 3HA-tag modified receptors were also detected in the IP sample analysis, but the signal of the bands was not increased and was inhomogeneous for all samples. In the IP analysis the wt receptor, in which the 3HA-tag is absent, lacks a signal band. The IP of the H_6-IL-2Rγ-3HA and JAK3-EGFP complex was not detected in the WB analysis, although JAK3-EGFP was present in the cell lysate. This led to the conclusion that, in our experimental settings, the protein complex was not stable enough to be co-immunoprecipitated and analysed. For further

experiments, a DNA ratio of 1.5 µg H_6-IL-2Rγ-3HA and 1.0 µg JAK3-EGFP as well as 1.5 µg AbK-tRNA synthetase/$tRNA^{AbK}$ was used.

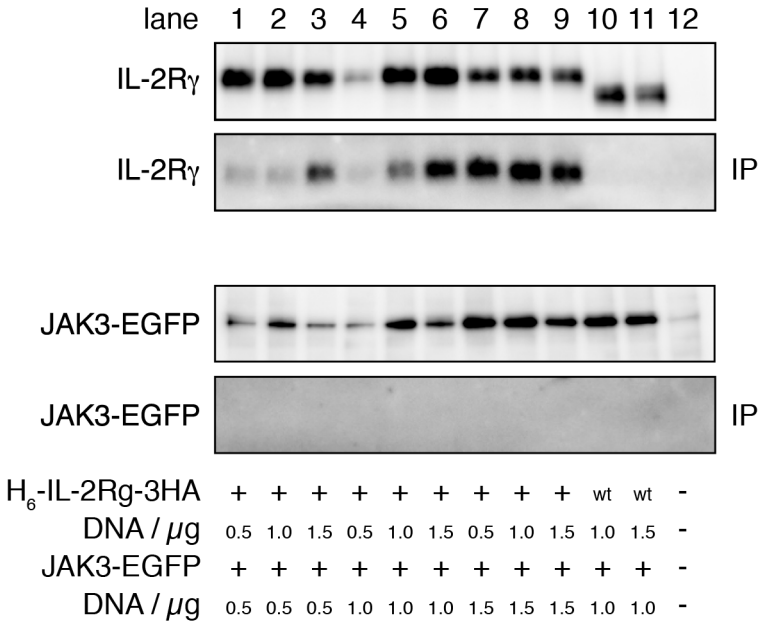

Figure 11.2.3: Immunoprecipitation and western blot analysis of H_6-IL-2Rγ-3HA. To establish an IP protocol, HEK293T cells were transfected with different DNA ratios of H_6-IL-2Rγ or H_6-IL-2Rγ-3HA and JAK3-EGFP. After the cell lysis and IP (3HA-affinity-tag) a WB analysis was made, which showed the protein expression of the H_6-IL-2Rγ-3HA constructs and JAK3-EGFP in all samples. The receptor signal after the IP was inhomogeneous and an increased signal was only measured in some samples. The wt receptor lacking the 3HA-tag was not increased and was located slightly beneath the other receptor bands due to its reduced size. An IP and WB analysis of JAK3-EGFP bound to the receptor was not possible with our IP protocol.

In the following step, an IP with the TAG receptor mutants was made in order to distinguish between the two H_6-IL-2Rγ-TAG-3HA populations. For this reason, HEK293T cells expressing the different mutants were analysed by WB as described earlier. Figure 11.2.4 shows the WB data with three different kinds of receptors: the full-length ECD mutants (green box, lanes 1 - 3), the full-length Box1 motif mutants (blue box, lanes 4 - 8) and the truncated Box1 motif mutants (red box, lanes 4 - 8) as well as two positive control lanes with the wt receptor (lanes 9 and 10). The truncated Box1 motif mutants showed a stepwise patterning on the membrane, which represents their different molecular sizes. However, it was not possible to increase the full-length receptor population with IP. Only

for the mutant E275Ab and the wt receptor samples an accumulation of the protein was detected (Figure 11.2.4, orange box, lanes 8 - 10). The strong band in all lanes of the IP data represents the heavy chain of a fragmented antibody, which was stained during the immunostaining process. The WB data are consistent with the microscopy data discussed before and confirm the expression of truncated receptor populations at the membrane of living cells. The data also showed that the IP assay was not efficient enough to accumulate full-length receptor. For this reason, we stopped the experiments with the H_6-IL-2Rγ-TAG-3HA and propose instead cross-linking experiments with JAK3 highly abundant in the cytoplasm and easier to handle in IP assays.

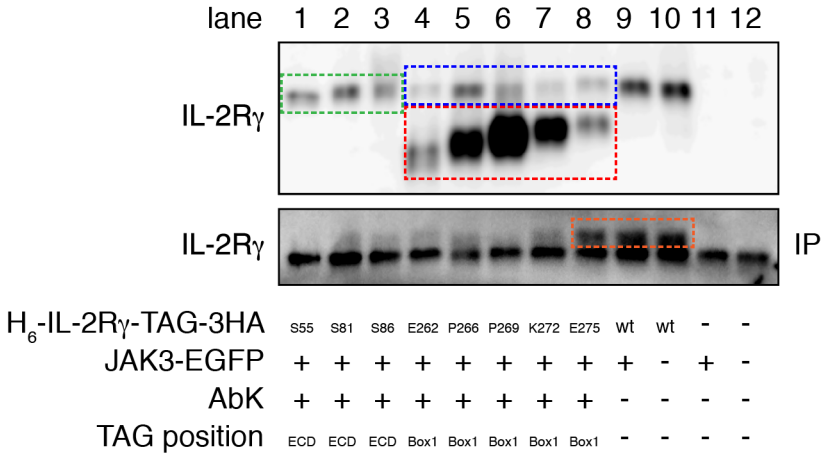

Figure 11.2.4: Immunoprecipitation and western blot analysis of H_6-IL-2Rγ-TAG-3HA mutants. Cells expressing the different receptor mutants and JAK3-EGFP were analysed by WB before and after IP. Three different receptor populations were detected: the full-length ECD (green box) and Box1 motif (blue box) mutants as well as the truncated Box1 motif mutants (red box). The WB analysis of the IP showed an increased protein concentration for E275Ab and the wt receptor. Furthermore, an unspecific signal in all samples was generated by a contamination of an antibody heavy chain fragment in the IP experiment.

IV Discussion and Outlook

The research of cell signalling pathways, especially their activation at the cell membrane, is difficult and time consuming. However, covalent fluorescent labelled receptors in combination with confocal microscopy are an excellent research tool to get a better understanding of such complicated cell pathways. To overcome the problem of site-specific covalent labelling, the previously reported method of GCE together with click chemistry was used and quantified in detail. For this purpose, we optimized the expression of the IL-4Rα by use of GCE and the uAA BCNK. To establish a convenient protocol for covalent labelling and to address various biological problems, the efficiency of the click reaction had to be analysed. For this reason, simple confocal imaging was combined with in solution FCS to convert the fluorescence intensities into particle numbers. First experiments of the labelling reaction between the strained alkyne of BCNK and the tetrazine-dye constructs exhibited a clearly reduced labelling efficiency with negligible background at the cell surfaces, which was analysed either by CRMI or by single cell FCCS. Moreover, the data confirmed that the labelling efficiency was depending both on the tetrazine-group used and the labelling concentration and time. The uAA BCNK displayed a major side reaction with thiol containing biomolecules. Titration experiments with IL-4-A647N confirmed that the quantification with the medium throughput method CRMI was reliable and, in addition, that the receptor population at the cell surface was accessible to fluorescent molecules. All IL-4Rα* mutants exhibited a reduced ligand occupancy, whereas labelling-sites in the ligand binding pocket (interaction effects) and near or on the activation loop (allosteric effects) were drastically decreased. In a three-colour experiment, the allosteric mutants (E141B and E189B) displayed a bimodal-shaped distribution for the ligand binding and the click labelling efficiency. In the following step, the click labelling efficiency of the occupied and non-occupied IL-4Rα* mutants was analysed. The click reaction showed a site-specific behaviour with different mean values for the click labelling efficiency, with a higher value for the D1-domain than the D2-domain. Moreover, a reduction of the efficiency in the occupied receptor state was detected for all mutants, except S44B and E189B, which represents a higher flexibility of these loops during ligand binding. The fluorescence

lifetime data of the ligand binding exhibited a domain rearrangement of the D1- and D2-domain around the linker region as well as a reorientation of the activation loop, which may trigger the JAK/STAT pathway activation. At last, the cell surface lifetime of IL-4Rα and its truncated version with and without EGFP-tag was measured. The data showed a short lifetime at the cell surface for the full-length receptor but a very long one for the truncated versions. Moreover, all receptor constructs measured were properly diffusing on the cell membrane. These results indicate that the signal for trafficking and the involved proteins bind between the full-length and truncated receptor tail. Nevertheless, the involved proteins and their positions at the receptor tail remain unclear.

In a further project, we analysed the location of the JAK/STAT pathway activation in experiments with the covalently modified IL-4-B ligand located in the Lo domains of a phase separated SLB. With a positively charged SLB, a ligand dependent recruitment of the IL-4Rα* and, in addition, the type 1 complex components, IL-2Rγ and JAK3-tRFP, were detected. However, the lifetime of the ligand SLB complex with NA was not stable enough for experiments with cell membrane specific JAK/STAT pathway activation.

Covalent cross-linking by photo-activatable AbK in combination with MS should be established to reveal important JAK/STAT pathway proteins responsible for trafficking and signalling. First, two important regions of the receptor tail were identified for their trafficking and endocytosis behaviour. IL-2Rγ tail truncation studies showed that the AA sequence between S286 - R306 (m35 and m45) was important for receptor JAK3 membrane localisation and CE formation, whereas the sequence between AA L261 - S286 (m5 - m25) was only important for JAK3 binding. Different IL-2Rγ ECD and Box1 motif mutants, modified with photo-activatable AbK and a C-terminal 3HA-tag, were expressed and were used to optimize an IP assay. The incorporation of AbK into the Box1 motif of the full-length receptor showed two receptor populations, a full-length and a truncated version. However, the IP of the receptor to concentrate the amount of protein and the simultaneous co-precipitation of the associated JAK3 have never been achieved.

12 Covalent click labelling of the IL-4Rα

In this thesis, the JAK/STAT pathway activation by the class I cytokine receptor IL-4Rα, with the help of covalent modifications of the pathway components, was analysed. One advantage of the covalent fluorescence modification is that spatiotemporal analysis of cell processes, without the risk of false signals, is possible. Labelling with fluorescent probes such as trisNTA-A647 or IL-4-A647N is usually done under equilibrium conditions to avoid dissociation. This approach often leads to problems, such as high background signal in cellular compartments and on the glass surface of the imaging slide or the restriction of the experimental setup. For example, receptor research with a fluorescently labelled ligand is limited to the occupied structure, which may influence the receptor behaviour and lead to incorrect results. Covalent click labelling reduces these background problems by a fast labelling step combined with several washing steps and, in addition, experiments with occupied and non-occupied receptors are possible. Moreover, long-term experiments, such as single particle tracking, to investigate receptor trafficking at the cell surface or their internalization pathways into the cell could be performed. The combination of GCE and click chemistry not only allows the site-specific labelling at various positions in the POI, it is also possible to use many different fluorescent labels or even other functionalities to address all kinds of scientific questions. Over the years, various studies showed in proof of principle experiments that protein labelling with click reactions yield acceptable fluorescence signals on the POI.[112, 113, 189] However, only few publications used a systematic approach to optimize and quantify the click labelling efficiency in live cell experiments. Most publications use WB assay to analyse the click reaction.[119, 124] One disadvantage of this method is that the results are not always compartment or protein specific, as the click labelling is often done in whole cell lysates and, for example, not exclusively at the cell membrane. Moreover, only fluorescence intensities are analysed by the WB method but particle numbers or concentrations are not. Another approach is the comparison of fluorescence microscopy data of the click reaction with another labelling technique, such as SNAP-tag or antibody labelling, which are not quantitative analysis methods either.[200, 201] A particle-based quantification method is the fluorescence fluctuation analysis, in which the sample is

imaged by a laser scanning unit and the intensity is correlated to result in a particle number per pixel. With this method, the fluorescent IEDDAC labelling of different GPCRs was analysed for its click labelling efficiency. Usage of the TCO* and tetrazine-fluorophore system led to various efficiencies and quantitative labelling of the clicked receptors was measured.[190] In our quantification method we used a two measurements approach, in which confocal imaging and in solution FCS were combined. The advantage of our method, compared to previously reported methods, is that the calibration is made in solubilized fluorophores and not in cells.[162, 163] Cell measurements are more prone to errors, time consuming and difficult to handle. Calibration in solution can be done within a couple of hours for three laser lines and, in addition, it offers a quality control for the microscope. Even in experiments performed over a longer period of time, at a confocal setup with lots of users or by use of different microscopes with various laser intensities, imaging results can be easily compared. Moreover, reference measurements with slow and time consuming FCCS showed similar results as CRMI. Titration experiments with the well-defined biological system of IL-4Rα* and IL-4-A647N also confirmed the superior performance of the CRMI method developed by our group.

Experiments with the GCE system showed an overall reduced expression level of all IL-4Rα* mutants. It is important for proper segmentation that the intracellular fluorescence signal, caused by receptors stuck in the expression machinery, is as low as possible, otherwise a false positive signal is segmented by the automated ImageJ plug-in. Therefore, we started our GCE expression experiments with the weaker expressing SV40 viral promoter. None of the tested mutants showed acceptable expression level, confirming that, for GCE, a strong promoter such as CMV is necessary. However, the system could not be improved for high expression levels but showed comparable protein levels similar to the IL-12Rα system expressed previously with the same system.[124] Moreover, the GCE system proved to be very selective for the site-specifically incorporated TAG stop codon, as labelling experiments with the GCE system but without a stop codon led to a neglectable background labelling. In studies published recently, the expression levels could either be increased by an optimized tRNA or by coupling of the tRNA synthetase to a nuclear export signal (NES), because the localization of the tRNA synthetase in the cytoplasm increases the expression level of

the POI.[202, 203] Another study optimized the expression levels by engineering the intracellular eukaryotic peptide chain release factor subunit 1 (eRF1), which is important to stop the translation at the three natural stop codons.[204] It is also crucial that the simple things like the cell line, the DNA ratio, the transfection reagent and the incubation time in uAA are optimized for the specific experimental setup, as it was done in our project.[186] In addition, the titration of the BCNK concentration showed that the levels of receptor expression can be regulated very easily. A similar concentration range was previously shown.[119, 186] This approach could be used to lower the expression levels in regions where single molecule methods operate. These methods are often limited because of too high expression levels when transient transfections are used. Furthermore, the different mutants, which were chosen depending on their position in the structure and their water surface accessibility, showed a huge variation in expression. Similar results for other proteins were also communicated by other groups leading to the conclusion that it is crucial to screen a mutant library for the expression levels at the beginning of a new labelling project.[189, 190]

Our first experiments of the click reaction showed that the charge of the fluorescent dye is important for the unspecific uptake and intracellular background of the tetrazine-dye construct. Since positively charged tetrazine-dye constructs were internalized in high quantity, only negatively charged fluorophore were used to label the IL-4Rα* ECD. Minor influences were detected for the tetrazine groups, which all showed a low internalization rate, with tet1 showing the lowest.[112, 135] On the other hand, the reactivity and hence the click labelling efficiency are strongly influenced by the tetrazine-groups. Click labelling efficiencies that were measured at the membrane of living cells followed the order of tet2, tet1 and tet3, representing the lowest efficiency and were in line with previous literature, too.[135, 205]

For the labelling reaction itself, the chosen tetrazine-dye concentration range was similar to results previously described in literature.[189, 190] Nevertheless, the concentration dependent click labelling efficiency as well as the kinetic of the labelling reaction at the membrane of living cells did not correspond with the results of in solution labelling with purified proteins.[112, 206] Our results showed a non-linear behaviour of the click labelling efficiency at increased tetrazine-dye concentrations. This may be caused by exclude

volume effects and electrostatic repulsion of the double negatively charged A568-tet1 or by the spatial orientation of the reactive groups at the cell surface. The kinetic data were interpreted as a two-step mechanism: first, a fast reaction taking place in the near surroundings of the cell surface and, second, a slow diffusion-controlled step leading two a flat slope. It may also be possible that a self-inhibition by the accumulation of tetrazine-dye conjugate at the cell surface interferes with the kinetic. The small increase of click labelling efficiency after temperature increase confirms the diffusion-controlled reaction model and showed that the whole receptor population on the membrane is accessible. Although the click labelling efficiency was reduced, the labelling reaction of the IL-4Rα* ECD was highly reproducible over more than one year.

Previous studies suggested showed that the strained triple bond can undergo an addition reaction with H_2O under acidic conditions.[207, 208] The formed ketone product is unreactive to the tetrazine-group. This small change in the reactive group of BCNK is probably not recognized by the BCNK-synthetase so that unreactive BCNK modified receptors are expressed at the surface of HEK293T cells. The EGFP signal of these unreactive receptors would lead to a reduced labelling efficiency. Nevertheless, this small unreactive receptor population itself could not explain the low labelling efficiency of the click system. Further addition reactions with thiol groups, in various oxidation forms, which interact with the strained triple bond of the BCNK molecule, were reported. For example, the glutathione cysteine, sulfenic acid or persulfides react with the BCN-group.[191, 192, 209] Moreover, the reactions between free thiol groups and the strained triple bond can spontaneously react or be catalysed under basic conditions.[210, 211] Similar reactions are also possible either in the cell growth media, which contains an undefined protein mixture when supplemented with FBS (contains glutathione), or BCNK reacts intracellularly alongside the secretory pathway with various proteins.[195] However, BCNK did not interact with the thiol groups of the incorporated cysteines of IL-4Rα*, which are located either in the D1-domain forming disulfide bridges or with a single cysteine near the ligand binding pocket, when supplemented within the growth medium. The missing interaction was proved by a titration experiment, with cells incubated with or without BCNK, which displayed the same signal behaviour.

13 IL-4Rα activation by its ligand IL-4

The BCNK modification leads to an overall reduction of the ligand binding. Especially in the binding pocket, the AA exchange to a BCNK leads to exactly the same results as the ones measured before *in vivo* by alanine screening and surface plasmon resonance spectroscopy.[73] However, with our approach of GCE in combination with CRMI *in vitro*, ligand binding could be analysed in order to measure kinetic data such as the K_d at the membrane surface of living cells. Moreover, proper ligand binding offers an effective and diagnostically conclusive result for proper receptor expression, localization and functionality. Therefore, an assay with easy handling for ligand binding studies would be a major advantage and would allow a fast screening of whole receptor mutant libraries. Receptor distributions of all mutants were measured under IL-4-A647N equilibrium conditions and resulted in a Gaussian-shaped normal distribution, whereas mutations in or near the activation loop were bimodally shaped. The bimodal distribution shape of the two mutants E141B and E189B changed during incubation at different concentration levels of ligand. This change seemed to be caused by the different affinities of the receptor populations. However, a differentiation between folded, partially folded and unfolded receptors is not possible by confocal microscopy. The bimodal distribution of the click labelling efficiency data gained from the three-colour experiment confirms the different receptor populations of the activation loop mutants, which are located at the cell membrane. Previously, a molecular switch was proposed for this region in the prolactin receptor.[182] Moreover, the increased structural flexibility of this loop highlights the potential transmission function between the ligand binding hotspot Y183 at the apex of the loop and the C-terminal transmembrane domain.[35] The L2–loop in the binding pocket of the receptor is another flexible region. This unpolar region shows a certain flexibility in all IL-4Rα crystal structures available. The flexibility of the loop as well as a backfolding of the BCNK head group in the hydrophobic core of the loop may lead to an increased click efficiency after ligand binding. The SPAAC reaction with a strained DBCO and an azide containing uAA also showed that the microenvironment of a protein is an important factor for proper reaction.[212] The comparison of the click labelling efficiency of the occupied and non-occupied IL-4Rα* displayed a common decrease of labelling for

the click reaction in the occupied structure. Therefore, a structural rearrangement of the receptor during ligand binding was proposed, which ended up in a more compact and stiffer ligand bound form. The reduced click efficiency in the D2-domain seems to be caused by the membrane proximity of the mutant positions. Previous literature indicates that the IEDDAC reaction rate is much faster in water than in unpolar solvents.[149] A similar reaction behaviour at the water-membrane interface, with a polar region at the top of the receptor and an unpolar region near the membrane, was suggested by our approach.[213] The click and CRMI approach allows structural insights in the dynamic properties of transmembrane receptor at the cell surface. To further test our system, receptor or protein constructs with known crystal structure and rearrangement behaviour should be tested or dynamic computer modelling should be performed. Further experiments with the viscosity sensor Cy3-tet2 confirmed a possible activation mechanism by a domain movement in the activation loop. Moreover, a huge lifetime variation in the linker region between the D1- and D2- domain during ligand binding was detected, which supports the model of a rearrangement process during ligand binding. Nevertheless, the kind and direction of the rearrangement could not be analysed with our experimental setup. However, it seems that the D2-domain stays perpendicular on the plasma membrane and that the D1-domain performs a search-like rotation mechanism. Similar rotation and scissor-like domain movements were already described before, but the analysis of such small structural variations remains difficult.[63, 64, 69] Even crystal structures of occupied and non-occupied receptors show only small variations. But crystal structures are only a short snapshot of the receptor dynamics in a solution environment and may not represent the receptor behaviour bound to the membrane of living cells.

Previous publications showed that the half-life of membrane proteins in eukaryotic cells range between a couple of minutes up to 100 h.[214, 215] In that broad time range, the endocytosis of cytokine receptors is located at the very beginning with half-lives between approximately 5 min to 24 h.[216-220] The IL-4R type 1 complex of IL-4Rα, IL-2Rγ and a radioactive ligand ^{125}I-IL-4 show a membrane surface half-life of about 5 - 10 min and a maximal plateau of approximately 20 min. The same half-life was also detected for the single IL-4Rα leading to the conclusion that the endocytosis process is independent of

IL-2Rγ.[221] Further experiments with the fluorescence tagged IL-4R type 1 components showed similar half-lives for the ligand independent internalization into CEs of about 8.5 min for IL-4Rα and 6.6 min for IL-2Rγ.[29] In experiments with our clicked full-length receptor we obtained slightly higher results with a receptor surface half-life of 40 min. The reduced internalization rate of the truncated receptor constructs supports our conclusion that the intracellular tail of the receptor controls the trafficking behaviour. Further kinetic studies could be performed with our approach. For example, the membrane half-life of the other IL-4R components or the recycling rate of the receptors, while using a quenchable system, could be determined. Previously, a similar labelling approach was used to analyse the protein turnover by the example of IL-12Rα.[124] In this earlier approach, a click labelling pulse was set and the whole cells were analysed by WB analysis, whereas in our approach, the specific position of the POI in the cell can be analysed by confocal microscopy.

14 JAK/STAT pathway activation from the membrane

Our experiments with phase separated SLBs proved to be very difficult because the membrane is very sensitive and quickly disrupts. Different buffer conditions and cell numbers were tested before the main experiments were performed. Moreover, a deformation of the membrane and the Lo domains, caused by the cells, was detected. Nevertheless, experiments with the phase separated SLB showed the localisation of the type 1 IL-4R complex in the ligand occupied Lo domain. However, overexpression of all the IL-4R components was necessary. To investigate the JAK/STAT pathway activation at a native receptor expression, starved HeLa cells transfected only with STAT6 as activation readout were incubated on a ligand presenting SLB. Control experiments showed that the complex of lipid, NA and IL-4-B was not stable for a longer period of time. For this reason, we switched to the previously reported streptavidin mutant TA.[198, 199] This mutant shows a longer half-life for the protein complex, but is only commercially available as a H_6-tag containing protein. As the H_6-tag interfered with our improved labelling protocol with the trisNTA-A647 fluorophore construct, the purification of a

tag-free variant was tried but was not successful. For this reason, we suggest to use click chemistry instead of trisNAT-A647 labelling to generate fluorescent protein label free receptor variants. Natural activation conditions with freely defusing transmembrane receptors and ligands are in general not possible to initiate with our system or with similar systems described before, which used covalent attachment of ligand and receptor constructs to the glass surface by Halo-tag binding. [58, 59] Therefore, the question whether JAK/STAT pathway activation can occur from the outer plasma membrane could not be answered and remains unclear. However, the approach of SLB bound ligand might be used to confirm the recruitment of downstream signalling components such as Rac1 and Pak1 or new factors might be discovered by co-localisation studies. Moreover, the quantification of the receptor system by calibrated imaging may help to understand the protein composition and ratios which are necessary for the JAK/STAT pathway activation at the surface of living cells.

We further investigated the pathway activation by screening different intracellular truncation mutants of IL-2Rγ to detect important regions for endocytosis. Different splicing forms and single AA polymorphism in the intracellular tail of the IL-2Rγ were previously reported and connected to (X)-SCID, confirming the importance of that region for receptor trafficking and signalling.[222] Although all receptors are expressed at the cell surface, a precise differentiation of important receptor regions is possible. The tail region between R306 and the C-terminal end has no influence at all on the receptor. AAs between S286 and R306 are important for CE formation whereas the region between the TMD and S286 is decisive for JAK3 binding. Similar truncation mutant experiments have already been done in our lab showing the same important tail regions for trafficking and JAK3 binding.[51] Rescue experiments with preformed CEs led to the trafficking of the truncated receptors into CEs. These results confirm that the formation of CEs and the trafficking into the CEs are differently regulated processes. One possible interaction candidate is the guanine-nucleotide-exchange factor (GEF) Vav2, which colocalises in CEs.[30] To identify further interaction partners, cross-linking with a photo-activatable uAA in combination with MS was planned. An IP assay was set up to concentrate the IL-2Rγ for MS. The purification of membrane proteins is known to be difficult, because the cell lysis and the separation of the protein from the membrane parts are hard to accomplish.

Most often, the receptors are lost during the centrifugation step in bigger membrane patches, which leads to a drastic reduction of the receptor concentration in the supernatant. In addition, hydrophobic parts of the protein are prone to stick to surfaces and, thus, also reduce the concentration. For this reason, different lysis buffers, supplemented with the detergents NP-40 or triton X-100, and incubation times were tested. However, a sufficient receptor concentration has never been achieved, although an IP was used to concentrate the receptor. Moreover, the receptor expression with GCE led to two receptor populations at the surface of living cells, a full-length receptor and a truncated one, which ended at the TAG stop codon. A similar expression is also possible for the ECD mutants, but the short polypeptides are degraded whereas receptor peptides with a TMD are already incorporated in the membrane and fast degradation is not possible anymore.

In conclusion, the covalent fluorescence labelling of the IL-4R system revealed not only a receptor rearrangement during ligand binding but the membrane half-lives of the occupied and non-occupied full-length receptors were also obtained. Moreover, the recruitment of the type 1 receptor complex at the membrane of living cells, by a SLB surface bound IL-4 ligand, was confirmed. Experiments with truncated IL-2Rγ exhibited receptor tail regions which are important for trafficking or JAK3 binding. These diverse results display the broad applicability and the convincing advantages of covalent protein modification.

V Bibliography

[1] C. Liongue, R. Sertori, A. C. Ward, *J Immunol* **2016**, *197*, 11-18.

[2] R. L. Kennedy, T. H. Jones, *J Endocrinol* **1991**, *129*, 167-178.

[3] M. D. Turner, B. Nedjai, T. Hurst, D. J. Pennington, *Bba-Mol Cell Res* **2014**, *1843*, 2563-2582.

[4] S. R. Holdsworth, P. Y. Gan, *Clin J Am Soc Nephro* **2015**, *10*, 2243-2254.

[5] D. Richter, I. Moraga, H. Winkelmann, O. Birkholz, S. Wilmes, M. Schulte, M. Kraich, H. Kenneweg, O. Beutel, P. Selenschik, D. Paterok, M. Gavutis, T. Schmidt, K. C. Garcia, T. D. Muller, J. Piehler, *Nature communications* **2017**, *8*, 15976.

[6] R. Morris, N. J. Kershaw, J. J. Babon, *Protein Sci* **2018**, *27*, 1984-2009.

[7] C. A. Dinarello, *European Journal of Immunology* **2007**, *37*, S34-S45.

[8] K. Skogstrand, C. K. Ekelund, P. Thorsen, I. Vogel, B. Jacobsson, B. Norgaard-Pedersen, D. M. Hougaard, *J Immunol Methods* **2008**, *336*, 78-84.

[9] J. J. Babon, I. S. Lucet, J. M. Murphy, N. A. Nicola, L. N. Varghese, *Biochem J* **2014**, *462*, 1-13.

[10] C. P. Lim, X. Cao, *Mol Biosyst* **2006**, *2*, 536-550.

[11] E. N. Gurzov, W. J. Stanley, E. G. Pappas, H. E. Thomas, D. J. Gough, *FEBS J* **2016**, *283*, 3002-3015.

[12] S. Bose, S. Banerjee, A. Mondal, U. Chakraborty, J. Pumarol, C. R. Croley, A. Bishayee, *Cells-Basel* **2020**, *9*.

[13] M. Murakami, M. Narazaki, M. Hibi, H. Yawata, K. Yasukawa, M. Hamaguchi, T. Taga, T. Kishimoto, *Proceedings of the National Academy of Sciences of the United States of America* **1991**, *88*, 11349-11353.

[14] J. S. Greiser, C. Stross, P. C. Heinrich, I. Behrmann, H. M. Hermanns, *The Journal of biological chemistry* **2002**, *277*, 26959-26965.

[15] R. Ferrao, H. J. Wallweber, H. Ho, C. Tam, Y. Franke, J. Quinn, P. J. Lupardus, *Structure* **2016**, *24*, 897-905.

[16] T. Matsuda, J. Feng, B. A. Witthuhn, Y. Sekine, J. N. Ihle, *Biochem Biophys Res Commun* **2004**, *325*, 586-594.

[17] J. Feng, B. A. Witthuhn, T. Matsuda, F. Kohlhuber, I. M. Kerr, J. N. Ihle, *Mol Cell Biol* **1997**, *17*, 2497-2501.

[18] P. Saharinen, K. Takaluoma, O. Silvennoinen, *Mol Cell Biol* **2000**, *20*, 3387-3395.

[19] P. Saharinen, O. Silvennoinen, *Journal of Biological Chemistry* **2002**, *277*, 47954-47963.

[20] D. Ungureanu, J. H. Wu, T. Pekkala, Y. Niranjan, C. Young, O. N. Jensen, C. F. Xu, T. A. Neubert, R. C. Skoda, S. R. Hubbard, O. Silvennoinen, *Nat Struct Mol Biol* **2011**, *18*, 971-U921.

[21] A. V. Toms, A. Deshpande, R. McNally, Y. Jeong, J. M. Rogers, C. U. Kim, S. M. Gruner, S. B. Ficarro, J. A. Marto, M. Sattler, J. D. Griffin, M. J. Eck, *Nat Struct Mol Biol* **2013**, *20*, 1221-+.

[22] J. Braunstein, S. Brutsaert, R. Olson, C. Schindler, *The Journal of biological chemistry* **2003**, *278*, 34133-34140.

[23] S. Rengachari, S. Groiss, J. M. Devos, E. Caron, N. Grandvaux, D. Panne, *Proceedings of the National Academy of Sciences of the United States of America* **2018**, *115*, E601-E609.

[24] G. M. Delgoffe, D. A. Vignali, *JAKSTAT* **2013**, *2*, e23060.

[25] K. Kurgonaite, unv. Diss. thesis, TU Dresden (Dresden), **2013**.

[26] T. D. Mueller, J. L. Zhang, W. Sebald, A. Duschl, *Biochim Biophys Acta* **2002**, *1592*, 237-250.

[27] R. D. May, M. Fung, *Cytokine* **2015**, *75*, 89-116.

[28] T. Weidemann, R. Worch, K. Kurgonaite, M. Hintersteiner, C. Bokel, P. Schwille, *Biophysical journal* **2011**, *101*, 2360-2369.

[29] H. Gandhi, R. Worch, K. Kurgonaite, M. Hintersteiner, P. Schwille, C. Bokel, T. Weidemann, *Biophysical journal* **2014**, *107*, 2515-2527.

[30] K. Kurgonaite, H. Gandhi, T. Kurth, S. Pautot, P. Schwille, T. Weidemann, C. Bokel, *Journal of cell science* **2015**, *128*, 3781-3795.

[31] J. F. Bazan, *Immunol Today* **1990**, *11*, 350-354.

[32] K. Nelms, A. D. Keegan, J. Zamorano, J. J. Ryan, W. E. Paul, *Annu Rev Immunol* **1999**, *17*, 701-738.

[33] J. F. Bazan, *Proceedings of the National Academy of Sciences of the United States of America* **1990**, *87*, 6934-6938.

[34] J. B. Spangler, I. Moraga, J. L. Mendoza, K. C. Garcia, *Annual Review of Immunology Vol 33* **2015**, *33*, 139-+.

[35] T. Weidemann, S. Hofinger, K. Muller, M. Auer, *J Mol Biol* **2007**, *366*, 1365-1373.

[36] X. Wang, P. Lupardus, S. L. Laporte, K. C. Garcia, *Annu Rev Immunol* **2009**, *27*, 29-60.

[37] T. Hage, W. Sebald, P. Reinemer, *Cell* **1999**, *97*, 271-281.

[38] C. A. McElroy, J. A. Dohm, S. T. Walsh, *Structure* **2009**, *17*, 54-65.

[39] C. A. McElroy, P. J. Holland, P. Zhao, J. M. Lim, L. Wells, E. Eisenstein, S. T. Walsh, *Proceedings of the National Academy of Sciences of the United States of America* **2012**, *109*, 2503-2508.

[40] A. Yoshimura, T. Zimmers, D. Neumann, G. Longmore, Y. Yoshimura, H. F. Lodish, *The Journal of biological chemistry* **1992**, *267*, 11619-11625.

[41] D. J. Hilton, S. S. Watowich, L. Katz, H. F. Lodish, *The Journal of biological chemistry* **1996**, *271*, 4699-4708.

[42] M. Rozakis-Adcock, P. A. Kelly, *The Journal of biological chemistry* **1991**, *266*, 16472-16477.

[43] M. J. van den Eijnden, L. L. Lahaye, G. J. Strous, *Journal of cell science* **2006**, *119*, 3078-3086.

[44] A. E. Kelly-Welch, E. M. Hanson, M. R. Boothby, A. D. Keegan, *Science* **2003**, *300*, 1527-1528.

[45] A. Kelly-Welch, E. M. Hanson, A. D. Keegan, *Sci STKE* **2005**, *2005*, cm9.

[46] M. Chen, A. Cheng, Y. Q. Chen, A. Hymel, E. P. Hanson, L. Kimmel, Y. Minami, T. Taniguchi, P. S. Changelian, J. J. OShea, *Proceedings of the National Academy of Sciences of the United States of America* **1997**, *94*, 6910-6915.

[47] M. Kawamura, D. W. McVicar, J. A. Johnston, T. B. Blake, Y. Q. Chen, B. K. Lal, A. R. Lloyd, D. J. Kelvin, J. E. Staples, J. R. Ortaldo, et al., *Proceedings of the National Academy of Sciences of the United States of America* **1994**, *91*, 6374-6378.

[48] S. L. LaPorte, Z. S. Juo, J. Vaclavikova, L. A. Colf, X. Qi, N. M. Heller, A. D. Keegan, K. C. Garcia, *Cell* **2008**, *132*, 259-272.

[49] J. L. Boulay, J. J. O'Shea, W. E. Paul, *Immunity* **2003**, *19*, 159-163.

[50] M. Akaiwa, B. Yu, R. Umeshita-Suyama, N. Terada, H. Suto, T. Koga, K. Arima, S. Matsushita, H. Saito, H. Ogawa, M. Furue, N. Hamasaki, K. Ohshima, K. Izuhara, *Cytokine* **2001**, *13*, 75-84.

[51] H. Gandhi, unv. Diss. thesis, TU Dresden (Dresden), **2014**.

[52] J. Piehler, C. Thomas, K. C. Garcia, G. Schreiber, *Immunol Rev* **2012**, *250*, 317-334.

[53] C. Gorby, J. Martinez-Fabregas, S. Wilmes, I. Moraga, *Front Immunol* **2018**, *9*, 2143.

[54] S. Elliott, T. Lorenzini, D. Yanagihara, D. Chang, G. Elliott, *The Journal of biological chemistry* **1996**, *271*, 24691-24697.

[55] S. Wilmes, O. Beutel, Z. Li, V. Francois-Newton, C. P. Richter, D. Janning, C. Kroll, P. Hanhart, K. Hotte, C. J. You, G. Uze, S. Pellegrini, J. Piehler, *Journal of Cell Biology* **2015**, *209*, 579-593.

[56] C. You, T. T. Marquez-Lago, C. P. Richter, S. Wilmes, I. Moraga, K. C. Garcia, A. Leier, J. Piehler, *Sci Adv* **2016**, *2*, e1600452.

[57] A. R. Kim, J. C. Ulirsch, S. Wilmes, E. Unal, I. Moraga, M. Karakukcu, D. Yuan, S. Kazerounian, N. J. Abdulhay, D. S. King, N. Gupta, S. B. Gabriel, E. S. Lander, T. Patiroglu, A. Ozcan, M. A. Ozdemir, K. C. Garcia, J. Piehler, H. T. Gazda, D. E. Klein, V. G. Sankaran, *Cell* **2017**, *168*, 1053-+.

[58] S. Lochte, S. Waichman, O. Beutel, C. You, J. Piehler, *J Cell Biol* **2014**, *207*, 407-418.

[59] T. Wedeking, S. Lochte, O. Birkholz, A. Wallenstein, J. Trahe, J. Klingauf, J. Piehler, C. You, *Small* **2015**, *11*, 5912-5918.

[60] J. Gent, P. van Kerkhof, M. Roza, G. Bu, G. J. Strous, *Proceedings of the National Academy of Sciences of the United States of America* **2002**, *99*, 9858-9863.

[61] R. J. Brown, J. J. Adams, R. A. Pelekanos, Y. Wan, W. J. McKinstry, K. Palethorpe, R. M. Seeber, T. A. Monks, K. A. Eidne, M. W. Parker, M. J. Waters, *Nat Struct Mol Biol* **2005**, *12*, 814-821.

[62] A. J. Brooks, W. Dai, M. L. O'Mara, D. Abankwa, Y. Chhabra, R. A. Pelekanos, O. Gardon, K. A. Tunny, K. M. Blucher, C. J. Morton, M. W. Parker, E. Sierecki, Y. Gambin, G. A. Gomez, K. Alexandrov, I. A. Wilson, M. Doxastakis, A. E. Mark, M. J. Waters, *Science* **2014**, *344*, 1249783.

[63] O. Livnah, E. A. Stura, S. A. Middleton, D. L. Johnson, L. K. Jolliffe, I. A. Wilson, *Science* **1999**, *283*, 987-990.

[64] I. Remy, I. A. Wilson, S. W. Michnick, *Science* **1999**, *283*, 990-993.

[65] S. N. Constantinescu, L. J. S. Huang, H. S. Nam, H. F. Lodish, *Mol Cell* **2001**, *7*, 377-385.

[66] S. N. Constantinescu, T. Keren, M. Socolovsky, H. Nam, Y. I. Henis, H. F. Lodish, *Proceedings of the National Academy of Sciences of the United States of America* **2001**, *98*, 4379-4384.

[67] J. Staerk, J. P. Defour, C. Pecquet, E. Leroy, H. Antoine-Poirel, I. Brett, M. Itaya, S. O. Smith, W. Vainchenker, S. N. Constantinescu, *Embo J* **2011**, *30*, 4398-4413.

[68] E. E. Matthews, D. Thevenin, J. M. Rogers, L. Gotow, P. D. Lira, L. A. Reiter, W. H. Brissette, D. M. Engelman, *FASEB J* **2011**, *25*, 2234-2244.

[69] A. H. Pillet, V. Lavergne, V. Pasquier, F. Gesbert, J. Theze, T. Rose, *J Mol Biol* **2010**, *403*, 671-692.

[70] S. Tenhumberg, B. Schuster, L. Zhu, M. Kovaleva, J. Scheller, K. J. Kallen, S. Rose-John, *Biochem Biophys Res Commun* **2006**, *346*, 649-657.

[71] C. D. Krause, G. Digioia, L. S. Izotova, J. Xie, Y. Kim, B. J. Schwartz, O. V. Mirochnitchenko, S. Pestka, *Cytokine* **2013**, *64*, 286-297.

[72] J. J. Strunk, I. Gregor, Y. Becker, Z. Li, M. Gavutis, E. Jaks, P. Lamken, T. Walz, J. Enderlein, J. Piehler, *J Mol Biol* **2008**, *377*, 725-739.

[73] J. L. Zhang, I. Simeonowa, Y. Wang, W. Sebald, *J Mol Biol* **2002**, *315*, 399-407.

[74] C. Lamaze, A. Dujeancourt, T. Baba, C. G. Lo, A. Benmerah, A. Dautry-Varsat, *Mol Cell* **2001**, *7*, 661-671.

[75] G. J. Doherty, H. T. McMahon, *Annual review of biochemistry* **2009**, *78*, 857-902.

[76] M. Zerial, H. McBride, *Nature reviews. Molecular cell biology* **2001**, *2*, 107-117.

[77] H. W. Platta, H. Stenmark, *Curr Opin Cell Biol* **2011**, *23*, 393-403.

[78] P. H. Chen, H. Yao, L. J. Huang, *Front Endocrinol (Lausanne)* **2017**, *8*, 78.

[79] J. Cendrowski, A. Maminska, M. Miaczynska, *Cytokine Growth Factor Rev* **2016**, *32*, 63-73.

[80] H. T. McMahon, E. Boucrot, *Nature reviews. Molecular cell biology* **2011**, *12*, 517-533.

[81] T. Kirchhausen, D. Owen, S. C. Harrison, *Cold Spring Harb Perspect Biol* **2014**, *6*, a016725.

[82] S. Sigismund, T. Woelk, C. Puri, E. Maspero, C. Tacchetti, P. Transidico, P. P. Di Fiore, S. Polo, *Proceedings of the National Academy of Sciences of the United States of America* **2005**, *102*, 2760-2765.

[83] I. R. Nabi, P. U. Le, *J Cell Biol* **2003**, *161*, 673-677.

[84] M. T. Howes, M. Kirkham, J. Riches, K. Cortese, P. J. Walser, F. Simpson, M. M. Hill, A. Jones, R. Lundmark, M. R. Lindsay, D. J. Hernandez-Deviez, G. Hadzic, A. McCluskey, R. Bashir, L. Liu, P. Pilch, H. McMahon, P. J. Robinson, J. F. Hancock, S. Mayor, R. G. Parton, *J Cell Biol* **2010**, *190*, 675-691.

[85] S. Mayor, R. G. Parton, J. G. Donaldson, *Cold Spring Harb Perspect Biol* **2014**, *6*.

[86] A. P. A. Ferreira, E. Boucrot, *Trends Cell Biol* **2018**, *28*, 188-200.

[87] X. R. Bustelo, V. Sauzeau, I. M. Berenjeno, *Bioessays* **2007**, *29*, 356-370.

[88] C. Lamaze, T. H. Chuang, L. J. Terlecky, G. M. Bokoch, S. L. Schmid, *Nature* **1996**, *382*, 177-179.

[89] S. T. Sit, E. Manser, *Journal of cell science* **2011**, *124*, 679-683.

[90] L. Johannes, S. Mayor, *Cell* **2010**, *142*, 507-510.

[91] A. Subtil, A. Hemar, A. Dautryvarsat, *Journal of cell science* **1994**, *107*, 3461-3468.

[92] N. Sauvonnet, A. Dujeancourt, A. Dautry-Varsat, *J Cell Biol* **2005**, *168*, 155-163.

[93] A. Grassart, A. Dujeancourt, P. B. Lazarow, A. Dautry-Varsat, N. Sauvonnet, *EMBO Rep* **2008**, *9*, 356-362.

[94] A. Grassart, V. Meas-Yedid, A. Dufour, J. C. Olivo-Marin, A. Dautry-Varsat, N. Sauvonnet, *Traffic* **2010**, *11*, 1079-1091.

[95] C. Basquin, N. Sauvonnet, *Commun Integr Biol* **2013**, *6*, e24243.

[96] C. Bokel, M. Brand, *Cold Spring Harb Perspect Biol* **2014**, *6*.

[97] E. Morelon, A. Dautry-Varsat, *Journal of Biological Chemistry* **1998**, *273*, 22044-22051.

[98] S. R. Hofmann, A. Q. Lam, S. Frank, Y. J. Zhou, H. L. Ramos, Y. Kanno, D. Agnello, R. J. Youle, J. J. O'Shea, *Mol Cell Biol* **2004**, *24*, 5039-5049.

[99] L. S. Park, D. Friend, H. M. Sassenfeld, D. L. Urdal, *The Journal of experimental medicine* **1987**, *166*, 476-488.

[100] C. Basquin, M. Trichet, H. Vihinen, V. Malarde, T. Lagache, L. Ripoll, E. Jokitalo, J. C. Olivo-Marin, A. Gautreau, N. Sauvonnet, *Embo J* **2015**, *34*, 2147-2161.

[101] R. Y. Tsien, *Annual review of biochemistry* **1998**, *67*, 509-544.

[102] S. J. Remington, *Protein Sci* **2011**, *20*, 1509-1519.

[103] P. Dedecker, F. C. De Schryver, J. Hofkens, *Journal of the American Chemical Society* **2013**, *135*, 2387-2402.

[104] T. Kanda, K. F. Sullivan, G. M. Wahl, *Curr Biol* **1998**, *8*, 377-385.

[105] A. Bialkowska, X. Y. Zhang, J. Reiser, *BMC Genomics* **2005**, *6*, 113.

[106] C. D. Spicer, B. G. Davis, *Nature communications* **2014**, *5*, 4740.

[107] O. Boutureira, G. J. Bernardes, *Chemical reviews* **2015**, *115*, 2174-2195.

[108] Y. Tian, Q. Lin, *ACS Chem Biol* **2019**, *14*, 2489-2496.

[109] J. M. Tharp, A. Ehnbom, W. R. Liu, *RNA Biol* **2018**, *15*, 441-452.

[110] C. J. Noren, S. J. Anthony-Cahill, M. C. Griffith, P. G. Schultz, *Science* **1989**, *244*, 182-188.

[111] J. W. Chin, T. A. Cropp, J. C. Anderson, M. Mukherji, Z. Zhang, P. G. Schultz, *Science* **2003**, *301*, 964-967.

[112] K. Lang, L. Davis, S. Wallace, M. Mahesh, D. J. Cox, M. L. Blackman, J. M. Fox, J. W. Chin, *Journal of the American Chemical Society* **2012**, *134*, 10317-10320.

[113] C. Uttamapinant, J. D. Howe, K. Lang, V. Beranek, L. Davis, M. Mahesh, N. P. Barry, J. W. Chin, *Journal of the American Chemical Society* **2015**, *137*, 4602-4605.

[114] K. L. Kiick, E. Saxon, D. A. Tirrell, C. R. Bertozzi, *Proceedings of the National Academy of Sciences of the United States of America* **2002**, *99*, 19-24.

[115] A. J. Link, M. K. S. Vink, D. A. Tirrell, *Nat Protoc* **2007**, *2*, 1879-1883.

[116] K. E. Beatty, J. D. Fisk, B. P. Smart, Y. Y. Lu, J. Szychowski, M. J. Hangauer, J. M. Baskin, C. R. Bertozzi, D. A. Tirrell, *Chembiochem : a European journal of chemical biology* **2010**, *11*, 2092-2095.

[117] Z. Yu, Y. Pan, Z. Wang, J. Wang, Q. Lin, *Angewandte Chemie* **2012**, *51*, 10600-10604.

[118] C. P. Ramil, Q. Lin, *Current opinion in chemical biology* **2014**, *21*, 89-95.

[119] T. Peng, H. C. Hang, *Journal of the American Chemical Society* **2016**, *138*, 14423-14433.

[120] Y. Ge, X. Fan, P. R. Chen, *Chem Sci* **2016**, *7*, 7055-7060.

[121] T. Plass, S. Milles, C. Koehler, C. Schultz, E. A. Lemke, *Angewandte Chemie* **2011**, *50*, 3878-3881.

[122] T. Plass, S. Milles, C. Koehler, J. Szymanski, R. Mueller, M. Wiessler, C. Schultz, E. A. Lemke, *Angewandte Chemie* **2012**, *51*, 4166-4170.

[123] S. H. Alamudi, R. Satapathy, J. Kim, D. Su, H. Ren, R. Das, L. Hu, E. Alvarado-Martinez, J. Y. Lee, C. Hoppmann, E. Pena-Cabrera, H. H. Ha, H. S. Park, L. Wang, Y. T. Chang, *Nature communications* **2016**, *7*, 11964.

[124] Y. G. Mideksa, M. Fottner, S. Braus, C. A. M. Weiss, T. A. Nguyen, S. Meier, K. Lang, M. J. Feige, *Chembiochem : a European journal of chemical biology* **2020**.

[125] T. S. Elliott, A. Bianco, J. W. Chin, *Current opinion in chemical biology* **2014**, *21*, 154-160.

[126] T. S. Elliott, F. M. Townsley, A. Bianco, R. J. Ernst, A. Sachdeva, S. J. Elsasser, L. Davis, K. Lang, R. Pisa, S. Greiss, K. S. Lilley, J. W. Chin, *Nature Biotechnology* **2014**, *32*, 465-U186.

[127] S. Mayer, K. Lang, *Synthesis-Stuttgart* **2017**, *49*, 830-848.

[128] K. J. Lee, D. Kang, H. S. Park, *Mol Cells* **2019**, *42*, 386-396.

[129] K. Lang, J. W. Chin, *Chemical reviews* **2014**, *114*, 4764-4806.

[130] H. C. Hang, C. Yu, D. L. Kato, C. R. Bertozzi, *Proceedings of the National Academy of Sciences of the United States of America* **2003**, *100*, 14846-14851.

[131] J. C. Maza, J. R. McKenna, B. K. Raliski, M. T. Freedman, D. D. Young, *Bioconjugate chemistry* **2015**, *26*, 1884-1889.

[132] Y. Wu, H. Zhu, B. Zhang, F. Liu, J. Chen, Y. Wang, Y. Wang, Z. Zhang, L. Wu, L. Si, H. Xu, T. Yao, S. Xiao, Q. Xia, L. Zhang, Z. Yang, D. Zhou, *Bioconjugate chemistry* **2016**, *27*, 2460-2468.

[133] A. C. Knall, C. Slugovc, *Chemical Society reviews* **2013**, *42*, 5131-5142.

[134] E. Kozma, O. Demeter, P. Kele, *Chembiochem : a European journal of chemical biology* **2017**, *18*, 486-501.

[135] B. L. Oliveira, Z. Guo, G. J. L. Bernardes, *Chemical Society reviews* **2017**, *46*, 4895-4950.

[136] H. Wu, N. K. Devaraj, *Top Curr Chem (Cham)* **2016**, *374*, 3.

[137] Kenry, B. Liu, *Trends Chem* **2019**, *1*, 763-778.

[138] A. Darko, S. Wallace, O. Dmitrenko, M. M. Machovina, R. A. Mehl, J. W. Chin, J. M. Fox, *Chem Sci* **2014**, *5*, 3770-3776.

[139] R. A. A. Foster, M. C. Willis, *Chemical Society reviews* **2013**, *42*, 63-76.

[140] J. Sauer, R. Sustmann, *Angewandte Chemie-International Edition in English* **1980**, *19*, 779-807.

[141] G. B. Cserep, O. Demeter, E. Batzner, M. Kallay, H. A. Wagenknecht, P. Kele, *Synthesis-Stuttgart* **2015**, *47*, 2738-2744.

[142] J. Sauer, D. K. Heldmann, J. Hetzenegger, J. Krauthan, H. Sichert, J. Schuster, *Eur J Org Chem* **1998**, *1998*, 2885-2896.

[143] D. R. Soenen, J. M. Zimpleman, D. L. Boger, *Journal of Organic Chemistry* **2003**, *68*, 3593-3598.

[144] F. Thalhammer, U. Wallfahrer, J. Sauer, *Tetrahedron Lett* **1990**, *31*, 6851-6854.

[145] F. Liu, Y. Liang, K. N. Houk, *Journal of the American Chemical Society* **2014**, *136*, 11483-11493.

[146] F. Liu, R. S. Paton, S. Kim, Y. Liang, K. N. Houk, *Journal of the American Chemical Society* **2013**, *135*, 15642-15649.

[147] W. Blokzijl, M. J. Blandamer, J. B. F. N. Engberts, *Journal of the American Chemical Society* **1991**, *113*, 4241-4246.

[148] J. F. Blake, D. Lim, W. L. Jorgensen, *Journal of Organic Chemistry* **1994**, *59*, 803-805.

[149] J. W. Wijnen, S. Zavarise, J. B. F. N. Engberts, M. Charton, *Journal of Organic Chemistry* **1996**, *61*, 2001-2005.

[150] A. Meijer, S. Otto, J. B. F. N. Engberts, *Journal of Organic Chemistry* **1998**, *63*, 8989-8994.

[151] M. R. Karver, R. Weissleder, S. A. Hilderbrand, *Bioconjugate chemistry* **2011**, *22*, 2263-2270.

[152] N. K. Devaraj, R. Weissleder, *Accounts of chemical research* **2011**, *44*, 816-827.

[153] H. Wu, N. K. Devaraj, *Accounts of chemical research* **2018**, *51*, 1249-1259.

[154] J. R. Lakowicz, *Principles of fluorescence spectroscopy*, 3rd ed., Springer, New York, **2006**.

[155] P. P. Mondal, A. Diaspro, *Fundamentals of fluorescence microscopy exploring life with light*, Springer Netherlands, Dordrecht, **2014**.

[156] H. P. Latscha, U. Kazmaier, H. A. Klein, *Photochemie. In: Organische Chemie*, Springer-Lehrbuch. Springer Spektrum, Berlin, Heidelberg, **2016**.

[157] J. Krieger, Practical Course Biophysics: Fluorescence Correlation Spectroscopy, **2013**.

[158] R. L. Price, W. G. Jerome, *Basic confocal microscopy*, Springer Science+Business Media, New York, **2011**.

[159] T. Weidemann, P. Schwille, *Methods in enzymology* **2013**, *518*, 43-70.

[160] T. Weidemann, P. Schwille, in *Handbook of Single-Molecule Biophysics* (Eds.: P. Hinterdorfer, A. E Oijen), Springer US, New York, NY, **2009**.

[161] K. Bacia, E. Haustein, P. Schwille, *Cold Spring Harb Protoc* **2014**, *2014*, 709-725.

[162] T. Weidemann, M. Wachsmuth, T. A. Knoch, G. Muller, W. Waldeck, J. Langowski, *J Mol Biol* **2003**, *334*, 229-240.

[163] A. Z. Politi, Y. Cai, N. Walther, M. J. Hossain, B. Koch, M. Wachsmuth, J. Ellenberg, *Nat Protoc* **2018**, *13*, 1445-1464.

[164] E. Haustein, P. Schwille, *Annu Rev Biophys Biomol Struct* **2007**, *36*, 151-169.

[165] T. Weidemann, J. Mucksch, P. Schwille, *Curr Opin Struct Biol* **2014**, *28*, 69-76.

[166] J. Widengren, U. Mets, R. Rigler, *J Phys Chem-Us* **1995**, *99*, 13368-13379.

[167] T. Kohl, P. Schwille, *Adv Biochem Eng Biotechnol* **2005**, *95*, 107-142.

[168] Y. Sun, A. Periasamy, *Methods Mol Biol* **2015**, *1251*, 83-107.

[169] R. Hartig, Y. Prokazov, E. Turbin, W. Zuschratter, *Methods Mol Biol* **2014**, *1076*, 457-480.

[170] Y. Tanaka, M. R. Bond, J. J. Kohler, *Mol Biosyst* **2008**, *4*, 473-480.

[171] T. A. Nguyen, M. Cigler, K. Lang, *Angewandte Chemie* **2018**, *57*, 14350-14361.

[172] I. Coin, *Current opinion in chemical biology* **2018**, *46*, 156-163.

[173] H. W. Ai, W. J. Shen, A. Sagi, P. R. Chen, P. G. Schultz, *Chembiochem : a European journal of chemical biology* **2011**, *12*, 1854-1857.

[174] J. Das, *Chemical reviews* **2011**, *111*, 4405-4417.

[175] R. Worch, C. Bokel, S. Hofinger, P. Schwille, T. Weidemann, *Proteomics* **2010**, *10*, 4196-4208.

[176] E. P. Petrov, T. Ohrt, R. G. Winkler, P. Schwille, *Phys Rev Lett* **2006**, *97*, 258101.

[177] C. B. Muller, A. Loman, V. Pacheco, F. Koberling, D. Willbold, W. Richtering, J. Enderlein, *Epl-Europhys Lett* **2008**, *83*.

[178] P. O. Gendron, F. Avaltroni, K. J. Wilkinson, *J Fluoresc* **2008**, *18*, 1093-1101.

[179] M. Szabelski, D. Ilijev, P. Sarkar, R. Luchowski, Z. Gryczynski, P. Kapusta, R. Erdmann, I. Gryczynski, *Appl Spectrosc* **2009**, *63*, 363-368.

[180] M. Kraich, M. Klein, E. Patino, H. Harrer, J. Nickel, W. Sebald, T. D. Mueller, *BMC Biol* **2006**, *4*, 13.

[181] S. Lata, A. Reichel, R. Brock, R. Tampe, J. Piehler, *Journal of the American Chemical Society* **2005**, *127*, 10205-10215.

[182] R. Dagil, M. J. Knudsen, J. G. Olsen, C. O'Shea, M. Franzmann, V. Goffin, K. Teilum, J. Breinholt, B. B. Kragelund, *Structure* **2012**, *20*, 270-282.

[183] D. J. Hilton, S. S. Watowich, P. J. Murray, H. F. Lodish, *Proceedings of the National Academy of Sciences of the United States of America* **1995**, *92*, 190-194.

[184] A. Belfiore, D. LeRoith, *Principles of Endocrinology and Hormone Action*.

[185] V. Duppatla, M. Gjorgjevikj, W. Schmitz, M. Kottmair, T. D. Mueller, W. Sebald, *Bioconjugate chemistry* **2012**, *23*, 1396-1405.

[186] L. Jakob, A. Gust, D. Grohmann, *Biochem Biophys Rep* **2019**, *17*, 1-9.

[187] E. Kozma, I. Nikic, B. R. Varga, I. V. Aramburu, J. H. Kang, O. T. Fackler, E. A. Lemke, P. Kele, *Chembiochem : a European journal of chemical biology* **2016**, *17*, 1518-1524.

[188] G. Beliu, A. J. Kurz, A. C. Kuhlemann, L. Behringer-Pliess, M. Meub, N. Wolf, J. Seibel, Z. D. Shi, M. Schnermann, J. B. Grimm, L. D. Lavis, S. Doose, M. Sauer, *Commun Biol* **2019**, *2*, 261.

[189] F. Neubert, G. Beliu, U. Terpitz, C. Werner, C. Geis, M. Sauer, S. Doose, *Angewandte Chemie* **2018**, *57*, 16364-16369.

[190] R. Serfling, L. Seidel, A. Bock, M. J. Lohse, P. Annibale, I. Coin, *ACS Chem Biol* **2019**, *14*, 1141-1149.

[191] R. van Geel, G. J. Pruijn, F. L. van Delft, W. C. Boelens, *Bioconjugate chemistry* **2012**, *23*, 392-398.

[192] E. Galardon, D. Padovani, *Bioconjugate chemistry* **2015**, *26*, 1013-1016.

[193] D. J. McGarry, M. M. Shchepinova, S. Lilla, R. C. Hartley, M. F. Olson, *ACS Chem Biol* **2016**, *11*, 3300-3304.

[194] H. Tian, T. P. Sakmar, T. Huber, *Chemical communications* **2016**, *52*, 5451-5454.

[195] T. Bakkum, T. van Leeuwen, A. J. C. Sarris, D. M. van Elsland, D. Poulcharidis, H. S. Overkleeft, S. I. van Kasteren, *ACS Chem Biol* **2018**, *13*, 1173-1179.

[196] M. Kubankova, I. Lopez-Duarte, J. A. Bull, D. M. Vadukul, L. C. Serpell, M. de Saint Victor, E. Stride, M. K. Kuimova, *Biomaterials* **2017**, *139*, 195-201.

[197] R. Worch, Z. Petrasek, P. Schwille, T. Weidemann, *J Membr Biol* **2016**.

[198] C. E. Chivers, E. Crozat, C. Chu, V. T. Moy, D. J. Sherratt, M. Howarth, *Nat Methods* **2010**, *7*, 391-393.

[199] C. E. Chivers, A. L. Koner, E. D. Lowe, M. Howarth, *Biochem J* **2011**, *435*, 55-63.

[200] H. E. Murrey, J. C. Judkins, C. W. Am Ende, T. E. Ballard, Y. Fang, K. Riccardi, L. Di, E. R. Guilmette, J. W. Schwartz, J. M. Fox, D. S. Johnson, *Journal of the American Chemical Society* **2015**, *137*, 11461-11475.

[201] T. Schvartz, N. Aloush, I. Goliand, I. Segal, D. Nachmias, E. Arbely, N. Elia, *Mol Biol Cell* **2017**, *28*, 2747-2756.

[202] R. Serfling, C. Lorenz, M. Etzel, G. Schicht, T. Bottke, M. Morl, I. Coin, *Nucleic Acids Res* **2018**, *46*, 1-10.

[203] I. Nikic, G. Estrada Girona, J. H. Kang, G. Paci, S. Mikhaleva, C. Koehler, N. V. Shymanska, C. Ventura Santos, D. Spitz, E. A. Lemke, *Angewandte Chemie* **2016**, *55*, 16172-16176.

[204] W. H. Schmied, S. J. Elsasser, C. Uttamapinant, J. W. Chin, *Journal of the American Chemical Society* **2014**, *136*, 15577-15583.

[205] J. A. Wagner, D. Mercadante, I. Nikic, E. A. Lemke, F. Grater, *Chemistry* **2015**, *21*, 12431-12435.

[206] S. V. Mayer, A. Murnauer, M. K. von Wrisberg, M. L. Jokisch, K. Lang, *Angewandte Chemie* **2019**, *58*, 15876-15882.

[207] B. Gibson, J. M. M. Verkade, N. S. Barta, J. C. Hodges, F. L. Van Delft, *Chim Oggi* **2013**, *31*, 18-21.

[208] B. Spangler, S. Yang, C. M. Baxter Rath, F. Reck, B. Y. Feng, *ACS Chem Biol* **2019**, *14*, 725-734.

[209] T. H. Poole, J. A. Reisz, W. L. Zhao, L. B. Poole, C. M. Furdui, S. B. King, *Journal of the American Chemical Society* **2014**, *136*, 6167-6170.

[210] B. D. Fairbanks, E. A. Sims, K. S. Anseth, C. N. Bowman, *Macromolecules* **2010**, *43*, 4113-4119.

[211] Y. Sun, X. W. Ma, K. Cheng, B. Y. Wu, J. L. Duan, H. Chen, L. H. Bu, R. P. Zhang, X. M. Hu, Z. X. Deng, L. Xing, X. C. Hong, Z. Cheng, *Angew Chem Int Edit* **2015**, *54*, 5981-5984.

[212] S. C. Reddington, E. M. Tippmann, D. D. Jones, *Chemical communications* **2012**, *48*, 8419-8421.

[213] M. K. Singh, H. Shweta, M. F. Khan, S. Sen, *Phys Chem Chem Phys* **2016**, *18*, 24185-24197.

[214] F. F. Chu, D. Doyle, *The Journal of biological chemistry* **1985**, *260*, 3097-3107.

[215] J. F. Hare, K. Taylor, *Proceedings of the National Academy of Sciences of the United States of America* **1991**, *88*, 5902-5906.

[216] M. Yamaguchi, M. Michishita, K. Hirayoshi, K. Yasukawa, M. Okuma, K. Nagata, *The Journal of biological chemistry* **1992**, *267*, 22035-22042.

[217] Z. Marijanovic, J. Ragimbeau, K. G. Kumar, S. Y. Fuchs, S. Pellegrini, *Biochem J* **2006**, *397*, 31-38.

[218] I. S. Hitchcock, M. M. Chen, J. R. King, K. Kaushansky, *Blood* **2008**, *112*, 2222-2231.

[219] K. P. Stone, A. J. Kastin, H. Hsuchou, C. Yu, W. Pan, *J Neurochem* **2011**, *116*, 544-553.

[220] C. M. Henriques, J. Rino, R. J. Nibbs, G. J. Graham, J. T. Barata, *Blood* **2010**, *115*, 3269-3277.

[221] K. Friedrich, W. Kammer, I. Erhardt, S. Brandlein, S. Arnold, W. Sebald, *Eur J Biochem* **1999**, *265*, 457-465.

[222] C. K. Lim, H. Abolhassani, S. K. Appelberg, M. Sundin, L. Hammarstrom, *Allergy Asthma Clin Immunol* **2019**, *15*, 2.

VI Appendix

15 Chemicals

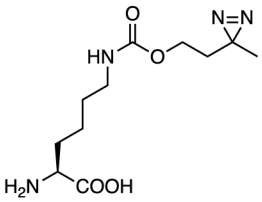

AbK

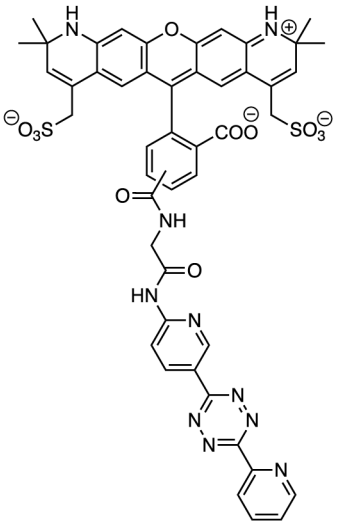

Alexa568-tet1

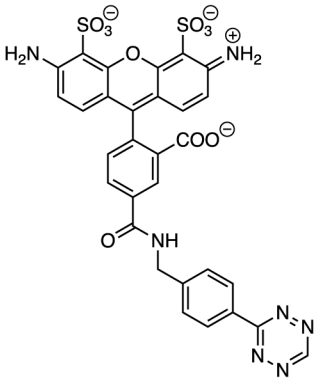

Alexa488-tet2

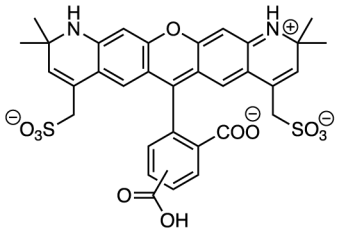

Alexa568-COOH

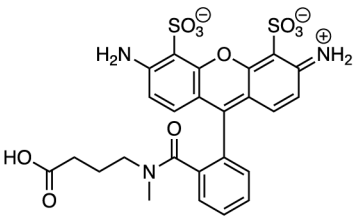

ATTO488-COOH

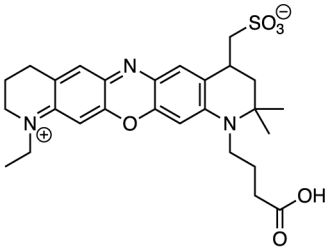

ATTO655-COOH

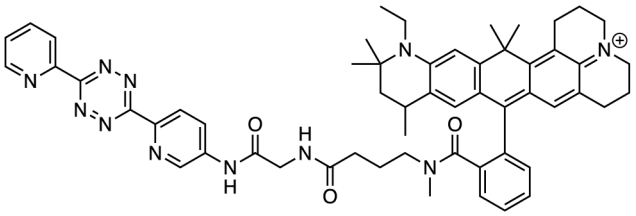

ATTO674N-tet1

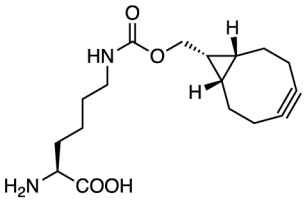

BCNK (endo)

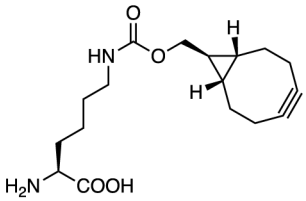

BCNK (exo)

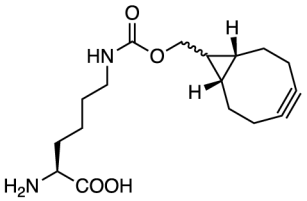

BCNK (mix)

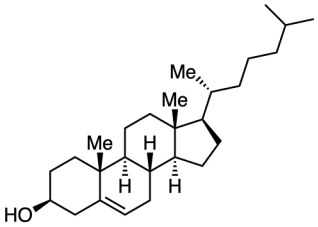

Cholesterol

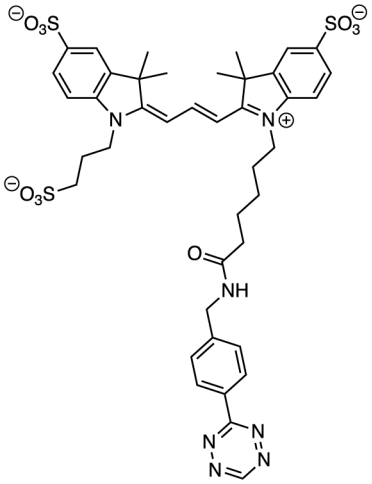

Cy3-tet2

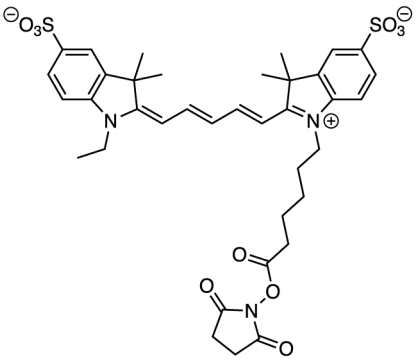

Cy5-NHS

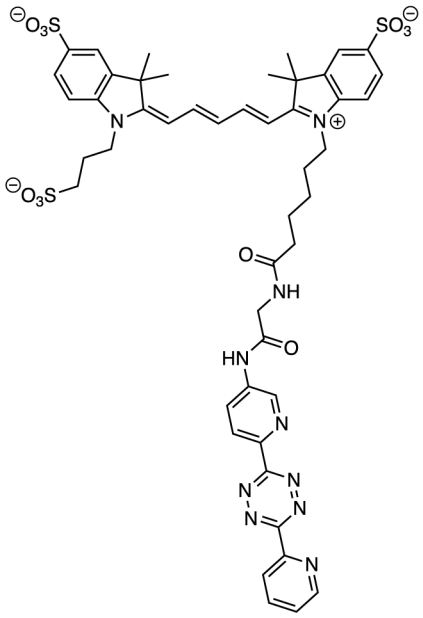

Cy5-tet1

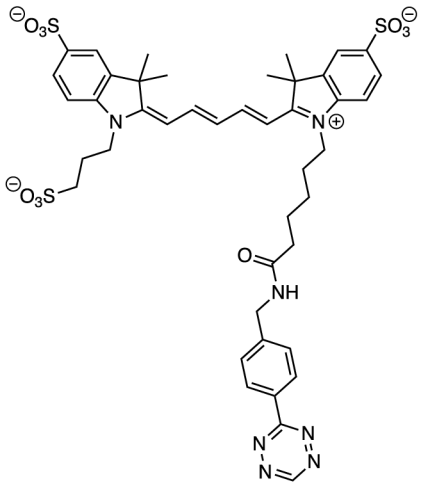

Cy5-tet2

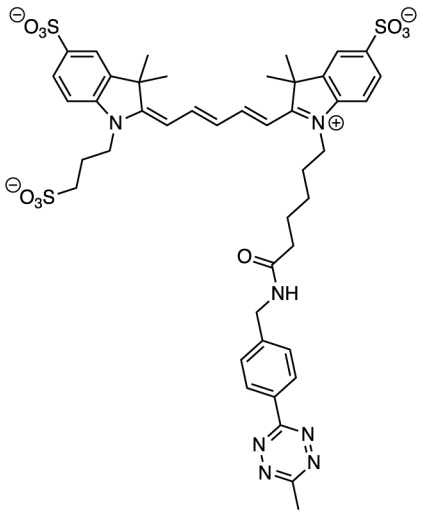

Cy5-tet3

DOPC
18:1 (Δ9-cis)

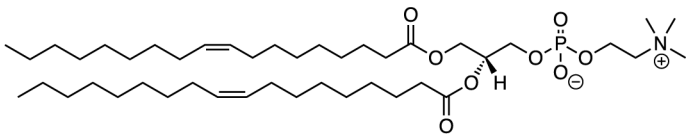

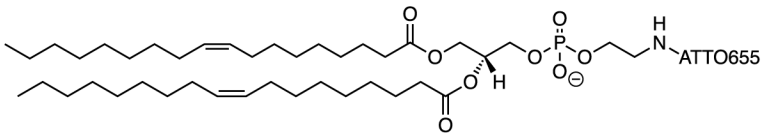

DOPE-ATTO655
18:1 (Δ9-cis)

DOTAP
18:1 (Δ9-cis)

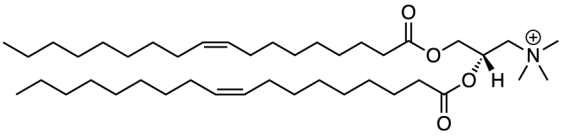

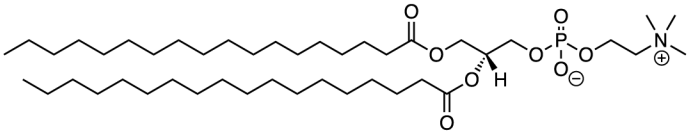

DSPC
18:0

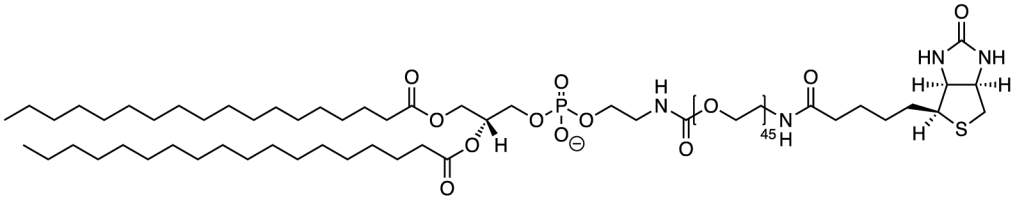

DSPE-PEG(2000)-Biotin
18:0

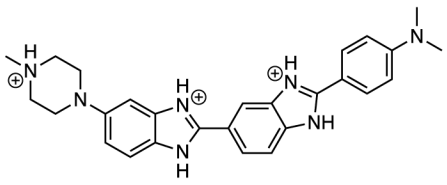

Hoechst 34580

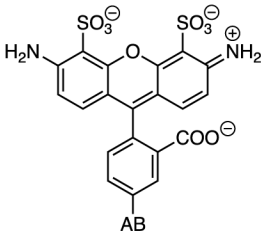

IL-4-AB-Alexa488

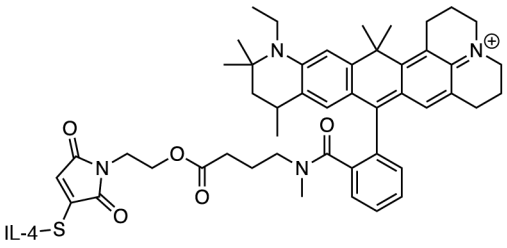

IL-4-ATTO647N

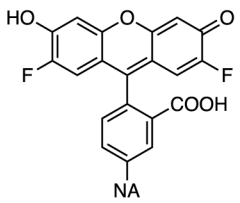

NeutrAvidin-Oregon Green 488

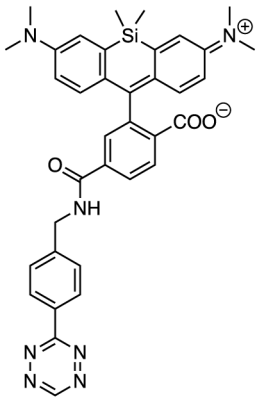

SiR-tet2

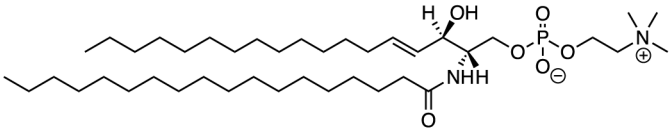

Sphingomyelin
18:0

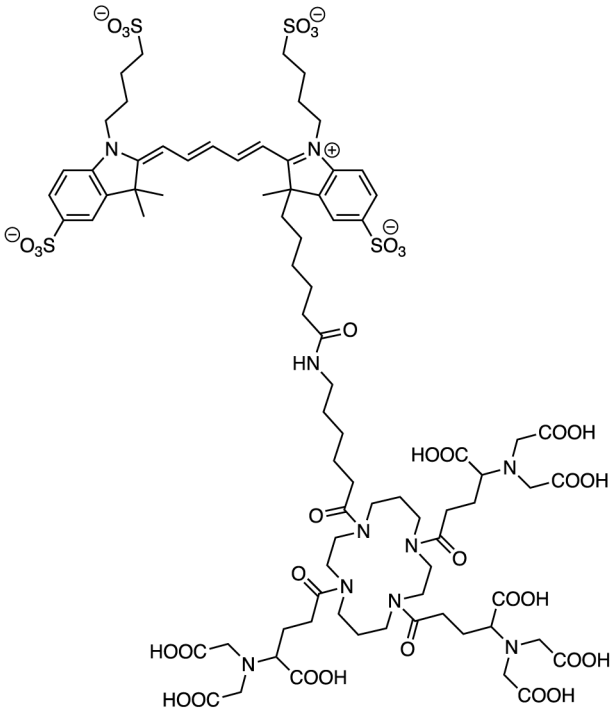

trisNTA-Alexa647

16 Protein sequences

Selected representations of important DNA/protein constructs used in this study:

IL-4 (N38C, F82D)

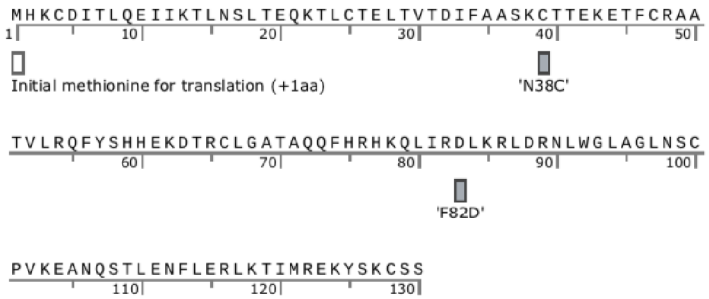

CMV_H_6-IL2Rg

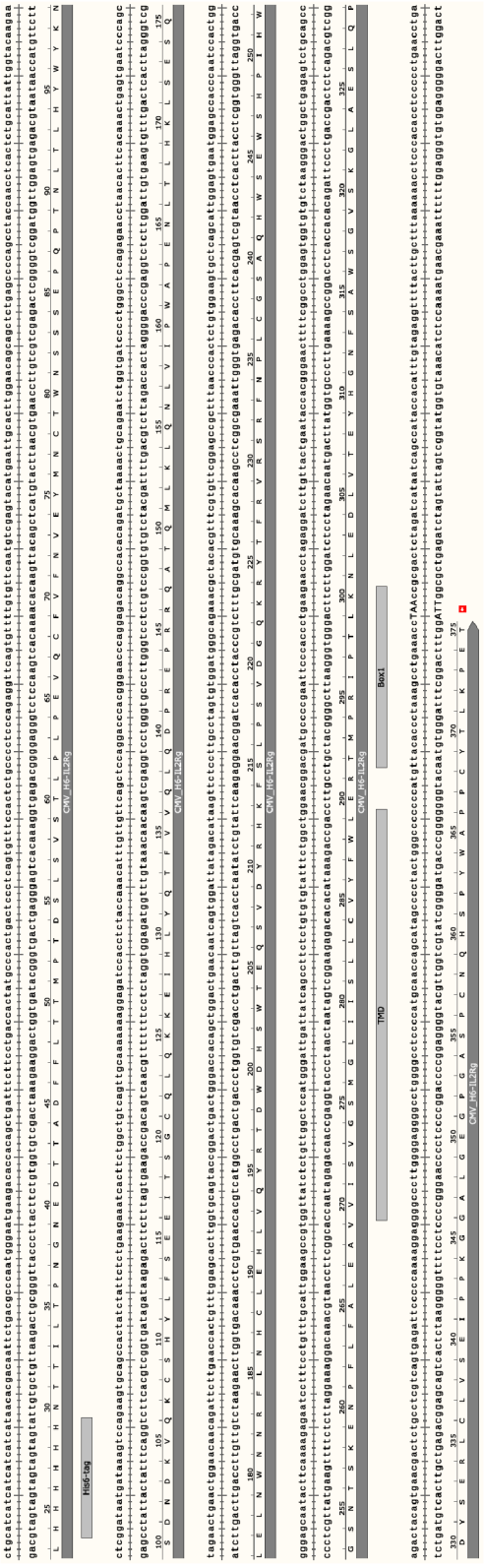

CMSV_H_6-IL2Rg-m5

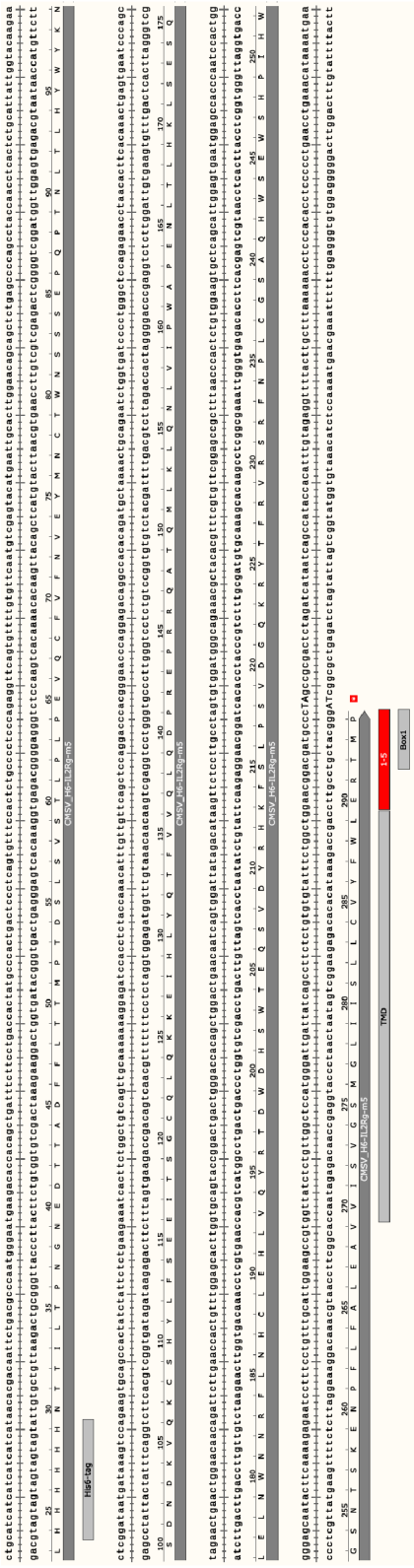

CMV_H6-IL2Rg-S55TAG-3HA

CMV_H6-IL4Ram266-K97TAG

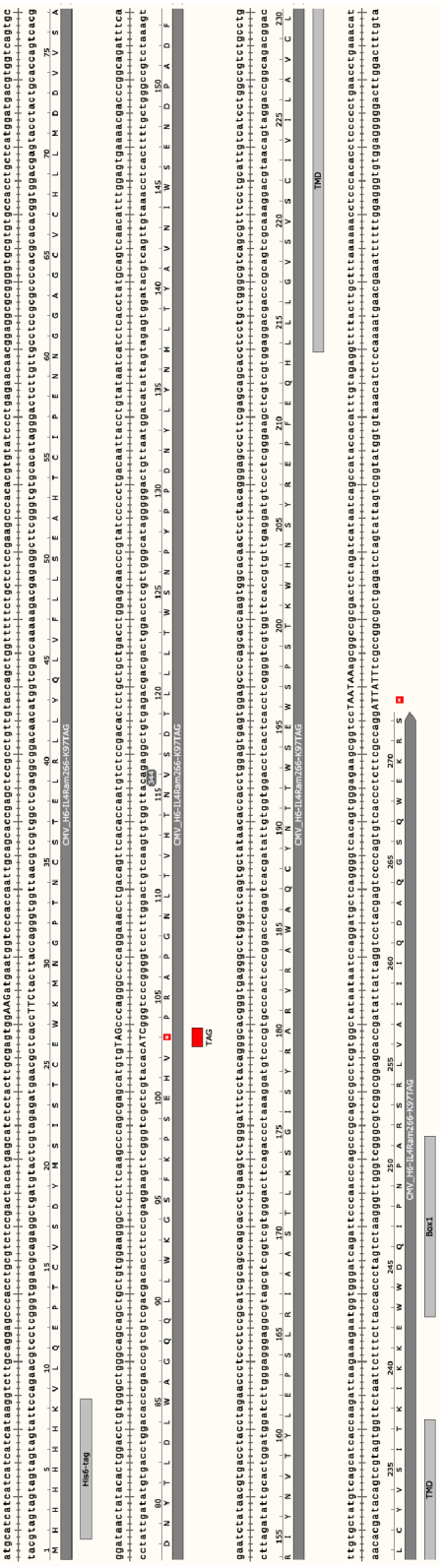

CMV_H6-IL4Ram266-K97TAG-EGFP

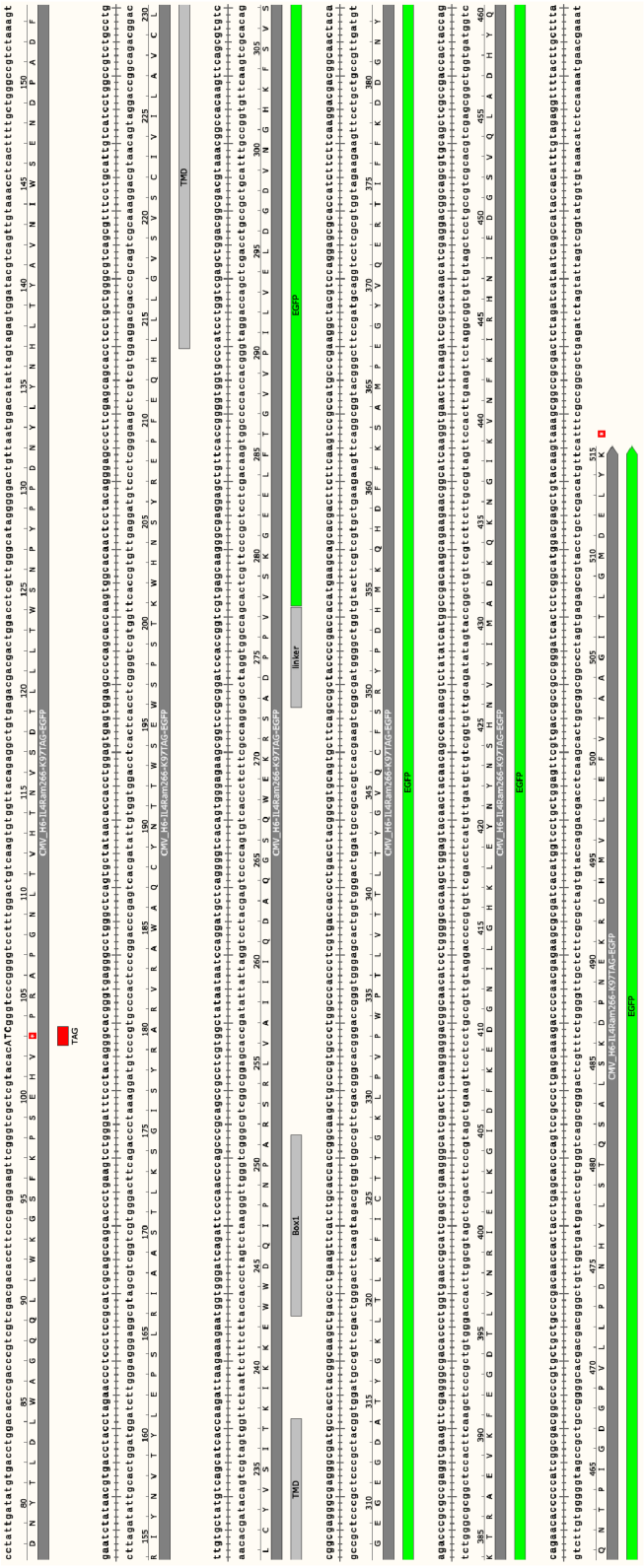

CMV_H6-IL4Ra-K97TAG

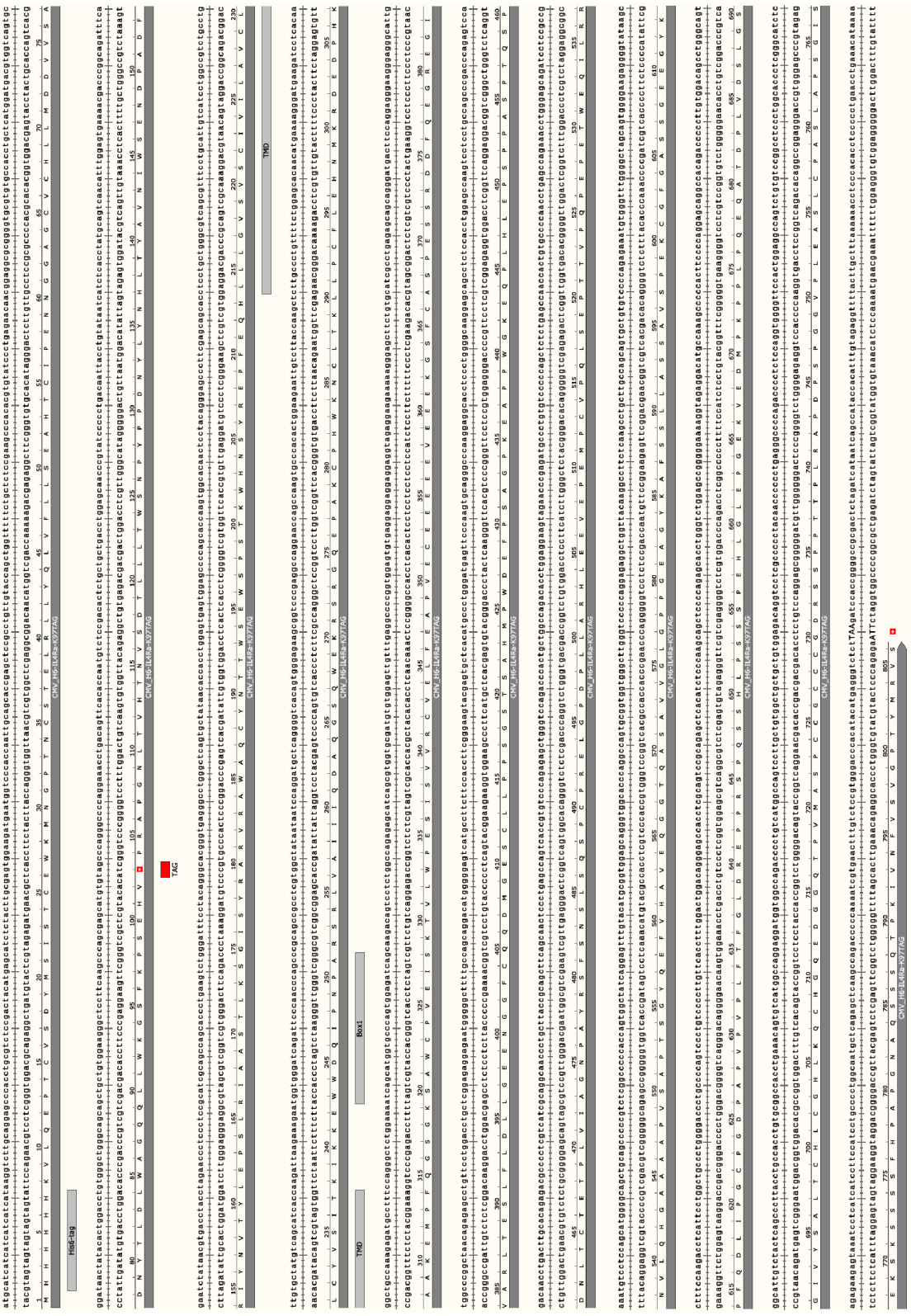

CMV_JAK-EGFP

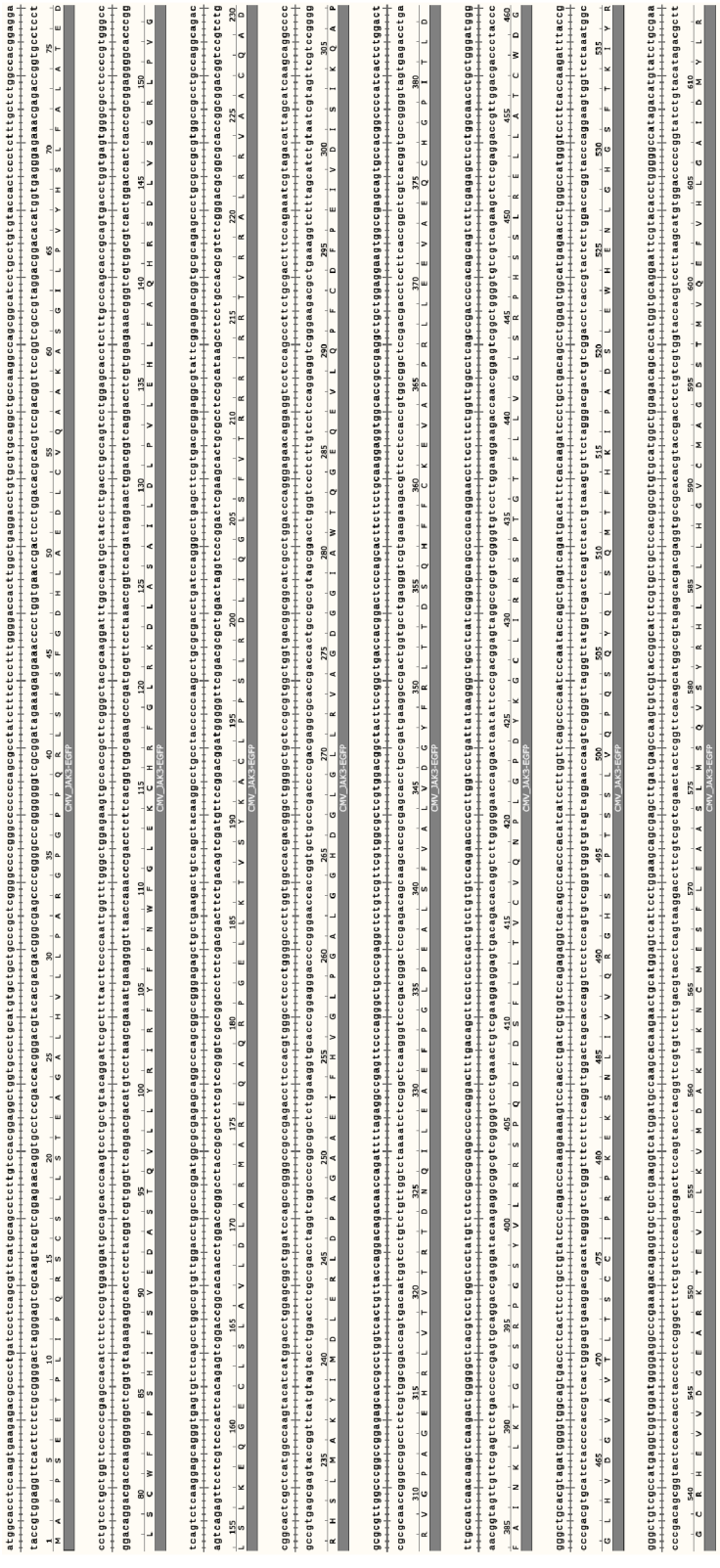

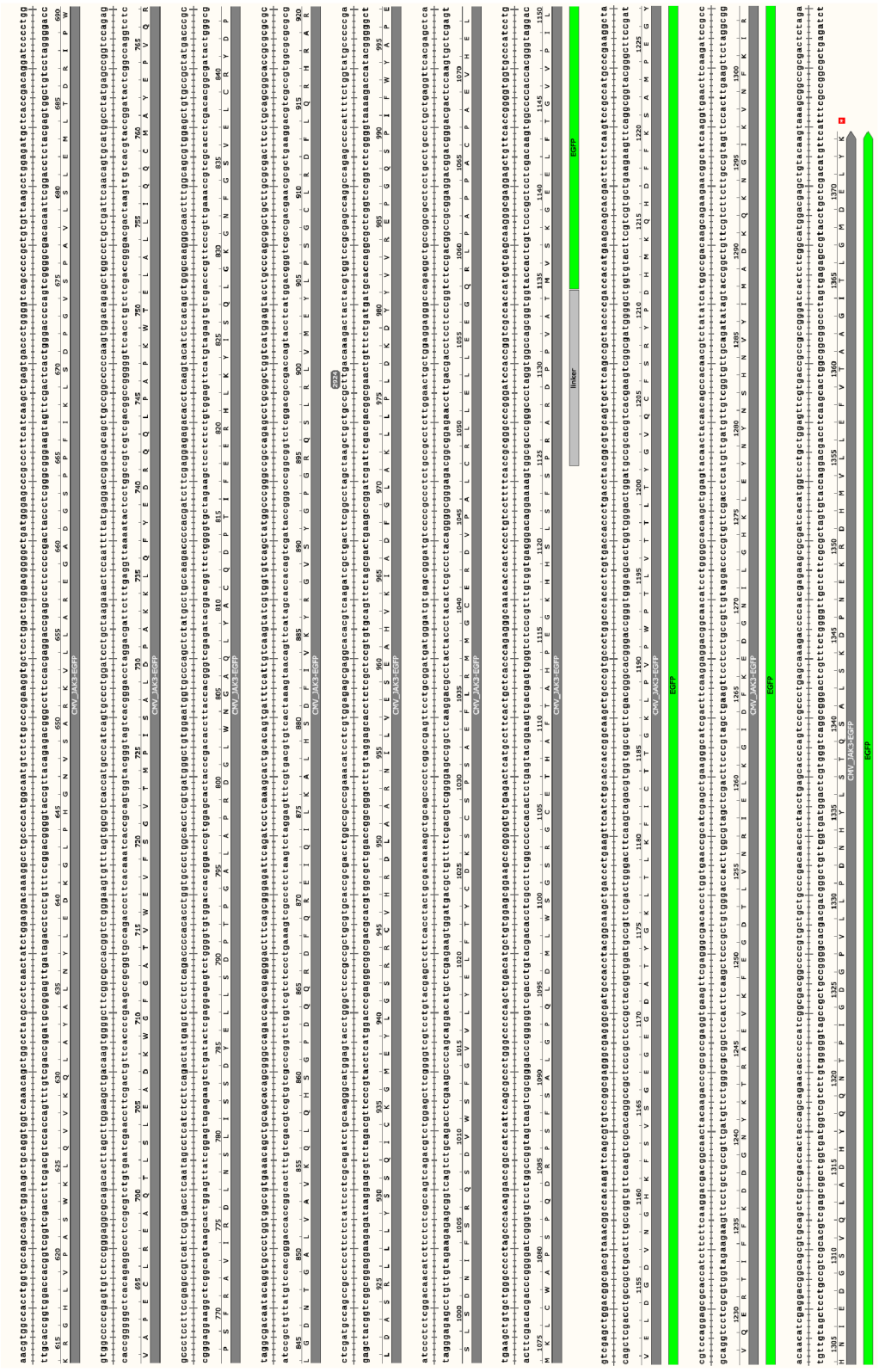

CMV_STAT6

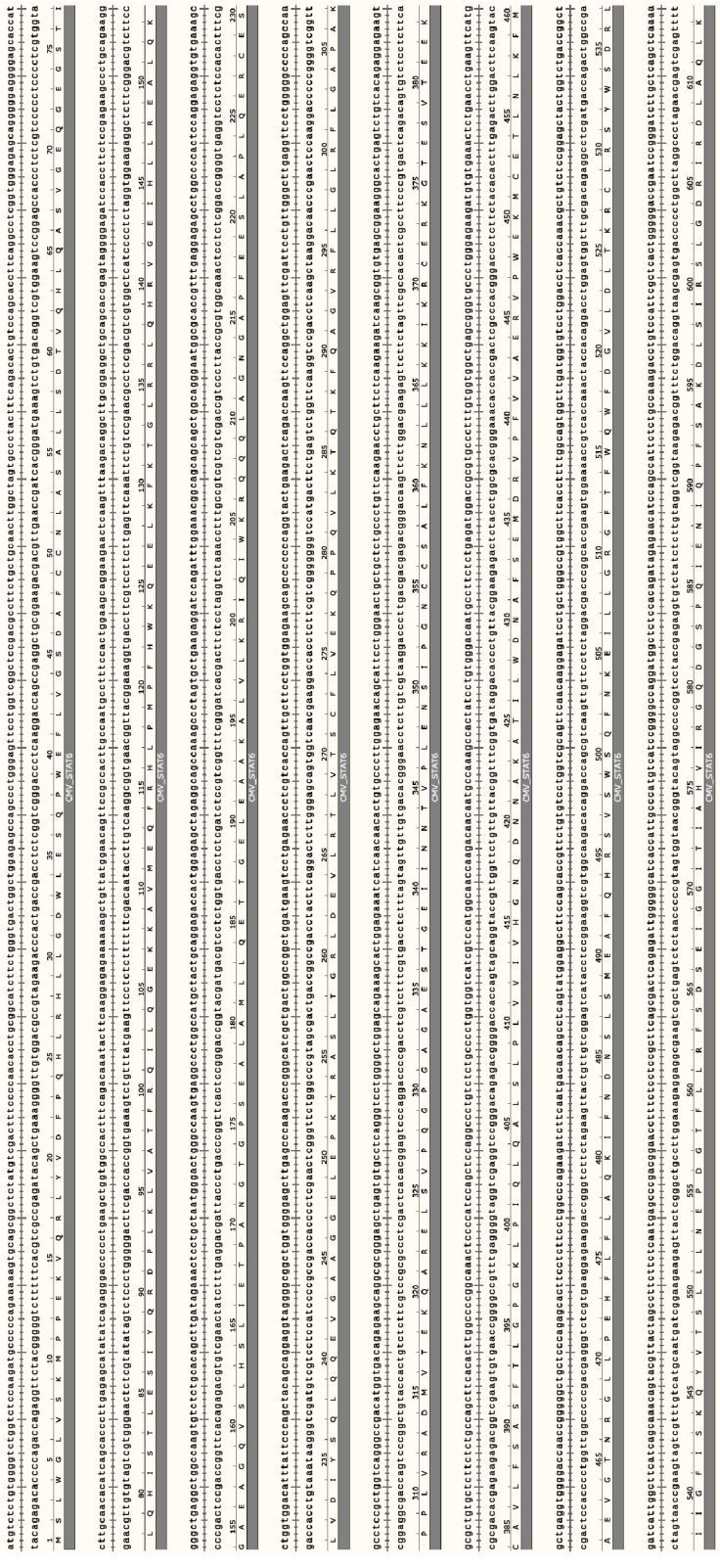

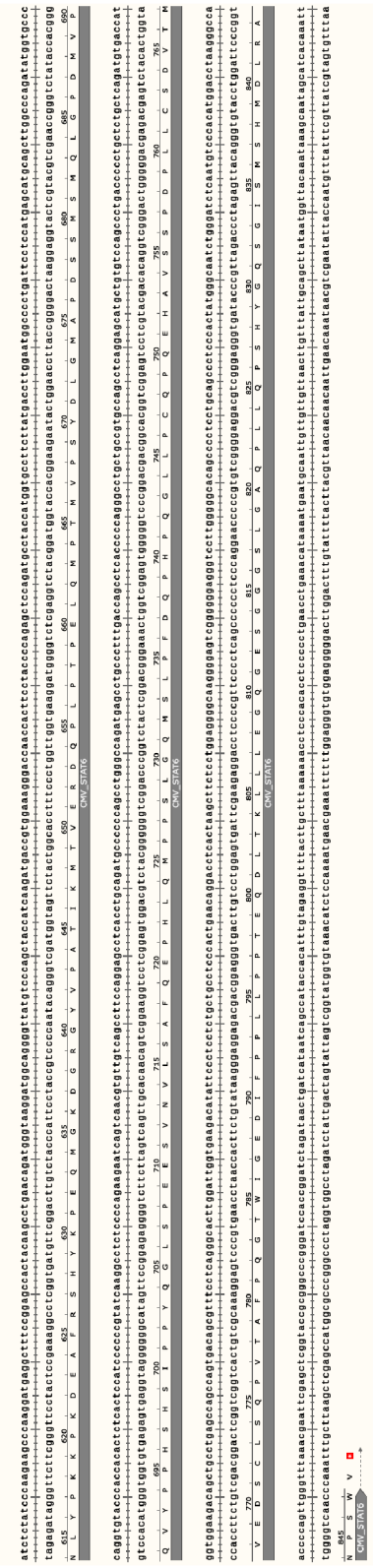

pc2SV_2xME-EGFP

SE323_wtPylRS_4xPylT-new-BCNK-mutations

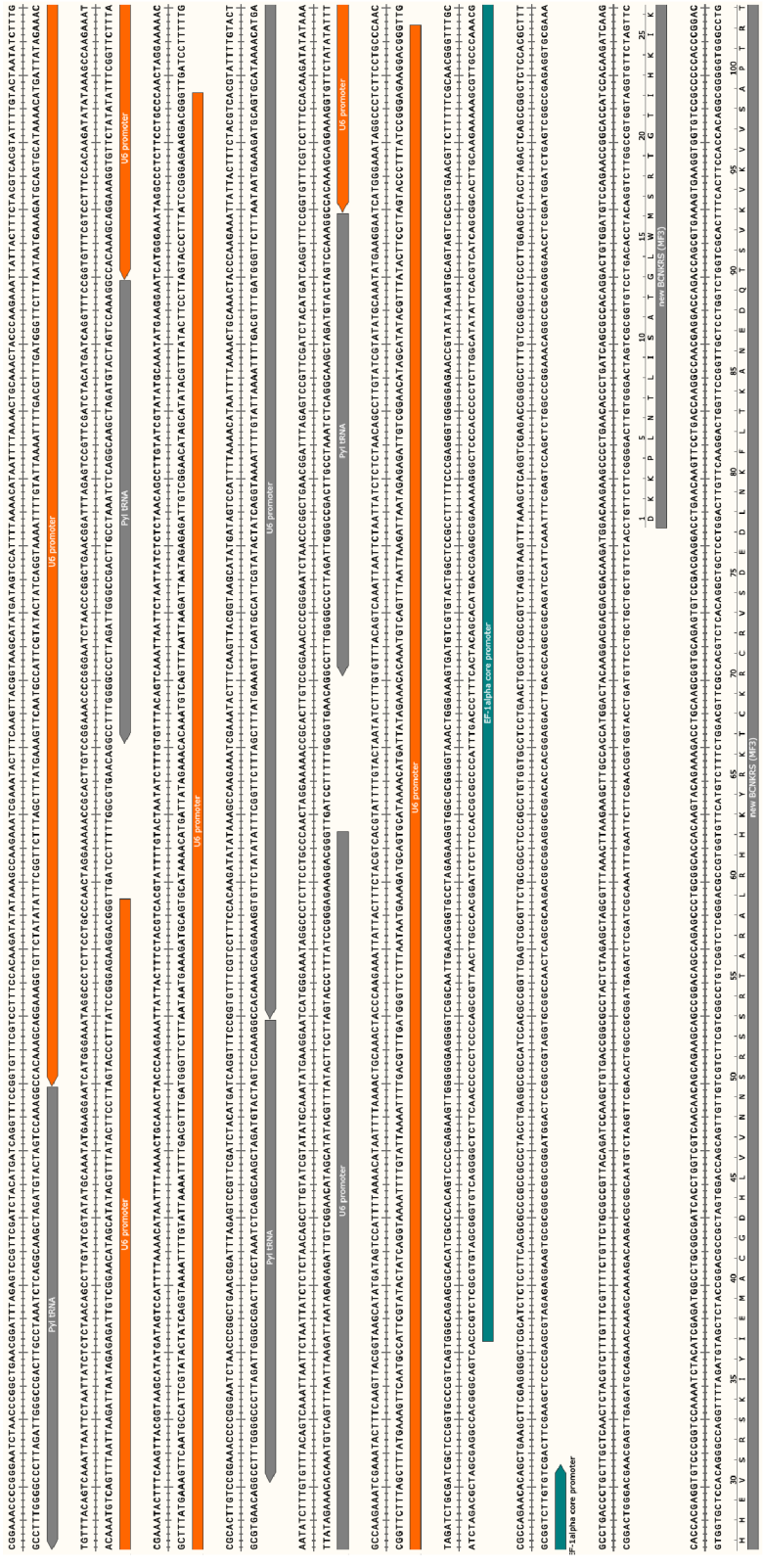

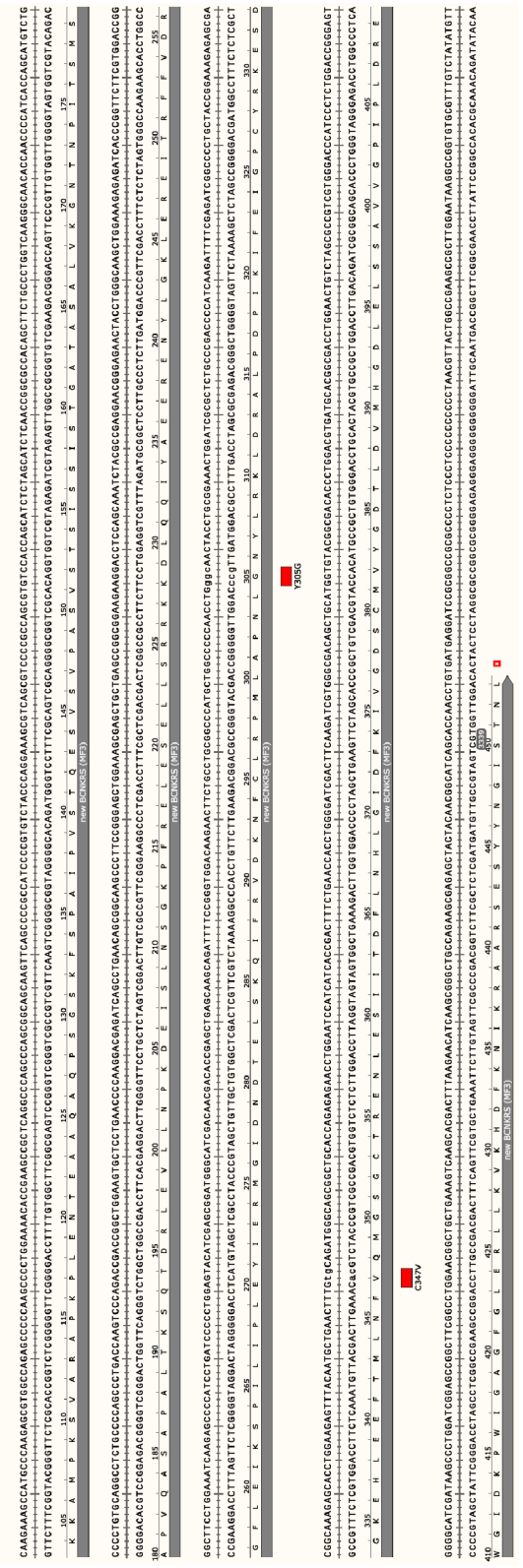
new BsmAI (MF3)
new BsmAI (MF3)
new BsmAI (MF3)
new BsmAI (MF3)
new BsmAI (MF3)
C347V
Y305G